

VT-Forschungsbericht 2017-02

**Experimental Study of Oxyfuel
Combustion for Stationary Gas
Turbine Applications**

Bhavin K. Kapadia

Deutsches Zentrum für Luft- und Raumfahrt
Institut für Verbrennungstechnik
Stuttgart



DLR

**Deutsches Zentrum
für Luft- und Raumfahrt**



Herausgeber

Deutsches Zentrum
für Luft- und Raumfahrt

**Institut für
Verbrennungstechnik**

Pfaffenwaldring 38-40
70569 Stuttgart

Telefon
Telefax

(0 7 11) 68 62 - 3 08
(0 7 11) 68 62 - 5 78

Als Manuskript gedruckt.
Abdruck oder sonstige Verwendung
nur nach Absprache mit dem Institut gestattet.

D93, Stuttgart

Experimental Study of Oxyfuel Combustion for Stationary Gas Turbine Applications

A thesis accepted by the Faculty of Aerospace Engineering and Geodesy
of the University of Stuttgart in partial fulfillment of the requirements
for the degree of Doctor of Engineering Sciences (Dr.-Ing.)

by

Bhavin K. Kapadia

born in Valsad, Gujarat, India

Main Referee:	Prof. Manfred Aigner
Co-Referee:	Prof. Henning Bockhorn
Date of Defence:	29.06.2016

Institute of Combustion Technology for Aerospace Engineering
University of Stuttgart

2017

Acknowledgements

My employment at the Institute of Combustion Technology at DLR, Stuttgart for this research subject has been a most enlightening and joyful experience, thanks to the supportive nature of many colleagues.

Firstly, I would like to thank Prof. Manfred Aigner for reviewing my work, as well as the opportunity to pursue research at the institute with the excellent facilities at hand. I would like to extend my gratitude to Prof. Henning Bockhorn for reviewing and evaluating the dissertation. I especially thank Dr. Wolfgang Meir for the guidance and inputs into different aspects of this work. In depth discussions with him on swirl stabilized combustion were captivating and extremely helpful. I extend my heartfelt gratitude to Dr. Peter Kutne for his constant guidance on the different measurement campaigns. His support and suggestions during the Raman measurements and experiments on the high pressure optical test rig (HIPOT) have been most valuable.

I am thankful to Dr. Michael Stoehr for the support with the flow velocity measurements and data analysis. I am grateful to Dr. Isaac Boxx for the assistance with the high speed measurements on the HIPOT test rig. The construction and operation of the HIPOT test rig would not have been possible without the support of Mr. Tobias Rapp and Mr. Jochen Eichhorn. I am also thankful to Mr. Jens Kreeb, Mr. Ralph Bruhn and the workshop for their quick response to finishing mechanical components for running the experiments. I extend my thanks to Dr. Jan Hendrick Starcke for the help with chemical kinetic calculations on oxyfuel flames.

During my stay at the institute many colleagues have also become good friends and their presence has been a source of inspiration. My parents, brother and friends have been a source of constant moral support during this process. I am grateful to them for that.

Contents

Nomenclature	ix
Abstract	xiii
Kurzfassung	xv
List of Figures	xvii
List of Tables	xxiii
1 Introduction	1
1.1 Carbon capture and storage	1
1.2 Oxyfuel Combustion	3
2 Background	7
2.1 Gas turbines	7
2.1.1 Gas turbine combustors	9
2.1.2 Swirl flows and flame stabilization	12
2.1.3 Combustion instabilities	16
2.2 Aspects of oxyfuel gas turbines and combustion	18
2.2.1 Gas turbine cycles for oxyfuel combustion	18
2.2.2 Characteristics of oxyfuel combustion with CO ₂ dilution	21
3 Methodology	25
3.1 Burner configurations	25
3.1.1 Atmospheric pressure burner configuration	25
3.1.2 HIPOT rig and elevated pressure burner	27
3.2 Investigative techniques	30
3.2.1 OH*-chemiluminescence imaging	31
3.2.2 Particle image velocimetry (PIV)	33
3.2.3 Laser Raman spectroscopy	37
3.3 Approach for investigating swirl stabilized oxyfuel flames	41

3.4	Experimental setup: Atmospheric pressure	44
3.4.1	Gas supply, burner instrumentation and control	44
3.4.2	OH*-chemiluminescence imaging and PIV setup	46
3.4.3	Laser Raman spectroscopy setup	48
3.4.3.1	Raman measurements: Calibration and data analysis	51
3.5	Experimental setup: Elevated pressure (5 bar)	53
3.5.1	Simultaneous high speed OH*-chemiluminescence imaging/PIV setup	54
3.6	Measurement uncertainty	55
3.6.1	Burner operation and flame reproducibility	56
3.6.2	Uncertainty in Raman measurements	57
3.6.3	Uncertainty in PIV measurements	61
4	Previous Work	65
4.1	Burner operation regimes	65
4.2	Detailed characterization of standard flames	68
4.2.1	Stable combustion: Flame A	69
4.2.2	Thermo-acoustic oscillations: Flame B	71
4.2.3	Lean blow out: Flame C	72
5	Results	73
5.1	Oxyfuel and air flames at atmospheric pressure	73
5.1.1	Oxyfuel flames at comparable thermal power	75
5.1.1.1	Effect of variation of oxidizer composition	75
5.1.1.2	Effect of variation of equivalence ratio	84
5.1.1.3	Effect of variation of thermal loading	86
5.1.2	Oxyfuel flames at comparable inlet velocities	88
5.1.2.1	Effect of variation of oxidizer composition	88
5.1.2.2	Effect of variation of equivalence ratio	94
5.1.2.3	Effect of increase in inlet velocity	95
5.1.3	Thermo-acoustic oscillation mechanism	98
5.1.4	Thermo-chemical states of swirl stabilized oxyfuel flames	100
5.2	Comparison of air and oxyfuel flames at atmospheric pressure	111
5.3	Difference between atmospheric pressure and elevated pressure burner	118
5.4	Oxyfuel and air flames at elevated pressures	120
5.4.1	Effect of preheating and elevated pressure	120
5.4.2	Effect of change in thermal power and equivalence ratio for air and 30 % O ₂ oxyfuel flames	121
5.4.3	Burner aerodynamics at elevated pressures	128

6 Conclusions	139
Bibliography	143

Nomenclature

Abbreviations

- ADC** Analogue to digital converter.
- ASU** Air separation unit.
- AZEP** Advanced zero emissions power plant.
- CARS** Coherent anti-Stokes Raman spectroscopy.
- CC** Combined cycle.
- CCD** Charge-coupled device.
- CCS** Carbon capture and storage.
- CES** Clean energy system.
- CFD** Computational fluid dynamics.
- CLC** Chemical looping combustion.
- CMOS** Complementary metal-oxide semiconductor.
- DLE** Dry low emissions.
- DLN** Dry low NO_x.
- DLR** Deutsches Zentrum fuer Luft und Raumfahrt.
- DOE** Department of Energy.
- FLOX[®]** Flameless Oxidation.
- GT** Gas turbine.
- GTMC** Gas turbine model combustor.
- HAB** Height above burner.
- HPT** High pressure turbine.
- HRSG** Heat recovery steam generator.
- HTT** High temperature turbine.
- ICCD** Intensified charge-coupled device.
- IGCC** Integrated gasification combined cycle.
- IRZ** Inner recirculation zone.
- ISL** Inner shear layer.
- LDA** Laser Doppler anemometry.
- LNG** Liquefied natural gas.
- LP(P)** Lean premixed prevaporized.

LPT Low pressure turbine.
MILD Moderate and intense low oxidation dilution.
Nd:YAG Neodymium-doped Yttrium Aluminium Garnet.
NETL National Energy Technology Laboratory.
NIST National Institute of Standards and Technology.
ORZ Outer recirculation zone.
OSL Outer shear layer.
PIV Particle image velocimetry.
PLIF Planar laser induced fluorescence.
POD Proper orthogonal decomposition.
PVC Precessing vortex core.
RMS Root mean squared.
RQL Rich-Quench-Lean.
SCOCC Semi-closed oxy-combustion cycle.
ST Steam turbine.
TIT Turbine inlet temperature.
USB Universal serial bus.

Greek notations

Δ Finite difference operator.
 Λ Electronic energy level of a molecule.
 Ω Solid angle.
 Σ Summation operator.
 α Polarization coefficient of a molecule.
 ϵ Efficiency of photon detection system.
 ϵ_o Permittivity of a molecule.
 ϵ_{random} Random error in measurement of a quantity.
 ϵ_{sys} Systematic error in measurement of a quantity.
 η Thermodynamic efficiency.
 γ Adiabatic index.
 λ_0 Wavelength of incident electromagnetic wave (nm).
 μ_f Fluid viscosity (N/s m²).
 $\mu_{H,Y}$ Coefficient denoting proportion of hydrogen in a species Y.
 ω_0 Frequency of electromagnetic wave incident on molecule (rad/s).
 ω_v Natural frequency of oscillation of a molecule (rad/s).
 ω_e Wave number of molecular vibrational state (cm⁻¹).
 ϕ_j j^{th} POD mode.
 ρ Density (kg/m³).

ρ_p PIV particle Density (kg/m^3).
 σ Standard deviation of multiple samples of a measurable quantity.
 τ Time period of oscillation (s).
 τ_s Particle relaxation time (s).
 ν_0 Frequency of incident electromagnetic wave (Hz).
 ν_k Raman frequency shift (Hz).
 φ Equivalence ratio.
 φ_D Acoustic damping ($\text{J}^2/\text{m}^3\text{s}$).

Roman notations

E Electrical field vector.
a Gas flow acceleration (m/s^2).
p Polarization vector of a molecule.
u Velocity field.
x Locations of velocity measurements.
A Number of images recorded.
B Number of velocity measurements in a velocity field.
 $F(\mathbf{r})$ Cylindrical symmetry function.
 $G_i(\mathbf{T})$ Temperature dependent calibration coefficient for molecule i .
I Image pixel intensity.
 $M \times N$ Image pixel resolution.
 P_L Incident Laser intensity (W/m^2).
 $P(\mathbf{x})$ Projection function.
 P_i Intensity of Raman signal from i^{th} species in a mixture (W/m^2).
 Q_{meas} Measured mean value of a given physical quantity.
 Q_{true} True value of a given physical quantity.
Q Molecular co-ordinate representing its vibration.
Re Non-dimensional Reynolds number.
R Order of POD decomposition.
R Geometric radius (mm) of burner part e.g nozzle.
S Non-dimensional swirl number.
T Temperature of gas (K).
 X_Y Mole fraction of a species Y .
Y Notation for a molecular species in combustion.
 $Z_{H,flame}$ Mass fraction of hydrogen atoms at any location in a flame.
 $Z_{H,fuel}$ Mass fraction of hydrogen atoms at any location in a fuel.
f Fuel mixture fraction.
g Camera gain factor.

i Image number index.
i Horizontal pixel index of an image.
j Vertical pixel index of an image.
k Velocity field location index.
l Length of sampled Raman scattering signal.
l Characteristic dimension (m).
*m**x**n* PIV interrogation volume resolution.
n_i Number of molecules of species *i* in sampled region.
n Number density of gas molecules (1/m³).
p' Pressure fluctuation (Pa).
p Pressure (bar).
p_∞ Ambient pressure (bar).
q' Heat release fluctuation (W).
r Compressor pressure ratio.
r Radial reference position (m).
u Axial flow velocity (m/s).
w Tangential flow velocity (m/s).
x Horizontal particle displacement.
y Vertical particle displacement.
d_p Particle diameter (m).
f Focal length of optical device.
J Molecular rotational quantum number.
St Non-dimensional Stokes number.
U Gas velocity surrounding particle (m/s).
U_p Particle velocity (m/s).
U_s Particle slip velocity (m/s).
V Control volume (m³).
v Molecular vibrational quantum number.
V_{avg} Average inlet flow velocity (m/s).

Universal constants

c Speed of light in vacuum (2.99792458 x 10⁸ m/s).
h Planck's constant (6.62606957 x 10⁻³⁴ m² kg/s).
k Boltzmann constant (1.3806488 x 10⁻²³ m² kg/s²K).

Abstract

Oxyfuel combustion is a concept proposed for the implementation of carbon capture and storage (CCS) technologies in coal and gas turbines power plants to prevent emission of CO₂ into the atmosphere. In order to apply the concept to gas turbines power plants, they have to be modified or alternatively new cycles need to be developed for using this concept. Amongst the different cycles proposed those involving O₂ and CO₂ as working fluid offer simplicity of design together with promising carbon capture and cycle efficiencies. New burners need to be designed for use in such oxyfuel gas turbines. The combustion characteristics of such burners would strongly depend on the proportion of O₂ and CO₂ in the oxidizer. The physical and chemical properties of such mixtures are different from air which has been vastly used in gas turbine flames. In this work oxyfuel combustion with a mixture of O₂ and CO₂ as oxidizer has been studied experimentally using a well-researched methane-air swirl burner with an optically accessible combustion chamber. Partially premixed swirl stabilized oxyfuel flames have been investigated using optical measurement techniques at atmospheric and elevated pressure conditions. The effect of changing parameters such as CO₂ dilution, flow velocity, equivalence ratio, and thermal power on flame stabilization, flow field and flame chemistry has been studied. Optical measurement techniques such as OH*-chemiluminescence imaging, particle image velocimetry (PIV) and laser Raman spectroscopy have been used to characterize the flames. The investigations were performed under conditions of comparable thermal power and inlet flow velocity for different CO₂ dilutions. A strong dependence of the flame shape and stability on CO₂ dilution was observed at similar thermal powers and inlet flow velocities. Flames containing less than 26 % O₂ in the oxidizer could not be stabilized, while 26 % O₂ flames showed poor stabilization over a wide operating range. Flames with 30 % O₂ were predominantly stable over a large range of operation and had a typical conical swirl flame shape. Flames with an O₂ concentration higher than 30 % showed a flat flame shape and excited thermo-acoustic oscillations. The change in flame shape was accompanied by a change in the flow field and coherent flow structures. A comparison to air flame behavior showed similarity between the influences of CO₂ dilution in oxyfuel flames to a change in equivalence ratio for air flames. This similarity was correlated to a change in laminar flame speeds of the two flame types. The Raman measurements revealed that

despite similar conical flame shape of 30 % O₂ oxyfuel and lean air flames, the stabilization of the oxyfuel flame was poorer due to the lower reactivity. The measurements also showed that a large amount of CO is produced in such flames in the IRZ (inner recirculation zone) and differences in heat transfer characteristics produces contrasting effects in the burnt gases in the IRZ and ORZ (outer recirculation zone). The 30 % O₂ flame and air flames were investigated under elevated pressure conditions with a modified version of the atmospheric burner with optical access to the combustion chamber. At conditions of increased oxidizer preheat and elevated pressure an unconventional flame shape was observed, where the flame burned at close proximity to the burner plate and chamber windows. Both oxyfuel and air flames showed this behavior pointing to a limited suitability of the burner under elevated pressure conditions. A change in burner aerodynamics at elevated pressure was identified as the cause for the unconventional flame shape. The burner design for oxyfuel gas turbines is dependent on the CO₂ dilution intended to be used. The investigations showed unsuitability of using partially premixed combustion for low O₂ concentrations. The high O₂ concentration flames are thought to be suitable for a staged combustion concept where the higher reactivity of such flames would be useful for pilot flame stabilization and keeping overall temperatures in an acceptable region for the gas turbine. At the end of the work the differences between air and oxyfuel combustion are summarized and an overview is presented of burner configurations favorable for use in real oxyfuel gas turbines.

Kurzfassung

Die Oxyfuel-Verbrennung ist eine von verschiedenen Methoden zur CO_2 -Abscheidung und Speicherung, um die Emission des Treibhausgases CO_2 aus Kraftwerksprozessen in die Atmosphäre zu verhindern. Diese Technik kann für Kohle wie auch für Gasturbine-Kraftwerke angewendet werden. Es wurden mehrere thermodynamische Zyklen für die Oxyfuel-Verbrennung vorgeschlagen. Die Zyklen, die für O_2 und CO_2 als Oxidator ausgelegt sind, sind weniger komplex und vielversprechend in Bezug auf die CO_2 -Abtrennungs- und Energieeffizienz. Um diese Zyklen in Gasturbinen anzuwenden, sind jedoch neue Brennerkonzepte erforderlich. Das Verhalten von Flammen mit O_2/CO_2 -Mischung als Oxidator weicht von Luft-Flammen ab, weil die physikalischen und chemischen Eigenschaften der beteiligten Gase unterschiedlich sind. In dieser Dissertation wurde die Oxyfuel-Verbrennung mit O_2 und CO_2 als Oxidator in einem drallstabilisierten Gasturbinen-Modellbrenner mittels optischer Messmethoden untersucht, um die Unterschiede zur Verbrennung mit Luft als Oxidator zu analysieren. Teil-vorgesichtete Oxyfuel-Drallflammen wurden mit OH^* -Chemilumineszenz, Particle Image Velocimetry (PIV) und Raman-Spektroskopie unter atmosphärischen und Hochdruckbedingungen charakterisiert. Anhand dieser Methoden wurde der Einfluss von Parametern wie der O_2 -Konzentration, dem Äquivalenzverhältnis, der Strömungsgeschwindigkeit und der thermischen Leistung auf die Flammeneigenschaften studiert. Die Flammenform und Stabilität hing dabei stark von der O_2 -Konzentration ab. Die Flammen mit weniger als 26 % O_2 waren über einen großen Betriebsbereich instabil. Die Flammen mit 30 % O_2 hatten eine konische Flammenform und zeigten die beste Stabilität mit geringen thermoakustischen Schwingungen. Thermoakustische Instabilitäten traten bei Flammen mit mehr als 30 % O_2 auf. Der Abstand der Flamme zur Brenneroberfläche wurde mit zunehmender O_2 -Konzentration geringer, so dass die Flammen flacher wurden. Die Flammformänderung zeigte Auswirkungen auf das Strömungsfeld und auf kohärente Flammenstrukturen. Die Änderung der Flammform korrelierte mit der laminaren Flammengeschwindigkeit, die für höhere O_2 -Konzentrationen im Oxidator zunimmt. Ein Vergleich mit Luftflammen zeigte, dass die Änderung der Flammenform, die durch Variation der O_2 Konzentration im Oxidator bei Oxyfuel-Flammen entsteht, dem Verhalten in Luftflammen bei Änderung

des Äquivalenzverhältnis ähnelt. Trotz der Ähnlichkeit der Flammenform von Luftflammen und Oxyfuelflammen mit 30 % O₂, brannten die Oxyfuelflammen auf Grund geringerer chemischer Reaktivität weniger stabil im Vergleich zu Luftflammen. Die Raman-Messungen ergaben relativ hohe CO-Konzentrationen in der inneren Rezirkulationszone und Unterschiede in der Wärmeübertragung in der inneren und äußeren Rezirkulationszone im Vergleich zu Luftflammen. Eine modifizierte Version des atmosphärischen Brenners wurde unter erhöhtem Druck (5 bar) und bei erhöhter Oxidatortemperatur untersucht. Dabei wurden (insbesondere) Oxyfuelflammen mit 30 % O₂ und Luftflammen untersucht. Unter diesen Bedingungen wurde für Luft- und Oxyfuelflammen eine unkonventionelle Flammenform beobachtet mit einer Flammenstabilisierung nah an der Brenneroberfläche und den Brennkammerfenstern. Diese eher ungünstige Flammenform wurde durch eine Änderung der aerodynamischen Eigenschaften des Brenners erklärt. Die Untersuchungen haben gezeigt, dass das Brennerdesign in Oxyfuel-Gasturbinen stark von der geplanten CO₂-Verdünnung im Oxidator abhängt. Für einen Oxidator mit weniger als 30 % O₂ ist die teil-vorgemischte Verbrennung auf Grund der geringen Reaktivität nicht geeignet. Ein Oxidator mit höherem O₂-Anteil zeigt eine vorteilhafte Stabilisierung und die damit verbundene hohe Flammentemperatur könnte mit einem gestuften Verbrennungssystem reduziert werden. Am Ende der Arbeit wurden die Unterschiede zwischen Oxyfuel- und Luftverbrennung zusammengefasst und Brenner-Modifikationen sowie Konfigurationen zur Anwendung in technischen Oxyfuelbrennern vorgestellt.

List of Figures

2.1	Open Brayton cycle for gas turbines.	8
2.2	Cross-section of different types of combustors in gas turbines, when observing the gas turbine from the exhaust nozzle. Black color represents flow not participating in combustion.	9
2.3	Typical annular combustor configuration (adapted from wikipedia).	10
2.4	Radial swirl generator block (swirler).	13
2.5	Typical swirl flow flame stabilization mechanism.	14
2.6	Variation of pressure, heat release and flow characteristics during a single phase of oscillation.	17
2.7	Semi-closed oxy-combustion cycle with CO ₂ as working fluid (Based on Amann [1]).	19
2.8	The basic Graz thermodynamic cycle for oxyfuel gas turbines (based on Jericha [2]).	20
2.9	Variation of heat capacity of different gases (from NIST database).	21
2.10	Experimental and simulated laminar flame speed of different oxyfuel mixtures at 3 bar and 473 K preheat [3].	23
3.1	Atmospheric partially premixed swirl burner configuration.	26
3.2	Test rig for measurements at elevated pressures.	28
3.3	Burner assembled in high pressure rig.	29
3.4	High pressure swirl stabilized burner configuration.	30
3.5	Abel projection of an axisymmetric function for a parallel beam.	32
3.6	Basic principle of 2-component 2-d PIV measurement technique.	34
3.7	Correlation of particle light scattering images for obtaining velocity information.	35
3.8	Energy level diagram explaining elastic and inelastic scattering of electromagnetic radiation by molecules.	38
3.9	Typical vibrational Raman spectrum for scattering by different species in a near stoichiometric premixed methane air flame using a 532nm Nd:YAG laser.	40

3.10	Typical swirl burner stable operation map for air flames.	42
3.11	Overview of experiments performed and associated measurement techniques used to characterize oxyfuel flames.	44
3.12	Gas supply, instrumentation and control for operating burner under atmospheric conditions.	45
3.13	Simultaneous OH*-chemiluminescence imaging and stereoscopic PIV setup.	46
3.14	Setup of laser Raman spectroscopy for oxyfuel flames at atmospheric pressure.	49
3.15	An example of a 300 laser-shot averaged 1-d Raman spectrum for a premixed methane-air matrix burner flame at atmospheric conditions.	50
3.16	Devices used for the calibration of laser Raman Spectroscopy signal.	51
3.17	Simultaneous high speed PIV/OH*-chemiluminescence imaging setup for elevated pressure experiments.	55
3.18	Schematic showing perspective error in 2-component PIV due to out of plane particle motion.	62
4.1	Images of CH ₄ /air flames visible luminescence at different thermal powers and equivalence ratios.	66
4.2	Thermo-acoustic frequency for air flames shown in figure 4.1.	67
4.3	Average inlet velocity and inlet Reynolds number at different equivalence ratios (flames shown in figure 4.1) for a characteristic diameter d=25 mm.	68
4.4	Sketch of flow entering the combustion chamber.	68
4.5	Resultant velocity contours superimposed with velocity vectors for Flame A, B and C. Images on right show a combined OH*-chemiluminescence and mean temperature (K).	70
5.1	Stable flame operation region for different inlet Reynolds number and oxidizer composition	74
5.2	Average of 200 short exposures OH*-chemiluminescence images (85 mm x 110 mm) showing flame structures at 14.3 kW ($\varphi = 0.76$), 16.6 kW ($\varphi = 0.88$) and 20 kW ($\varphi = 1.06$) for different O ₂ mole fractions.	76
5.3	RMS of 200 short exposure OH* chemiluminescence images (85 mm x 110 mm) of different oxyfuel flames at 14.3 kW ($\varphi = 0.76$), 16.6 kW ($\varphi = 0.88$) and 20 kW ($\varphi = 1.06$) for different O ₂ mole fractions.	77
5.4	Streamlines colored by intensity of stream function (80 mm x 105 mm section) from 200 single shot stereo-PIV measurements at powers of 14.1 kw, 16.5 kW and 19.8 kW for O ₂ mole fractions of 29.8 % and 33.5 %.	79
5.5	Average of OH*-chemiluminescence (80 mm x 105 mm section) for flames shown in figure 5.4.	80

5.6	Profiles of average velocity components V_x (radial) and V_y (axial) from 200 single shot stereo-PIV measurements of flames at power of 14.1 kw ($\varphi = 0.71$) with O_2 mole fractions of 29.8 % and 33.5 % in the oxidizer.	82
5.7	Vectors of 1st and 2nd mode of POD from single shot stereo-PIV of flames at power of 14.1 kw ($\varphi = 0.71$) with O_2 mole fractions of 29.8 % and 33.5 % O_2 in oxidizer. Background coloured by flow rotation along an axis perpendicular to plane of paper.	83
5.8	Profiles of radial component of average velocity from 200 single shot stereo-PIV of flames at different φ with O_2 mole fractions of 30 % and 34 % in oxidizer.	85
5.9	Average of 200 short exposure OH^* chemiluminescence images showing flame structure at two different thermal loading ranges for $\varphi = 0.76$ and $\varphi = 1.06$ with different O_2 mole fractions 26.5 %, 30.5 %, 35.4 %, 39.5 %.	87
5.10	Average of 200 short exposure OH^* chemiluminescence images (85 mm x 110 mm chamber section) showing flame structure at an average inlet velocity of ~ 6 m/s for two equivalence ratios and different O_2 mole fractions.	89
5.11	Average of 200 shot PIV data showing streamlines (colored by stream function value) for flames operated at an average inlet velocity ~ 6 m/s for two equivalence ratios and different O_2 mole fractions.	90
5.12	Contour of absolute velocity in the combustion chamber at inlet velocity of ~ 6 m/s for $\varphi = 0.83$ with different O_2 mole fractions 26 %, 29 %, 34 %.	92
5.13	Vectors of 1st mode of POD and RMS of velocity (80 mm x 65 mm chamber section) for flames at $\varphi = 0.83$ and average inlet velocity of ~ 6 m/s for different O_2 mole fractions. POD image background colored by rotation in the symmetry plane.	93
5.14	Average of 200 short exposure OH^* chemiluminescence images (85 mm x 110 mm chamber section) showing the flame structure at two different inlet velocity ranges of ~ 6 m/s and ~ 12 m/s for $\varphi = 0.83$ with different O_2 mole fractions 26 %, 29 %, 34 %.	96
5.15	Streamlines colored by stream-function showing the average (200 PIV images) flow field at two different inlet velocity ranges of ~ 6 m/s and ~ 12 m/s for $\varphi = 0.83$ with different O_2 mole fractions 26 %, 29 %, 34 %.	97
5.16	Streamlines of average flow emerging from the chamber inlet overlapped (39 mm x 105 mm) with binary Abel inverted OH^* -chemiluminescence image at an inlet velocity of ~ 6 m/s for $\varphi = 0.83$ with different O_2 mole fractions.	99
5.17	Locations in the combustion chamber where Raman measurements have been performed for the oxyfuel flames.	101

5.18	Average temperature and species distribution contours for Flame 1 and Flame 2 from Raman measurements (Note: Crosses and numbers in figures 5.18(a) and 5.18(b) represent points for detailed chemical state discussion)	102
5.19	Scatter plots showing Temperature of gas mixture in Flame 1 at different locations.	105
5.20	Scatter plots showing distribution of methane concentration in gas for Flame 1 at different locations.	106
5.21	Scatter plots showing distribution of water concentration in gas for Flame 1 at different locations.	107
5.22	Scatter plots showing the temperature of gas mixture in Flame 2 at different locations.	109
5.23	Comparison of air (visible flame luminosity) and oxyfuel.	112
5.24	Comparison of oxyfuel and air flame behavior at average inlet flow velocity of 12 m/s using averaged OH*-chemiluminescence images.	113
5.25	Premixed laminar flame speeds of methane mixtures with air and oxyfuel at 1 atm at 298 K.	115
5.26	Oxidizer to fuel momentum and velocity ratios at flow entry into the combustion chamber for different flames in figure 5.24	116
5.27	Comparison of oxyfuel and air flames using Raman spectroscopy information from different flames on symmetry plane of swirl burner.	117
5.28	Methane-air flame stabilization at similar operating conditions using the two burners at atmospheric pressure conditions and 300 K gas inlet temperature.	119
5.29	30 % O ₂ oxyfuel flames at $\varphi = 0.95$ showing the effect of change in pre-heating ((a) and (b)) as well as the effect of increase in pressure ((b) and (c)) of operation.	122
5.30	Average and RMS images of 200 short exposure OH*-chemiluminescence for oxyfuel and air flames under similar conditions at elevated pressure (5 bar) for $\varphi=0.87$ and $V_{avg} \approx 16$ m/s.	123
5.31	An uncorrelated sequence of short exposure OH*-chemiluminescence images for oxyfuel and air flames under similar conditions at 5 bar for $\varphi=0.87$ and $V_{avg} \approx 16$ m/s.	125
5.32	Average and RMS images of 200 short exposure OH*-chemiluminescence for oxyfuel and air flames under similar conditions at 5 bar for $\varphi=0.87$ and $V_{avg} \approx 31$ m/s.	126
5.33	Average images (200 exposures) of OH*-chemiluminescence for oxyfuel and air flames at different inlet velocities and $\varphi=0.99$ at pressure of 5 bar.	127

5.34	Average flow field streamlines overlaid with absolute velocity contours in background representing a 40 mm x 65 mm section of the combustion chamber. Non-reacting flow and reacting flow for natural gas air flames at 1.5 bar and average inlet velocity of 31 m/s and $\varphi=0.83$ shown.	129
5.35	Flow characteristic (37 mm x 20 mm section) and Fourier analysis frequency spectrum of 1st and 2nd mode of the non-reacting air flow at 1.5 bar for an average inlet velocity of 31 m/s.	130
5.36	Flow characteristic (37 mm x 20 mm section) and Fourier analysis frequency spectrum of 1st and 2nd mode of the reacting air flow at 1.5 bar for an average inlet velocity of 31 m/s and $\varphi=0.85$	131
5.37	Method used for numbering phases of pressure oscillations for phase resolved analysis.	132
5.38	Combined OH*-chemiluminescence (left) and PIV (right) phase averaged images corresponding to different phases of pressure oscillations in the combustion chamber for the air flame at 1.5 bar in table.3.7	133
5.39	Average flow field streamlines overlaid with absolute velocity contours in background representing 37 mm x 65 mm section of combustion chamber. Non-reacting flow and reacting flow for natural gas air flames at 5 bar and average inlet velocity of 31 m/s and $\varphi=0.83$ shown.	135
5.40	Fourier analysis spectrum of temporal component of 1st and 2nd modes from POD analysis of flow information representing a 40 mm x 20 mm section of the combustion chamber close to the burner surface for non-reacting oxyfuel conditions at 1.5 bar.	136
5.41	Abel inverted OH*-chemiluminescence half images of preheated air and oxyfuel flames with $V_{avg}=31$ m/s and $\varphi=0.83$ at 1.5 bar and 5 bar. . . .	136
5.42	Sketch of Coanda effect for fluid flow near curved surface.	137

List of Tables

3.1	Flame conditions used for OH*-chemiluminescence imaging experiments to study the effect of oxidizer composition on oxyfuel flame stabilization at atmospheric pressure for comparable thermal power.	48
3.2	Flame conditions for simultaneous OH*-chemiluminescence imaging and PIV measurements to study the effect of oxidizer composition on oxyfuel flame stabilization at atmospheric pressure for comparable thermal power.	48
3.3	Flame conditions for simultaneous OH*-chemiluminescence imaging and PIV measurements to study the effect of oxidizer composition on oxyfuel flame stabilization at atmospheric pressure for comparable inlet velocities.	48
3.4	Operating conditions of Oxyfuel flames investigated using laser Raman spectroscopy.	51
3.5	Flame conditions used to study the effect of preheat and pressure on oxyfuel flames using OH*-chemiluminescence imaging.	53
3.6	Flame operating conditions for comparing air and oxyfuel flames at elevated pressure using OH*-chemiluminescence imaging.	54
3.7	Flame conditions used to understand the role of burner aerodynamics on flame stabilization.	56
3.8	Temperature and composition (% mole fraction) of 3 calibration flames used for error estimation.	58
3.9	Percentage relative error in different quantities for 3 calibration flames as a result of uncertainty in CARS reference measurements (ϵ_T - Temperature) and flame conditions ($\epsilon_{flow-air}$ - Air flow and $\epsilon_{flow-fuel}$ - Methane flow).	59
3.10	Relative standard deviation of different quantities in stable calibration flames denoting the fluctuations ϵ_{int} in instantaneous Raman measurements.	60
3.11	Resultant uncertainty ϵ_{res} in instantaneous measurements of different quantities in the three different calibration flames.	60
5.1	Adiabatic flame temperatures (K) of different flames with different oxyfuel oxidizers from calculations at 300 K at 1 bar conditions	78

5.2	Premixed laminar flame speeds of different methane-oxyfuel oxidizers from calculations at 300 K at 1 bar conditions	84
5.3	Flow split variation with composition for flames with average velocity of ~ 6 m/s and $\varphi = 0.83$ at HAB=6 mm.	91
5.4	Convective delay times of fresh charge to the heat release zone for 26 %, 29 % and 34 % O ₂ flames for $\varphi = 0.83$	100
5.5	Conditions of oxyfuel flames with Raman measurements where V_{in-avg} is the average inlet velocity based on diameter of 25 mm, Re_{inlet} is inlet Reynolds number for same diameter, and T_{adia} is adiabatic flame temperature for inlet temperature of 293 K.	101
5.6	Composition of natural gas for high pressure experiments.	124

1

Introduction

1.1 Carbon capture and storage

As the focus on environment friendly energy increases, conventional sources such as coal, oil and natural gas remain significant contributors in meeting the world energy demand for the near future. These sources are expected to continue the release of CO₂ into the atmosphere. Coal, gas and oil sources contribute to 81 % of world's energy as of 2009 and 66 % of electricity comes from these sources [4]. In 2007, the European Commission declared to reduce the emission of greenhouse gases by 20 % of their levels from 1990 until 2020 and increase the use of renewable energy to 20 % in the framework of the 20-20-20 target. In order to meet these targets focus has been directed towards different technologies encompassing improvements in the efficiency of combustion devices and development of renewable energy sources. Another approach to completely mitigate the effects of CO₂ involves capture of the gas using carbon capture and storage (CCS) concepts. In the United States, the DOE/NETL CCS 2010 roadmap [5] targets the deployment of advanced CO₂ capture technologies till 2030. Existing power plants however need to be modified in order to reduce CO₂ release into the atmosphere.

Various methods have been proposed for carbon capture. Unlike conventional power plants, CCS plants are affected by an energy penalty that comes with separating and storing CO₂. The overall electrical plant efficiency and carbon capture efficiency hence become important parameters for the design of such plants [6]. The application of CCS to existing power plants can vary in the degree of complexity. The different approaches are classified into the following [7]:

- Post Combustion Capture
- Oxyfuel Combustion
- Chemical looping combustion

– Pre-Combustion Capture

The easiest approach for implementing CCS in existing power plants is post combustion capture. It involves the use of a scrubber for separating the CO₂ from the exhaust gas [8]. The currently available technologies for flue gas CO₂ separation consist of chemical sorbent or membrane based systems. This involves minimum changes to existing power plants and exerts minimum efficiency penalty [9]. Considerable research is being done to make the systems compact and efficient [10]. However, typical CO₂ concentration in exhaust gases from natural gas or pulverised coal power plants is between 3 % to 15 %. Hence large volumes of exhaust gases have to be circulated for separating CO₂.

Unlike post-combustion capture oxyfuel combustion requires further modification of the power plant. Oxyfuel combustion uses either pure oxygen or oxygen diluted with CO₂ and/or H₂O instead of air as working fluid. Since the temperatures reached with pure oxygen can be very high and beyond the range of conventional materials, the dilution is used to reduce temperatures. The products of such a combustion consist mainly of CO₂ and H₂O. The CO₂ can be separated by water vapour condensation. The CO₂ separation efficiency hence for oxyfuel combustion is close to 100 %. Another benefit of the combustion only with O₂ instead of air is that the amount of NO_x generated is significantly lower. In order to obtain oxygen for combustion, an air separation unit (ASU) is required, which is an energy penalty on such systems. Efficient ASUs' are therefore also an important topic of research. Oxyfuel combustion has been extensively used in metal cutting, glass furnaces, and boilers, however implementation of the method in steam or gas turbine cycles requires research. New combustors and turbines have to be developed, which can deal with the new working fluids. An alternative strategy to oxyfuel combustion is the use of chemical looping combustion (CLC) [11]. It consists of two cycles which are connected, one where a metal oxide is reduced by fuel with products being CO₂/H₂O and another where the metal is oxidized and fed into the fuel cycle. The requirement of an air separation unit is circumvented.

In pre-combustion capture the hydrocarbon fuels are converted to obtain CO and H₂. The CO and H₂O are converted to CO₂ and H₂ by using the water gas shift reaction. The CO₂ is then separated for storage and the H₂ is used for power generation in a fuel cell or gas turbine. The hydrocarbon conversion can be achieved through steam reforming or by using partial oxidation/gasification [10]. The former involves reaction of hydrocarbon with steam and is limited to light hydrocarbons, while in the latter hydrocarbons react with pure oxygen and can be extended to solid and liquid hydrocarbons. The use of pre-combustion capture is particularly suited to the integrated gasification combined cycle IGCC systems which use a wide variety of solid fuels.

Both, coal and gas power plants can be modified for CCS. Each of the above mentioned CCS concepts have advantages and disadvantages which vary depending on the

size and type of power plant used. Which of these concepts would emerge as the primary technology is unclear, as much of the ideas are still topics of active research. The topic of interest in this thesis involves the use of oxyfuel combustion in gas turbines.

1.2 Oxyfuel Combustion

For coal and other steam power plants the extent of development of carbon capture technologies is significantly greater than that for gas turbine power plants. Many pilot projects have been proposed and some such as the oxyfuel combustion plants by Vattenfall (Schwarze Pumpe) [12] have shown successful operation. The DOE/NETL CCS roadmap [5] and Global CCS status report 2014 [13] give an overview of the projects proposed by various nations. Significant focus has been directed towards the implementation of CCS for coal power plants [14]. However for gas turbine power plants the development has not been that extensive. The use of post combustion capture for gas turbines requires no modification of the combustor and turbine, although the power plant cycle needs to be modified for carbon capture. Both oxyfuel combustion and pre-combustion capture need modification of the burner and turbine. Since the use of IGCC power plants is on the rise in the last few decades, significant fundamental and practical knowledge has been gathered in this area [15]. This experience is useful for developing pre-combustion gas turbine CCS systems.

In the case of oxyfuel combustion new burner configurations have to be developed. As the CO₂ capture efficiencies of oxyfuel combustion is significantly higher, there exists potential for its use in the carbon capture cycle. However, to date the application of oxyfuel combustion to gas turbines has not been looked into in detail. The working medium consists of O₂, CO₂ and H₂O instead of air [1, 2, 16, 17, 18]. The combustion temperatures resulting from pure O₂ combustion are very high and need to be reduced by using CO₂ or H₂O dilution. The physical properties of CO₂ and H₂O are different to those of air [19]. CO₂ has a much higher density, heat capacity and is also more active in absorbing radiation [20]. It is also more active than N₂ chemically due to higher chaperon efficiency and hence influences the laminar burning velocity [21, 22]. Modification and development of new burners and turbines that can operate with the working fluids is therefore required. It is unclear which concept of flames, premixed, non-premixed or partially premixed would be most suitable for use with oxyfuel combustion.

Swirl stabilized burners are widely used for flame stabilization in gas turbines [23, 24]. At the DLR Stuttgart vast experience and understanding of the fundamental aspects of swirl stabilized combustion dynamics has been gathered using model swirl burners [25, 26, 27, 28]. Both premixed [29, 30] and partially premixed [31, 32] types of air flames have been studied. Basic understanding of flame stabilization, thermo-acoustic

oscillations, and swirl flame dynamics has been obtained through the use of optical diagnostics. This forms a good basis for drawing comparisons between air combustion and oxyfuel combustion, so as to make recommendations for design of oxyfuel burners. Partially premixed flames are known to have a more stable operating characteristics over a wide operating range. This is due to the presence of fuel rich combustion zones which assist flame stabilization. Hence a partially premixed configuration has been chosen for investigating oxyfuel combustion.

This dissertation summarizes experimental investigations that have been performed with oxyfuel flames in order to draw comparisons with swirl stabilized air combustion. The oxyfuel oxidizer used consists of O_2 and CO_2 . The proportion of these two molecular species changes flame speed, flame temperature and hence stabilization. The effect of change in proportion of these two molecules on flame stability is investigated to give recommendations on the types of burner concepts that would be suitable for use in oxyfuel gas turbines. A canonical version of a swirl burner has been used for the experiments. The experiments are divided into two parts with the first involving investigations on an atmospheric burner configuration. In the second part investigations at elevated pressure and closer to real gas turbine conditions have been performed on a modified version of the atmospheric burner. The effect of change in oxidizer composition, equivalence ratio, inlet velocity and thermal loading has been studied. In order to characterize the flames and obtain a relevant comparison of their behavior various optical diagnostics have been used to obtain heat release, flow field, and acoustic information. OH^* -chemiluminescence imaging has been used to understand changes in flame shape and stability with the variation of the above parameters. Flow field information is obtained by means of particle image velocimetry (PIV) measurements of certain flames. Laser Raman spectroscopy has been performed on selected flames under atmospheric conditions to obtain further point-wise information about composition and temperature. A comparison to air flames has been performed to highlight changes that can be expected with oxyfuel operation. The presence of thermo-acoustic oscillations was found to be a consistent feature of this burner over a wide range of operation. This topic has also been looked into in detail to draw relevant conclusions when comparing oxyfuel and air swirl flames.

The following chapters describe in detail different aspects of the work. Chapter 2 looks into the state of art in gas turbine combustion and summarizes oxyfuel gas turbine cycles and research into oxyfuel combustion that has been done to date. Chapter 3 describes the burner configurations, optical and laser measurement techniques and setups used at atmospheric and high pressure conditions as a part of the investigative methodology. Chapter 4 summarizes the research performed to date on the burner configuration using methane-air flames. Chapter 5 discusses the results of the investigations. The results are separated into those from atmospheric and elevated pressure experiments, along with

1. INTRODUCTION

relevant comparisons to air flames from previous and current work. This is followed by the conclusions in chapters 6, where relevant recommendations for using burners with oxyfuel flames and areas which need further inquiry are highlighted.

2

Background

The development of a gas turbine operating on oxyfuel combustion involves the redesign of different components of the gas turbine. In section 2.1 a brief introduction into gas turbines and the typical characteristics of swirl stabilized flames is presented. A significant proportion of flames studied during this work exhibited thermo-acoustic instabilities. A brief introduction into this phenomenon is presented in section 2.1.3. The most significant change that would occur with using oxyfuel gas turbines is the change in working fluid. In order to accommodate this and at the same time maintain high plant and carbon capture efficiency, different thermodynamic cycles have been proposed. These cycles influence burner configurations that would be suitable for such gas turbines. Section 2.2 reviews these different cycles. In section 2.2 the differences in oxyfuel and air combustion which have been investigated by other researchers are presented.

2.1 Gas turbines

The gas turbine as a mechanical device has a history which can be traced back to the 18th century [33]. The modern gas turbine as we know it gained prominence through its use in aircraft in the early part of the 20th century. The gas turbine has since then been used for various applications ranging from stationary power generation, marine vehicles, automobiles, locomotives and tanks. Although each of these applications places special requirements on the device, the basic principle of operation has remained the same. The figure 2.1 [34] describes the most basic form of the Brayton cycle for the operation of gas turbines with air as working fluid. The main components of the system are the compressor, which compresses air to higher pressures at which point the air enters the combustor, where fuel is combusted at constant pressure to increase the enthalpy of the air, which is then made to expand across a turbine to extract work. In aviation, a part of the air is used to generate impulse for moving the aircraft, while a part of the turbine energy is used for driving compressors, fans, or propellers. For gas turbines used in

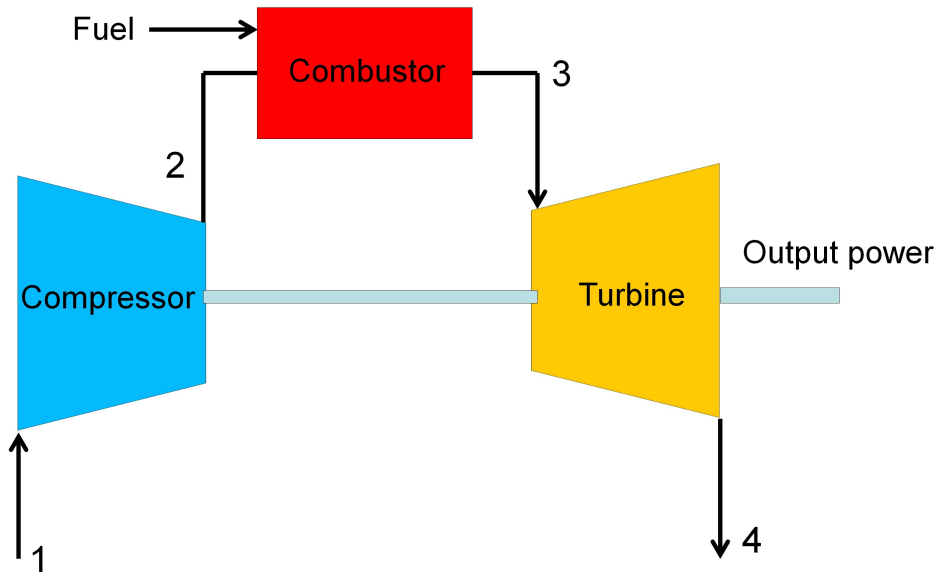


Figure 2.1: Open Brayton cycle for gas turbines.

power generation (industrial), almost all of the turbine energy is distributed between the compressor and an electric generator. The efficiency of such an ideal cycle is a function of the pressure ratio r (ratio of pressure at compressor outlet to compressor inlet) given in the expression below.

$$\eta = 1 - \left(\frac{1}{r}\right)^{\gamma-1/\gamma} \quad (2.1)$$

where η is the efficiency, γ is the adiabatic index of the working fluid.

Each application places differing requirements on the construction of the gas turbine. For aviation, weight, emissions, reliability of operation, safety and fuel consumption are defining characteristics. While for power generation efficiency, fuel flexibility and emissions among other parameters like reliability are of great focus. Saravanamuttoo [35] and Wilson [36] present the basic theory and criteria for the design of gas turbines. The major components of an industrial gas turbine are the inlet, compressor, combustor, turbine and exhaust. Each of the individual components is complex and requires a specific design. The basic functional requirement of the compressor is to use minimum energy to compress the air to the required pressures for the combustor. The combustor ensures that the fuel is burned completely, and that the products with required energy and temperature are delivered to the turbine, which in turn extracts the maximum possible energy from the burned products. The actual process of design of each of these individual components are topics in themselves, which again are greatly influenced by the type of application, due to which there are numerous configurations corresponding to each component that have emerged over the years. The above references provide a more exhaustive look into

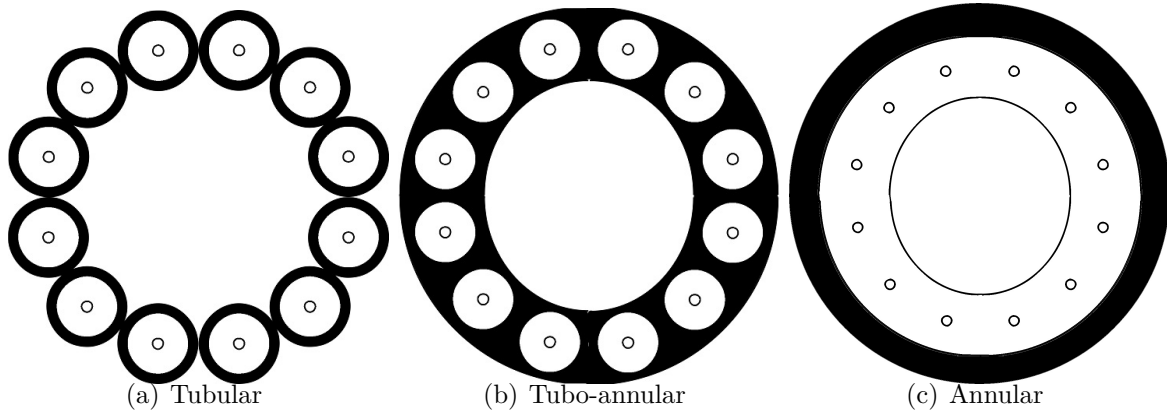


Figure 2.2: Cross-section of different types of combustors in gas turbines, when observing the gas turbine from the exhaust nozzle. Black color represents flow not participating in combustion.

these configurations. Since its invention the gas turbine has greatly evolved in terms of efficiency (higher pressure ratios, component efficiency), reliability, material temperature limits, emissions and weight among other parameters. The gas turbine cycles for industrial applications have also incorporated numerous changes like combined cycles CC and gasification in the form of integrated gasification combined cycles (IGCC) [15]. The development of a gas turbine using a different working fluid from air as in the case of oxyfuel gas turbines requires careful consideration and redesign at the macroscopic cycle level and at a gas turbine component level. An overview of the cycles proposed for oxyfuel combustion is presented later. The scope of this work concentrates on outlining important characteristics of swirl stabilized oxyfuel flames and identifying differences in relation to typical air swirl flames. Thereby laying a groundwork for the development of suitable oxyfuel burner concepts. A brief summary of combustors used for air combustion in gas turbines is given below.

2.1.1 Gas turbine combustors

The typical configurations of combustors have evolved significantly over the years with more focus on combustion emissions due to its direct impact on the environment and concerns of global warming. The basic combustor configurations being used in gas turbines are tubular (can), turbo-annular (can-annular) and annular [24]. The figure 2.2 shows a sketch of the different types of combustors. The annular form of combustor has become almost a standard for aviation applications due to advantages in terms of lightness and structural strength, while tubular and turbo-annular combustors still find application in stationary gas turbines. Modern gas turbine combustors must meet a range of important requirements such as stable flame over a wide operating range, low emissions, acceptable

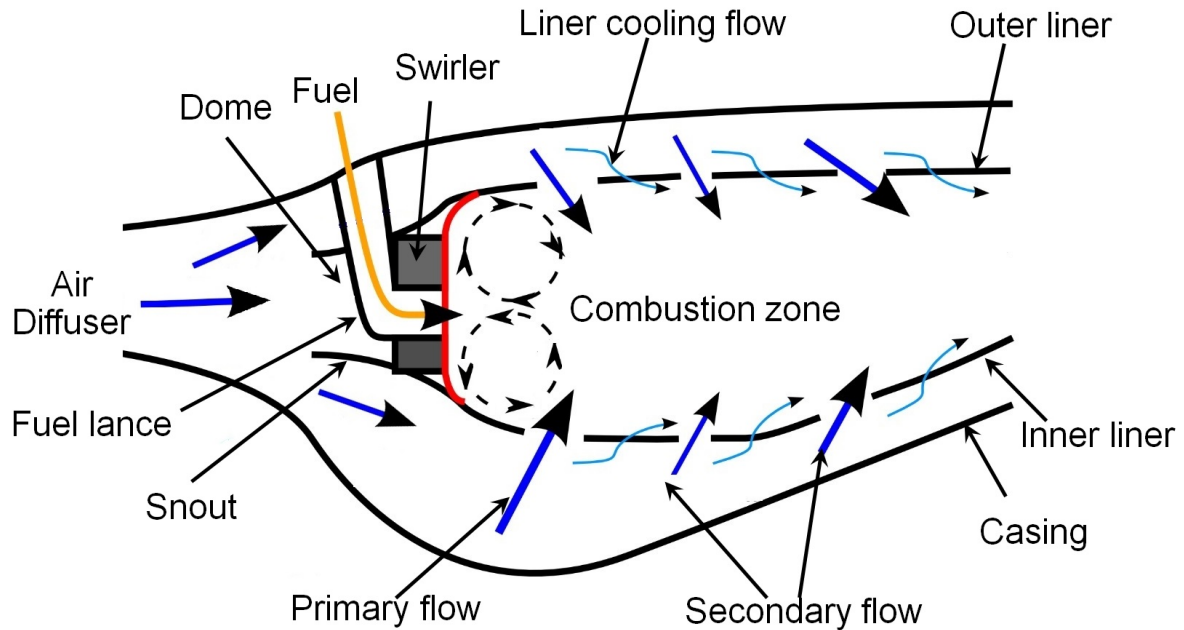


Figure 2.3: Typical annular combustor configuration (adapted from wikipedia).

temperature profile for turbine inlet, sufficient material cooling, high altitude relight capability (for aviation), and high combustion efficiency. The figure 2.3 shows the typical arrangement of a single burner section of an annular combustor. The high temperature and pressure air is made to slow down with the help of a diffuser. Part of the air flow enters the dome which houses the fuel supply and swirlers. The swirled flow helps in mixing the air and fuel which is ignited by an igniter (not shown) to form and stabilize the flame. The rest of the flow is directed along the annulus between the casing and the liners from where it enters the combustion zone in the form of primary and secondary flow. These flows help in regulating the temperatures after combustion to values specified for the turbine inlet. The placement of the secondary holes is crucial to obtain an acceptable temperature profile (pattern factor) for the turbine. In order to lower liner temperatures, part of the flow is also directed for its cooling in the form of effusion holes or slots on the liner.

The stabilization of flames in gas turbines is achieved by the formation of a zone in the combustor where burned products and fresh gas can mix so as to form a self-sustaining stable combustion region. It is also referred to as a flame anchoring zone. The manner in which this is typically achieved is through the use of bluff-bodies or swirlers. The figure 2.3 shows the formation of this zone with the aid of swirlers. The flow entering the dome passes through the swirlers which assist in the formation of a recirculation zone. The primary flow entering the combustion chamber further assists in the formation of this zone. The flows are highly turbulent enabling rapid mixing. A similar effect can be achieved by replacing the swirler with a bluff body. This type of flame stabilization

however has been typically used in Ramjet engines or turbojet engine after-burners. The challenges in terms of cooling the bluff body, stable operation over a wide range, and acceptable pressure drops across the combustor have restricted its use in gas turbines. The use of swirlers for flame stabilization has become almost a standard practice. The swirl flow provides a stable recirculation zone over a wide operating range. The following section presents some basic features of swirl flows. Both industrial and aviation gas turbines often use swirlers for flame stabilization.

Based on where the fuel is introduced into the air stream relative to the main combustion zone the flames formed can be classified as premixed, partially premixed or non-premixed. In premixed combustion the fuel and oxidizer are uniformly mixed prior to entering the combustion zone. In partially premixed combustion, only a certain fraction of the fuel is considered to be mixed with the oxidizer while entering the combustion chamber. As the name suggests non-premixed (diffusion) flames rely on the mixing of fuel and oxidizer in the combustion chamber. Industrial and aviation gas turbine combustors have evolved to use advantages of these different forms of combustion to meet operating criteria. As industrial gas turbines have rather stringent emission standards to meet, along with a demand for fuel flexibility lean premixed (prevaporized) LP(P) concepts have been used. The NO_x emissions in combustors are known to be caused mainly due to the thermal NO_x pathway [37] which is associated with high combustion temperatures. Such combustors use lean premixed combustion to reduce temperatures and therefore NO_x emissions. Lefebvre [24] provides examples of solutions from different engine manufacturers in implementing these concepts in a series of Dry Low NO_x DLN or Dry Low Emission DLE combustors. For aviation application partially premixed and non-premixed forms of combustion have been used due to its reduced risk of flashback and more stable operation in comparison to premixed flames. Lower NO_x emissions in such combustors are achieved through Rich-Quench-Lean RQL combustion where the primary combustion zone is kept rich for good flame stabilization. A large quantity of primary flow (figure 2.3) is used to complete the oxidation and reduce flame temperatures. This reduces the time associated with high temperature products present in the combustion chamber and hence thermal NO_x .

Presently both industrial and aviation gas turbines are in the process of undergoing another evolution to meet future emission targets. The GEnx (www.geaviation.com) engine boasts of the first use of premixed combustion in an aviation gas turbine which has been limited due to fears of stable operation. The benefit of reduced NO_x emissions from such burners in industrial gas turbines promises similar gains in aviation. To meet future fuel flexibility and emission requirements in industrial gas turbines an alternate form of combustion referred to as distributed combustion is being attempted. The combustion is characterized by a large region of heat release resulting in lower temperature increase due

to combustion and hence smaller temperature gradients in the combustor. This enables further reduction of NO_x emissions. The concept relies on the mixing of large amounts of hot exhaust gas with fresh charge. Burners based on this principle have been termed flameless oxidation FLOX[®] [38], high temperature air combustion (HTAC) [39], moderate and intense low oxidation dilution (MILD combustion) [40].

The question as to which type of burner from this array of burners that have been developed for air combustion would be most suited for oxyfuel combustion gas turbines is unanswered. The vast experience with swirl stabilized flames serves as a good basis for such an effort. The complexity of actual gas turbine combustors presents a significant challenge to understanding chemical kinetic and fluid dynamic aspects of the combustion process. Hence over the years simplifications of actual gas turbine combustors have been developed, while maintaining essential features of gas turbine burners [23, 28, 41]. The ease of application of optical diagnostic techniques (described in section 3.2) to such combustors has provided important understanding of the complex processes, while simultaneously providing validation data for numerical modeling tools. The section 3.1.1 presents one such burner used at DLR Stuttgart which has been extensively studied. This has been used for the investigations in this work. A summary of the important characteristics of swirl flames using air in the burner is presented in chapter 4. The burner forms the basis to highlight differences of oxyfuel combustion to air combustion. This is the content of the chapter on results. But before that, the following section presents the basics of swirl flows and flame stabilization.

2.1.2 Swirl flows and flame stabilization

Due to the widespread use of swirling flow in gas turbines and other applications, this type of flow has been of great research interest under both non-reacting and reacting conditions. Gupta [23] presents a comprehensive summary of the research into swirl flows, its characteristic features and application in devices ranging from reciprocating internal combustion engines and gas turbine combustors to cyclone separators. The extent of swirl that can be generated by different devices is defined by a non-dimensional number known as the swirl number S . The number at a given plane is a ratio of tangential momentum flux to the axial momentum flux multiplied by an equivalent nozzle radius. It is given by the following expression for a cylindrical co-ordinate system:

$$S = \frac{\int_0^R 2\pi \rho u w r \, dr}{R \left(\int_0^R 2\pi \rho r u^2 \, dr + \int_0^R (p - p_\infty) r \, dr \right)} \quad (2.2)$$

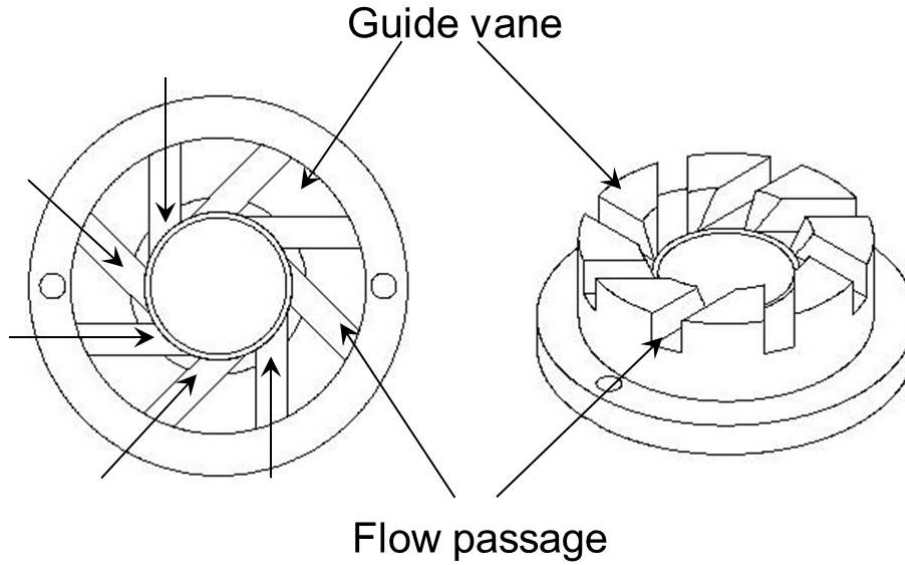


Figure 2.4: Radial swirl generator block (swirler).

where, r is the radial position on the plane, u is component of velocity perpendicular to plane, w is tangential component of velocity in the plane, and R is the nozzle radius, p is pressure at a given radial position, p_∞ is ambient pressure.

Swirl can be generated using three configurations:

- Tangential entry
- Guided vanes (swirl vane pack or swirler)
- Direct rotation

The tangential entry swirl generators rely on two flows, a primary axial flow and a tangential flow to induce swirl. High pressure losses in them have reduced their application to gas turbine burners. The guided vane system is the most commonly used due to the low pressure drop required to generate the same quantity of swirl and the ease of packaging in gas turbines. An example of a radial guided vane swirl generator or swirler from a burner that has been used for experimental investigations in this work is shown in figure 2.4. The flow is guided radially by means of guide vanes to impart swirl before it turns axially to enter the combustion chamber. Based on whether the flow is predominantly radial or axial, guided vane swirlers are classified into radial and axial type. Direct rotation swirl generators rely on swirl created from rotating cylindrical chambers which impart swirl through wall interaction and gas viscosity. Their efficiency in swirl generation is low.

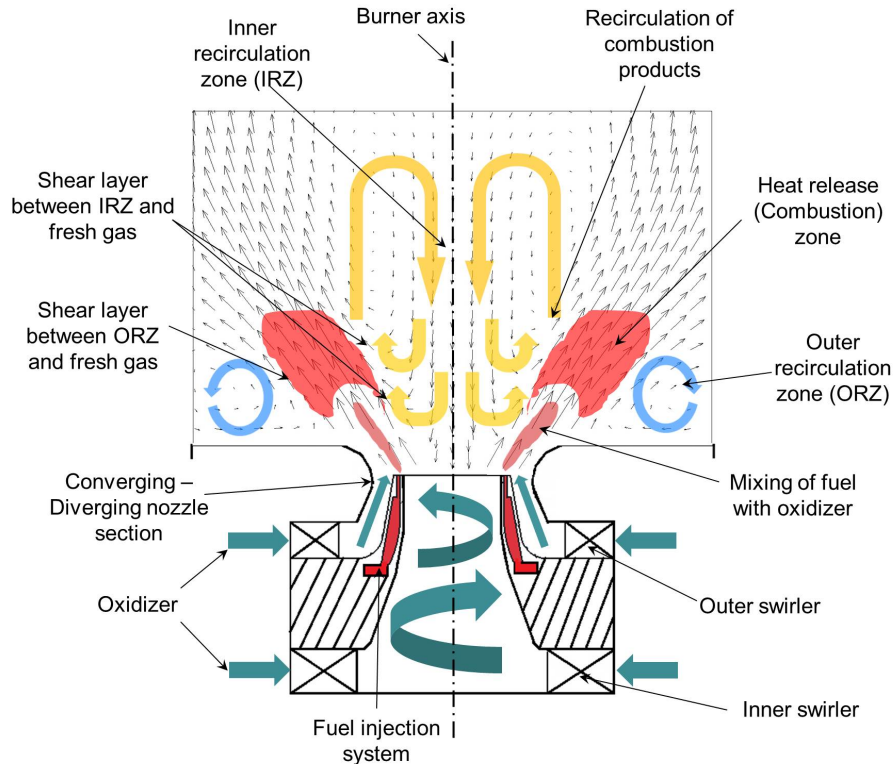


Figure 2.5: Typical swirl flow flame stabilization mechanism.

The extent of swirl imparted, determines the features of swirl flows made to expand into unconfined surroundings. Low swirl numbers ($S \leq 0.6$) do not impact the flow significantly, with the flow being similar to a jet flow with no flow reversal from the predominant flow direction. However with higher swirl, a reversal of the flow opposing the general flow direction appears forming a recirculation zone. This is caused due to vortex breakdown occurring in the main flow at high swirl. The formation of this recirculation zone is used in swirl burners for flame stabilization. The figure 2.5 shows the characteristic time averaged high swirl flow field and how this assists flame stabilization. The configuration of the swirl generator blocks is typical for gas turbine burners and has also been used in the current work. The configuration consists of two axially offset radial swirler blocks which introduce annular swirling oxidizer flow into the combustion chamber. The direction of the swirl can be co-swirling or counter-swirling. The fuel is introduced between the two swirling flows. It must be noted that this is typical of a non-premixed or a partially premixed burner. In premixed burners the fuel is introduced upstream in the swirler blocks to allow time for mixing. The flow enters the combustion chamber through a converging diverging nozzle section. At high swirl numbers a flow reversal as shown occurs. The higher swirl numbers cause radial pressure gradients as a result of centripetal acceleration of the swirling flow [23]. These gradients are highest where the swirl flow enters the combustion chamber causing the lowest pressure along the burner axis. This low

pressure entrains flow entering the combustion chamber forming an inner recirculation zone (IRZ). Upon entering the combustion chamber the pressure along the burner axis recovers. The converging diverging nozzle is used to further increase these axial gradients to assist formation of recirculation zones. The geometry of this section of the burner influences the recirculation zone size [42]. The entrainment of surrounding fluid as in a jet flow results in the formation of an outer recirculation zone (ORZ) between chamber walls and incoming flow.

The formation of recirculation zones facilitate the mixing of high temperature burnt combustion products with fresh gas and hence flame anchoring. This happens along the two shear layers formed between the incoming flow and the IRZ as well as between the incoming flow and the ORZ. The flame stretch effects in such regions can be expected to be crucial to flame stabilization. Turbulent flame stabilization is governed by a number of parameters such as chemical kinetics, flame stretch, turbulent mixing, and heat transfer. Large flame stretch is known to cause flame extinction [43]. In premixed flames, interaction of burnt and unburnt gas is crucial for flame stabilization, while in non-premixed and partially premixed flames diffusion of reactants and mixing with burnt gas plays an important role. The process of swirl flame stabilization is hence very complex. The heat release therefore occurs in the aerodynamically and chemically most favorable regions [42]. During the course of this work it is demonstrated that the oxyfuel oxidizer chemistry significantly influences flame stabilization location.

High swirl flows are inherently unstable and a consequence of this is the occurrence of vortex breakdown in the bulk flow and formation of the IRZ. While a time averaged flow field appears as shown in the figure 2.5, an instantaneous flow field reveals together with the turbulent motion another structure. For non-reacting flows the process of vortex breakdown has been linked to the formation of a coherent fluid dynamic structure known as the precessing vortex core PVC [23, 41]. The PVC is best described as a helical vortex that extends from burner inlet into the combustion chamber that is a state of precession along the burner axis. Due to its precession, it affects the flow in a periodic manner and is located in the shear layers between the incoming flow and recirculation zones. Syred summarizes studies on this structure in reacting and non-reacting swirl flows. The presence of combustion however enhances or suppresses this structure [41, 44] and its existence has been shown to be dependent on density gradients present at the inlet of flow into the combustion chamber [45]. The PVC has been shown to play a crucial role in the process of mixing of burnt and unburnt gas in the burner investigated [30, 46]. This fluid dynamic structure is typical to the swirl flame burner which has been used for experimental investigations during this work. In the absence of a PVC in flames the process of mixing of unburnt and burn gas has been shown to be dominated by non-

coherent vortices in the flow [44, 47]. Coherent periodic vortex shedding is however also possible as seen during this work.

Swirl flames are therefore very complex, and under certain conditions also susceptible to instabilities. As mentioned earlier, the need for low NO_x emission has led to the development of LP(P) combustors using swirl flames. This form of combustion has been shown to be susceptible to thermo-acoustic oscillations. The following section presents some basics of thermo-acoustic oscillations.

2.1.3 Combustion instabilities

Combustion instabilities refer to a condition where periodic heat release fluctuations occur in a burner. When the heat release fluctuations are associated with acoustic modes of the system, they are referred to as thermo-acoustic instabilities. The existence of such fluctuations is very detrimental to the mechanical components in combustion devices. The fluctuating heat release causes fluctuating power outputs, vibration, thermal stresses, material fatigue and premature failure. Continuous flow devices such as rocket engines and gas turbines can be subject to such instabilities. The mechanism of oscillations has been described by the Rayleigh criterion [48] as shown in equation 2.3.

$$\int_0^{\tau} \int_0^V p'(x, t) q'(x, t) dv dt > \int_0^{\tau} \int_0^V \varphi_D(x, t) dv dt \quad (2.3)$$

where, p' and q' are pressure and heat release fluctuations, τ the time period of the oscillation, V is the control volume, φ_D is the acoustic damping in the control volume.

The amplitude of the oscillations increases till the magnitude of damping effects becomes comparable to that of the excitation leading to limit cycle oscillations (stable repeatable periodic oscillations). The tendency of gas turbines to produce these oscillations under certain conditions is due to the coupling of the fluctuations in the flow and combustion process with acoustic modes that are present in the system. The figure 2.6 shows an illustration of the interaction between heat release, pressure and flow fluctuations. This coupling of heat and pressure fluctuations can occur if the phase difference between the heat release and pressure fluctuations is $<90^\circ$ as per the Rayleigh criterion. The change in heat release leads to a change in pressure which influences flow processes in a cyclic manner. Lieuwen [49] describes the flow processes which could cause instabilities to be the following:

1. Acoustic coupling of fuel feed line
2. Oscillations in equivalence ratio
3. Oscillations in atomization, vaporization and mixing

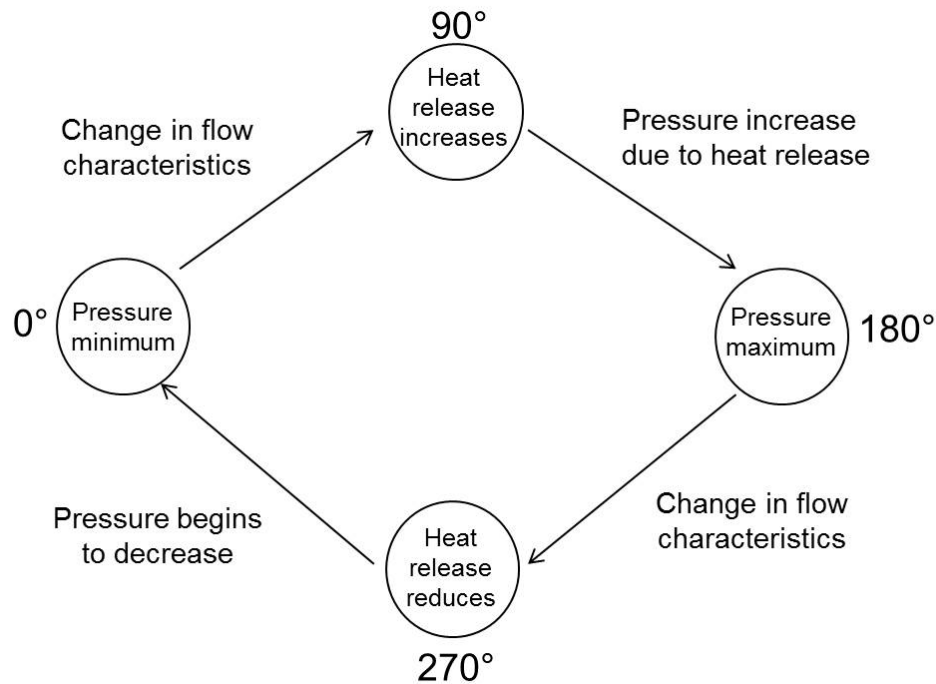


Figure 2.6: Variation of pressure, heat release and flow characteristics during a single phase of oscillation.

4. Oscillations in flame area

5. Presence of coherent vortical structures in the flow

Each of these sources influences the heat release process and is associated with a time-scale. The time-scale corresponds to the time required for the unburnt charge to reach a combustible state, and then proceed to maximum heat release. Since gas turbines are continuous flow devices, this time scale is referenced to the start of a given physical process. In non-premixed gaseous combustion for example this time-scale is associated with the time required for fuel, air and burnt gas to mix and reach a combustible state. The process coincides with the convection of fresh charge to a reactive state and can therefore be calculated as a convective time-scale. This can be similarly extended to vaporization and mixing in liquid fuel combustion or just mixing of products and reactants by vortex interaction in premixed combustion. The different sources described above influence the time scale of mixing and combustion of unburnt charge. When any of these or a combination of these time scales correlates with a natural acoustic mode present in the combustion system, the Rayleigh criterion is satisfied leading to self-sustained oscillations. Therefore burner, combustion chamber geometry and design play a very important role in thermo-acoustic oscillations as they essentially control all of the above parameters. The modeling, prediction and control of these dynamic effects over the entire

operating range of a gas turbine burner is complex, requiring experimental investigation, acoustic analysis, and computational fluid dynamic simulation CFD [49]. The elimination of thermo-acoustic oscillations can therefore be very complex and specific to each burner configuration. The burner used in this work also excited thermo-acoustic oscillations under certain conditions. The details of this study are presented in section 4.2.2.

2.2 Aspects of oxyfuel gas turbines and combustion

The use of oxyfuel combustion in gas turbines involves a change in the working fluid and an adaption for CO₂ capture. The process of oxyfuel combustion requires the use of air separators for obtaining oxygen, which imposes a direct penalty on the oxyfuel gas turbine cycle. New thermodynamic cycles are therefore required to optimize the plant and carbon capture efficiencies. In this section an overview of the cycles proposed for oxyfuel gas turbines is given to highlight the differences to air cycles. Subsequently, the direct impact of using different working fluids on the combustion is presented, along-with investigations that have been carried out by other researchers into oxyfuel combustion.

2.2.1 Gas turbine cycles for oxyfuel combustion

The benefit of CCS power plants is the large CO₂ capture in comparison to traditional power generation [6, 10, 50]. The efficiency of such power plants is therefore a measure of not only the net electrical power generated, but also the quantity of CO₂ captured for a given energy input.

As oxyfuel gas turbines involve a different type of working fluid compared to air gas turbines, cycles using different working fluids have been proposed to maximize electrical and capture efficiencies. These cycles can be broadly classified into three types based on the composition of the working fluid. The working fluid can be either CO₂, H₂O or a combination of the two. These working fluids also indicate the main diluent used for reducing the high temperatures of oxyfuel combustion in the combustor. In order to improve the cycle efficiency most of such cycles have been proposed to be operated at higher pressures than air cycles. The cycles which use CO₂ as working fluid are the MATIANT cycle [16], COOPERATE cycle [17, 51], COOLENERG cycle [52], and more recently the semi-closed oxy-combustion cycle SCOCC [1, 18]. Additional cycles which use liquefied natural gas LNG have also been proposed [53]. The cycles which use H₂O are the water cycle from Clean Energy System CES [54, 55], S-Graz cycle [56], and those from Gabrielli [7]. There also exist variations of the Graz cycle and the SCOCC which use a mixture of CO₂ and H₂O as working fluid [57]. Further new concepts such as chemical-looping combustion CLC [58] where oxygen is obtained through the reduction of

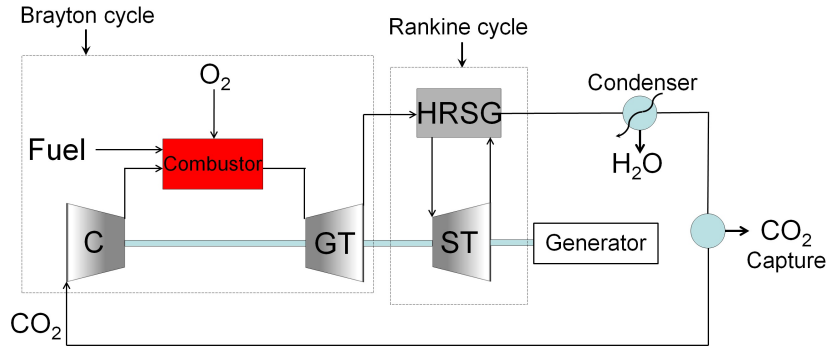


Figure 2.7: Semi-closed oxy-combustion cycle with CO_2 as working fluid (Based on Amann [1]).

a metal oxide have been suggested for reducing the penalty of obtaining oxygen. Advanced zero emissions power plant AZEP concept is also one of such cycles [59]. Kvamsdal [6] provides an overview of the different cycles along with a study comparing them. Significant optimization of these thermodynamic cycles based on simulation work has been performed by numerous research groups from where the cycles have been developed [2, 60, 61, 62, 63]. In the context of this work a detailed look into each of these different cycles is not relevant and hence only two examples of cycles based on CO_2 and $\text{CO}_2/\text{H}_2\text{O}$ as working fluid are briefly described. Both cycles are based on the principle of combining Brayton and Rankine cycles. However, the cycles vary considerably in the degree of their complexity and the number of independent components required.

The figure 2.7 shows the SCOCC cycle which uses mainly CO_2 as the working fluid. The additional components relative to the standard Brayton cycle are the heat recovery steam generator HRSG, steam turbine ST, condenser and CO_2 capture unit. Compressed CO_2 is supplied to the combustion chamber where combustion with fuel and O_2 occurs. The products first expand through a gas turbine GT before being sent to the HRSG where steam is heated to power a ST. Both turbines enable work extraction through a generator. The products of combustion are subjected to water condensation to separate CO_2 which is ready for capture and storage. Ulfsnes [64] studied the effect of transient coupling of the different cycle components and concluded that these effects influence the cycle behavior significantly.

The Graz cycle which uses $\text{CO}_2/\text{H}_2\text{O}$ as working fluid is shown in figure 2.8. Although the basic concept of combining the Brayton and Rankine cycles remains, the number of additional components in this system is significantly higher. The compressors (C1,C2,C3), combustor, high temperature turbine HTT form the Brayton cycle while the low pressure turbine LPT, condenser, de-aerator, HRSG and high pressure turbine HPT form the Rankine cycle. The combustor therefore uses both water vapor and CO_2 to reduce temperatures. The products of combustion expand through two turbines (HTT

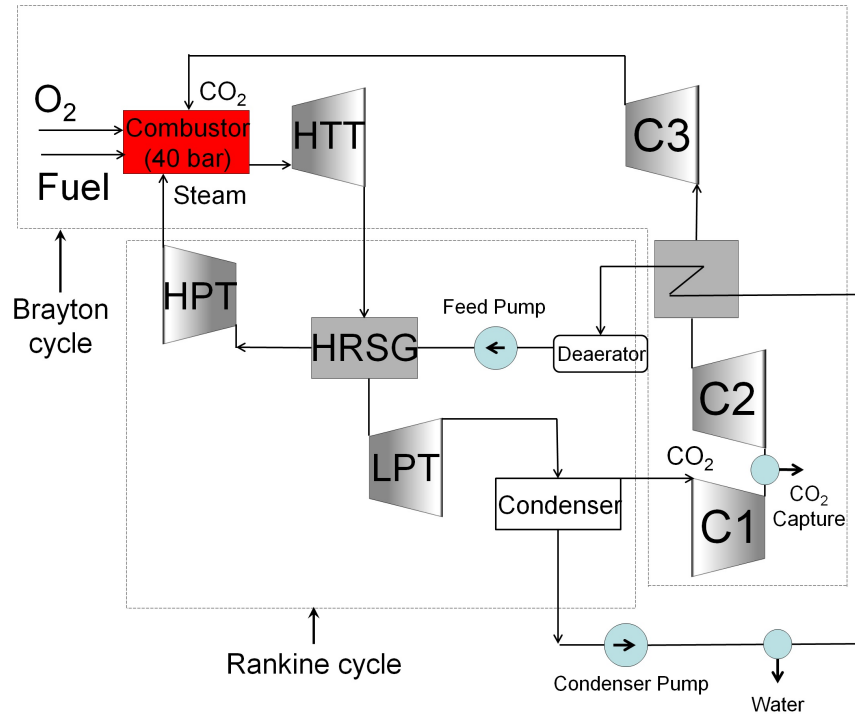


Figure 2.8: The basic Graz thermodynamic cycle for oxyfuel gas turbines (based on Jericha [2]).

and LPT) with the HRSG used to supply steam for the HPT. The expanded combustion products after the LPT pass through the condenser where the separation of CO_2 occurs, part of which is compressed and reintroduced into the combustion chamber. This cycle has been further modified (S-Graz cycle) with the inclusion of fuel reforming and use of only steam as working fluid to improve cycle efficiency [56].

Kvamsdal [6] performed a comparative study of different carbon capture technologies including the SCOCC, water cycle and S-Graz cycle using a power plant with no carbon capture as a reference. The S-Graz process was found to have the highest net plant efficiency of 49 % while SCOCC and water cycles showed 47 % and 45 % respectively. The CO_2 capture efficiency was highest for the SCOCC and the cycle has the additional benefit of lesser complexity. The author cited additional parameters such as technological maturity to be pivotal in determining which of the cycles would see practical use. However, the oxyfuel gas turbine with CO_2 as working fluid does show promise. The development of such power plants requires redesign of different components, such as turbines, compressors and combustors. This dissertation looks into the combustion aspects of such a cycle. The use of CO_2 in the combustion process plays a critical role in determining combustion behaviour. The following section looks into studies which investigate the direct impact of using CO_2 dilution in oxyfuel combustion.

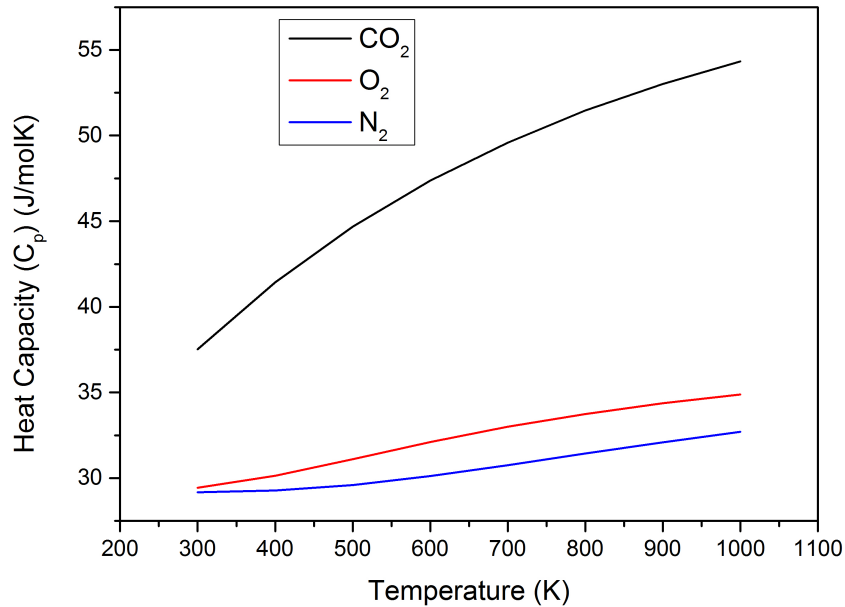


Figure 2.9: Variation of heat capacity of different gases (from NIST database).

2.2.2 Characteristics of oxyfuel combustion with CO₂ dilution

The use of pure oxygen for combustion in practical applications can be found in metal cutting, welding and glass furnaces where exceptionally high temperatures (2800 °C to 3500 °C) are required [65]. Other applications include rocket engines where liquefied hydrogen and oxygen are mixed to provide thrust. Air contains 21 % O₂ by volume. With an increase in the concentration of O₂ the rate of oxidation increases. In the absence of a diluent such as N₂ as in air, the heat of combustion is distributed between products causing exceptionally high temperatures. The above applications use these effects for obtaining high temperatures and rates of combustion. For oxyfuel combustion applied to gas turbines this is an additional challenge as these high temperatures cannot be sustained by conventional materials for a long period. The combustion temperatures can be reduced by the use of a diluent such as CO₂. Since the air separation process for obtaining oxygen is an energy penalty on such power plants, oxyfuel combustion in gas turbines is required at near stoichiometric conditions to reduce the wastage of O₂. An efficient way of regulating combustion temperatures is therefore by altering the extent of CO₂ dilution during combustion. The replacement of N₂ with CO₂ influences the oxyfuel combustion process in three ways:

- Change in thermodynamic and physical properties
- Participation in chemical reactions
- Increased radiation heat transfer

In the following section the influence of the use of CO₂ on the combustion process is described, together with a summary of the different investigations performed by researchers to characterize this influence. Firstly, the difference in thermodynamic, physical and chemical properties to nitrogen is described followed by a review of flame investigations.

The figure 2.9 (data from NIST [66]) compares the heat capacity at constant pressure (C_p) of CO₂, O₂ and N₂. The heat capacity of CO₂ is 1.3-1.7 times higher than that of N₂ in the temperature range up to 1000 K. The heat capacity of mixtures containing different proportions of O₂/CO₂ would lie in a range between the respective curves and would be higher than that of air. The higher heat capacities influence the adiabatic flame temperatures which can be attained after combustion. For a fixed stoichiometry, CO₂ concentration hence can significantly influence flame temperatures. Based on calculations using GRI-Mech 3.0 [67] and Cantera software [68], the adiabatic flame temperatures at 1 bar and 300 K for CH₄/O₂/CO₂ reactants near stoichiometric ($\varphi=0.98$) combustion were estimated in the range of 1600 K to 2200 K for compositions containing 26 % to 38 % O₂ (by volume) in a mixture of O₂ and CO₂. For comparison the temperature for a CH₄/air mixture with the same equivalence ratio is 2188 K. Other than the influence on flame temperatures the differences in thermal conductivity and viscosity also influence heat transfer and fluid flow. The thermal conductivity and viscosity of CO₂ are lesser than those of N₂ [37]. However these influences are expected to be of lesser significance [19, 69].

CO₂ has been shown to be much more active chemically than N₂. A study by Yossefi [70, 71] simulated the influence of N₂ replacement with CO₂ under constant pressure, constant volume and plug flow reactor conditions with methane and ethane. The CO₂ was shown to speed up the combustion rate under constant pressure conditions and reduce it under constant volume conditions. CO₂ participates actively in combustion through the following reaction [72, 73]:



Laminar burning velocities of CH₄/O₂/CO₂ and CH₄/air were calculated and compared to experimental data by Liu [21, 22]. The reduction of burning velocity was attributed to the presence of CO₂ and its active participation in chemical reactions through the above reaction. The figure 2.10 shows the change in laminar flame speed based on measurements performed at the DLR Stuttgart [3]. The laminar flame speeds were determined using two mechanisms namely, the GRI Mech 3.0 [67] and the RDv06-NGQ. The second mechanism has been developed at the DLR Stuttgart [74] based on a mechanism from Petersen [75]. The proportion of CO₂ drastically changes the laminar flame speed in comparison to a representative mixture for air containing 80 % N₂ and 20 % O₂. An increase in the O₂ concentration from 30 % to 40 % nearly triples the laminar flame speed

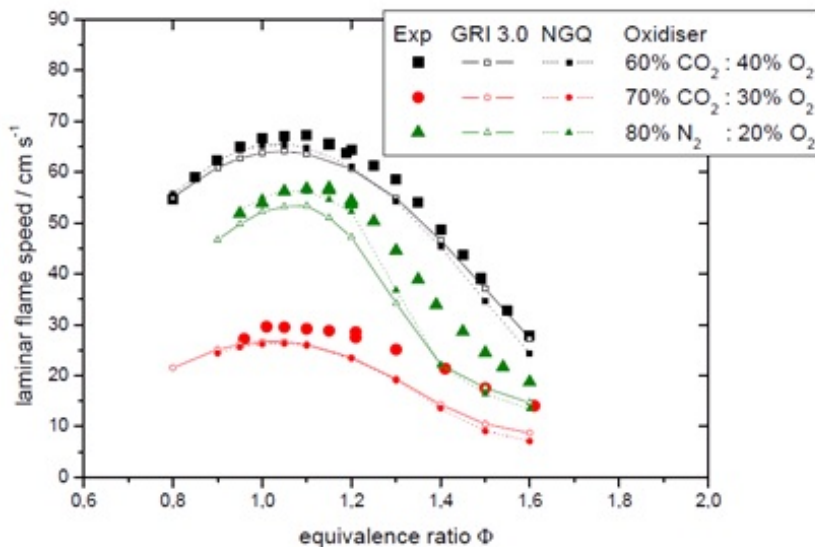


Figure 2.10: Experimental and simulated laminar flame speed of different oxyfuel mixtures at 3 bar and 473 K preheat [3].

for the entire range of equivalence ratios. The laminar flame speed of the 40 % O_2 flames is also higher than that of the representative air mixture. The concentration of O_2 is therefore an important parameter.

In order to determine the influence of radiation heat transfer Ju [20] performed premixed laminar flame speed simulations for flames replacing N_2 with CO_2 showing that the re-absorption due to CO_2 increases laminar burning velocities and extends flammability limits. Similar conclusions were reached in another study by Ruan [76]. Maruta [77] determined experimentally extinction characteristics of counter-flow CH_4/CO_2 and O_2/CO_2 flames under elevated pressure conditions. At elevated pressures an increase in extinction limits was attributed to the re-absorption of radiation. In view of the differences to N_2 the use CO_2 as a diluent in oxyfuel combustion would change flame behavior. Below a brief review of the investigations performed to date with methane-oxyfuel flames is given.

Turbulent jet flame investigations for oxyfuel mixtures have been performed by Lallemand [78], and Sautet [79] for technical furnace burner applications. The flames were of non-premixed nature using natural gas as fuel and pure oxygen without CO_2 dilution. Detailed measurements pertaining to furnace characteristics were performed under the OXYFLAM project at the IFRF (International Flame Research Foundation). The flame lengths were shown to be 2 to 3 times shorter than comparable air flames. Ditaranto et al. [80] performed experiments using premixed CH_4 /oxyfuel flames in a slot flame configuration for oxyfuel gas turbine applications. The effect of oxygen enrichment on flame stability was studied. Different regions of flame stabilization were observed. The oxyfuel

flames with less than 40 % O_2 concentration excited low frequency oscillations similar to air flames. With an increase in the O_2 concentration the flames excite thermo-acoustic oscillations that correspond to different mode of oscillations in the system. With very large O_2 concentration flashback is reported. Williams [81] investigated two (30 % O_2 /1 % N_2 /69 % CO_2 and 34 % O_2 /1 % N_2 /65 % CO_2) oxyfuel mixtures with fuels ranging from methane to different syn-gas compositions in a premixed swirl stabilized combustor with optical access. The results are presented in the form of flame photographs and exhaust gas emissions of CO and NO_x for different equivalence ratios and in the power range of 14.3-16.3 kW. The additional benefit of low NO_x emissions is highlighted and the CO emissions were found to be comparable to that of air flames. Amato [19] performed experiments to determine the blow off limits of oxyfuel flames in comparison to air flames and showed that the flames are more prone to blow off in comparison to air flames due to kinetic effects.

The studies performed to date on swirl stabilized oxyfuel flames lack a detailed characterization with fluid dynamic, heat release and flame stabilization information at atmospheric and elevated pressure conditions. A detailed comparison of methane-oxyfuel and methane-air flames would provide a much needed guideline for the use of conventional burners with oxyfuel mixtures and/or the redesign they require. The use of a partially premixed form of combustion for oxyfuel swirl flames has not yet been documented. At high CO_2 dilution the better stabilization that has been traditionally associated with this form of combustion would benefit oxyfuel flames. The turbine inlet temperatures (TIT) of oxyfuel turbines must lie in the range of conventional turbines i.e. 1600 K. With reduced O_2 concentration and stoichiometric partially premixed combustion this condition could be achieved. However, it is unclear if such flames can be stabilized in a conventional burner. The combination of parameters discussed above differentiating oxyfuel combustion to air combustion makes prediction of flame behavior difficult. The experimental investigations in this thesis address the specific impact of using different O_2/CO_2 concentrations on a partially premixed swirl burner under different operating conditions ranging from atmospheric operation to elevated pressures (5 bar). Optical diagnostic measurements have been made to quantify the impact of varying different parameters on flame behavior. The following chapter presents the methodology used to study swirl stabilized oxyfuel flames.

3

Methodology

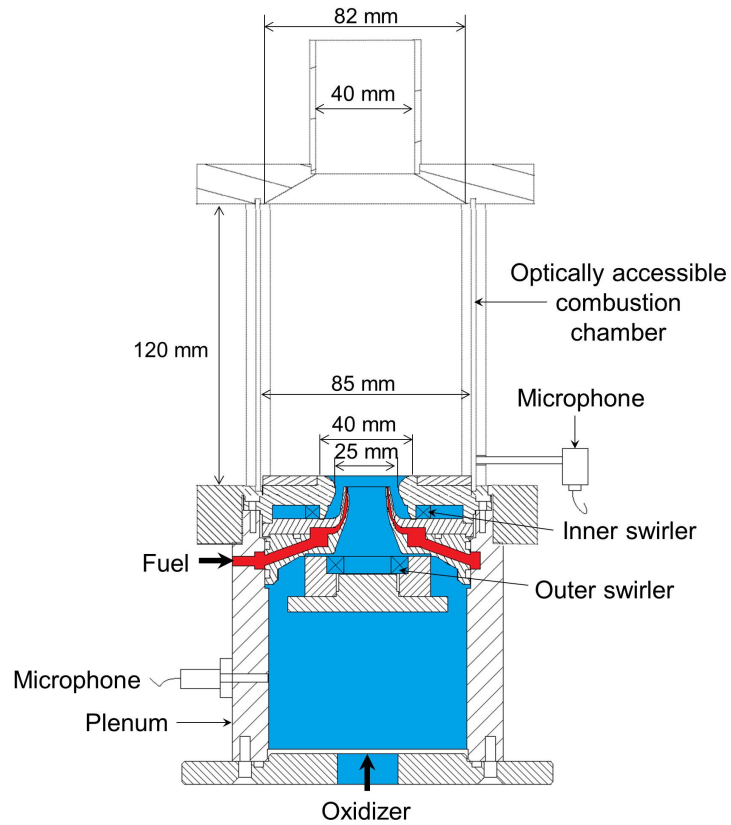
The variation of parameters such as equivalence ratio, inlet flow velocities, oxidizer temperature and operating pressure influences the characteristics of swirl stabilized flames. This influence is discernible through change in the flame stabilization, flow field and the thermo-chemical state of the flame. The investigations have been carried out at atmospheric and elevated pressure conditions. This chapter describes the approach used for the investigations. Firstly, a description of the burner and combustion chamber configurations used is given in section 3.1. Secondly, the fundamental aspects of the optical measurement techniques and relevant data analysis techniques are presented in section 3.2. Finally, the experimental setups along-with the measurement techniques applied for the investigations under atmospheric and elevated pressures are shown in sections 3.4 and 3.5. The method of data analysis, measurement uncertainty and error is also discussed.

3.1 Burner configurations

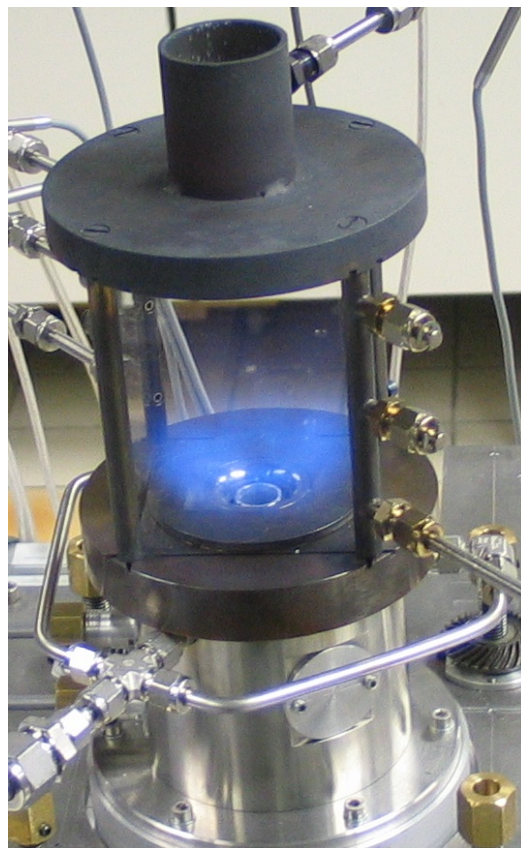
A partially premixed swirl burner has been used for the investigations. The burner was subsequently adapted for operation at elevated pressures. Both configurations were constructed with an optical access for the use of optical diagnostics. The following section describes in detail the burner and combustion chamber for both pressure conditions.

3.1.1 Atmospheric pressure burner configuration

The burner geometry used for the experiments is based on an aviation gas turbine application. The burner has been designed to replicate energy densities that are typically obtained in stationary gas turbines (10-40 MW/m³). A sketch illustrating a cross-section of the burner/chamber geometry is shown together with a photograph of the burner in operation in figure 3.1. The oxidizer enters the burner through the plenum and is then directed into two co-swirling swirlers which are mounted at an axial offset. The flow



(a) Burner and chamber cross-section



(b) Photograph with flame

Figure 3.1: Atmospheric partially premixed swirl burner configuration.

from the inner swirler enters a converging nozzle section with a diameter of 15 mm at its outlet. The flow through the outer swirler enters a converging diverging nozzle. This nozzle has a neck diameter of 25 mm followed by a divergence contoured to a diameter 40 mm. This geometry assists the formation of the IRZ (see section 2.1.2). The fuel is introduced into the combustion chamber through 72 channels with $0.5 \times 0.5 \text{ mm}^2$ cross-section which form a ring around the inner swirler nozzle. The location of these channels is 4.5 mm below the exit plane of the burner. The fuel and air hence partially mix before entering the combustion chamber, which is of a square cross section (85 mm x 85 mm) and 120 mm height. The combustion chamber has optical access by means of quartz windows on 4 sides. The products of combustion are exhausted into the surroundings through a 40 mm diameter exhaust nozzle. The acoustic behavior of the flames can be recorded with microphones in the combustion chamber and the plenum. Due to the high temperatures in the combustion chamber an indirect probe arrangement is used to direct the acoustic signal to a microphone. The plenum has a direct microphone arrangement to record acoustics. The microphone signals were recorded on a computer using an ADC (analog to digital converter) and LabView Signal Express software. The burner also referred to as the gas turbine model combustor GTMC has been the subject of numerous investigations (experimental and numerical) that have been documented in various publications. The data generated from the optical diagnostics has also been used for the validation of numerical modeling tools. A summary of the different publications using methane/air flames is the subject of chapter 4.

The burner was operated using O_2/CO_2 premixed in different proportions and air as oxidizer with CH_4 as fuel. The flow rates of the different gases were regulated by means of calibrated mass-flow controllers which were computer controlled through an in house LabView control program. The details of the setup are presented in the section 3.4

3.1.2 HIPOT rig and elevated pressure burner

In order to perform the studies at elevated pressures, a suitable housing for the burner and combustion chamber is required that can sustain the high thermal power, temperatures and pressures. The test facility must also be able to simulate gas turbine combustor inlet conditions. The high pressure optical test rig (HIPOT) was constructed for this purpose at the DLR during the course of this work. The test rig is of a blow down nature for oxyfuel oxidizers using a high pressure gas supply source for operation. The figure 3.2 shows the test facility. The test rig is modular in nature and consists of different sections performing distinct functions with a maximum thermal loading of 300 kW and maximum operating pressure of 40 bar. Not shown in the figure is the high flow rate oxidizer and fuel flow rate facility required to supply the test rig. The large supply of

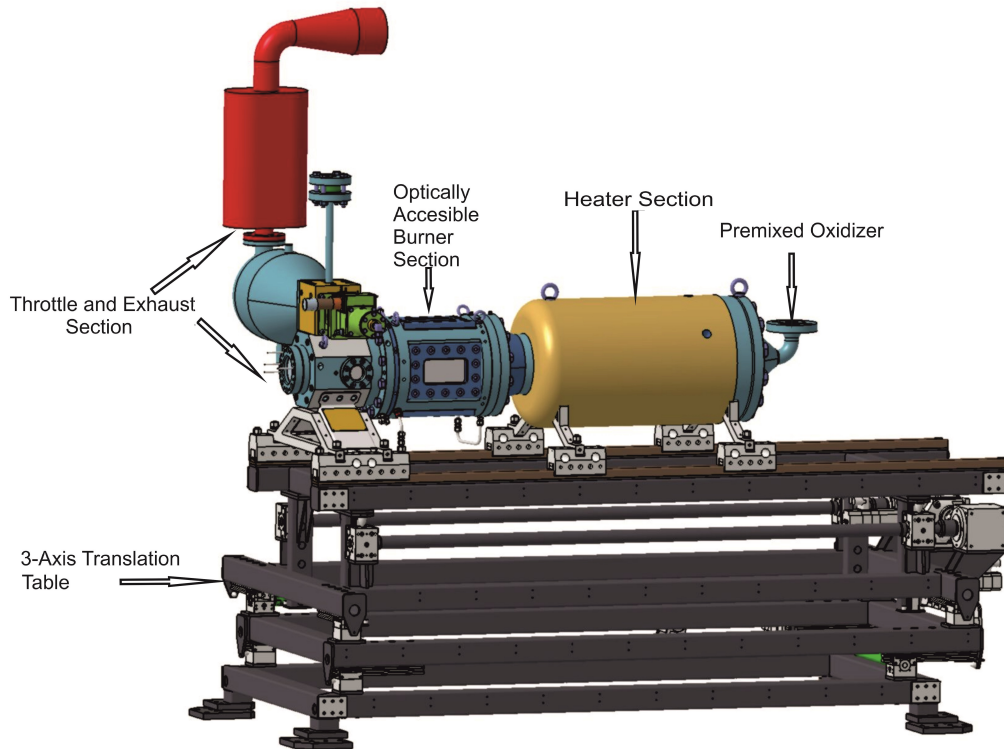


Figure 3.2: Test rig for measurements at elevated pressures.

CO₂ required to simulate oxyfuel conditions at elevated pressure was obtained by means of a bundle of liquid CO₂ which was equipped with a 45 kW vaporizer. Up to 120 g/s of gaseous CO₂ could be supplied. An oxygen supply also constituting of high pressure gas bundles capable of supplying 50 g/s of O₂ was setup. The O₂ and CO₂ could be premixed and supplied to the rig. An air supply capable of delivering up to 200 g/s was also connected to the rig for cooling and burner operation. The oxidizer (air or oxyfuel mixtures) enters the heater section after entering the rig. Here the gas could be heated up to 800 K by means of a custom built 192 kW electrical heater (Osram Sylvania) to simulate real combustor inlet conditions. The heated oxidizer then enters the optically accessible burner section.

Figure 3.3 shows a cross-section of the optical section with the burner mounted in it. Quartz windows in the high pressure housing and combustion chamber have been used for observing the flame and allowing the application of laser diagnostic measurement techniques. An optical access of 110 mm x 180 mm is available on 4 sides of the combustion chamber. The detailed burner configuration which is based on the atmospheric burner as described above is shown in figure 3.4. The heated oxidizer enters the plenum which has the swirlers and fuel injection that is geometrically the same as that used for the atmospheric experiments. It employs a double swirl configuration with the injection of fuel in between the two swirling flows. The fuel used for the high pressure experiments

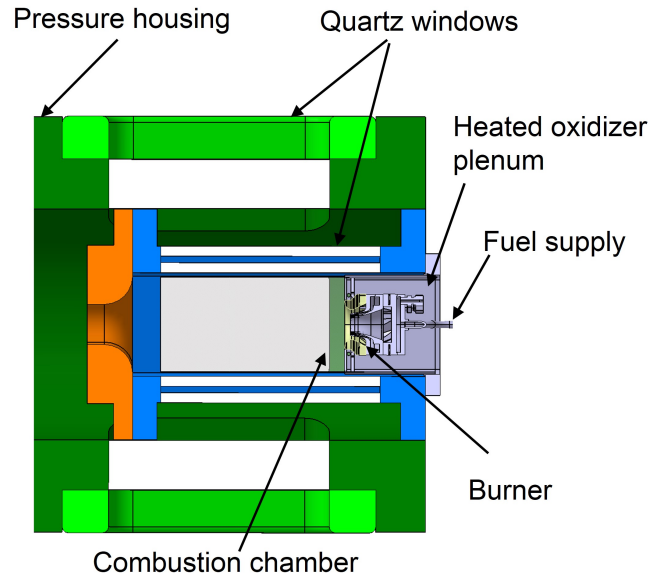


Figure 3.3: Burner assembled in high pressure rig.

was natural gas in comparison to methane for the atmospheric cases. The composition of the natural gas used typically consisted of 89-95 % CH_4 , 3-4.5 % C_2H_6 , 0.6-1.0 % C_3H_8 , 1-2.5 % N_2 and 0.8-1.4 % CO_2 . At higher thermal powers burner cooling is important especially due to the increased radiation effect of using CO_2 as oxidizer. The burner was therefore cooled using flow impingement to the back of the face plate. Part of the oxidizer (approximately 16 %) which is directed from the plenum into the swirlers, is directed to the back of the burner face plate by means of impingement cooling holes and then re-introduced through a 1 mm wide slit into the main combustion chamber. The combustion chamber is water cooled by means of a closed water circuit built into it. The temperature of the chamber is regulated by a control program. Each side of the combustion chamber contains two quartz glass windows which are mounted in parallel with an offset of 2.85 mm. The gap between the windows is used to pass cooling air to maintain window temperatures. The windows provide an effective view of 130 mm x 85 mm of the combustion chamber. The plenum of the burner and the combustion chamber are instrumented with thermo-couples and pressure probes to measure, monitor and control different operating parameters. Acoustic pressure oscillations were measured using piezo-resistive pressure transducers (Kistler 4045A10/4045A20) that could be mounted at different points in the test rig. Due to the high temperatures and pressures in the rig, conventional microphones were not used. The pressure fluctuation measurement in the combustion chamber was performed similar to that at atmospheric conditions using an indirect arrangement. The fluctuations in the combustion chamber were directed through a steel pipe to the transducer which was mounted externally on the test rig.

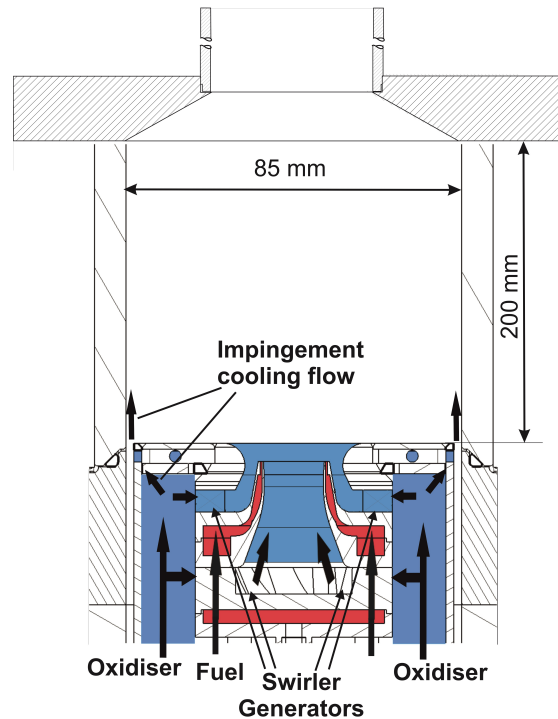


Figure 3.4: High pressure swirl stabilized burner configuration.

The combustion products exit the combustion chamber through a 18 mm converging nozzle. The diameter of the nozzle is lesser than that used for atmospheric conditions (40 mm exhaust nozzle) to reduce the acoustic coupling of the throttle section with the burner. The burnt gas temperature is initially reduced by means of mixing with air before it enters the throttle section where final temperature reduction occurs by means of water injection. The resultant mixture is carried through a muffler into the exhaust ventilation system. The test rig is mounted on a translation table. The translation table allows for the 3-axis movement of the test rig while performing laser diagnostic measurements. The entire test rig was monitored and controlled by means of an in-house LabView control program.

3.2 Investigative techniques

The use of optical diagnostics including those based on lasers has contributed significantly to the understanding of combustion phenomena. Practical combustion processes are governed by the interaction of fluid dynamics and combustion chemistry. This interaction is central to all phenomena relating to pollutant emissions and flame stabilization and is therefore a determining factor in burner design. Measurement in a combustion environment is a significant challenge, due to the high temperatures and turbulent conditions under which most practical devices function. Traditional probe measurements tend to

influence flow and combustion phenomena. The advantage of using optical/laser measurement techniques is their lack of or minimal interference with the combustion process. As the methods are optical, an obvious prerequisite is relevant access to the combustion process as seen in the burner and combustion chamber configurations introduced in the previous section. The use of optical diagnostics has also facilitated the development of numerical modeling tools by providing data for validation [82]. This is an active area of combustion research. Hoeinghaus [83] provides an exhaustive summary of the laser measurement techniques used for understanding different aspects of combustion. In this section an overview of the measurement techniques used for characterizing oxyfuel flames is presented. The associated tools for analyzing data from each of the measurement techniques are also explained. OH*-chemiluminescence imaging, particle image velocimetry PIV and laser Raman spectroscopy have been applied to understand flame behavior. The OH*-chemiluminescence imaging was used to obtain basic flame stabilization information, while the PIV information characterized the flame fluid dynamics. Laser Raman spectroscopy was used to obtain detailed information regarding the chemical composition of the turbulent flames. In addition to the use of optical diagnostics acoustic pressure measurements were taken for analyzing the thermo-acoustic oscillations in the system. The details regarding each of these are provided in the experimental setups in sections 3.4 and 3.5. A brief review of the fundamentals of the optical measurement techniques is provided in the following section before introducing each measurement technique applied to the above burners.

3.2.1 OH*-chemiluminescence imaging

The process of combustion leads to the formation of many intermediate species. The intermediate species formed consist of ground state and electronically excited radicals. Chemiluminescence is the spontaneous emission of electromagnetic radiation by electronically excited radicals when returning to their ground states. Hydrocarbon flames are known to excite chemiluminescence of the hydroxyl radical (OH*) and methyldyne radical (CH*) together with broadband emissions of CO₂*. A return to the ground state of such molecules typically occurs within a few nanoseconds. The OH* emission occurs at 309 nm while that of CH* occurs at 431, 390 and 314 nm. In hydrocarbon flames the intensity of OH*-chemiluminescence is high due to the following reaction [84, 85].



This reaction is related to the oxidation of the fuel and therefore the OH*-chemiluminescence has been often correlated with the heat release rate in a flame. The exact nature of this correlation is unclear, however many researchers have used this approach to study

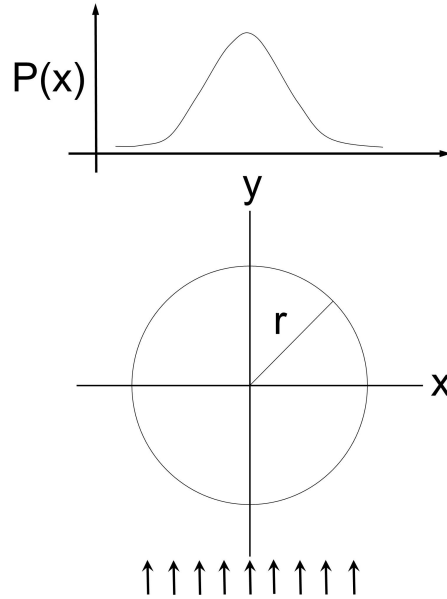


Figure 3.5: Abel projection of an axisymmetric function for a parallel beam.

flame behavior qualitatively [86, 87, 88]. The chemiluminescence can be captured using UV lenses and imaged using intensified cameras. The flame heat release images are obtained from short exposures. Several such short exposures are collected and corrected for background noise, and imaging sensor sensitivity to obtain averaged flame heat release information. The technique however provides line of sight information from a flame. If the flame is axisymmetric an Abel [89] deconvolution of the integrated data can be applied to obtain planar heat release information. Tomographic reconstruction has been used in cases where no symmetry exists to obtain spatial heat release data [90, 91]. The figure 3.5 illustrates the principle behind the Abel inversion. The projection $P(x)$ of a cylindrically symmetric function $F(r)$ is given by,

$$P(x) = 2 \int_x^{\infty} \frac{F(r)r \, dr}{\sqrt{r^2 - x^2}} \quad (3.2)$$

where r and x are radial and lateral co-ordinates as shown in the figure. Conversely if the integrated information is available in the form of line of sight integrated OH* chemiluminescence data, the function can be determined with an inverse Abel transformation given by,

$$F(r) = -\frac{1}{\pi} \int_r^{\infty} \frac{dP}{dx} \frac{dx}{\sqrt{r^2 - x^2}} \quad (3.3)$$

The inverse transformation is determined by numerical integration using different methods such as direct discretization, Nestor-Olsen [92], and Fourier-Hankel [93]. The

use of OH*-chemiluminescence provides qualitative heat release information from a flame and hence can be used to discern basic flame stabilization characteristics [27].

3.2.2 Particle image velocimetry (PIV)

The estimation of velocity in turbulent flows is challenging. Traditionally methods such as pitot tubes or hot wire anemometers have been used to obtain point-wise velocity information. However these methods are intrusive and have limitations in obtaining instantaneous planar flow information. The use of laser measurement methods has become common practice. The two methods often used in turbulent combusting flows include Laser-Doppler anemometry LDA [94] and PIV [95, 96]. These techniques are minimally invasive in nature. The flow is seeded with fine particles which exert a negligible influence on the flow characteristics when criteria regarding particle size and density are met. This has led to extensive use of such techniques in different applications involving reactive and non-reactive flows. The advantage of PIV is the ability to obtain planar velocity fields. With the use of stereoscopic PIV 3-component velocity information can be obtained. The method has also been extended to obtain 3-dimensional velocity fields in the form of tomographic PIV [96]. Here a brief summary of the fundamentals behind the method is presented. The technique uses seeding of the fluid flow with particles. The particles are irradiated with laser light, which is scattered to obtain a Mie scattering signal representing the particle location. Using a pulsed laser system successive images separated by a few microseconds indicating particle location can be obtained. The figure 3.6 shows the principle of the measurement technique. Typically a Nd:YAG laser at a wavelength of 532 nm is used to form a light sheet using cylindrical lenses. The light sheet is directed to the region of interest, which in this case is the flow emanating from a burner. Small diameter particles are introduced into the flow being investigated. The scattered light from consecutive laser pulses is recorded by CCD or CMOS cameras. The particles are said to replicate the gas phase velocity for the case when the slip between the particle and gas phase is minimum. The slip of a particle in a fluid flow with acceleration is given by [95],

$$U_s = U_p - U = d_p^2 \frac{(\rho_p - \rho)}{18\mu_f} \mathbf{a} \quad (3.4)$$

where U_s is the particle slip velocity, U_p is the particle velocity and U is gas velocity, d_p is particle diameter, μ_f is gas viscosity, ρ_p is particle density, ρ is gas density and \mathbf{a} is acceleration of gas. The step response of a particle having much larger density than the fluid is given by

$$U_p(t) = U \left[1 - \exp\left(-\frac{t}{\tau_s}\right) \right] \quad (3.5)$$

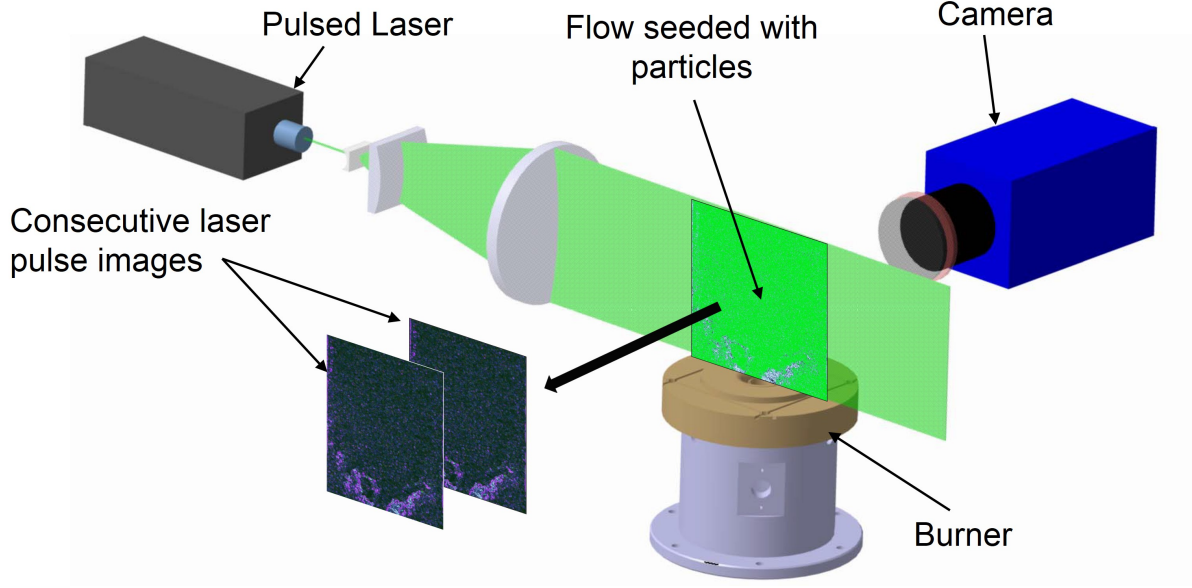


Figure 3.6: Basic principle of 2-component 2-d PIV measurement technique.

where τ_s is the relaxation time given by

$$\tau_s = d_p^2 \frac{\rho_p}{18\mu\rho} \quad (3.6)$$

The ability of a particle to follow the flow is determined by the dimensionless Stokes number which is given by:

$$St = \frac{\tau_s U}{l} \quad (3.7)$$

where U is the characteristic flow velocity and l represents a characteristic dimension. $St \ll 1$ represents flows where the particles take the velocity of the fluid flow. The type of particles used is determined by this number, which can be reduced by reducing the relaxation time τ_s , which in turn can be reduced by using small particle diameter and density. For the experiments conducted here TiO_2 particles of $1\mu\text{m}$ diameter were used.

The velocity information is extracted from the consecutive images by correlating particle displacement information using digital image processing. The following exemplary (Fig. 3.7) image shows the conceptual arrangement for velocity determination in an imaged region of the flow field containing $M \times N$ pixels. The two images represent particle information recorded at two time instances by using a pulsed laser. In order to obtain velocities at different locations in the flow field the image is subdivided into interrogation volumes. The interrogation volumes shown are of square type, however geometrical shapes such as circles and ellipses can also be used. The Image 1 and Image 2 represent the two images obtained from consecutive laser pulses. The discrete cross-correlation function for

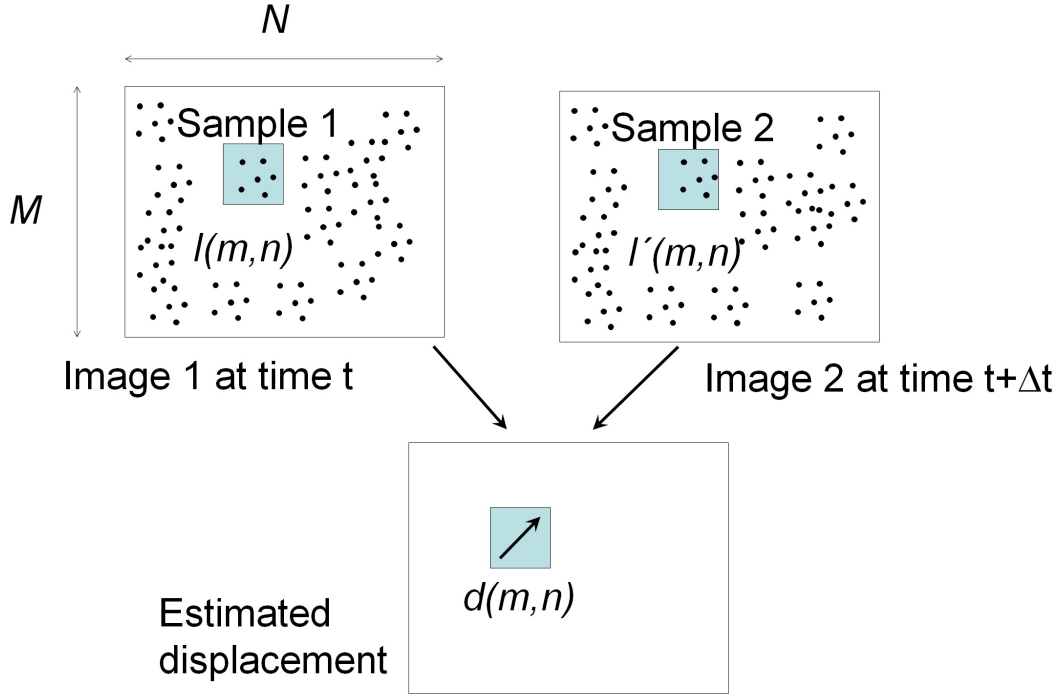


Figure 3.7: Correlation of particle light scattering images for obtaining velocity information.

the image pairs for an interrogation volume of $m \times n$ size for a particle displacement x and y is given by [95]:

$$R_{II}(x, y) = \sum_{i=-m/2}^{m/2} \sum_{j=-n/2}^{n/2} I(i, j) I'(i + x, j + y) \quad (3.8)$$

where $I(i, j)$ and $I'(i, j)$ represent the image intensity at respective locations in the interrogation volumes of the first and second image. The cross correlation values are obtained for a sample displacement x, y . This process is repeated for different combinations of a range of displacements ($-A \leq x \leq A, -B \leq y \leq B$) forming a correlation matrix of $2A+1 \times 2B+1$. The cross-correlation function with the highest value is then chosen as the particle displacement. The velocity components in the respective directions are obtained by dividing the displacements with the time between laser pulses (image captures). It must be noted that with the above procedure only 2-component velocity information can be obtained. Stereoscopic PIV employs a two camera arrangement to obtain 3-component velocity information.

For the investigations in this work, the stereoscopic PIV technique has been used at atmospheric conditions to determine the change in velocity field with different operating conditions. The measurements were performed at a repetition rate of 5 Hz. At elevated pressures 2-component high repetition rate (3 kHz) PIV has been used to understand

flame dynamics. The PIV data is typically represented in the form of average or RMS fluctuations of multiple measurements. Phase-correlated mean values have been used in the case of thermo-acoustic oscillations to illustrate flame and flow dynamics. An additional technique which is often used to resolve coherent turbulent flow features is proper orthogonal decomposition POD [97]. The method divides a velocity field into mean and fluctuating components. For the fluctuating part, spatial and temporal components are evaluated by decomposition so that the components form an orthonormal bases. These orthonormal bases are referred to as the modes in the system. Mathematically for a series of A velocity vector fields $\mathbf{u}_i(\mathbf{x}_k)$ ($i=1\dots A$) measured at B locations \mathbf{x}_k ($k=1\dots B$) the instantaneous velocity field can be written as

$$\mathbf{u}_i(\mathbf{x}_k) = \bar{\mathbf{u}}_i(\mathbf{x}_k) + \mathbf{u}'_i(\mathbf{x}_k) \quad (3.9)$$

where $\bar{\mathbf{u}}_i$ is the mean velocity field and $\mathbf{u}'_i(\mathbf{x}_k)$ the fluctuating component. The velocity field when decomposed into different modes using a POD can be written as

$$\mathbf{u}'_i(\mathbf{x}_k) = \bar{\mathbf{u}}_i(\mathbf{x}_k) + \sum_{j=1}^R a_{ij} \phi_j(\mathbf{x}_k) \quad (3.10)$$

where a_{ij} are the mode coefficients that represent the projection of the velocity field \mathbf{u}'_i on mode $\phi_j(\mathbf{x}_k)$ and R ($1 \leq R \leq A$) is the order of the decomposition. The modes are orthonormal in that they follow the following requirement

$$\langle \phi_i \cdot \phi_j \rangle = \delta_{ij} \quad (3.11)$$

where δ_{ij} is the Dirac delta function. The mode coefficients are related to the velocity fluctuation as in equation 3.12.

$$a_{ij} = \langle \mathbf{u}'_i \cdot \phi_j \rangle \quad (3.12)$$

Each POD mode contributes a specific fraction to the fluctuating kinetic energy. The reader is referred to Stoehr [98] for a more detailed account of how the kinetic energy and POD modes are related. The first or lower order modes represent the flow fluctuations which contain higher fluctuating kinetic energy which decreases with the order of the modes. The POD analysis technique is used to identify these high energy low order modes to differentiate coherent flow features from the turbulent flow dynamics.

The evaluation of the POD modes leads to an eigenvalue problem for a matrix size of $A \times A$. The determination of the modes can be done using the method of snapshots [99] when the number of spatial locations (B) of velocity measured significantly exceeds the number of samples obtained. A commercial software (Davis 8.0 [100]) provided with the PIV system was used to evaluate the raw PIV images to obtain the velocity vectors. Subsequently a POD analysis was carried out in the same software.

3.2.3 Laser Raman spectroscopy

Laser Raman spectroscopy is based on the Raman scattering effect that was first observed by C.V Raman in liquids [101]. Raman scattering has been explained by classical electromagnetic theory and quantum theory. Both treatments are presented briefly to understand the process. The classical electromagnetic explanation is based on the polarization that molecules are subjected to when they are irradiated with electromagnetic waves. The polarization of the molecule causes changes in the electric/magnetic field in the molecule giving rise to electromagnetic waves called scattered radiation. The polarization vector \mathbf{p} for a molecule with incident electromagnetic waves having an electric field vector \mathbf{E} is given by [102]

$$\mathbf{p} = \alpha\epsilon_o\mathbf{E} \quad (3.13)$$

where α is the polarization coefficient of the molecule, and ϵ_o is the permittivity. The polarization coefficient α is given by a static and varying component in the case that a molecule is set into vibration due to incident radiation about a co-ordinate Q

$$\alpha = \alpha_0 + \left(\frac{\partial\alpha}{\partial Q}\right)_0 Q \quad (3.14)$$

If the reference co-ordinate of the molecule is set to oscillate at a natural frequency ω_v , so that

$$Q = Q_0 \cos\omega_v t \quad (3.15)$$

then by substitution for α and Q in equation 3.13 for an incident wave with frequency ω_0 yields

$$\mathbf{p} = \alpha_0\epsilon_o\mathbf{E}_0\cos\omega_0 t + \left(\frac{\partial\alpha}{\partial Q}\right)_0 \frac{Q_0\mathbf{E}_0}{2} [\cos(\omega_0 - \omega_v)t + \cos(\omega_0 + \omega_v)t] \quad (3.16)$$

The first term on the right is the elastic Rayleigh scattering of the incident radiation, while the other terms represent the inelastic Raman scattering of the molecule. The inelastic scattering is known as Stokes (frequency reduced) and anti-Stokes (frequency increased). The quantum theory explains the scattering of electromagnetic radiation by molecules through change in energy levels or quantum numbers of the electrons and hence molecule [102]. The quantum numbers correspond to rotational (J), vibrational (v) and electronic (Λ) energy levels of the molecules. Excitation can be obtained through a change in the rotational, vibrational and electronic states of a molecule. The excitation of molecules to higher electronic states is used in fluorescence and near-resonant Raman spectroscopy. For conciseness, only the rotational and vibrational Raman effect is described here. The figure 3.8 shows as an example of the rotational and vibrational energy

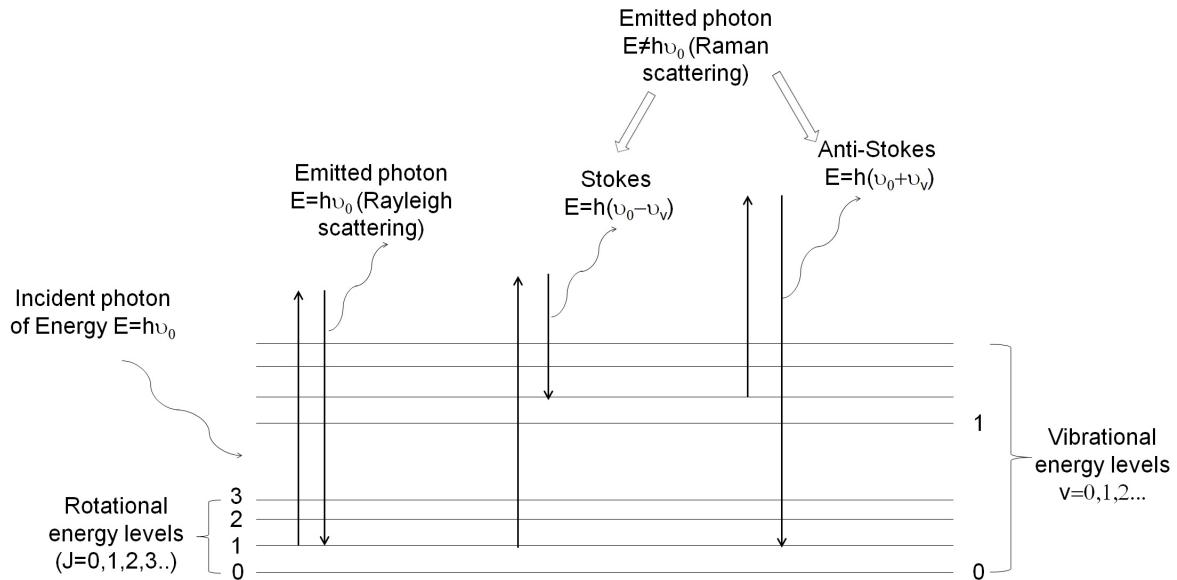


Figure 3.8: Energy level diagram explaining elastic and inelastic scattering of electromagnetic radiation by molecules.

levels of a molecule which is subject to an incident electromagnetic radiation (photon) with energy

$$E = h\nu_0 \quad (3.17)$$

where h is the Planck's constant and ν_0 is the frequency of the electromagnetic wave which is related to the speed of light in vacuum c by the expression $c=\lambda_0\nu_0$. The wavelength of the wave is given by λ_0 .

If a molecule does not change the energy level during a scattering process, it is referred to as Rayleigh scattering. However if the scattering results in the molecule transitioning to another state, the scattering is inelastic and called Raman scattering. The Raman scattering shown is referred to as the Q-branch transition which is governed by vibrational level selection rule of $\Delta v=\pm 1$ and $\Delta J=0$. Similarly if the molecule transitions to another rotational level, the scattering is referred to as rotational Raman scattering. Such scattering is governed by rotational level selection rule of $\Delta J=0, \pm 2$. Since the frequency of the emitted photon is similar to that of the incident photon, experimental resolution of the frequency shift is difficult. For combustion diagnostic applications vibrational modes are typically used due to the higher frequency shift. The difference in energy of the photon corresponds to the difference in energies of the vibrational levels given by $E=h\nu_v$. The statistical probability of the different quantum vibrational states that a molecule in equilibrium can achieve is obtained by the Boltzmann distribution. It has been determined that in combustion diagnostics even at high temperatures (up to

2400 K) molecules remain mostly in the ground state with $v=0$. Hence Stokes type of Raman scattering is used for combustion laser Raman spectroscopy.

The molecules present in combustion typically are CO_2 , O_2 , H_2O , CO , N_2 and CH_4 have at least one vibration mode which is Raman active. The Raman shifts for the vibrational modes of these molecules are known. This is used in combustion diagnostics to detect Raman signals from such molecules present by focusing high intensity laser radiation into a small region in a flame (an interrogation volume). The Raman signal depends on the composition (number density of molecular species and temperature) in the interrogation volume. For such a system the intensity of the Raman signal P_i from a particular species i irradiated with a laser with power P_L is given by [102]

$$P_i = P_L n_i \left(\frac{\partial \sigma_i}{\partial \Omega} \right) \Omega l \epsilon \quad (3.18)$$

where the partial differential is referred to as the molecule scattering cross-section, n_i is the number of molecules of the species i , Ω is the solid angle of detection, l is the length of sampled region, and ϵ the efficiency of the detection system. The molecular scattering cross-section is dependent on the particular combustion species and its temperature. It is however also dependent on the frequency of the laser which is used to excite vibrational modes in the molecule. For simplicity the dependence of the scattering cross-section in a diatomic molecule is given in the equation 3.19. The detailed expression with corresponding molecular constants is found in Eckbreth [102]:

$$\frac{\partial \sigma_i}{\partial \Omega} \propto \frac{(v_0 - v_k)^4}{[1 - e^{-hc\omega_e/kT}]} \quad (3.19)$$

where v_0 is the incident electromagnetic wave frequency, v_k is the scattered Raman frequency, ω_e is the vibration wave number ($\omega_e=v_e/c$) for the given vibrational state, k is the Boltzmann constant, T is the temperature. The numerator of the above expression denotes the frequency shift which occurs for a given molecule. The fourth power dependence is from the distribution of radiation from a polarized molecule. The denominator represents the Boltzmann distribution of different states at a given temperature. Different molecules would give rise to different frequency shifts. The Raman scattering signal is therefore collected by means of an optical setup and directed to a spectrometer to resolve the frequencies. The signal is then collected by means of a photo-multiplier or a camera. A typical frequency spectrum when a 532 nm Nd:YAG laser is used in methane/air flames is shown in figure 3.9. The spectrum is based on measurements and shows the Raman shifts for the different combustion species. The different species can therefore be identified based on the frequency shift and the number density from the intensity of the signal. For certain pairs of species such as CO_2/O_2 and CO/N_2 there is a spectral overlap. This must be accounted for during the analysis of the measurement

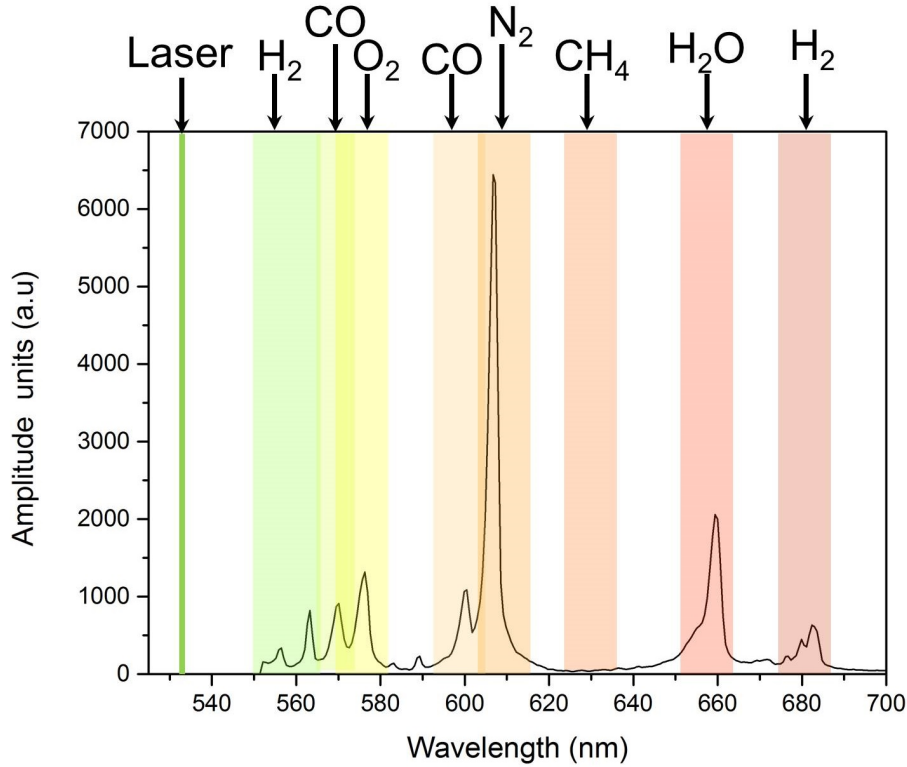


Figure 3.9: Typical vibrational Raman spectrum for scattering by different species in a near stoichiometric premixed methane air flame using a 532nm Nd:YAG laser.

data. This can be done by determining coefficients referred to as cross-talk coefficients which determine the influence of individual species on the overlapping sections of the spectrum.

The scattering cross-section of different species also have a temperature dependence due to the change in distribution of molecular vibration states. The different dependencies in equations 3.18 and 3.19 can be combined into a temperature dependent calibration coefficient $G_i(T)$ for each species giving the following expression,

$$n_i = \frac{P_i}{P_L G_i(T) f_i(T)} \quad (3.20)$$

where $f_i(T) = 1/[1 - e^{-hcw_e/kT}]$.

The calibration coefficients must be determined experimentally for gases which need to be measured at temperatures which are relevant for the combustion measurements. The details of the calibration process and data evaluation is provided in the following section. Using Raman scattering the concentration of major combustion species in a flame can be obtained. The concentration of minor species formed during the combustion process is assumed to be negligible. The temperature of the species can be estimated using the

expression

$$T = \frac{p}{nk} \quad (3.21)$$

where p is ambient pressure, $n = \sum n_i$ is the number density of gas molecules and k is the Boltzmann constant. The relation between individual species number density and their mole fractions is given by.

$$n_i = \frac{p}{k} \cdot \frac{X_i}{T} \quad (3.22)$$

From the equation 3.19 it is seen that the Raman scattering cross-section increases when a higher frequency of laser light is used to excite vibration modes. The cross-section of the Raman scattering process is quite low and relatively high laser energy is required to obtain a detectable scattering signal. A mobile Raman laser system developed at the DLR using Nd:YAG lasers has been used for the measurements performed in this work. Details regarding the system are provided in the measurement setup. Laser Raman spectroscopy has been used to determine the chemical state at different locations in two oxyfuel flames. The Raman measurements have been used to draw a detailed comparison to air flames.

3.3 Approach for investigating swirl stabilized oxy-fuel flames

The above mentioned burner configurations and optical techniques have been used for characterizing oxyfuel flames under atmospheric and elevated pressures. The effect of varying parameters such as flow velocity, flame stoichiometry and oxidizer composition on flame stability has been investigated. A simple way of depicting the effect of varying different parameters on flame stability is a burner stability map. The figure 3.10 shows an example of such a map for a burner operating with methane/air. The average inlet flow velocity is a measure of the quantity of oxidizer (air) that is being introduced into the burner and is correlated to the percentage of maximum rated thermal power. Typically such a map is made for air flame burners to determine the limits of stability. For the case of oxyfuel flames, an additional parameter needs to be taken into account. This is the CO₂ dilution in the oxidizer. The oxidizer in the case of oxyfuel flames investigated here is a mixture of O₂ and CO₂. The extent of change in flame stabilization due to change in CO₂ dilution is not known. Since the stoichiometry of a flame is determined by the ratio of fuel to oxygen, for a fixed equivalence ratio higher CO₂ dilution increases the total inlet flow velocity. For example if a methane flame is operated at 20 kW and $\varphi=0.98$ using two oxidizers containing 26 % and 30 % O₂ by volume (rest is CO₂), the flow rates of CH₄ and O₂ for both cases are 33.47 slpm, and 66.99 slpm respectively. However, the CO₂

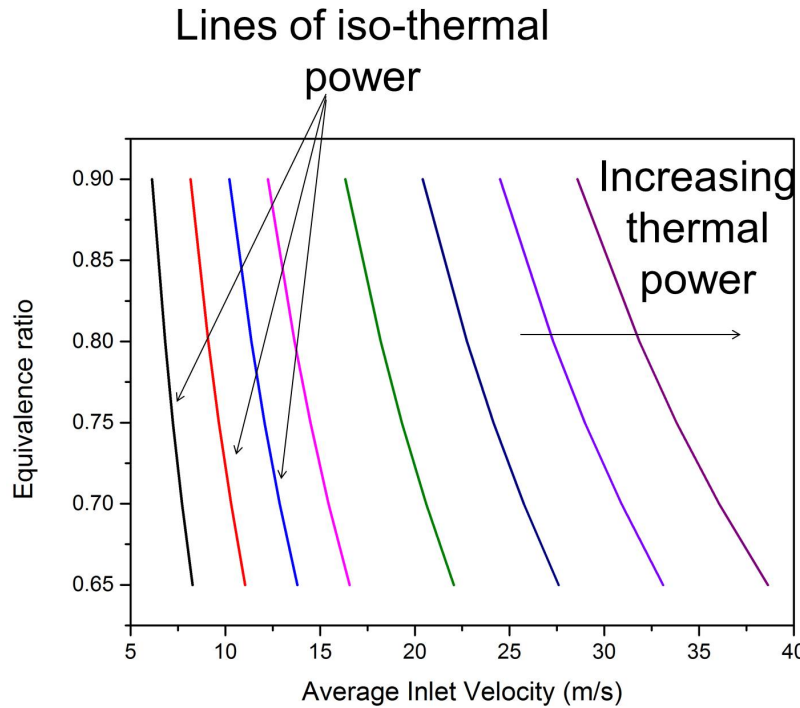


Figure 3.10: Typical swirl burner stable operation map for air flames.

flow rates are 189.5 slpm and 155.4 slpm. Thus at similar thermal powers different inlet flow conditions would exist for different O_2 concentrations in the oxidizer. Conversely if the burner is operated using different oxidizers at the same flow velocity, the quantity of O_2 supplied to the burner increases as the O_2 concentration in the oxidizer increases. Therefore a 30 % O_2 flame at $\varphi=0.98$ with an average inlet velocity of 12 m/s would have 15 % more thermal power than a 26 % O_2 flame at the same conditions. Hence, in order to completely understand the effect of using different oxidizers, experiments comparing flame characteristics at similar thermal powers and similar inlet velocities have to be performed.

Under atmospheric conditions the flame characteristics and limits of stable operation for different CO_2 dilutions have been determined using OH^* -chemiluminescence imaging. The flow fields of selected flames have been characterized by means of simultaneous PIV/ OH^* -chemiluminescence imaging. Additionally laser Raman spectroscopy measurements performed on two characteristic oxyfuel flames have been used to identify differences in temperature and concentration fields relative to air flames. A comparison to air flames which have been extensively studied (see 4) is drawn based on these results. Subsequently, the effect of operating selected oxyfuel flames at elevated pressure has been studied. The impact of changing parameters such as preheat and pressure to values closer to actual turbine conditions is determined and a comparison to air flames operated under similar conditions is also made. OH^* -chemiluminescence imaging at low repetition rate

(10 Hz) as well as simultaneous high repetition (3 kHz) OH*-chemiluminescence imaging and PIV have been applied to the elevated pressure experiments. The high repetition rate measurement technique is used to better resolve the unconventional burner aerodynamics that have been observed. The effect of using the modified burner for elevated pressure has been studied to identify the differences in the two burners.

The study of the oxyfuel flames is therefore classified into the following:

1. Atmospheric pressure investigations
 - (a) Oxyfuel flames at comparable thermal powers
 - (b) Oxyfuel flames at comparable inlet velocities
 - (c) Thermo-chemical states of turbulent swirl stabilized oxyfuel flames
2. Difference between atmospheric pressure and elevated pressure burner
3. Oxyfuel flames at elevated pressures
 - (a) Effect of preheat and pressure on flame behavior
 - (b) Effect of change in thermal power and equivalence ratio on air and oxyfuel flames
 - (c) Burner aerodynamics at elevated pressure

The burner aerodynamics was a critical parameter at elevated pressure. It has been looked into in detail to differentiate from the impact of oxyfuel mixtures on flame stability. The figure 3.11 shows the association between the different investigations and the experimental techniques applied. The three major setups used are differentiated based on operating pressure as the following:

- Atmospheric setup
 1. OH*-chemiluminescence imaging and PIV
 2. Laser Raman spectroscopy
- Elevated pressure
 1. Simultaneous OH*-chemiluminescence imaging and PIV

In the following section the three setups used are described. Since the OH*-chemiluminescence imaging setup is the simplest and also an integral part of other setups, it is not dealt with separately. Only gross changes from the standard configuration for this technique are mentioned at relevant locations. The manner in which the gases were supplied to the burner, the necessary instrumentation and control devices are also described.

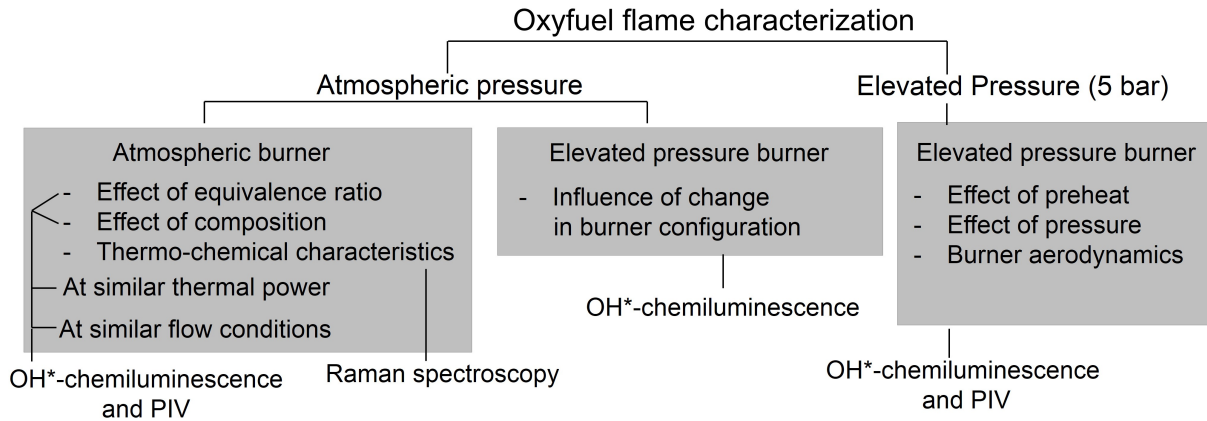


Figure 3.11: Overview of experiments performed and associated measurement techniques used to characterize oxyfuel flames.

3.4 Experimental setup: Atmospheric pressure

The two major experimental setups used for atmospheric pressure oxyfuel flame studies are presented along with a description of the basic infrastructure required to operate the burner. The description is divided into three sub-sections:

1. Gas supply, burner instrumentation and control
2. OH*-chemiluminescence imaging and PIV setup
3. Laser Raman measurement setup

3.4.1 Gas supply, burner instrumentation and control

The figure 3.12 shows a sketch of the arrangement for operating and controlling the burner with oxyfuel flames. A system of pressurized gas cylinders containing CO₂, O₂ and CH₄ with a purity of 99.5 % was used to operate the burner. CO₂ liquifies at normal temperature (20 °C) with an increase in pressure. The phase change when using CO₂ cylinders can lead to significant cylinder cooling and drop in supply pressure and flow rates. A gas bundle with 12 CO₂ cylinders was used to distribute the total mass undergoing phase change and hence maintaining supply pressures. This was used for the characterization of oxyfuel flames at comparable thermal powers. For the study at comparable velocity, a single CO₂ cylinder arrangement was used with a cylinder heater blanket to compensate for the effects of cooling. The supply for all gases was regulated to a pressure of 7.5 bar at the inlet of the Coriolis mass flow meters. Siemens Danfoss Coriolis mass flow meters were used to measure the flow rates [103]. The series MASS 2100 with DI 1.5, DI 3 and DI 15 were used for CH₄, O₂ and CO₂. The flow rates were

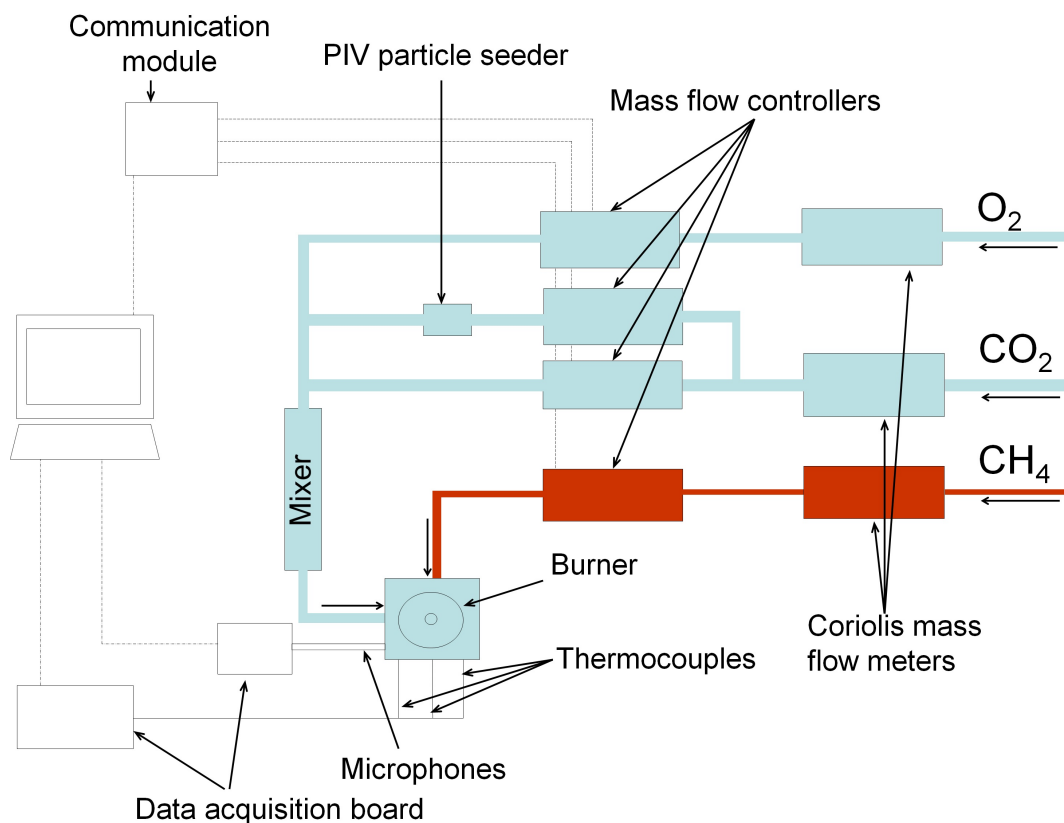


Figure 3.12: Gas supply, instrumentation and control for operating burner under atmospheric conditions.

controlled by means of calibrated Brooks 5853S (CO_2 and O_2), and 5851S (CH_4) mass flow controllers [104]. The Coriolis flow meters, and mass flow meters were connected to a control computer by means of a communication module.

The oxidizer consisting of different proportions of O_2 and CO_2 was premixed before entering the burner by means of a custom made mixer [105]. While performing PIV measurements a part of the CO_2 was directed into a seeder containing $1\mu m$ TiO_2 particles. This flow was then re-introduced into the main flow. The quantity of seeding flow was controlled by means of flow controllers to maintain the required total flow. A valve was used to enable and disable the seeding of the flow. The oxidizer and fuel temperatures were monitored and recorded by means of thermocouples mounted in the supply line just before the burner. Thermocouples mounted on the combustion chamber posts and exhaust nozzle were used to assess the equilibrium of the flame relative to the surroundings during the measurements. K-type thermocouples were used for the experiments. The flow devices and instrumentation were controlled and monitored by means of a LabView program from a computer. Data-logging of all control parameters was performed for back-referencing and verification. The acoustic signals from the combustion chamber and the plenum of the burner were recorded by means of microphones connected to a computer.

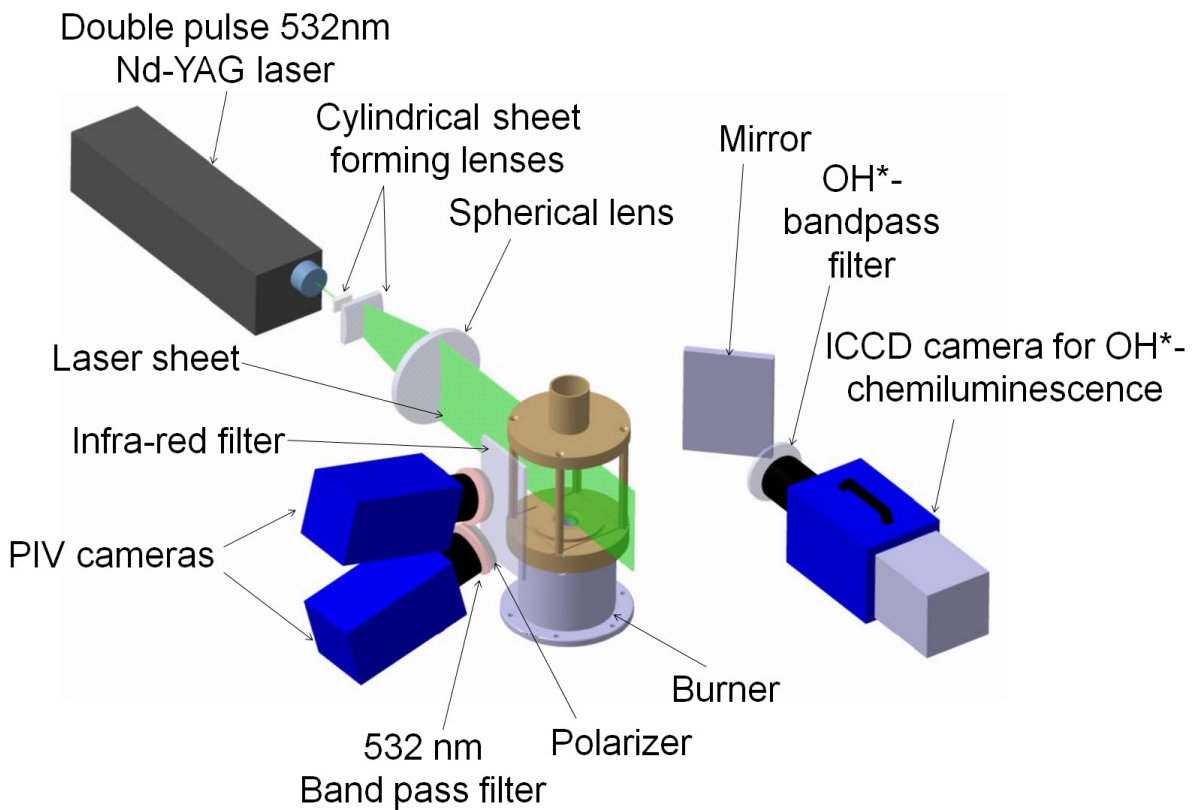


Figure 3.13: Simultaneous OH*-chemiluminescence imaging and stereoscopic PIV setup.

Type 4939 condenser microphones from Bruel and Kjaer were used to record pressure fluctuations in the combustion chamber. The microphones had built-in pre-amplifiers of Type 2670 and were powered by a multi-channel power supply Type 2829 also from Bruel and Kjaer. The signal was recorded using a USB data-acquisition board (National Instruments NI-9215) which was connected to a computer which had LabView Signal Express software installed on it. The above basic setup was similar during investigations with different optical measurement techniques.

3.4.2 OH*-chemiluminescence imaging and PIV setup

The figure 3.13 shows the setup for the simultaneous OH*-chemiluminescence imaging and stereoscopic PIV measurements performed on the oxyfuel flames. The PIV measurements were performed using the commercially available LaVision-FlowMaster system. The system consists of a frequency doubled Nd:YAG laser (NewWave Solo 120, 120 mJ per pulse at 532 nm) with a dual head with a repetition rate of 5 Hz. A laser sheet of 105 mm height and approximately 1 mm width was formed using two anti-reflex coated cylindrical lenses with ($f_1=12.7$ mm and $f_2=200$ mm) and a spherical lens ($f_3=650$ mm). The laser sheet was overlapped with the symmetry plane of the combustion chamber. Two

double shutter CCD cameras (LaVision Imager Intense, 1376 x 1040 pixels) equipped with wide angle ($f=16$ mm, $f/1.4$) objectives were used to capture the particle Mie scattering signal. A bandpass filter (532 ± 5 nm) isolated the Mie scattering signal, while a polarizer was used to reduced flame luminosity. Scheimpflug adapters were used for both cameras to align their focal planes with that of the laser sheet. The cameras were located close to the laser sheet in order to view the entire length of the combustion chamber. The cameras were protected from flame radiation by means of an infra-red filter mounted in front of it.

For the OH*-chemiluminescence imaging at constant inlet flow velocity a CCD camera similar to that for the PIV has been used together with an intensifier (LaVision IRO). For the investigations performed at constant thermal power, a ICCD camera from Roper Scientific (512 x 512 pixels) was used. The UV signal from OH*-chemiluminescence was captured by an achromatic Halle UV lens ($f=100$ mm). An interference filter with transmission in the 295-340 nm region was used to detect the OH*-chemiluminescence at around 310 nm. The acoustic behavior of the flame was recorded by means of calibrated microphones placed in the plenum and combustion chamber (15 mm above burner surface, see figure 3.1(a)). The pressure signal was recorded at a sampling rate ranging from 1 kHz to 100 kHz. The PIV laser was triggered externally by means of a signal generator so that the OH*-chemiluminescence camera captured the flame image $18.6 \mu\text{s}$ before the PIV laser was triggered. The average duration between the laser pulses was varied between $20 \mu\text{s}$ to $40 \mu\text{s}$ to obtain the best possible velocity correlation for the given flow conditions. The exposure time for the PIV cameras was $5 \mu\text{s}$. The OH*-chemiluminescence exposure was controlled by means of an intensifier, set to a gate width of $50 \mu\text{s}$. In order to obtain statistically significant average information up to 400 exposures were recorded.

As mentioned earlier, the influence of oxidizer composition variation was studied in two parts at atmospheric conditions. Firstly, the effect of the oxidizer composition at comparable thermal power was studied using OH*-chemiluminescence imaging. The table 3.1 shows the operating conditions for the OH*-chemiluminescence imaging measurements. For selected flames during this study (operating conditions in table 3.2) simultaneous OH*-chemiluminescence imaging and PIV measurements were performed. PIV measurements on the 26.5 % O₂ concentration flames were not performed due to the low frequency instability, while flames with 39.5 % O₂ posed a significant measurement challenge due to the high flame temperatures which resulted in rapid window fowling and poor signal quality. These experiments were performed without a sonic nozzle before the burner plenum. In the subsequent atmospheric experiments a sonic nozzle was fitted in the oxidizer inlet piping to provide better boundary conditions. The nozzle choked the incoming flow, thereby isolating effects of upstream piping on the flame behavior as well as reduc-

Composition	φ	Inlet velocity V_{avg} (m/s)					
		0.75		0.88		1.06	
	P(kW)	14.3	20	16.6	25	20	30
26.5 %O ₂		11.7	17.7	11.9	17.9	12.1	18.1
30.5 %O ₂		10.3	15.5	10.5	15.7	10.7	16
35.4 %O ₂		9.2	13.8	9.4	14.2	9.6	14.8
39.5 %O ₂		8.4	12.6	8.5	12.8	8.8	13

Table 3.1: Flame conditions used for OH*-chemiluminescence imaging experiments to study the effect of oxidizer composition on oxyfuel flame stabilization at atmospheric pressure for comparable thermal power.

Composition	φ	Inlet velocity V_{avg} (m/s)		
		0.71	0.83	0.99
	P(kW)	14.1	16.5	19.8
29.8 %O ₂		10.3	10.5	10.7
33.5 %O ₂		9.2	9.4	9.6

Table 3.2: Flame conditions for simultaneous OH*-chemiluminescence imaging and PIV measurements to study the effect of oxidizer composition on oxyfuel flame stabilization at atmospheric pressure for comparable thermal power.

ing the influence of flame thermo-acoustics on flow controller operation. The operating conditions for investigations at comparable inlet velocities is shown in table 3.3.

3.4.3 Laser Raman spectroscopy setup

Laser Raman spectroscopy has been used to obtain detailed chemical composition and turbulence flame interaction information. The spontaneous Raman scattering cross-sections for most gaseous species in combustion are small. In order to obtain a good signal to noise

Composition	φ	Thermal power (kW)			
		0.83		0.98	
	V_{avg} (m/s)	5.8	11.6	5.8	11.6
26.1 %O ₂		7.9	15.8	9.3	18.6
29.4 %O ₂		9.1	18.3	10.7	21.4
33.7 %O ₂		10.3	20.7	12.9	25

Table 3.3: Flame conditions for simultaneous OH*-chemiluminescence imaging and PIV measurements to study the effect of oxidizer composition on oxyfuel flame stabilization at atmospheric pressure for comparable inlet velocities.

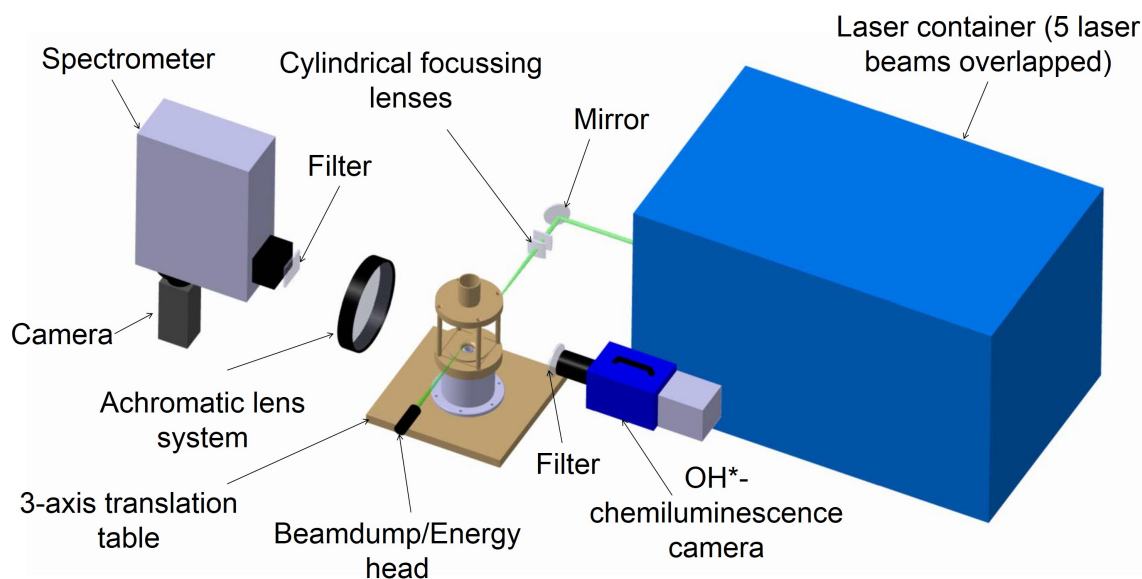


Figure 3.14: Setup of laser Raman spectroscopy for oxyfuel flames at atmospheric pressure.

ratio significant laser energy is required. For this purpose a mobile Raman system developed at the Institute of Combustion Technology, DLR, Stuttgart consisting of 3 Nd:YAG double pulse lasers (Spectra-Physics Model PIV 400) was used to obtain a 532 nm laser beam. The individual laser pulse duration is 7 ns. The pulses are overlapped to form a pulse train which repeats at 10 Hz. The peak power of the pulse train is reduced by directing it through a pulse stretcher which divides the pulse train into multiple sub-beams through a series of beam-splitting and reflective mirrors [106]. All the beams are combined to form a single beam which has a pulse duration of 350 ns. This is done to reduce the occurrence of breakdown (plasma generation) when the pulse train is focused into the interrogation volume. The risk of damaging combustion chamber windows by intense laser irradiation is also reduced. The figure 3.14 shows the setup used for laser Raman spectroscopy. The laser pulse train emerges from the laser container where it is directed towards the investigation region by means of mirrors. Two perpendicularly arranged cylindrical lenses ($f=300$ mm) were used to form a non-distinct point of focus with an average diameter of ≤ 0.5 mm. The length of the focus could be changed by varying the distance between the lenses. This was done to reduce the risk of laser induced breakdown in the interrogation volume. A laser pulse energy of 0.9 J was focused into the investigation volume placed in the axial symmetry plane of the burner. Laser energy heads placed in the laser container and after the burner as shown were used to record the laser energy for each pulse.

The Raman scattering signal was collected perpendicular to the laser beam by using an achromatic lens system with 150 mm aperture. The lens focused the signal onto

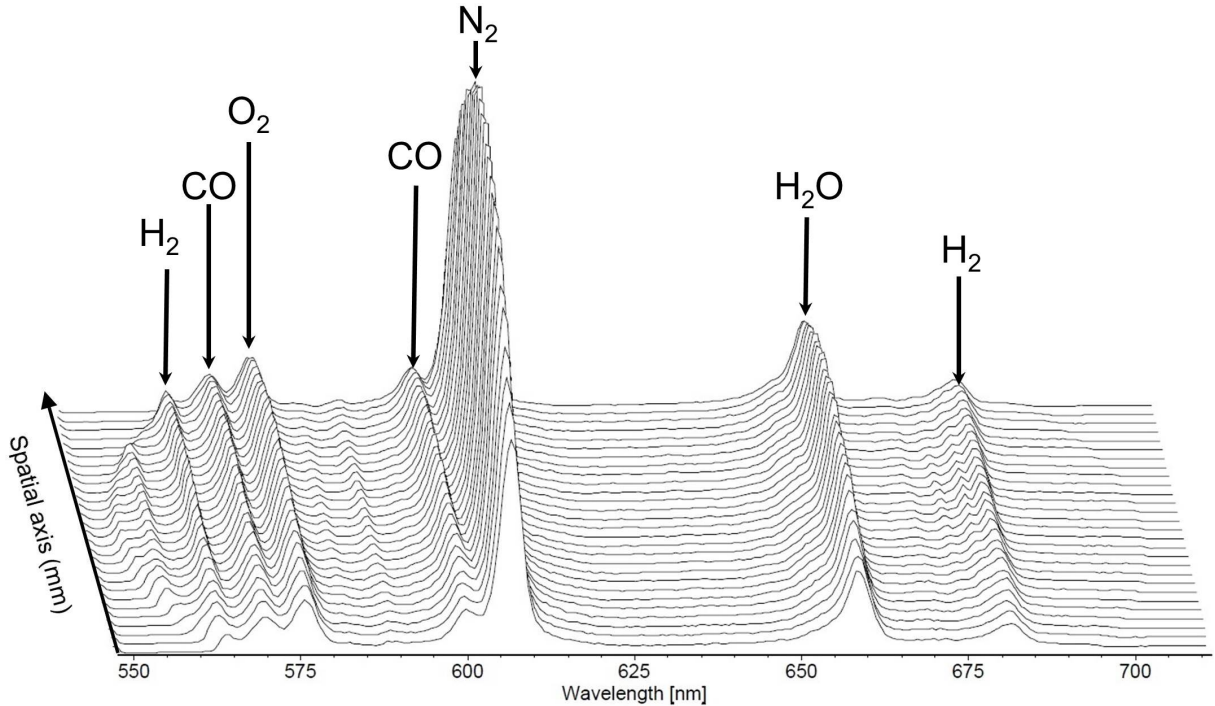


Figure 3.15: An example of a 300 laser-shot averaged 1-d Raman spectrum for a premixed methane-air matrix burner flame at atmospheric conditions.

the entrance slit of a spectrograph (SpectraPro 300i, Action Research, $f=300$ mm, 490 lines/mm, $f/4$, dispersion = 6 nm/mm). A holographic notch filter was placed in front of the entrance slit of the spectrometer to block elastically scattered light. The width of the slit was 1 mm and the height was 14 mm. A system magnification of 2 was used to view a 7 mm x 0.5 mm section of the beam. The Raman scattering of this 1-d section of the beam is imaged after spectral separation by the spectrometer onto a chip of an ICCD camera (1340x1300 pixels, Roper Scientific). The physical space and spectral dimension were binned on the chip to super pixels forming 268 pixels on the spectral axis and 28 points on the spatial axis. This yields a spatial resolution of 0.25 mm for the measurements. An example of a temporally averaged 1-d Raman signal from a premixed methane-air flame showing the spectral and physical space is shown in figure 3.15. For the experiments around 300 single laser shots were collected at each measurement location at a repetition rate of 10 Hz. The burner was mounted on a 3-axis translation table for the Raman measurements. During the measurements the laser beam and detection optics stay fixed as the burner was moved to obtain species information at different points in the flame. This was used to obtain 2-d temperature and species distributions. The flame conditions for these measurements are given in table 3.4. These flame conditions were chosen based on visible similarity to air flame configurations studied previously with the burner (Chapter 4).

Flame	Composition	O ₂ (slpm)	CO ₂ (slpm)	CH ₄ (slpm)	P (kW)
1	30 % O ₂	100.5	233.11	38	22.9
2	30 % O ₂	67	155.4	23.9	14.3

Table 3.4: Operating conditions of Oxyfuel flames investigated using laser Raman spectroscopy.

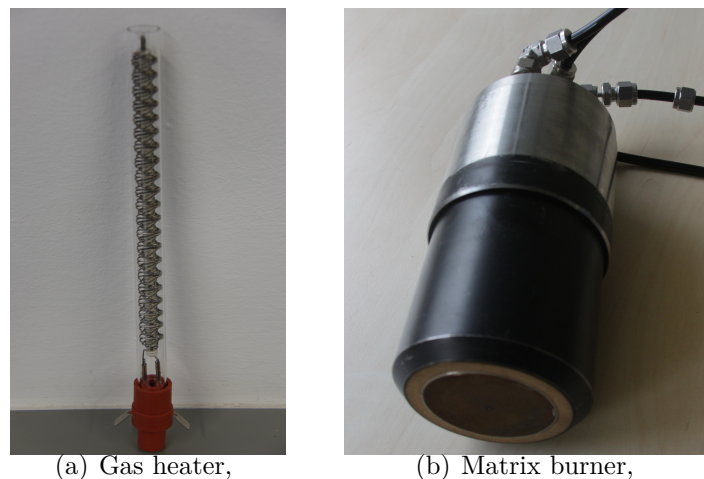


Figure 3.16: Devices used for the calibration of laser Raman Spectroscopy signal.

3.4.3.1 Raman measurements: Calibration and data analysis

The quantitative evaluation of Raman data requires calibration. For the calibration and evaluation of the Raman signal images, the spectral axis of the images (Fig 3.9 and 3.15) was divided into bands corresponding to the individual species. Calibration of these bands was obtained by using two reference configurations spanning different temperature ranges. Both reference configurations were setup in the same location as the burner shown in figure 3.14 to account for individual setup influences. Firstly, a temperature controlled single coil gas heater arrangement (shown in figure 3.16(a)) was used to heat gases such as air, CO₂, CO, CH₄ and H₂ from room temperature up to 900 K. The heated gas was made to flow through the measurement volume. Before taking the Raman scattering measurements a reference thermo-couple was used to determine the temperature of the gas in the measurement volume.

The second arrangement consisted of a 60 mm diameter matrix burner similar in construction to a McKenna burner [107] operated with premixed CH₄/air flames of varying equivalence ratio ($\varphi=0.8$ to 1.4) and flame temperatures. The burner is shown in figure 3.16(b). The Raman signal temperature dependence in the range from 1500 K to 2100 K for different species was obtained using this burner. A combination of 17 standard flames conditions were used to obtain calibration coefficients. Equilibrium composition of such flames were calculated at locations where CARS temperature measurements have been

performed previously [107, 108]. The equilibrium composition of the flames was calculated using GASEQ [109]. The uncertainty of the CARS temperature measurements is 3 %. For calibration the species concentrations below 3 % in the reference flames were not considered to reduce sensitivity of the calibration to uncertainties in these concentrations. The calibration coefficients based on the standard configurations can be written as the following

$$G_i(T) = \frac{k P_i T}{f_i(T) P_L X_i p g} \quad (3.23)$$

where p is the ambient pressure and g is the gain factor for the camera intensifier used, and X_i is the mole fraction of the given species i in the calibration reference. The term P_i refers to the intensity of Raman signal of a particular species which is calculated by taking into account any spectral overlap of neighboring species by the use of cross-talk coefficients. The rest of the terms in the expression are as described in equations 3.20 to 3.22.

The calibration coefficients together with the cross-talk coefficients are used to obtain concentration and temperature information. At each individual measurement location in the flame 300 laser pulse measurements at a repetition rate of 10 Hz were performed. An iterative Raman evaluation procedure in the form of a computer program developed at DLR Stuttgart has been used to analyze the measured data. The process involves the following basic steps:

1. Initially guess a temperature (T^*)
2. Evaluate calibration and cross-talk coefficients for the temperature (T^*)
3. Estimate species mole fractions
4. Evaluate temperature (T) based on ideal gas equation based on species mole fractions
5. If $(T^* - T) \leq 1$ K stop iteration, otherwise iterate till T value converges

For a more exhaustive account of the procedure, the reader is referred to Colombo [110] and Stopper [111]. In order to maintain setup similarity over several calibration measurements the laser beam profile was monitored and adjusted using a CCD to maintain consistent behavior. Additionally reference measurements in air were performed at the beginning and end of every measurement series to account for changes in beam alignment and detector characteristics by normalizing the detected signal intensity relative to the measured mean laser intensity.

Flame	Composition	Pressure	Preheat (K)	V_{avg}	P (kW)	φ
1	30 % O ₂	1.5	321	15.46	44.8	0.95
2	30 % O ₂	1.5	653	31.6	44.3	0.95
3	30 % O ₂	5	653	31.6	150	0.95

Table 3.5: Flame conditions used to study the effect of preheat and pressure on oxyfuel flames using OH*-chemiluminescence imaging.

3.5 Experimental setup: Elevated pressure (5 bar)

The section 3.1.2 described the test rig and burner used for these experiments. The high flow rates of CO₂ and O₂ were met using gas bundles and the fuel used was commercially available natural gas which was supplied by means of a high pressure compressor and storage system. The composition of the natural gas was monitored during the experiments by means of a gas-chromatograph. The arrangement for supplying gases to the burner was similar to that at atmospheric pressure (Fig 3.12) with adaptation to higher flow rates and supply pressures. Calibrated mass flow controllers were used to supply CO₂ (Bronkhorst IN Flow F-116 BI up to 120 g/s at 20 bar [112]), O₂ (Bronkhorst IN Flow F-206 AI up to 50 g/s at 20 bar [112]) and natural gas (Bronkhorst CORI Flow M55 up to 10 g/s at 20 bar [113]) to the burner. The entire test rig was controlled using LabView programs which have been developed at the institute.

OH*-chemiluminescence images were captured at a repetition rate of 10 Hz using an intensified CCD camera (LaVision Imager Intense). The camera was fitted with an achromatic UV lens (Halle, f=64 mm) and an interference filter similar to that used for the atmospheric experiments. The exposure time used for the intensifier varied from 5 to 15 μ s. 200 short exposure images were recorded and averaged with corresponding background and chip sensitivity corrections. The effects of preheat, pressure, and thermal loading were studied. The table 3.5 shows the operating conditions for the investigations. The oxidizer preheat temperature was measured by a thermo-couple mounted in the plenum of the burner. Flame thermo-acoustics oscillations were recorded using a probe tube, one end of which was in the combustion chamber while the other end was fitted with a piezo-resistive pressure transducer. A Kistler 4045A10/4045A20 pressure transducer with an amplifier unit (Kistler-4603B10) was used. The transducer was connected to a computer using a NI-9125 data acquisition box. The pressure signal was recorded by LabView Signal Express software. A comparison of air flames and oxyfuel flames under similar conditions was done to illustrate differences in oxyfuel and air flames at elevated pressures. The operating conditions for the comparison are shown in table 3.6. Flame stabilization data was obtained by OH*-chemiluminescence imaging. The oxyfuel and air flames studied revealed a non-typical flame shape as the pressure was increased.

	V_{avg}	Preheat (K)	P (kW)	φ
Air	16	653	51.6	0.87
		653	58.7	0.99
	31	648	103.2	0.87
		650	117.45	0.99
Oxyfuel	16	648	69.4	0.87
		653	79.3	0.99
	31	650	138.8	0.87
		650	158.6	0.99

Table 3.6: Flame operating conditions for comparing air and oxyfuel flames at elevated pressure using OH*-chemiluminescence imaging.

The burner aerodynamics played a crucial role at high pressure conditions. A deeper understanding of the underlying phenomena was facilitated by the use of simultaneous high speed OH*-chemiluminescence imaging and PIV diagnostics. The following section describes this setup. The stand alone OH*-chemiluminescence imaging setup is not dealt with separately due to the simplicity of the apparatus.

3.5.1 Simultaneous high speed OH*-chemiluminescence imaging/PIV setup

The setup of the simultaneous high speed PIV/OH*-chemiluminescence imaging experiments performed on the elevated pressure burner is shown in figure 3.17. For simplicity, only the burner without the test rig is shown in the image. The image shows the sheet forming optics used for the PIV and cameras for capturing PIV and OH*-chemiluminescence data. To capture the flame dynamics, velocity measurements were performed by PIV at a repetition rate of 3 kHz using a solid state Nd:YAG laser (Edge-wave, IS-6IIDE). The laser energy per pulse was 2.4-2.6 mJ at 532 nm and the laser pulse width was 8-10 ns. The time interval between PIV laser pulse pairs was 20 μ s. The laser beam was converted into a sheet by means of cylindrical lenses ($f_1 = -38.1$ mm to expand it, $f_2 = 500$ mm to collimate it and $f_3 = 700$ mm to focus it to a waist). The PIV signal was captured by a high speed CMOS camera (LaVision HSS5) with a 100 mm Tokina (f/2.8) objective fitted with a 532 nm band pass filter. A laser sheet of 20 mm width was used and imaged an area of 20 mm x 40 mm. This was captured on a camera chip with 256 x 512 pixels resulting in a resolution of 0.078 mm/pixel. A window size of 16 x 16 pixels with an overlap of 50 % was applied to determine velocity field using simple correlation. In order to obtain the velocity field of the entire combustion chamber, a scan of half the width of the combustion chamber was done. The average flow

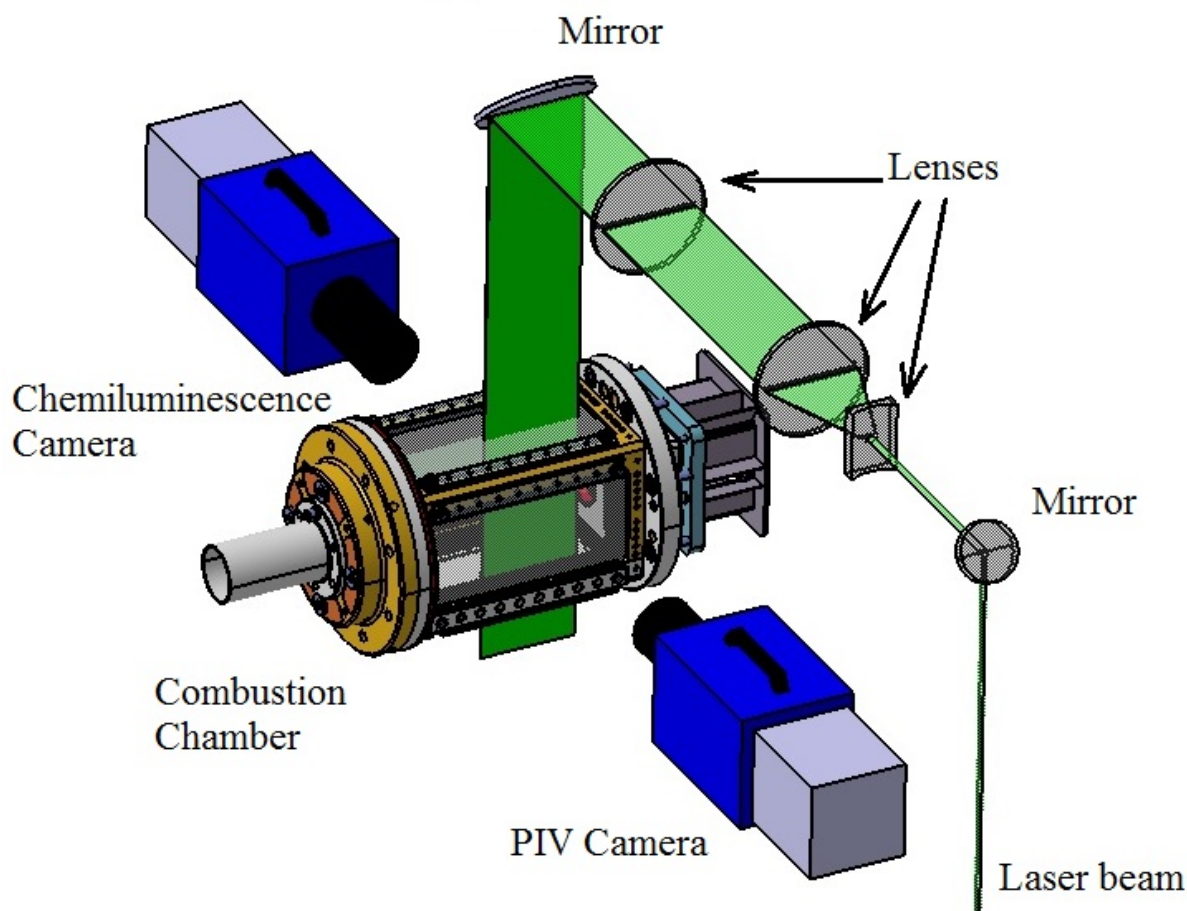


Figure 3.17: Simultaneous high speed PIV/OH*-chemiluminescence imaging setup for elevated pressure experiments.

field was obtained by overlapping different sections that were measured. The dynamics of the individual series of measurements were studied by applying a POD analysis. As the flame shapes were unconventional both reacting and non-reacting flows were studied. The non-reacting flows were studied for both air and oxyfuel flames. The table 3.7 shows the flame operating conditions studied with the measurement technique.

Along with the optical diagnostics, pressure fluctuations in the combustion chamber were recorded by means of a piezo-resistive pressure transducer as described previously.

3.6 Measurement uncertainty

The sources of measurement uncertainty are of a systematic and random nature [114]. The systematic error is a repeatable error that is related to the accuracy of the measurement method. The error is associated with the limitations of the measurement technique and its calibration. The random errors are a result of inherent variations in the measurement

	Condition	Pressure (bar)	Preheat (K)	P (kW)	ϕ
Air	Non-reacting and Reacting	1.5	653	30	0.83
		5	653	100	0.83
Oxyfuel	Non-reacting	1.5	648	69.4	0.00

Table 3.7: Flame conditions used to understand the role of burner aerodynamics on flame stabilization.

system and is related to sensitivity of the measurement method. The extent of random error in a measurement system is also denoted as the precision of the measurement. For the case of optical measurement techniques, the statistical nature of the quantum mechanical processes introduce a type of random error referred to as shot noise. The systematic errors are usually determined through calibration of the measurement device with a reliable reference. This is however quite difficult as it is not always possible to have an immaculate reference. The systematic error is correctable in the case such information exists. The random error is reduced by obtaining sufficient samples of the measurement. For any series of measurements the standard deviation σ is indicative of the range where 68.7 % of the measurements lie. The relative random error ϵ_{random} is expressed as:

$$\epsilon_{random} = \frac{\sigma}{Q_{meas}} \quad (3.24)$$

where σ is the standard deviation of the measured value.

The relative systematic error ϵ_{sys} is written as:

$$\epsilon_{sys} = \frac{Q_{meas} - Q_{true}}{Q_{true}} \quad (3.25)$$

where Q_{meas} is the measured value and Q_{true} is the true value.

An additional source of uncertainty is the reproducibility of flame conditions. The uncertainty in the experiments is therefore presented in three sections corresponding to the flame reproducibility followed by sources of systematic and random error in the Raman and PIV measurements.

3.6.1 Burner operation and flame reproducibility

The flame reproducibility refers to the repeatability of the given flame operating conditions and the fluctuations in different parameters defining this condition. This is related to the accuracy of the flow-control devices used, their stability of operation and sensitivity to environmental influences. The devices used to monitor and control the burner

operation at atmospheric pressure and elevated pressure were different. Hence, the uncertainty in flame reproducibility is separately discussed here. Firstly, the atmospheric condition is dealt with, followed by the elevated pressure scenario.

Calibrated mass flow controllers and Coriolis flow meters were used to define the operating conditions under atmospheric conditions. The uncertainty in the operating condition refers to the fluctuations in the measured value and the accuracy of the Coriolis flow meters. The Coriolis flow meters were used as immaculate references for the mass flow measurements. The fluctuations in the flow rates were less than 2 % for CO₂ and 1 % for O₂ and methane. The reproducibility of flame and combustion chamber conditions was obtained by ensuring that flames reach thermal equilibrium. The temperature of a reference thermo-element mounted on the combustion chamber cap varied less than 2 °C/minute when this condition was met. The OH*-chemiluminescence and acoustic recordings were repeated at least twice for a given operating condition to determine flame reproducibility. The flame shapes obtained for similar operating conditions were consistent. In the cases where PIV measurements were carried out, the influence of PIV seeding was documented by recording flame shape before and during the measurement. The effect on flame shape was minimal. The thermo-acoustic oscillation in the flame was recorded by calibrated microphones. The frequency of the consistent thermo-acoustic oscillation varied by ± 5 Hz for a given operating condition.

At high pressure conditions the calibrated flow controllers given in section 3.5 were used to control CO₂, O₂ and natural gas supply to the high pressure test rig. The accuracy in flow rate regulation for these flow controllers is within 1.5 % for CO₂ and O₂ as per manufacturer specification. For natural gas this value was within 1.0 %. The natural gas composition was monitored by means of a gas chromatograph. Any changes in composition during operation were corrected for after the experiment, in the form of corrected equivalence ratio. The differences in the set and actual conditions were minimal. The fluctuations in temperature of the thermocouple used to define oxidizer preheat condition varied typically by ± 3 °C (0.5 %). As in the atmospheric cases measurements were performed when the combustion chamber and burner reached near equilibrium conditions. Between operating points a typical duration of 5-10 minutes was given for this. The different flame conditions have been repeated at least two times. The fluctuations in the operating pressure of the test rig were negligible.

3.6.2 Uncertainty in Raman measurements

The uncertainty in the Raman measurements arises from errors in the calibration and from the statistical nature of the photon scattering and detection process. In the following section the two types of errors are estimated. Firstly, the errors in calibration are

Equivalence ratio	Temperature	CO ₂	O ₂	CO	N ₂	H ₂ O	H ₂
$\varphi=0.8$	1765 K	7.74	3.78	0.01	72.78	15.47	0.00
$\varphi=1.0$	1790 K	9.42	0.02	0.08	71.44	18.94	0.04
$\varphi=1.3$	1878 K	5.54	0.00	5.84	65.85	18.09	4.66

Table 3.8: Temperature and composition (% mole fraction) of 3 calibration flames used for error estimation.

estimated and their influence on the accuracy of the measurements is discussed. Secondly, the accuracy of the instantaneous measurements is discussed.

The temperature dependent calibration coefficients G_i in equation 3.23 are determined through the calibration process. For each calibration point, the uncertainty is associated with the extent of immaculacy of the reference condition and measurement of the species dependent Raman signal intensity. These sources of error can be summarized as uncertainty in:

- Reference temperature measurement T - Accuracy of thermo-couple and CARS thermometry
- Species mole fraction X_i - Reference flame composition
- Species signal intensity P_i - Optical setup consistency
- Laser intensity P_L measurement accuracy

In the equation 3.23, the influence of parameters such as detector gain and calculation of $f_i(T)$ is negligible. The ambient pressure varied minimally during the course of the experiments, hence this influence is also neglected. For the calibration in the temperature range up to 900 K gases with 99.95 % purity were used, hence, the uncertainty in composition is not significant. The accuracy of the thermocouples used for temperature measurements is 0.4 % (Sheathed K-Type thermo-couple - ES Electronic Sensor GmbH). The uncertainty in the calibration due to the reference gas heater measurements is hence negligible and not considered in detail. Reference calibration flames are therefore used to estimate errors in the Raman measurements. The temperature at the reference location of the calibration flames was measured using CARS thermometry. The uncertainty in the temperature measurements is 3 %. The composition of the flames has been determined through equilibrium calculations using GASEQ [109] software. An error in the composition therefore exists on account of uncertainty in CARS temperature. Additionally, the accuracy of flow controlling devices influences the flame conditions.

Both sources of calibration reference errors are determined using three calibration flames representing lean, stoichiometric and rich operation. The table 3.8 shows the

Equivalence ratio	Error Source	CO ₂	O ₂	CO	N ₂	H ₂ O	H ₂
$\varphi=0.8$	Temperature	0.05	0.43	-	0.03	0.07	-
	Air flow	1.00	4.45	-	0.08	1.00	-
	Methane flow	0.92	4.15	-	0.08	0.93	-
$\varphi=1.0$	Temperature	0.35	-	-	0.03	0.12	-
	Air flow	0.85	-	-	0.17	0.59	-
	Methane flow	1.52	-	-	0.27	0.33	-
$\varphi=1.3$	Temperature	1.50	-	1.42	0.00	0.44	1.83
	Air flow	2.08	-	3.26	0.34	0.43	4.91
	Methane flow	1.57	-	3.26	0.34	0.43	4.91

Table 3.9: Percentage relative error in different quantities for 3 calibration flames as a result of uncertainty in CARS reference measurements (ϵ_T - Temperature) and flame conditions ($\epsilon_{flow-air}$ - Air flow and $\epsilon_{flow-fuel}$ - Methane flow).

equilibrium composition for the three flames at the measured CARS temperatures. The deviation from the equilibrium flame composition has been estimated for the flames assuming 3 % higher and lower temperatures. The mass flow controllers used for the flames were calibrated using Coriolis flow meters (SITRANS DI 1.5). The uncertainty in the air and methane flow measurement from the device for the flow rates used is ± 1 %. The associated uncertainty propagates into the flame conditions and can be estimated for 1 % variation in the air and fuel flow. The table 3.9 summarizes the relative errors ϵ_T , $\epsilon_{flow-air}$ and $\epsilon_{flow-fuel}$ in composition as a result of variation in equilibrium temperature and burner flow conditions. For the lean and stoichiometric flames the error due to fluctuations in temperature are below 1 %. For the rich flame this value is in the range of 1-2 % for the species CO₂, CO and H₂. The fluctuations in air and fuel flow affect the composition more significantly than the equilibrium temperature uncertainty. The species which are most significantly influenced are O₂ for lean flames, and CO and H₂ for the rich flame. The uncertainty is however still under 5 %. It must be noted that for the lean flame the CO and H₂ mole fraction is of the order of 10^{-4} , similarly for the stoichiometric and rich flames the O₂ mole fraction is of the order 10^{-4} and lower. These concentrations were not considered for determining calibration coefficients of respective species to reduce the sensitivity of the calibration coefficients to uncertainties in concentrations.

The intensity of the Raman scattering signal P_i measured for a certain incident laser intensity P_L is dependent on the given optical setup. The uncertainty in the calibration due to changes in optical setup is negligible. The Raman signal intensity was also normalized relative to reference air measurements taken during the beginning and end of each set of calibration measurements to account for any changes. The uncertainty ϵ_L in the laser intensity measurement P_L is 3 % [115].

Equivalence ratio	Temperature	CO ₂	O ₂	CO	N ₂	H ₂ O	H ₂
$\varphi=0.8$	9	10.9	-28.8	-	2.85	8.9	-
$\varphi=1.0$	9.3	10.1	-	-	2.76	7.8	-
$\varphi=1.3$	9.2	16.2	-	41.5	3.6	8.1	25.71

Table 3.10: Relative standard deviation of different quantities in stable calibration flames denoting the fluctuations ϵ_{int} in instantaneous Raman measurements.

Equivalence ratio	Temperature	CO ₂	O ₂	CO	N ₂	H ₂ O	H ₂
$\varphi=0.8$	9.48	10.98	29.43	-	2.85	9.00	-
$\varphi=1.0$	9.77	10.25	-	-	2.78	7.83	-
$\varphi=1.3$	9.68	16.47	-	41.78	3.63	8.351	26.69

Table 3.11: Resultant uncertainty ϵ_{res} in instantaneous measurements of different quantities in the three different calibration flames.

The Raman scattering process is inherently stochastic as shot noise leads to varying intensities of the scattering signal for a certain laser energy focused into the investigation volume. The shot noise reduces for larger number of detected photons. For the calibration flames the conditions of temperature and composition are relatively stable. The relative standard deviation of different measured quantities is indicative of this statistical variation and hence precision of the measurement. The relative standard deviation (standard deviation/average value) ϵ_{int} in the instantaneous measurements of the different quantities is shown in table 3.10. The uncertainty in the measured values of species such as O₂, CO and H₂ is higher due to the lower concentrations present in the flame making accurate detection difficult. The concentrations of CO₂ in oxyfuel flames is at least 10 times higher than those in the above calibration flames. Hence the error in CO₂ concentration in an actual oxyfuel flame is expected to be significantly lower.

An estimate of the resultant error for an individual measurement due to the calibration and fluctuations in Raman scattering signal is obtained using the relation,

$$\epsilon_{res} = \sqrt{\epsilon_T^2 + \epsilon_{flow}^2 + \epsilon_L^2 + \epsilon_{int}^2} \quad (3.26)$$

where ϵ_T , ϵ_{flow} , ϵ_L and ϵ_{int} are relative errors from uncertainty in composition, laser intensity and statistical variation in Raman scattering signal. The resultant error in instantaneous value of different quantities for the calibration flames is given in table 3.11.

For actual flame measurements which are discussed in the results, the reproducibility of the scattered Raman signal intensity relative to the calibration measurements was obtained using reference air measurements. Thereby reducing an uncertainty due to changes in setup. As in the case of the calibration, beam quality was monitored constantly to

minimize any variations. The entire experiment was carried out in a temperature regulated room so as to minimize influences of random changes in temperature on optics and beam alignment. Additionally, a chemically stable region of the flame in the IRZ was used to obtain reference measurements. These reference measurements were taken at regular intervals during the course of a flame scan. This was used to normalize any effects of change in signal intensity as a result of change in beam alignment and window fouling. The uncertainty due to changes in beam alignment and window fouling is therefore negligible.

3.6.3 Uncertainty in PIV measurements

The PIV technique is a geometric calibration based measurement technique. An image of the object plane containing a reference in the form of a calibration target is used to obtain particle spatial information. The uncertainty in the spatial information and hence velocities are due to:

- Particle tracking
- Correlation analysis

The uncertainty in particle tracking originates from limitations in resolving actual particle trajectory and the optical calibration process. These limitations are systematic to the PIV technique. The particle position information is only available at two instances of time using conventional PIV, hence particle dynamics within this instance is not resolved. These errors are also extremely difficult to estimate without prior flow field information. The extent of these errors can however be minimized by choosing a smallest possible time interval between PIV laser pulses to resolve the range of velocities that are expected in the flow field. For time averaged flow field information these errors are also expected to be insignificant. The consistency of mapping the object plane to image plane during the course of measurements was ensured by crosschecking overlap of the laser sheet to the initial object plane. The detection and sheet forming optics were secured to reduce any drifts during the course of the measurements. The errors due to change in magnification or laser sheet movement are therefore negligible. The camera resolution and image processing determine the accuracy in determining the exact position of a particle. The ability of a PIV measurement to accurately estimate particle location is dependent on the number of pixels available per particle. The recommended resolution of 2-3 pixels/particle was used for the measurements [96]. No biases in determining the fractional displacement of the particles in the entire flow field were observed. The uncertainty in determining particle center is 0.1 of a pixel. For minimum and maximum

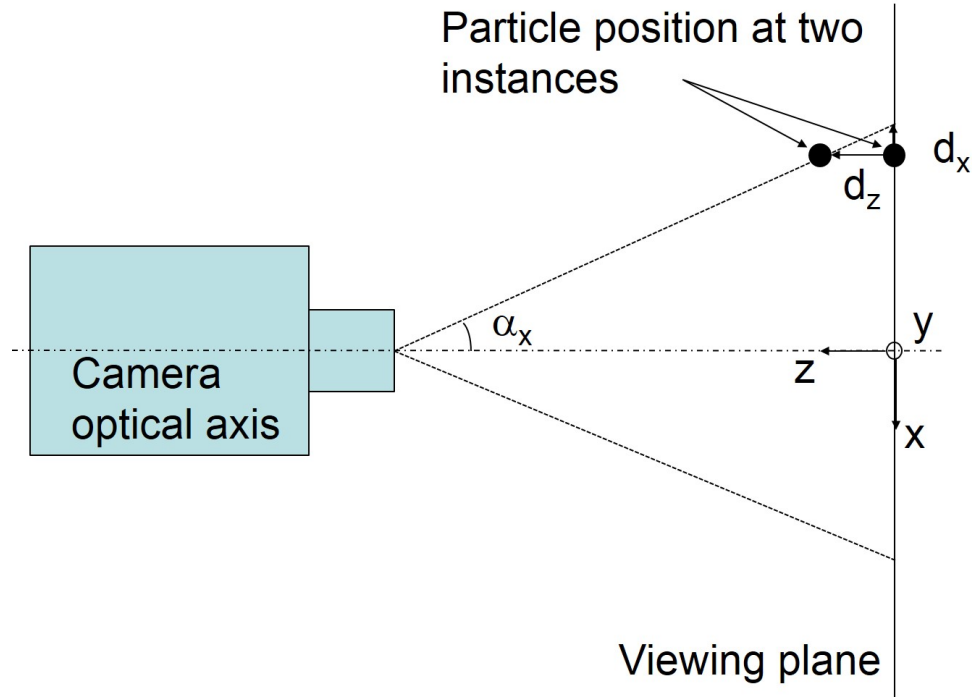


Figure 3.18: Schematic showing perspective error in 2-component PIV due to out of plane particle motion.

velocities of 0.1 m/s and 30 m/s which have been measured this corresponds to an uncertainty 1.5 % and 1 % in the velocity. Another source of error due to particle motion is its lag in attaining fluid velocity. For the particles used during the experiment the particle relaxation time required for the particle to reach fluid velocity for an oxyfuel flow containing 26 % O_2 in oxidizer and $\varphi=0.9$ at 753 K is determined. This was estimated to be 9.1×10^{-6} s. These flames were seen to have the largest flow gradients in the ISL. This is the region where the maximum flow acceleration is expected and errors due to particle lag can be high. A shear layer thickness of approximately 1 cm and flow velocity of 30 m/s results in a particle slip velocity of 0.81 m/s. This leads to an error in velocity due to slip of 2.72 %. Other errors such as that due to the uncertainty in the timing of the laser pulses are negligible as such variations are of the order of 1 ns.

In the case of two component PIV the presence of out of plane motion due to swirl leads to perspective errors where such motion is interpreted as in plane motion. The figure 3.18 depicts the perspective error. The out of plane displacement d_z of the particle is perceived as in plane displacement of $d_x = -d_z \tan \alpha_x$, where α_x is the perspective angle of the particle to the camera optical axis. The perspective error becomes zero if the offset or angle to camera optical axis is zero. A similar perspective error can be expected in the d_y displacement which is given by $d_y = d_z \tan \alpha_y$, where α_y is the perspective angle relative to y -direction. If 3-component data is available for a given flow field,

perspective errors for 2-component measurements can be estimated. Stereo-PIV data from atmospheric measurements has been used to estimate errors that can be expected in the 2-component PIV measurements at elevated pressure. A swirl flames with 34 % O_2 , $\varphi=0.83$ and $V_{avg}=12$ m/s which was similar to flames at elevated pressure was used for the error estimation. The 3-component velocity data from these measurements was combined with optical setup information such as distance of camera optics to object plane at elevated pressure to determine perspective angles in the 2-component measurements. The error in radial velocity V_x and axial velocity V_y due to out of plane velocity V_z is given by $\Delta V_x = V_z \tan \alpha_x$ and $\Delta V_y = V_z \tan \alpha_y$ where α_x and α_y are the perspective angles to the respective flow directions. The error in the axial velocity V_y due to out of plane motion was estimated to be under 2.5 %, except for a small region of flow stagnation where large out of plane motion resulted in 24 % error for an offset of 5.33 mm ($\alpha_y = 0.85^\circ$) from the camera optical axis. For the radial component the maximum error was 10.3 % at an offset of 3 mm ($\alpha_x = 0.48^\circ$) from the optical axis. This was in the region where large out of plane motion due to swirl was observed. The error is in the range of 3-8 % at other perspective angles. Although out of plane velocities are determined using stereoscopic PIV, the angle between the two cameras influences the sensitivity of the optics to out of plane and in plane motion [116]. These effects influence errors in the out of plane and in plane velocities differently. Lawson recommends camera angles in the range of 40 to 60° as a compromise to obtain best accuracy. A camera angle of 40° was used for the measurements.

An estimate of the error for the entire field of measurement is non-trivial. However, the above treatment estimates the largest errors that can be expected in the instantaneous measurements. For the stereoscopic-PIV the main sources of error are from sub-pixel resolution of the displacement and particle slip. Based on the above estimates of these errors, the maximum error in the instantaneous stereoscopic-PIV velocity measurement is expected to be around 3 % in the shear layers. For 2-component PIV measurements at elevated pressure an error of up to 24 % can be expected in stagnation zones near the burner inlet due to perspective effects. The PIV data has been largely used for obtaining average flow field information. For the averaged flow field these errors are expected to reduce by \sqrt{N} , where N is the number of measurements.

The image processing of the PIV data was performed using commercially available image processing software Davis 8.0. The instantaneous PIV velocity is spatially averaged due to the finite resolution of the camera and the window sizing used to obtain reliable velocity information. The window size hence smooths out fine structures that are present and influences the instantaneous, average and RMS vector field. The window size of 16x16 pixel used in this work resolved most of the dominant flow structures required for flow field comparisons. The quality of the flow field correlations for vector calculation

can be determined by obtaining statistics on the correlation characteristics in the measurement plane. The vectors obtained using a distinct correlation peak are referred to as first choice vectors. Vectors were removed based on the strength of correlation peaks obtained. A median filter eliminated spurious vectors. The percentage of first choice vectors detected is a method of assessing the quality of the entire flow field measurement. For the measurements using setup described in section 3.4.2, the first choice vectors constituted between 90 % to 99 % of the vectors obtained for the instantaneous measurements. The percentage of spurious rejected vectors was ≤ 1 %. For the high pressure measurements the percentage of first choice vectors was between 70 % to 91 %.

Like any other measurement technique the instantaneous PIV measurements can vary due to minor influences that effect the camera, the laser and the data analysis. Additionally velocities in a turbulent flow can vary considerably depending on the region of the flow. In order to draw appropriate conclusions the statistics need to be tested for convergence. A combination of 200 and 400 measured instances at atmospheric pressure and 4046 and 8092 samples at elevated pressure were processed for certain measurements. The change in average flow velocities was negligible.

4

Previous Work

The burner described in Chapter 3 has been used extensively for optical and laser based investigations in previous experiments. This chapter summarizes the work which has been done to date on the burner with air flames. It highlights the operating characteristics of the burner using methane-air flames, dominant flow features, and the presence of thermo-acoustic oscillations. The description of these characteristics provides an introduction into the parameters that are later considered for comparing the behavior of oxyfuel and air flames.

Firstly, an overview of the operating characteristics of the burner is given. Then detailed PIV measurements describing the flow fields are presented along-with Raman data for 3 standard flames. Thirdly, the important flow dynamics corresponding to coherent flow structures and thermo-acoustic oscillations that have been observed in the flames are presented.

4.1 Burner operation regimes

For CH_4 /air flames there are two independent parameters that can be varied in order to obtain the operating regime of the burner when inlet fuel and air temperature are kept constant. They are the thermal power and the equivalence ratio. At a constant thermal power a decrease in the equivalence ratio is accompanied by increasing the flow of oxidizer which results in a change in the average inlet velocity. By increasing the thermal power the velocity range is shifted to a higher value. The figure 4.1 shows images of visible flame luminescence for different flames operated with the burner using methane and air under atmospheric conditions with air fed at room temperature. The images have been obtained using a photo camera from experiments carried out at the DLR Institute of Combustion Technology by Stoehr and Weigand [117].

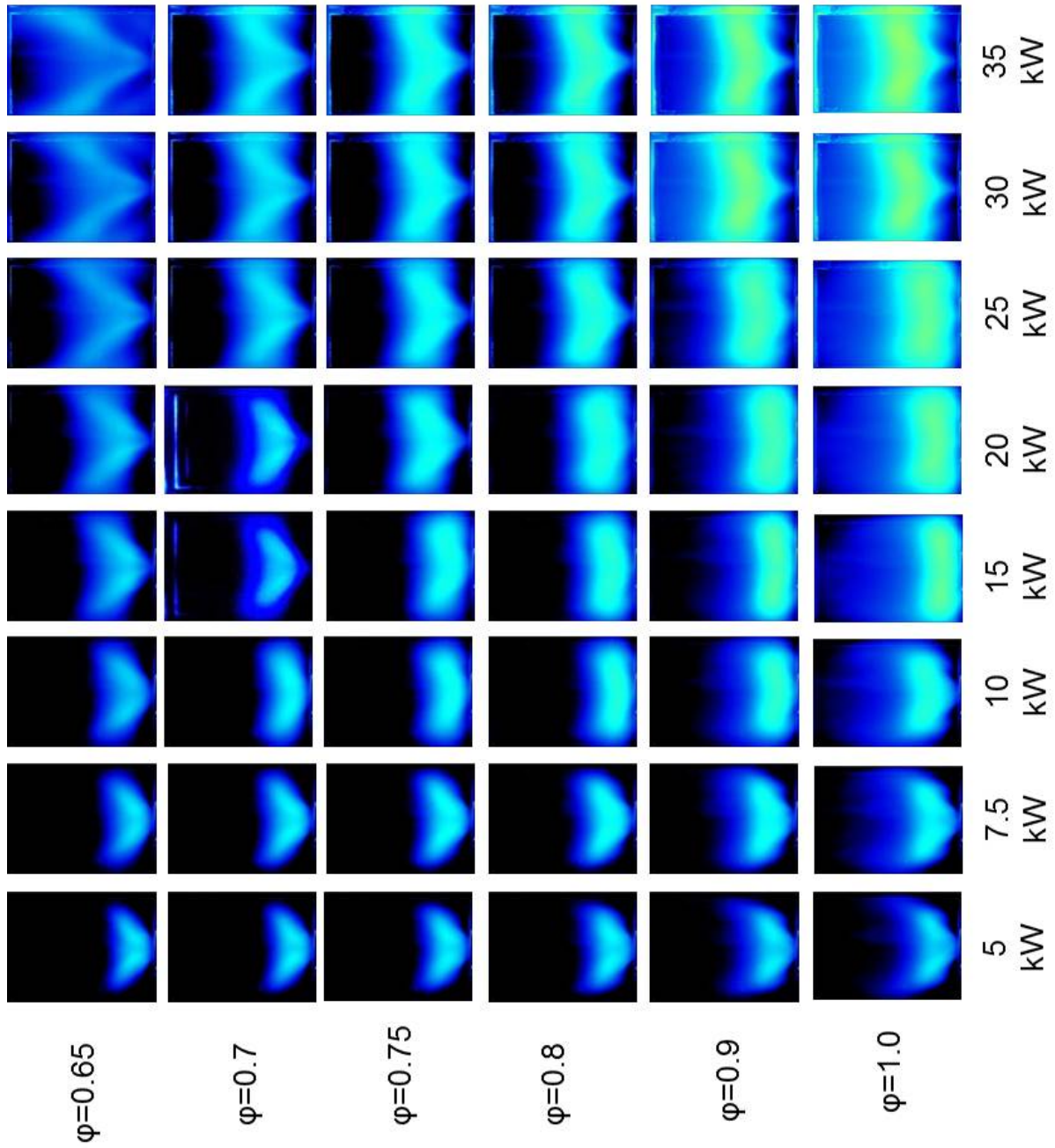


Figure 4.1: Images of CH₄/air flames visible luminescence at different thermal powers and equivalence ratios.

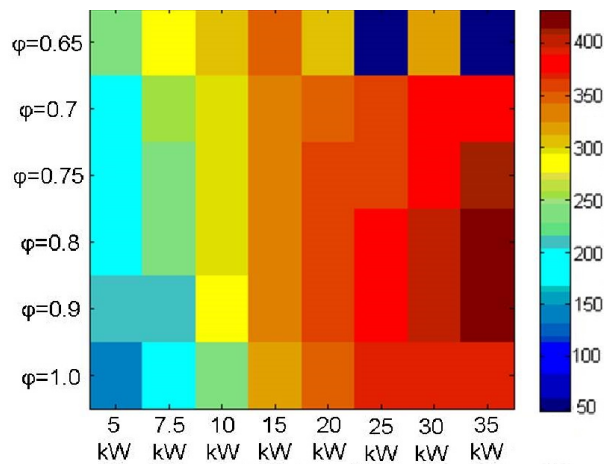


Figure 4.2: Thermo-acoustic frequency for air flames shown in figure 4.1.

All images are from Stoehr except for $\varphi=0.7$ at 15 kW and 20 kW. These images were obtained from the work by Weigand. The flames correspond to a configuration where no sonic nozzle was used at the inlet of the burner plenum. The flame shapes change with the operating conditions. For example at $\varphi=0.8$, the 5 kW flame has a conical shape, which transforms to a flatter form at 10 kW. This flame form persists until a power of 25 kW where the flame starts moving further downstream. The flames from this burner are classified into three typical flame shapes based on these changes. The shapes are referred to as the conical, flat and extended flat flame. The flat flame form is associated with the occurrence of thermo-acoustic oscillations. The figure 4.2 shows the frequency of oscillations for each of the flames. The increase in the thermal power at $\varphi=0.8$ also corresponds to an increase in the frequency of the thermo-acoustic oscillations. A similar trend is seen for $\varphi=0.75$, 0.9 and 1.0. At the leaner equivalence ratio of $\varphi=0.65$, a conically shaped flame is seen which persists from 5 kW to 35 kW. The frequency of the oscillations is lower and flame data showed no high intensity oscillations, indicating an absence of thermo-acoustic instabilities. The average inlet velocities and inlet Reynolds numbers calculated using the fuel and air flow rates and a characteristic diameter of 25 mm are shown in figure 4.3 for reference.

Swirl flames stabilization and dynamics is governed by complex processes, with an in-depth understanding still being actively researched. A complex combination of parameters such as reactant mixture properties, turbulent mixing, flow field and burner geometry determines flame dynamics. One such geometrical feature in this burner is the burner lip shown in the sketch below, which is thought to direct the flow laterally and assist formation of flatter flames (Fig.4.4). The effect of this geometrical feature on the flame shapes is described more clearly in the following chapter.

Of the series of flames which have been observed, focus has been directed to certain typical configurations that are relevant to gas turbine combustion. More precisely, 3

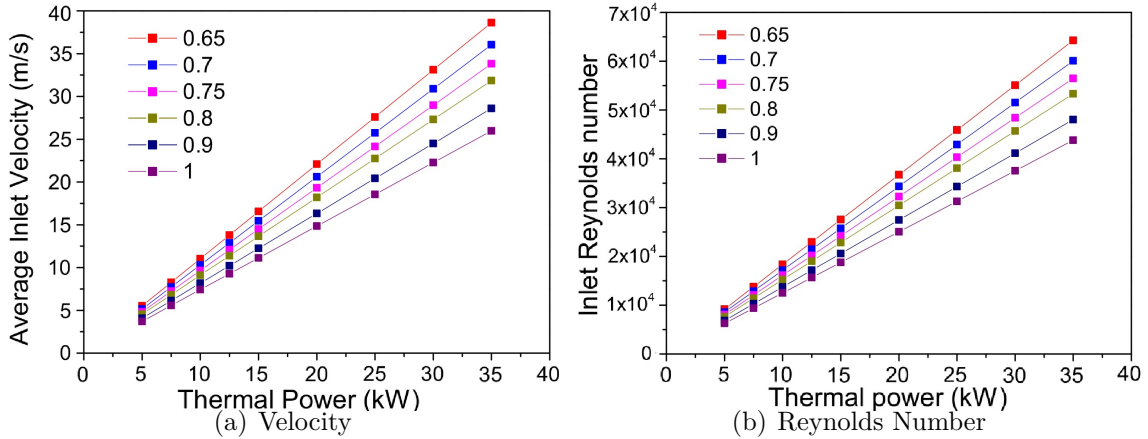


Figure 4.3: Average inlet velocity and inlet Reynolds number at different equivalence ratios (flames shown in figure 4.1) for a characteristic diameter $d=25$ mm.

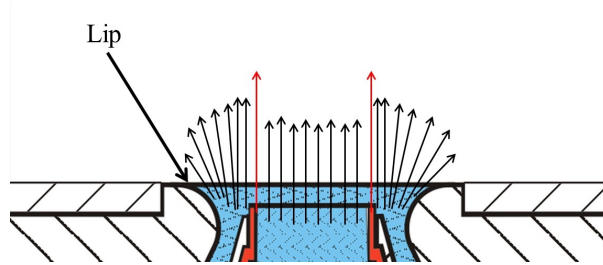


Figure 4.4: Sketch of flow entering the combustion chamber.

standard flames have been studied in greater detail and are the subject of significant literature. These flames being the 35 kW flame at $\phi=0.65$ and the 10.3 kW flame at $\phi=0.75$. These flames are also known as Flame A and B [25, 26]. The flame A burns stably and represents typical energy densities which are experienced in modern gas turbine combustors, while flame B has thermo-acoustic oscillations which is a problem of interest in lean premixed combustion. Together with these flames another flame called Flame C which operates close to the lean extinction limit ($\phi=0.55$ and $P=7.4$ kW) has also been investigated in detail. The detailed characterization of these flames has been done to serve the dual purpose of understanding the dynamics of stable and unstable swirl combustion, as well as providing experimental data for validating numerical simulation tools. The following section describes the three flames with important phenomena observed in them.

4.2 Detailed characterization of standard flames

The partially premixed nature of flames A, B and C was studied in detail by Meier [118]. Turbulence-chemistry interactions were studied using Raman scattering measurements. The flames were positioned in the connected flame region for non-premixed flames based

on measurements of velocity (Laser Doppler anemometry), reaction zone (CH-Laser Induced Fluorescence) and composition (Laser Raman Scattering). Weigand [25] presents detailed results characterizing flames A, B and C. The flame structure information was obtained using OH and CH-PLIF, and velocity information using three component LDV. Subsequently the flame flow field was measured using PIV. The figure 4.5 shows the PIV velocity field (background is colored by resultant velocity magnitude) along with Abel inverted OH*-chemiluminescence and temperature field for a plane through the burner axis for the three flames. The temperature contours were created using the interpolation of Raman data. The velocity and OH*-chemiluminescence information is from PIV/OH*-chemiluminescence experiments performed subsequently on the three flames (courtesy Stoehr) [119]. The change in the flame shapes is clearly evident. Flames A and C have a similar velocity contour, while in flame B the fresh charge is directed radially upon entry into the combustion chamber. As a result the extent of the ORZ is significantly reduced in comparison to the flames A and C. The IRZ (determined by the location of predominantly negative axial velocity) for flames A and C extends to a height of 73 mm and 70 mm in comparison to 62 mm for flame B. The shape of flame B is flatter as evident from the OH*-chemiluminescence (fig 4.5(d)) and the flame reaches maximum temperatures at a height of 20 mm across the width of the combustion chamber in comparison to 58 mm and 45 mm for flames A and C. Flames A and C are stable, while flame B exhibited thermo-acoustic oscillations at 295 Hz. The thermo-chemical state of the gas mixture at different locations in the combustion chamber has been described by Meier [26] using laser Raman spectroscopy. The following section summarizes some of the key findings in these flames.

4.2.1 Stable combustion: Flame A

The flame A displayed a typical conical flame shape seen for most operating conditions with the burner. The flow field consists of a distinct IRZ and ORZ. The region of heat release as evident from the OH*-chemiluminescence image resides in the inner shear layer. Raman measurements show that the combustion is completed at a height of about 58 mm above the burner and there is a significant amount of premixing of fuel and air that occurs before combustion. Other than having the typical IRZ, ORZ and shear layers between the recirculation zones, a PVC formed due to vortex breakdown at the burner inlet has been observed to be an important fluid mechanical structure affecting the mixing of burnt and unburnt gas. The presence of a PVC and its interaction with the flame have been studied in detail to obtain the information about flame stabilization location [46]. A series of flames ranging from 10 kW to 35 kW were operated at $\varphi=0.65$. PIV measurements at 5 Hz repetition rate and simultaneous OH-PLIF/PIV at 5 kHz were performed. Stagnation

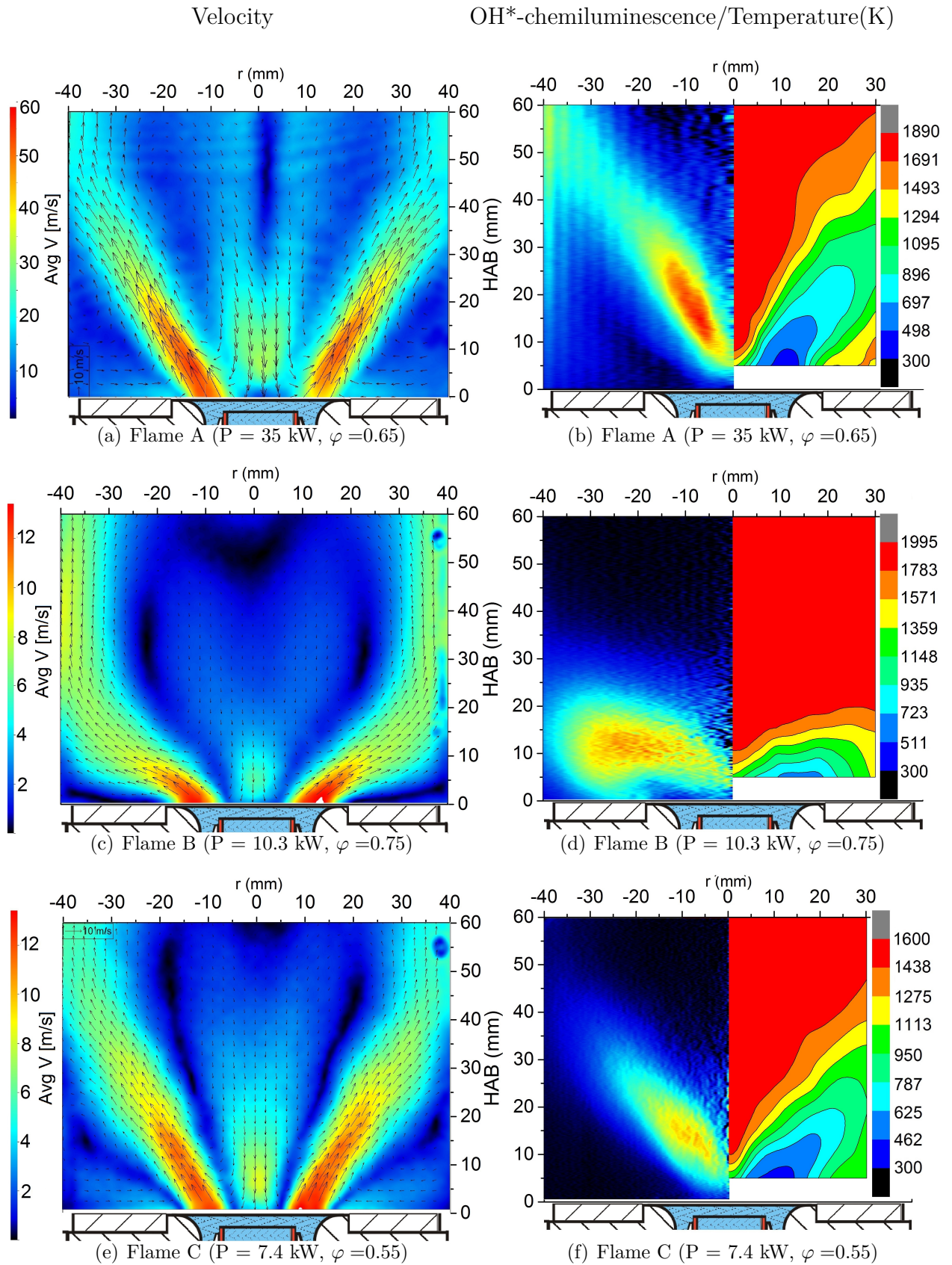


Figure 4.5: Resultant velocity contours superimposed with velocity vectors for Flame A, B and C. Images on right show a combined OH*-chemiluminescence and mean temperature (K).

points formed by the interaction of fresh charge and the PVC were identified as key to flame stabilization. In a comparative study involving similar flames, additional 10 kHz measurements were performed on the flame A along with flames at 10 and 20 kW. An increase in Damkoehler number of the flame led to increased instances of aerodynamic flame stretch related extinction. This resulted in the reaction zone stabilizing at further downstream locations of the combustion chamber.

4.2.2 Thermo-acoustic oscillations: Flame B

Unlike flame A this flame excited thermo-acoustic oscillations at approximately 295 Hz, due to which this flame is a subject of significantly greater research interest. Self sustaining thermo-acoustic oscillations occur when pressure and heat release oscillations in a system are separated by a phase of $\leq 90^\circ$ (see section 2.1.3). Giezendanner [27] performed phase resolved OH, CH and CH₂O PLIF to determine heat release information during a single phase of oscillation. Averaged images of OH, CH and CH₂O PLIF for 8 phases showed the variation of intensities over a single cycle. The variation of CH-PLIF and OH*-chemiluminescence intensities correlated well and were identified as indicators of heat release rate. Duan [120] presented phase resolved Raman and LDA measurements for the same flame explaining the mechanism behind the self-sustained oscillations. The difference in responses of the fuel and air supply to pressure fluctuations in the combustion chamber were shown to cause varying fluxes of fuel and air, and hence equivalence ratios in different regions of the burner during the period of an oscillation. The air flux was seen to lag behind that of the fuel by 20-80°.

Giezendanner [121] further illustrated the change in the IRZ and ORZ over a period of the thermo-acoustic cycle by the use of two line OH-PLIF temperature measurements. The increase in the velocities in the IRZ corresponded to the transport of burnt gas towards the burner inlet along with reduced heat release and combustion chamber pressure. In his doctoral thesis [122](in German) Giezendanner further illustrates the periodic change in heat release together with the axial pumping like motion of the IRZ over a cycle of oscillation. The cycle is divided into 4 sub-phases separated by a phase angle of 90° (see figure 2.6). The first involves the increase in the pressure in the combustion chamber and heat release rate and the axial movement of the IRZ away from burner surface, which is followed by the pressure and heat release reaching maximum values with the IRZ reaching its largest axial distance to the burner. After this the pressure and heat release rate in the chamber begin to reduce and the IRZ starts moving back towards the burner surface. In the final phase the heat release, pressure and IRZ location reach minimum values before the cycle repeats.

The flame B has been investigated to understand the presence of dominant fluid mechanical structures that influence turbulence-chemistry interactions in the flame. Amongst the Flames A, B and C, the occurrence of a PVC was first detected experimentally in this flame. Stoehr [123] describes the presence of a helical vortex structure in the shear layer between fresh incoming flow and the IRZ. Further simultaneous PIV and OH-PLIF experiments [31, 124] describe the influence of the vortical structures formed by the PVC on the mixing of burnt and unburnt gas. The vortical structure was seen to increase the mixing and hence facilitate combustion and flame stabilization. The high speed (order of 10 kHz) simultaneous OH-PLIF and PIV measurements are used to describe the complex interaction of the flow and combustion phenomena that determine the location of flame stabilization [125]. The interaction of the thermo-acoustic oscillation with the PVC was studied using a similar set of measurements by Steinberg [30]. The thermo-acoustic oscillations were seen to cause an axial extension of the PVC at the minimum pressure of the cycle and compression at the maximum. The PVC was shown to deflect the incoming flow radially and cause combustion in the ORZ. Although the PVC was seen to influence the local heat release rate, there was no direct correlation of these fluctuations to those from the thermo-acoustic, indicating that they were two independent physical phenomena which interacted in this configuration.

4.2.3 Lean blow out: Flame C

The flame C operates close to the conditions of lean blow out. The flame experiences random flame extinction where the flame stabilizes on the chamber exit nozzle for a short period before stabilizing again closer to the burner surface. The flow field, heat release zone information and temperature distribution based on Raman spectroscopy are shown in figures 4.5(e) and 4.5(f). The flame shape is very similar to flame A, with the main region of heat release located in the inner shear layer formed between the incoming flow and the IRZ. The thermo-chemical states examined using Raman spectroscopy showed [26] a larger proportion of leaner mixture fractions close to the burner exit which contribute to unfavorable flame stabilization. Stoehr [32] conducted experiments with simultaneous high speed OH-PLIF and PIV. The flame stretch effects in stagnation zones formed by the PVC and incoming flow at the flame root determined the ignition of fresh incoming gases. When extinction in these zones exceeded a period of 2 ms, flame blow out occurred. Improvement of conditions for combustion in these region were suggested for improving leaner operation.

5

Results

In this chapter, the results pertaining to the methodology described in chapter 3 are described. In section 5.1 the results from the atmospheric experiments are presented introducing the effect of change in parameters such as oxidizer composition, equivalence ratio, inlet velocity and thermal loading on flame stabilization, velocity field and chemical composition. Following this a comparison of the air flames and oxyfuel flames is performed explaining the major differences in section 5.2. A set of experiments in section 5.3 is used to highlight the main differences between the burner used at atmospheric conditions and that used at elevated pressure conditions. Lastly, in section 5.4 the investigations at elevated pressure are presented.

5.1 Oxyfuel and air flames at atmospheric pressure

The extent of CO₂ dilution in oxyfuel flames is an important parameter in determining flame stabilization. The O₂ concentrations for which stable flame operation could be obtained were determined at first. A decrease in O₂ concentration in the oxidizer expectedly reduced the envelope of stable flame operation due to a reduction in the flame speed and adiabatic flame temperatures. The figure 5.1 shows the stability limits of the flames as a function of the inlet Reynolds number and O₂ concentration. The Reynolds number is calculated using the minimum effective flow cross-section of the burner outer co-swirl nozzle (25 mm) with flow rate calculated for a temperature of 303 K and 1 atm pressure. The viscosity of the mixture is calculated using the Wilke formulation [37]. Each connected line represents constant power and equivalence ratio conditions at stable operation. The flame was considered unstable if during operation, significant fluctuations in heat release occurred accompanied with random blow out events. Flames which excited thermo-acoustic instabilities were regarded as stable since they were not close to blow out limits and were reproducible.

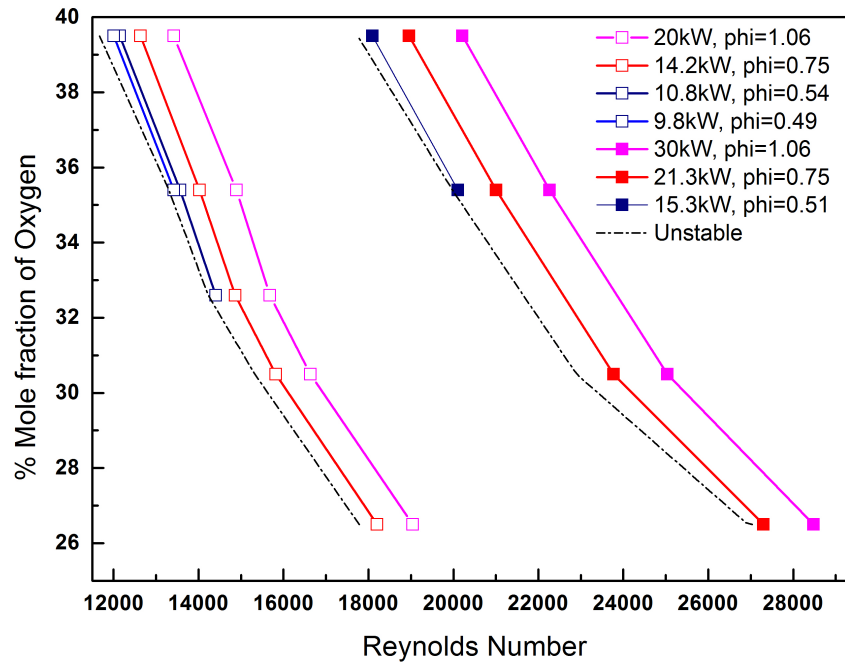


Figure 5.1: Stable flame operation region for different inlet Reynolds number and oxidizer composition

The plot shows two operating regions of the burner, one from $12,000 \leq Re \leq 19,000$ which corresponds to a thermal power of 10-20 kW and the second from $19,000 \leq Re \leq 28,000$ for 15-30 kW. Each curve in the $12,000 \leq Re \leq 19,000$ range starting from the left represents equivalence ratios of 0.49, 0.54, 0.75 and 1.06. Similarly for $19,000 \leq Re \leq 28,000$ the equivalence ratios are 0.51, 0.75 and 1.06. The increase in Reynolds number for similar thermal power is due to an increase in the CO_2 dilution. As the O_2 concentration in the oxidizer reduces the lean limit for flame stabilization reduces. Flames with acceptable stabilization close to stoichiometric operation were obtained for 26.5 % O_2 concentration. A further reduction in O_2 concentration led to very unstable flames. The results hence start with the 26.5 % O_2 concentration flames and describe the flame stabilization influence with increase in O_2 concentration up to 39.5 % O_2 . The laminar flame speeds of such mixtures are comparable to those of air. In practical systems higher O_2 concentrations would be associated with higher gas turbine inlet temperatures as such flames result in excessive flame temperatures (≥ 2400 K). Therefore O_2 concentrations higher than 39.5 % were not investigated.

The section 3.3 highlighted that the comparison of oxyfuel flames using different CO_2 dilutions needs to be performed for comparable thermal powers and comparable inlet velocities as both these parameters are not independent. Using the experimental setup

described in section 3.4.2 heat release and flow field information were obtained. Additionally a laser Raman scattering setup was used (section 3.4.3) to obtain a comparison of the thermo-chemical state to that of air flames. The results of the experimental investigations therefore are divided into the following:

1. Oxyfuel flames at comparable thermal powers
2. Oxyfuel flames at comparable inlet velocities
3. Thermo-chemical aspects of swirl stabilized oxyfuel flames

5.1.1 Oxyfuel flames at comparable thermal power

The results here pertain to OH*-chemiluminescence imaging, flame acoustic probe measurements and PIV measurements. The OH*-chemiluminescence images have been averaged from a collection of 200 short exposures (400 μ s). Acoustic measurements have been recorded in the combustion chamber and in the burner plenum using microphones with a sampling frequency of 10 kHz. The conditions for the experiments are given in table 3.1. The following figure 5.2 shows the averaged chemiluminescence images describing the influence of the variation of equivalence ratio and oxidizer composition on the flame stabilization. The intensity of the OH*-chemiluminescence can be compared as the settings of the camera and image intensifier used for the image capture were kept constant. The figures represent a 85 mm x 110 mm section of the combustion chamber. The figures also have details about the occurrence of thermo-acoustic oscillations in the form of combustion chamber amplitude (dB) and frequency (Hz). The average inlet velocity shown in the figures is calculated for the minimum flow area ($d=25$ mm) in the burner nozzle (section 3.1.1). The RMS of the OH*-chemiluminescence intensity for the same flames is shown in figure 5.3. In figure 5.4 the average velocity fields from the simultaneous OH*-chemiluminescence/PIV measurements on the flames in table 3.2 are shown in the form of streamlines. The corresponding averaged OH*-chemiluminescence images are shown for reference in figure 5.5. The following sections describe in detail the influence of varying different parameters on the flame shape and stability. It must be noted that these experiments were performed without a sonic flow nozzle at the inlet of the burner plenum.

5.1.1.1 Effect of variation of oxidizer composition

The first column of figure 5.2 represents the effect of variation in the oxidizer composition on flame stabilization at a thermal power of 14.3 kW. The images correspond to the first operating range of the burner from $12,000 \leq Re \leq 19,000$ (Fig.5.1). The flame moves

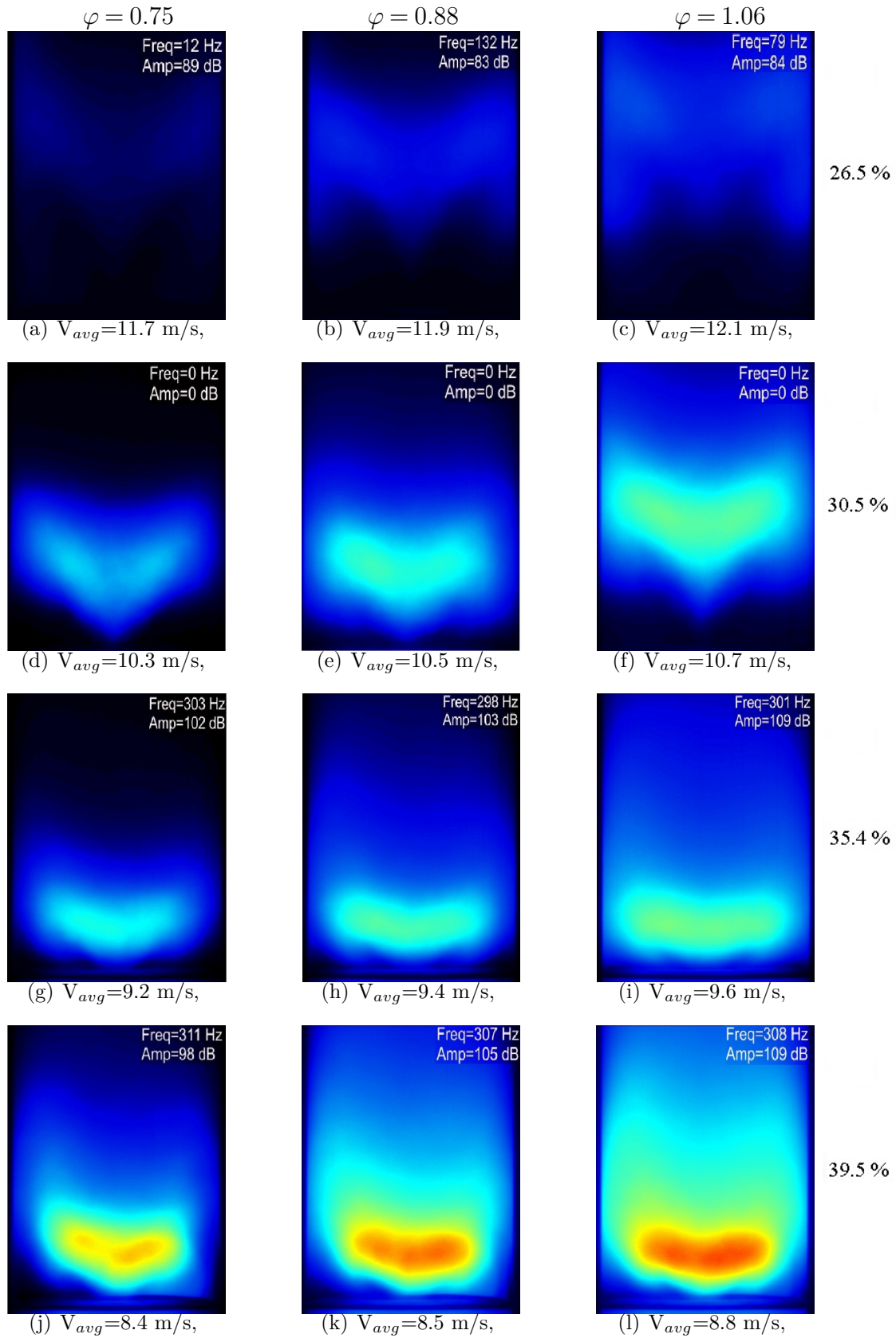


Figure 5.2: Average of 200 short exposures OH*-chemiluminescence images (85 mm x 110 mm) showing flame structures at 14.3 kW ($\varphi = 0.76$), 16.6 kW ($\varphi = 0.88$) and 20 kW ($\varphi = 1.06$) for different O₂ mole fractions.

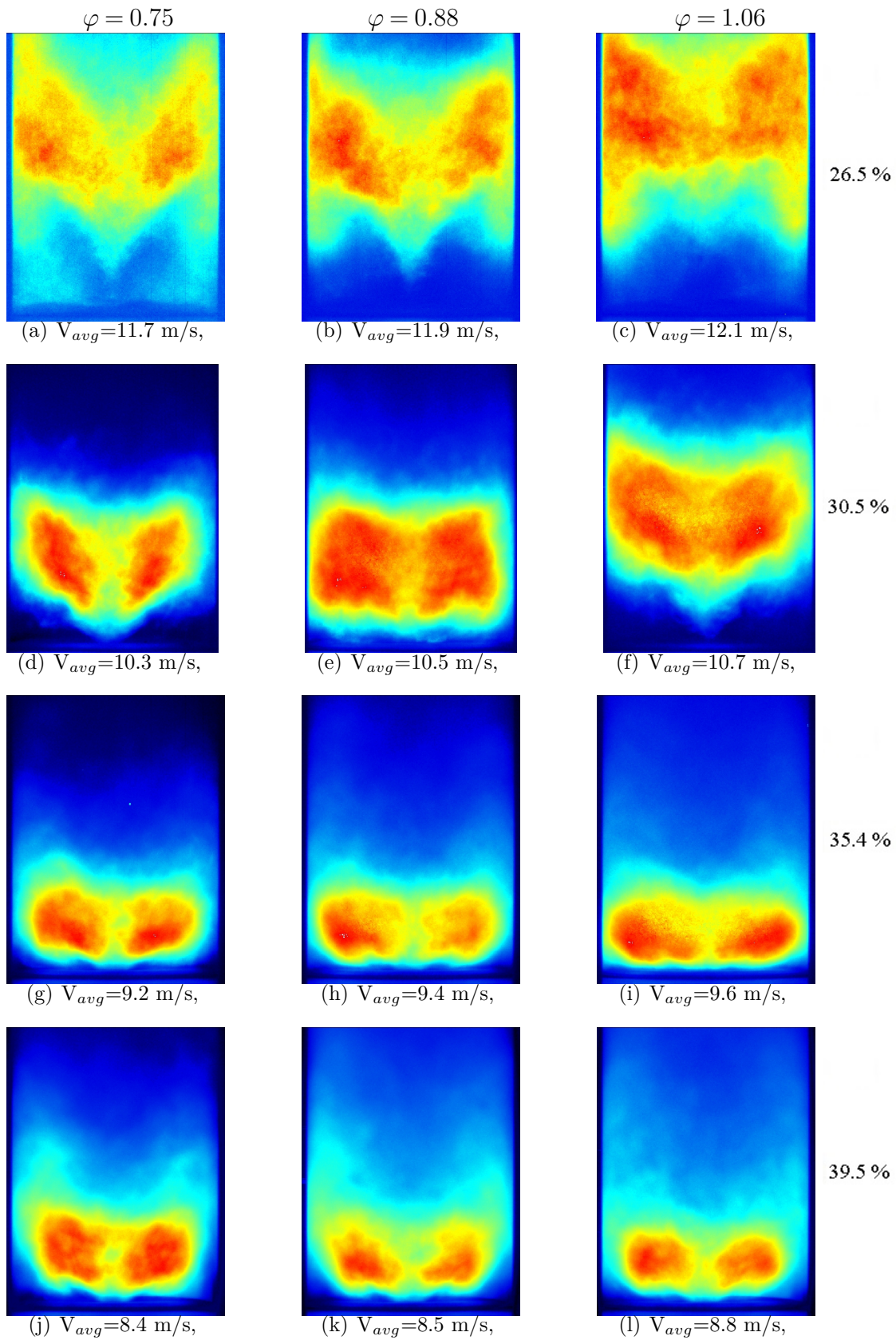


Figure 5.3: RMS of 200 short exposure OH^* chemiluminescence images (85 mm x 110 mm) of different oxyfuel flames at 14.3 kW ($\varphi = 0.76$), 16.6 kW ($\varphi = 0.88$) and 20 kW ($\varphi = 1.06$) for different O_2 mole fractions.

Composition	$\varphi=0.75$	$\varphi=0.88$	$\varphi=1.06$
26 %	1749	1904	2016
30 %	1927	2073	2172
34 %	2079	2204	2289
38 %	2205	2317	2383

Table 5.1: Adiabatic flame temperatures (K) of different flames with different oxyfuel oxidizers from calculations at 300 K at 1 bar conditions

closer to the burner surface with an increase in the O_2 concentration. At 26.5 % O_2 concentration the OH^* -chemiluminescence intensity is quite low, additionally the flame stabilizes at a significant distance downstream of the burner faceplate. The flame is not conically shaped as with air operation in this burner. These flames excited a low frequency (10-132 Hz) instability. As the O_2 concentration is increased, the flame takes on a conical shape for a concentration of 30.5 % O_2 resembling air flames and burning stably. A further increase in O_2 leads to the flames moving closer to the burner face and taking on a flatter flame form. This is similar to the methane-air flames observed for $\varphi=0.75-1.0$ with this burner (Chapter 4). The 39.5 % O_2 flames display a small amount of asymmetry. The reduced CO_2 dilution for these flames reduces the total flow rate and accentuates minor asymmetries in the oxidizer and fuel mixing. Flames with more than 30.5 % O_2 were seen to consistently excite thermo-acoustic instabilities. The intensity and frequency of the oscillations increased with the increase in O_2 concentration. The increased O_2 concentrations lead to a higher OH^* -chemiluminescence intensity which is indicative of an increase in the heat release rate and temperature. The adiabatic flame temperatures for different O_2 concentration flames calculated using GRI-mech 3.0 [67] in Cantera [68] are given in table 5.1 for reference. The temperature increases by 360 K to 460 K depending on the equivalence ratio as the O_2 concentration is increased from 26 % to 38 %.

The RMS images of the OH^* -chemiluminescence intensity (Fig. 5.3) further illustrate the change in location of the heat release for different oxidizers. The images have been normalized to the maximum intensity of fluctuation. Fluctuations in the heat release rate for the 26.5 % O_2 flame are located mostly in the ISL at a considerable distance downstream of the burner inlet. As the O_2 concentration increases, these fluctuations reduce in their extent, but remain in the ISL. At 35.4 % and 39.5 % the fluctuations are limited to a small region close to the burner surface. This points to faster localized combustion in high O_2 concentration flames. The different O_2 concentration flames react differently to changes in the equivalence ratio. This is discussed further below.

The typical flow field of swirl stabilized flames has been described in Chapter 2 (section 2.1.2). The effect of the change in O_2 concentration on the velocity field at a given thermal

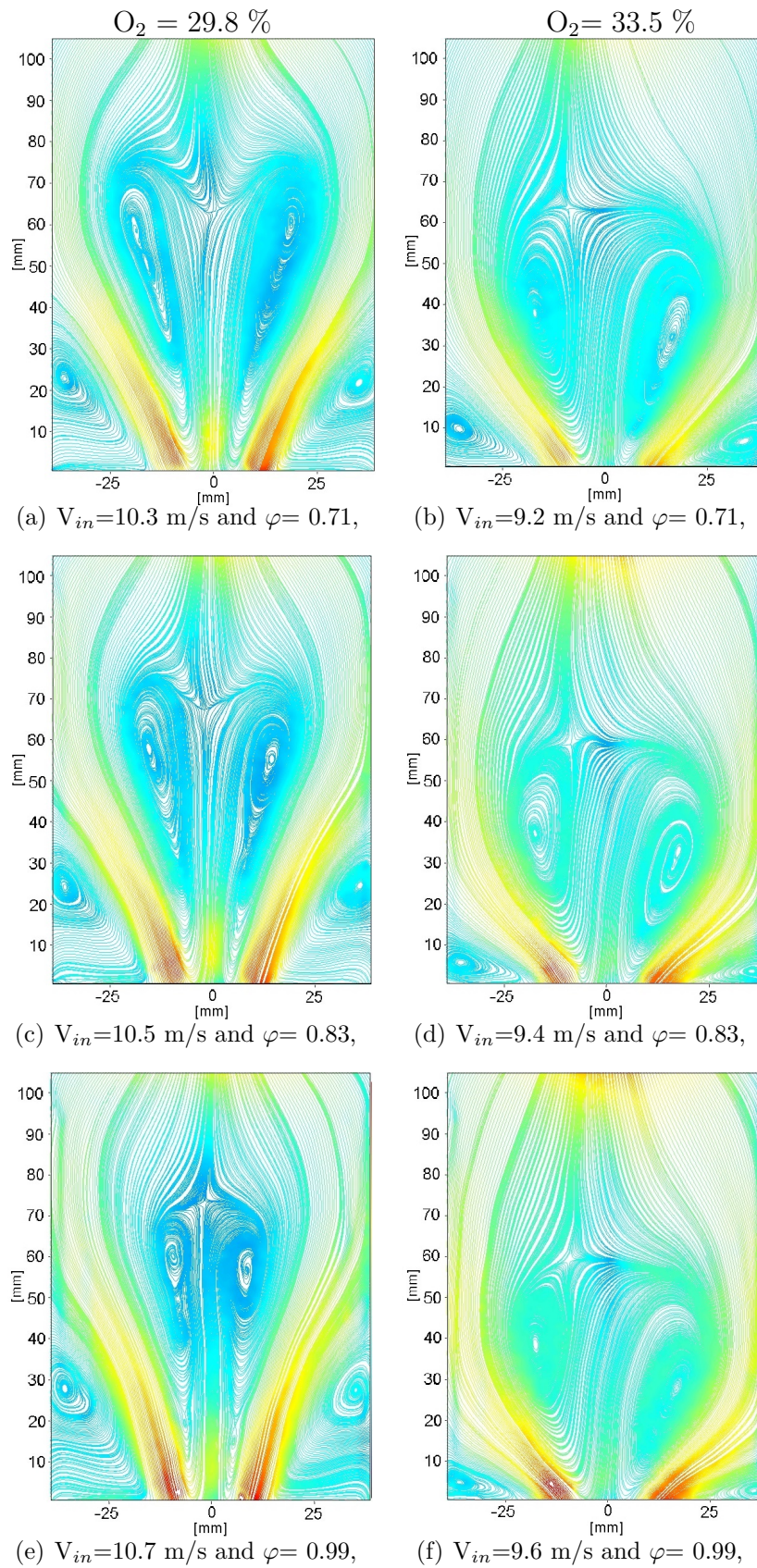


Figure 5.4: Streamlines colored by intensity of stream function (80 mm x 105 mm section) from 200 single shot stereo-PIV measurements at powers of 14.1 kW, 16.5 kW and 19.8 kW for O_2 mole fractions of 29.8 % and 33.5 %.

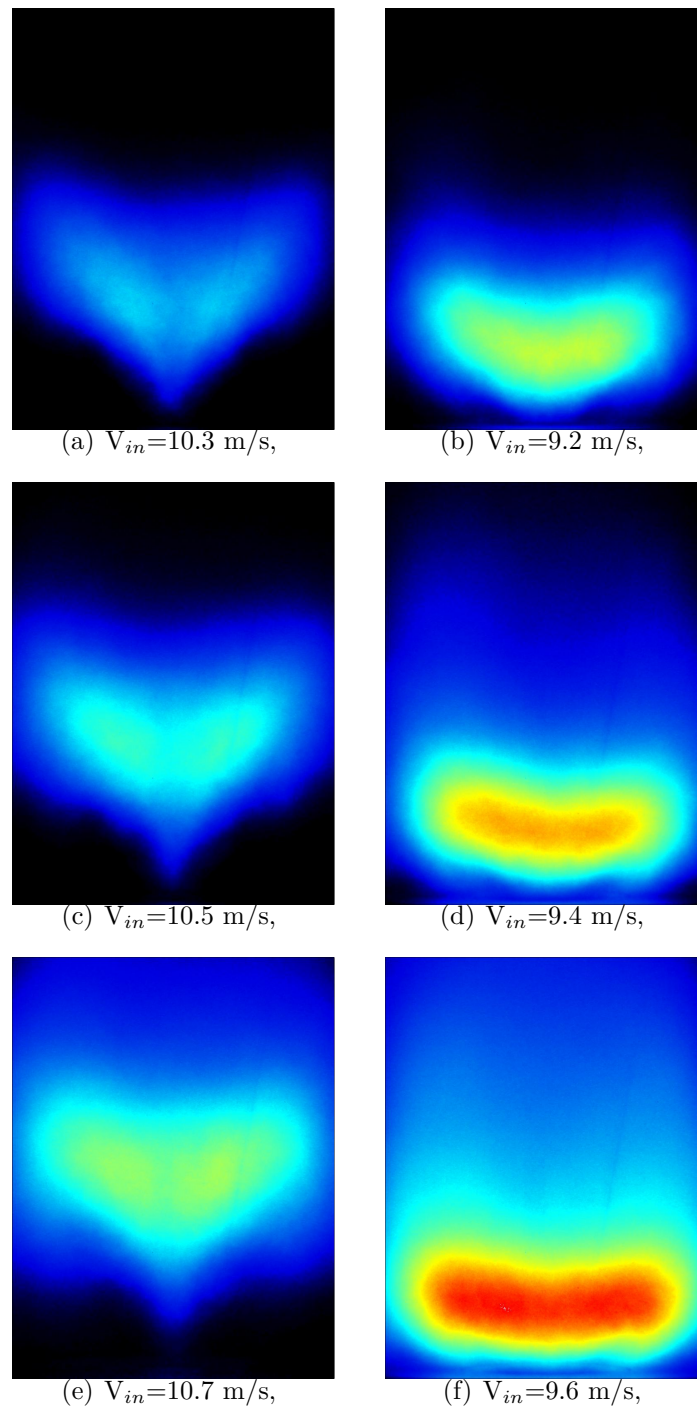


Figure 5.5: Average of OH* chemiluminescence (80 mm x 105 mm section) for flames shown in figure 5.4.

power is illustrated using streamlines in figures 5.4(a) and (b). The corresponding OH*-chemiluminescence images in figure 5.5 show the same change in flame location with change in O₂ concentration as described above. The images are for direct reference as the velocity measurements were performed after the stabilization study discussed above using the setup in section 3.4.2. At 29.8 % O₂ (figures 5.4(a), (c) and (e)), the fresh charge characterized by high velocities penetrates a significant distance into the combustion chamber before the streamlines diverge as a result of the combustion. The profiles of radial and axial components of the velocity at different height above burner face are shown in figure 5.6. The profiles elucidate this effect in detail. The proximity of the flame to the burner face is lesser for the 29.8 % O₂ case, due to which the maxima of radial (Fig 5.6(a)) and axial (Fig 5.6(b)) velocity components extend radially outwards gradually with HAB, from 2.5 mm, 6 mm and 9.6 mm. The swirling flow entering the combustion chamber gradually diverges before it encounters the heat release zone. For the 33.5 % flame the heat release is closer to the burner face. The peak in radial and axial velocity components diverges radially at a relatively small HAB of 6 mm. The immediate gas expansion due to combustion also results in a higher radial component of the velocity at similar locations when compared to the 29.8 % case. The extent of the IRZ which is represented by HAB up to which the negative values of the axial component of velocity exist is greater for the 29.8 % case where such values are observed up to a height of around 80 mm. For the 33.5 % O₂ the IRZ is compacter and extends to a height of 65 mm above the burner. The higher thermal expansion closer to the burner face due to combustion is thought to reduce the swirl number leading to the formation of a compacter IRZ. The change in flame position influences the velocity field considerably. This effect is explained in detail in section 5.1.2.

From previous work with methane-air flames on this burner a PVC formed by the vortex breakdown of the incoming flow has been observed (see section 2.1.2). This structure is known to influence the mixing processes and flame stabilization [32]. As the vortical structure precesses around the burner axis it intersects the plane of the PIV measurement during different phases of the precession. A consequence is the presence of rotation imparted to the flow at distinct locations pertaining to the PVC. Evidence of this can be extracted from the PIV data using POD analysis and has been used to determine the phase of the PVC [98]. The figure 5.7 shows the 1st and 2nd mode of the POD in the form of velocity vector images with a background colored by flow rotation about an axis perpendicular to the plane of measurement. The POD modes from PIV measurements performed by Stoehr [98] for air flames revealed a similar structure, indicating the presence of a PVC. The pairs of vortices with axially alternating sense of rotation represent the deflection of the incoming flow by the PVC. The black line is representative and is shown for ease of understanding depicting a projection of the 3-dimensional helical vortex

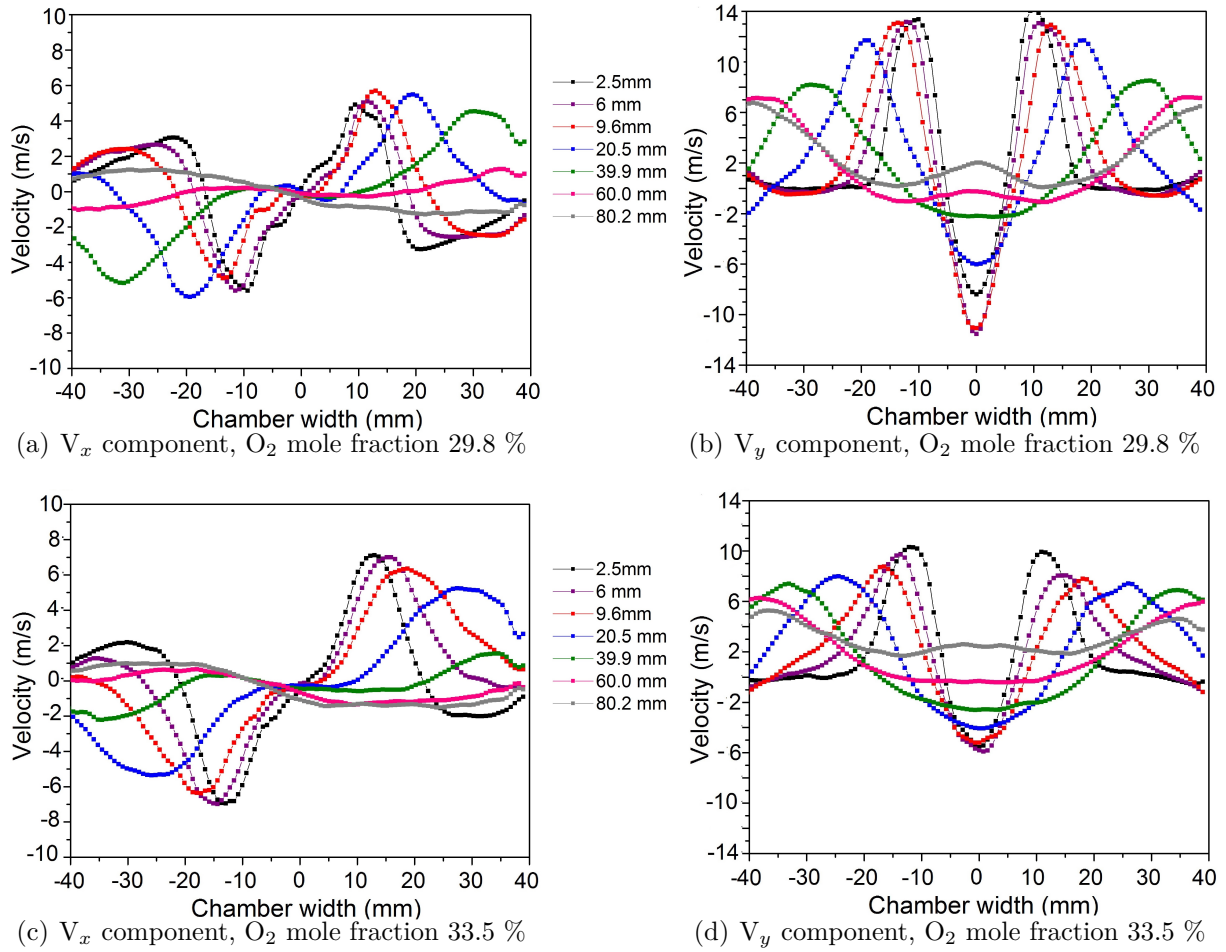


Figure 5.6: Profiles of average velocity components V_x (radial) and V_y (axial) from 200 single shot stereo-PIV measurements of flames at power of 14.1 kw ($\varphi = 0.71$) with O_2 mole fractions of 29.8 % and 33.5 % in the oxidizer.

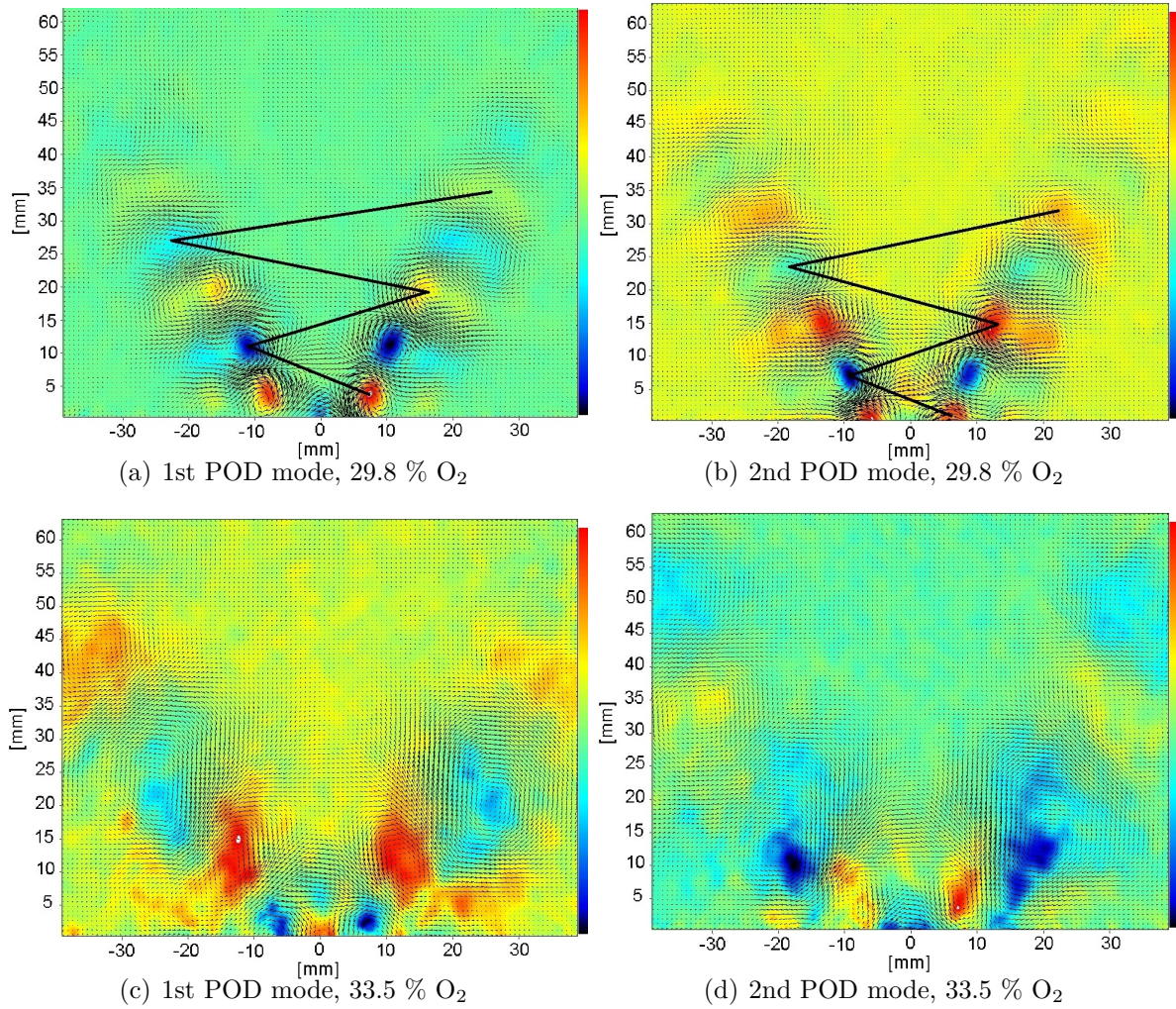


Figure 5.7: Vectors of 1st and 2nd mode of POD from single shot stereo-PIV of flames at power of 14.1 kw ($\varphi = 0.71$) with O_2 mole fractions of 29.8 % and 33.5 % O_2 in oxidizer. Background coloured by flow rotation along an axis perpendicular to plane of paper.

on the plane of measurement. The figure 5.7(b) showing the second mode is indicative of other phases of the PVC shifted by half the distance between axially adjacent vortices. The distinctness of the PVC gradually reduces with HAB. The stabilization of the flame closer to the burner face for the 33.5 % case reduces the distinctness of the PVC. An axial and radial distention of the PVC along-with an increase in size of vortices is seen. The movement of the flame closer to the burner surface expands the PVC in the radial and axial direction indicating a change in the flow dynamics.

The location of heat release in a flame is governed by a combination of parameters such as local flow velocity, mixing, temperature, turbulent flame speed (related to laminar flame speed and turbulence), local flame stretch and local quenching. The variation of the laminar flame speed of premixed flames as a function of equivalence ratio for different oxyfuel oxidizer compositions was shown in figure 2.10. As the oxidizer O_2 concentration

Composition	$\varphi=0.76$ (cm/s)	$\varphi=0.88$ (cm/s)	$\varphi=1.06$ (cm/s)
26 %	4.5	7.1	9.2
30 %	9.4	13.1	15.9
34 %	16	20.8	24.2
38 %	24.3	30	33.9

Table 5.2: Premixed laminar flame speeds of different methane-oxyfuel oxidizers from calculations at 300 K at 1 bar conditions

was increased from 30 % O₂ to 40 % O₂ the laminar flame speed almost doubled. The premixed laminar flame speeds at similar operating conditions as investigated above were calculated using an experimentally validated reaction mechanism (RDv06-NGQ) developed at the DLR-Institute of Combustion Technology, Stuttgart [3, 74]. The values of the laminar flame speeds are shown in table 5.2. For a given equivalence ratio it is seen that the laminar flame speed increases with an increase in O₂ concentration. At $\varphi=0.76$, the laminar flame speed for 38 % O₂ is 5.4 times that at 26 % O₂. This increase reduces to 3.68 times for $\varphi=1.06$. For comparison the values of experimentally measured laminar flame speeds of methane-air flames for the same equivalence ratios are 23, 31 and 37 cm/s. The adiabatic flame temperature of higher O₂ concentration flames is also higher (table 5.1). A combination of increased laminar flame speed and higher combustion temperatures hence assists the stabilization of higher O₂ concentration flames closer to the burner surface. As the CO₂ dilution reduces for the above cases, the lower inlet flow velocity also assists flame movement closer to the burner face. The 30 % O₂ flames show a stable conical flame shape similar to typical air flames. For flames having higher than 30 % O₂ the better flame stabilization coincided with the excitation of thermo-acoustic instabilities. In section 5.1.2 the effect of change in inlet velocity and oxidizer composition and flame stabilization is looked into in detail. The following section describes the effect of equivalence ratio on the different oxidizers.

5.1.1.2 Effect of variation of equivalence ratio

The figures 5.2(a),(b) and (c) compare the influence of an increase in equivalence ratio for the 26.5 % O₂ concentration flames. The increase in equivalence ratio is achieved at a constant oxidizer flow rate. The minimal increase in average inlet velocity is a result of the higher fuel flow rate. The increase in equivalence ratio produced varying effects in the different O₂ concentration flames, with all flames showing an increased region of chemiluminescence intensity due to the larger quantity of fuel. The 26.5 % O₂ concentration flames at $\varphi = 0.75$ excited low frequency oscillations, whose frequency increased at higher equivalence ratios. The shape and position of the 30.5 % O₂ flame

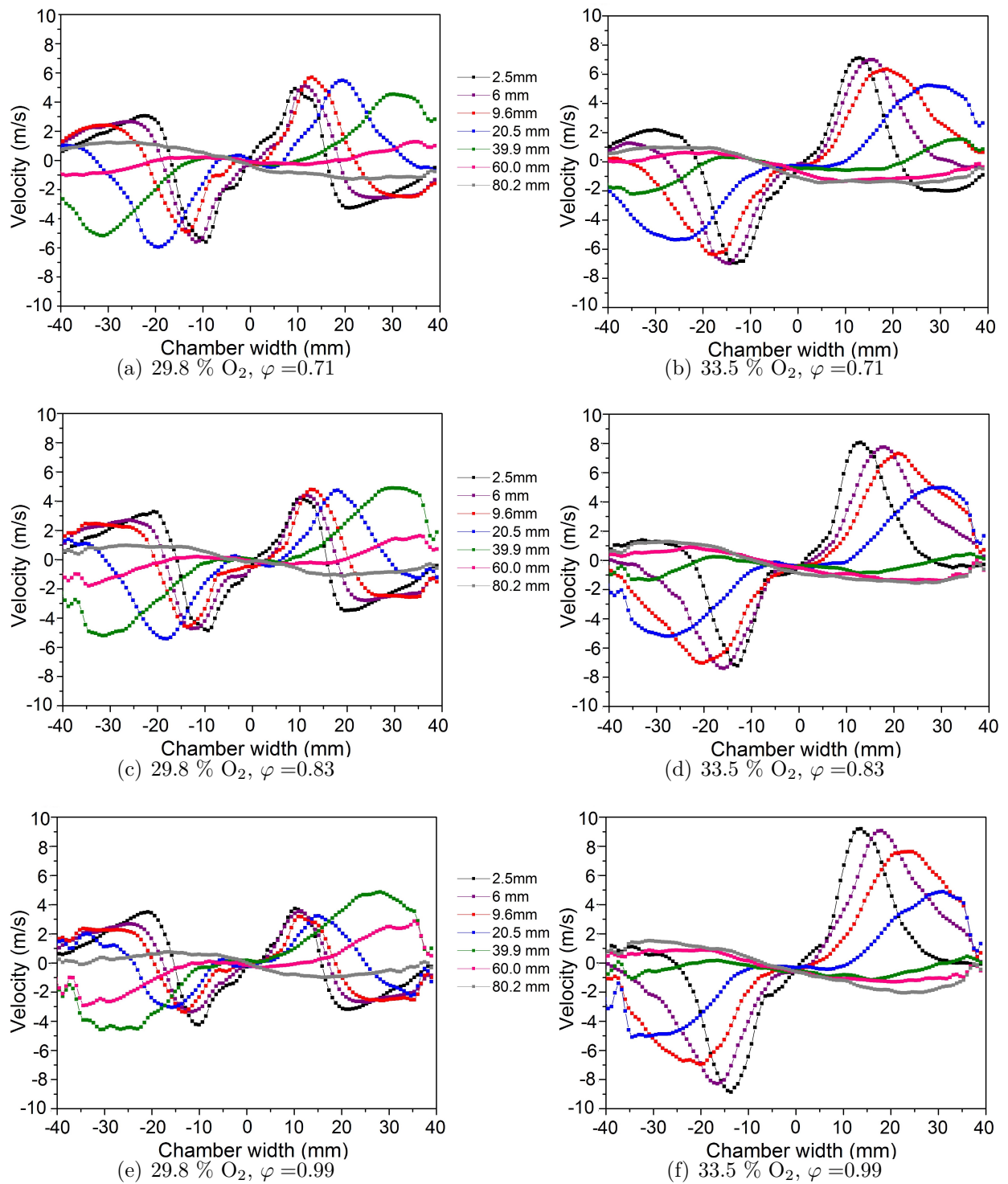


Figure 5.8: Profiles of radial component of average velocity from 200 single shot stereo-PIV of flames at different φ with O₂ mole fractions of 30 % and 34 % in oxidizer.

remains the same for an increase in the equivalence ratio from 0.75 to 0.88. The flame however moves further downstream as the equivalence ratio was increased from 0.88 to 1.06. This change in flame position was repeatable and represents a transition into an alternate stabilization location. The reason for this behavior is not clear and needs further investigation. For the 35.4 % and 39.5 % flames the flame shape remains similar and an increase in fuel flow results in the expansion of region of high chemiluminescence intensity. The RMS images of OH*-chemiluminescence intensity (Fig.5.3) reveal further differences in the flame behavior with change in the equivalence ratio. The heat release fluctuations which were predominantly located in the ISL for the 26.5 % and 30.5 % flames at lean conditions extend into the IRZ. In contrast, for the higher O₂ concentration flames these fluctuations remain in the ISL. As these flames also exhibited thermo-acoustic oscillations, the RMS images also depict the change in heat release over a cycle of oscillation. The notable change in flame behavior for the 26.5 % and 30.5 % O₂ oxidizers is suggestive of a higher sensitivity of such flames to change in equivalence ratio due to the lower reactivity of such oxidizers.

The influence of changes in equivalence ratio on the flow field for the 29.5 % flame is shown in 5.4(a), (c) and (e). The movement of the flame downstream corresponds to the narrowing of the IRZ near the burner inlet. The impact of this can be observed in the profiles of velocity (Fig. 5.8(a), (c) and (e)). As the equivalence ratio increases, the radial component of the velocity reduces throughout the flow field. For the 33.5 % flame the region of heat release remains relatively similar with an increase in equivalence ratio. However, the flow field is influenced due to the larger fuel flow. These effects are detectable in the velocity profiles in fig 5.8 ((b), (d) and (f)) where it is seen that the radial component of the velocity increases at different HAB. The POD modes for the the 29.5 % and 33.5 % O₂ flames revealed differences in the structure of the PVC (Fig. 5.7). The PVC for the 33.5 % flame moves radially relative to the 29.5 % flame. The difference in flame shape and PVC structure is thought to influence the mixing of fuel and oxidizer, inducing different reactions to changes in the equivalence ratio for the two oxidizers. In section 5.1.2 this effect is looked into with further detail at similar average inlet velocities for different oxidizers. The impact of a change in equivalence ratio on the flame behavior is weaker in comparison to the effect of change in oxidizer composition.

5.1.1.3 Effect of variation of thermal loading

A similar study to that described above was repeated for higher inlet velocities and hence higher thermal loading. The figure 5.9 compares the influence of higher thermal loading on flame structure and dynamics for two equivalence ratios of $\varphi = 0.75$ and $\varphi = 1.06$. A similar influence of the increase in O₂ concentration as seen above is observed. Due to the increased inlet velocities the flames occupy positions further downstream. The region

5. RESULTS

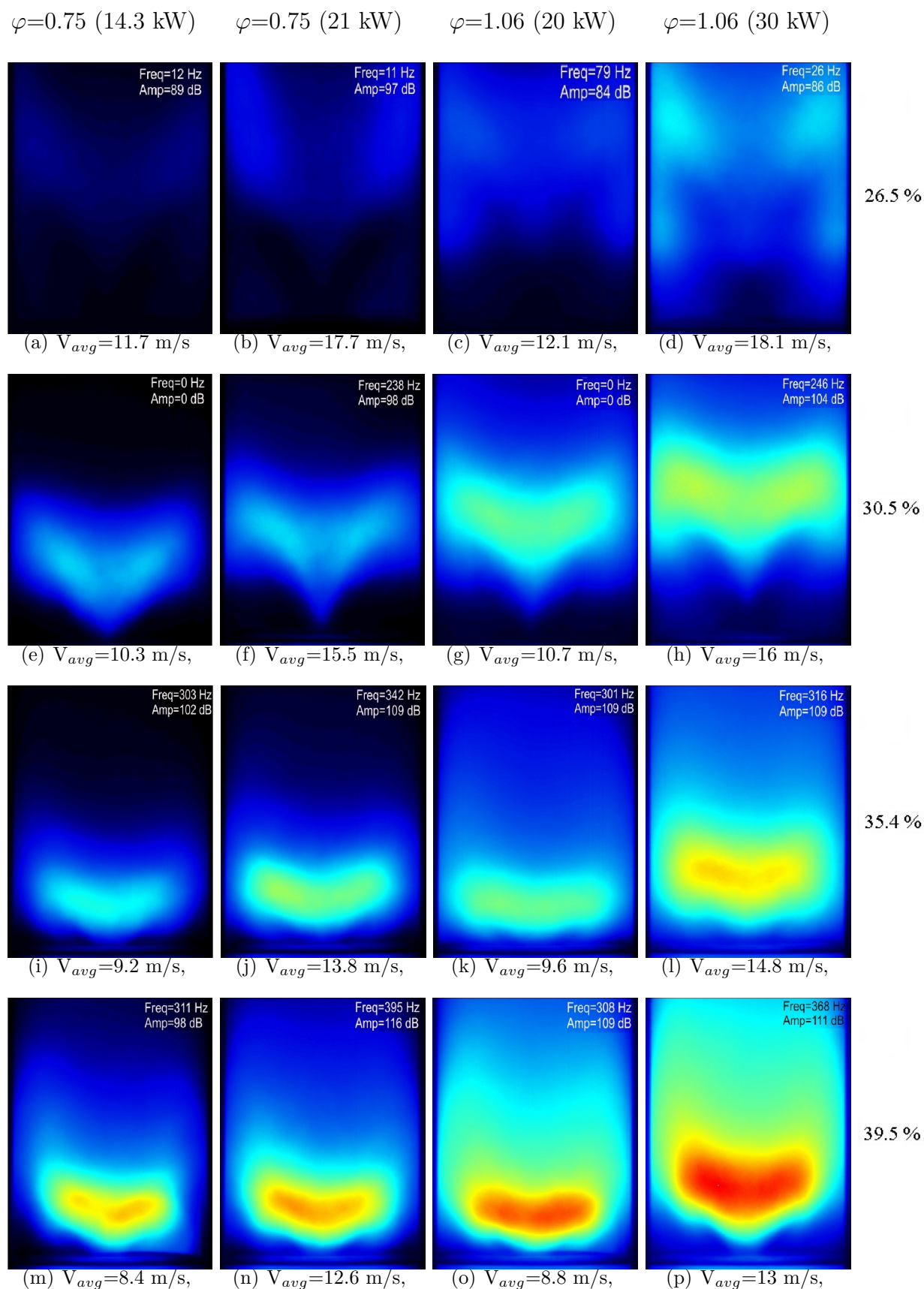


Figure 5.9: Average of 200 short exposure OH*chemiluminescence images showing flame structure at two different thermal loading ranges for $\varphi = 0.76$ and $\varphi = 1.06$ with different O₂ mole fractions 26.5 %, 30.5 %, 35.4 %, 39.5 %.

of higher OH*-chemiluminescence intensity increases due to the higher fuel content in the flames. The 26.5 % O₂ flames continue to display low frequency instabilities. The 30.5 % O₂ flame which burned stably at low powers begins to display thermo-acoustic oscillations. The reasons for this change in behavior are discussed further in the section on thermo-acoustic oscillations. The 35.4 % and 39.5 % O₂ flames exhibit an increase in thermo-acoustic oscillation amplitude and frequency. The increase in frequency is typical for a Helmholtz resonance. The link between the Helmholtz resonance and thermo-acoustic oscillations is discussed further in the following sections.

5.1.2 Oxyfuel flames at comparable inlet velocities

In the previous section the thermal power of the flames with different oxidizer compositions was kept constant, which resulted in a change in the inlet velocity. In this section inlet velocity is kept constant for different oxidizer compositions. This implies a constant volume flow for different O₂ concentrations. With increasing O₂ concentration in oxidizer, the quantity of fuel required for maintaining the same equivalence ratio increases resulting in an increase in the thermal power.

As in the previous section, the following sections look into the different types of oxidizers and their influence on flame stabilization by means of OH*-chemiluminescence and PIV measurements. Presence of thermo-acoustic if any is also described. The experimental setup corresponds to that described in section 3.4.2 and the operating conditions are given in table 3.3. The figures 5.10 and 5.11 show the average OH*-chemiluminescence and PIV images obtained from the measurements. Flames containing 26.1 %, 29.4 % and 33.7 % O₂ have been studied representing the typical flame shapes obtained in the burner. The effect of change in the oxidizer composition on flame behavior is discussed in the next section followed by the discussion on the effect of equivalence ratio and inlet velocity.

5.1.2.1 Effect of variation of oxidizer composition

The figure 5.10 highlights the effect of change in oxidizer composition on the flame shape. Significantly different from the stabilization of the constant thermal power flames shown in figure 5.2 was the behavior of the 26.1 % O₂ concentration flames. The flames stabilized slightly closer to the burner face than before and burnt relatively stably without the low frequency periodic oscillations observed previously. It must be noted that a sonic nozzle was used for these experiments. The high impedance of the sonic nozzle isolates any acoustic effects of the supply piping that could influence the flame behavior. The better stabilization of the 26.1 % O₂ flames here is thought to be related to this change, as their lower reactivity in comparison to other oxyfuel flames makes them susceptible to

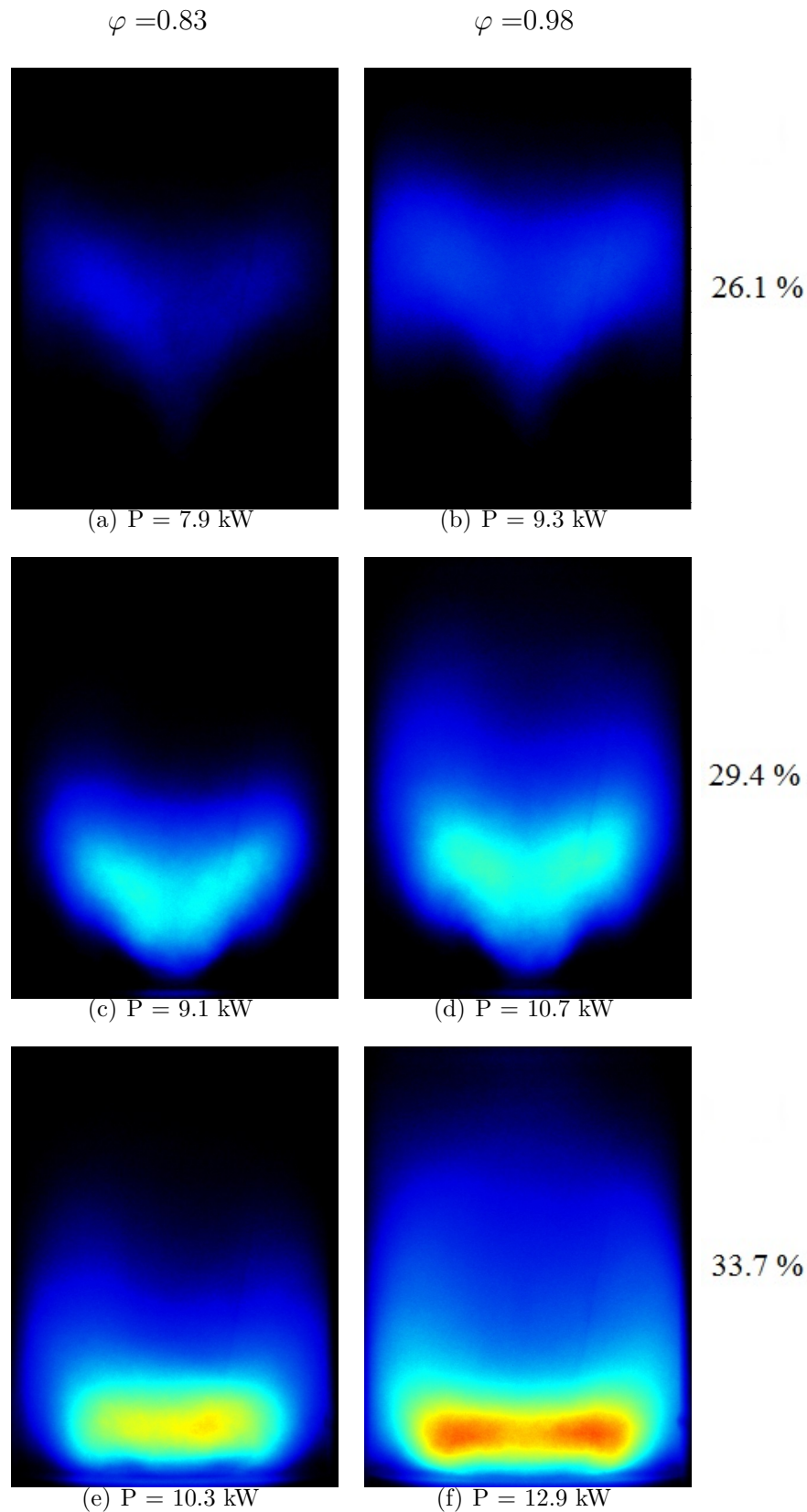


Figure 5.10: Average of 200 short exposure OH* chemiluminescence images (85 mm x 110 mm chamber section) showing flame structure at an average inlet velocity of ~ 6 m/s for two equivalence ratios and different O₂ mole fractions.

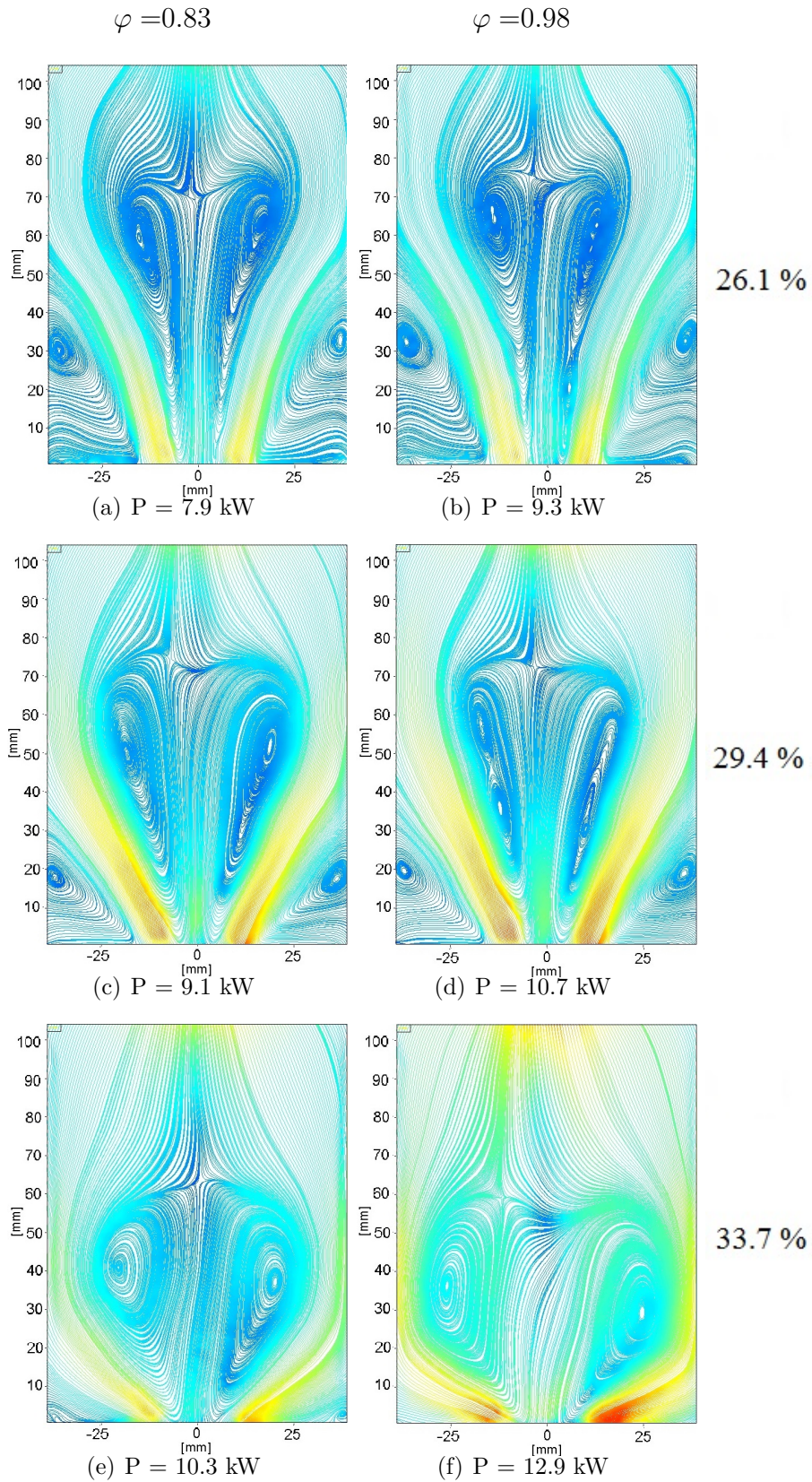


Figure 5.11: Average of 200 shot PIV data showing streamlines (colored by stream function value) for flames operated at an average inlet velocity ~ 6 m/s for two equivalence ratios and different O_2 mole fractions.

5. RESULTS

Composition	Total Flow (lpm)	% IRZ flow	% Main Flow	% ORZ
26.1 %	240	-4.09	124.2	-20.13
29.4 %	312	-3.80	107.5	-3.7
33.7 %	456	-3.27	103.27	0

Table 5.3: Flow split variation with composition for flames with average velocity of ~ 6 m/s and $\varphi = 0.83$ at HAB=6 mm.

small changes in flow conditions. The flames move closer to the burner face like in section 5.1.1.1 as the concentration of O_2 in the oxidizer is increased. This change in flame location also correlated with the occurrence of thermo-acoustic oscillations as seen previously. The flames in figures 5.10(a), (c) and (e) at $\varphi = 0.83$ are discussed at first. The flow field of these flames is shown in figures 5.11(a), (c) and (e). The increase in O_2 concentration in the oxidizer significantly changes the flow structure as before. Since the inlet flow velocities for all the flames are the same, this effect is largely attributed to the faster chemistry at higher O_2 concentrations. The lower flame speeds at 26.1 % O_2 concentration results in the flames stabilizing further downstream from the burner. As a result a large ORZ is formed which extends to almost 50 mm above the burner. The IRZ becomes compact as the O_2 concentration is increased, and it extends radially diverting the incoming flow significantly. The size of the ORZ reduces and nearly disappears for the 33.7 % O_2 flame. The angle of the incoming flow relative to the burner axis increases drastically as the O_2 concentration increases.

In order to obtain information about the proportion (volume) of incoming flow that is diverted into the IRZ and ORZ, the axial component of measured velocity is numerically integrated radially assuming cylindrical symmetry to obtain volume flow information. The flow is divided into 3 regions, based on the locations of flow reversal (flow being directed axially towards burner inlet). By doing so the amount of flow being redirected towards the burner inlet through the IRZ, and ORZ is obtained. The flows are calculated at a height of 6 mm above the burner surface. The table 5.3 shows the volume of total flow and percentage of total flow that is directed towards the burner inlet through the IRZ flow/ORZ flow (negative sign) and away from burner surface through the main flow (positive sign). In an ideal non-reacting case, this value would corresponding to the total volume flow through the burner. As the O_2 concentration in oxidizer increases from 26.1 % to 33.7 % the total volume of flow at a height of 6 mm increases. The movement of the flame closer to the burner causes the gas composition to change due to combustion, which results in gas expansion and a higher total volume flow. For the 26.1 % case a significant amount of the flow is redirected towards the inlet through the IRZ (4.09 %) and ORZ (20.13 %). The recirculating flow combines with the fresh flow entering the

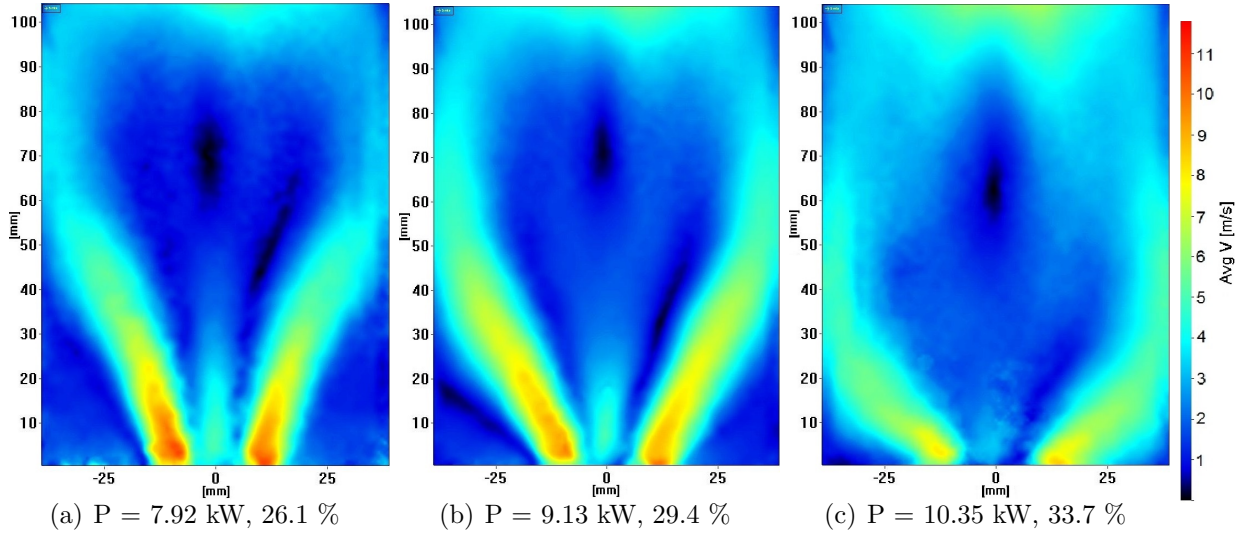


Figure 5.12: Contour of absolute velocity in the combustion chamber at inlet velocity of ~ 6 m/s for $\varphi = 0.83$ with different O_2 mole fractions 26 %, 29 %, 34 %.

combustion chamber from the burner inlet to give the burner main flow. As the flame moves closer to the burner for the 29.4 % case, fresh charge coming into the combustion chamber is heated and directed radially which reduces significantly the extent of the ORZ (3.7 %) and correspondingly reduces the main flow increase to 7.5 %. The percentage of IRZ flow reduces marginally. A further increase in the O_2 concentration causes the ORZ to become almost insignificant (fig 5.11(e)) and the flow increase in the main flow (3.27 %) corresponds mainly to the flow being directed towards the burner surface through the IRZ.

The location of heat release is governed by the interaction of flow parameters, heat transfer and chemistry. The location of heat release in turn influences the flow through the expansion of gases. The region of stable heat release hence occurs in locations where the interaction of the above parameters is most suitable for combustion. A change in the O_2 concentration changes the interaction of these parameters. The figure 5.12 shows contours of absolute velocities for the three flames. The flow velocities upon entry into the combustion chamber reduce as the O_2 increases although the volume flow through the burner for all three flames is the same. The lower reactivity of the 26.1 % O_2 flame shifts the heat release zone downstream where stabilization conditions are more suitable. The formation of a large recirculation zone results in more flow being directed towards the burner face and hence increases flow velocities at the inlet. The increase of O_2 concentration has the opposite influence. The higher charge reactivity assists flame stabilization closer to the burner face for a similar inlet velocity to the 26.1 % O_2 case. The flame serves as an obstruction to the fresh charge coming into the chamber and reduces flow velocities and directs the flow radially.

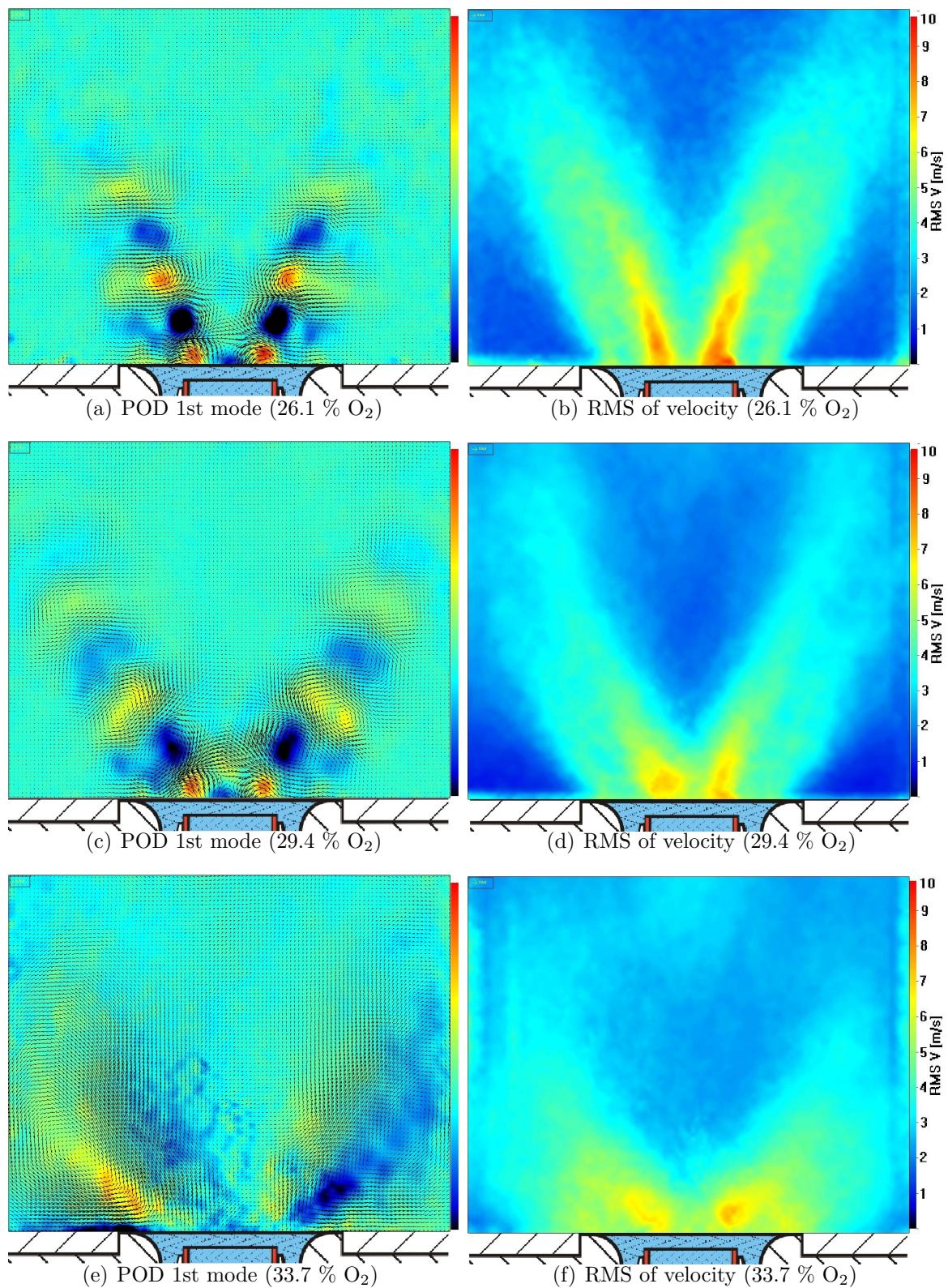


Figure 5.13: Vectors of 1st mode of POD and RMS of velocity (80 mm x 65 mm chamber section) for flames at $\varphi = 0.83$ and average inlet velocity of ~ 6 m/s for different O₂ mole fractions. POD image background colored by rotation in the symmetry plane.

The change in flame reactivity also influences turbulent mixing and dominant flow features. Information regarding the change in these structures was obtained by performing a POD analysis on the flow data. The swirl flames in this burner have been observed typically with a PVC as described previously. The figure 5.13 shows only the first mode of the POD (background coloured by flow rotation) for conciseness along with the RMS of the velocity for the 26.1 %, 29.4 % and 33.7 % O₂ flames at $\varphi = 0.83$. For the 26.1 % and 29.4 % flames a distinct PVC is observed. The change in location of the heat release causes the PVC to move radially as the O₂ concentration increase. This effect is similar to that observed previously. However, at 33.7 % this structure is no longer detected, instead, a large counter-rotating vortical structure is seen. In the case of a PVC at a given HAB the vortical structures depict the same sense of rotation. The difference in the sense of rotation for the 33.7 % case is indicative of a toroidal vortex formed possibly due to the detachment of the flow from the burner lip (refer figure 4.4). This is unlike the structure seen in similar flames for the studies with comparable thermal power. A PVC was detected in those flames as the O₂ concentration increased. The location of these dominant flow structures corresponds well to the location of high velocity fluctuations in the RMS images (Fig. 5.13(b), (d) and (f)). For the 26.1 % and 29.4% flames these fluctuations are thought to be caused mainly by the PVC. The mechanism of mixing of the co-swirling air flows for the 33.7 % O₂ flame is not PVC dominated. The intensity of the fluctuations in the ISL formed between IRZ and fresh gas flow reduces with increase in O₂ concentration. The PVC has been shown in previous studies to be crucial to the mixing of burnt and fresh gas and therefore flame stabilization in this burner. Large shearing stresses were also correlated to flame extinction [32]. The presence of larger flow fluctuations in the PVC region of the 26.1 % flame together with low flame reactivity are indicative of difficult flame stabilization conditions. These conditions improve through reduction in velocity fluctuations as the flame approaches the burner face for 30 % and 34 % O₂ concentration oxidizers.

An increase in the turbulent flame speed at higher O₂ concentration is one of the main factors responsible for flame stabilization closer to the burner surface. The increase in O₂ concentration reduces the flow velocity of the fresh charge entering the combustion chamber. The change in flame shape is accompanied by a change in the dominant flow features in which no PVC is observed as the O₂ concentration in the flame was increased. The movement of the flame closer to the burner face also consistently excited thermo-acoustic oscillations. This is discussed in detail in the following sections.

5.1.2.2 Effect of variation of equivalence ratio

The figures 5.10(a) and (b) show the change in OH*-chemiluminescence for the 26.1 % O₂ flames with equivalence ratio. The corresponding velocity fields are shown in figures

5.11(a) and (b). An increase in the equivalence ratio leads to a larger region of OH*-chemiluminescence intensity due to the higher fuel flow into the combustion chamber. The impact of change in equivalence ratio on the flow field for the 26.1 % flame is not discernible. The IRZ and ORZ maintain a very similar nature at the two equivalence ratios. For the 29.4 % flame a slight reduction in the lateral extent of the IRZ is seen and corresponds to an increase in the size of the ORZ. For the 33.7 % flame the effect is the opposite, where the higher fuel flow causes a widening of the IRZ. The incoming fresh gas is directed further radially in comparison to that at $\varphi=0.83$. This is similar to the impact of the change in equivalence ratio observed at comparable powers in section 5.1.1.2. The change in O₂ concentration has been shown to influence the structure of the PVC. The PVC which is mainly responsible for mixing in the 26.1 % and 29.4 % is no longer detected in the 33.7 % flame. The difference in the mixing of the two basic flame shapes observed in the burner (conically shaped and flat) explains this behavior and needs further investigation. However since the effects are not as significant as that due to the change in oxidizer, it is not a topic of great focus.

5.1.2.3 Effect of increase in inlet velocity

The study described in the previous section was repeated at higher inlet flow velocities to ascertain its impact on flame behavior. The flames were operated at an average inlet velocity of approximately 12 m/s. Like in the previous sections the effect of change in this parameter on flame stabilization is studied with respect to changes in oxidizer composition and equivalence ratio. The effect of an increase in the inlet velocity on the heat release is shown in figure 5.14 with the average OH*-chemiluminescence images. The change in corresponding velocity fields is shown in 5.15. For the 26.1 % O₂ concentration flames the increase in inlet velocity causes the region of heat release to increase and widen as the quantity of fuel increases. The flow field remains very similar to that at 6 m/s with a slight widening of the IRZ. In the case of the 29.4 % O₂, the flame moves further downstream. The higher flow velocities and higher thermal power increases the region of heat release as expected. The velocity field stays for both 26.1 % and 29.4 % flames relatively similar with distinct IRZ and ORZ. For the 33.7 % case the flame is no longer as close to the burner face as before and takes on the shape of the third typical flame type observed in the burner, which is the extended flat flame. The flow field of the flame shows a clear ORZ unlike before. The 29.4 % and 33.7 % flames at 12 m/s have distinct thermo-acoustic oscillations. The reasons behind this are explained in the next section. The dominant flow features present in the flow were determined using a POD analysis and it was seen that a PVC exists for all O₂ concentrations. The movement of the flame closer to the burner causes the PVC to move radially and reduces the HAB to which it extends. With an increase in the equivalence ratio the 26.1 % and 33.7 % flames

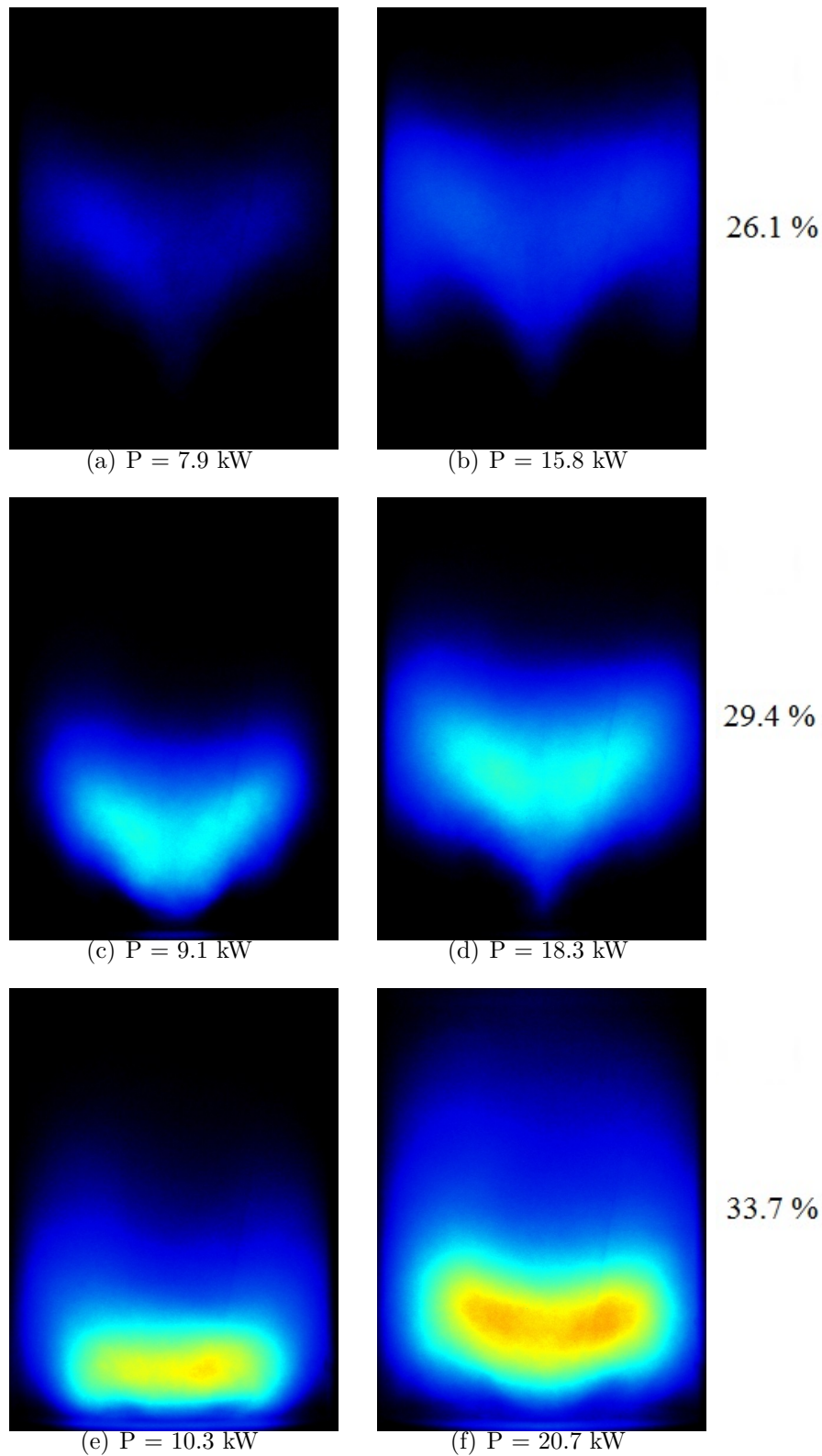


Figure 5.14: Average of 200 short exposure OH* chemiluminescence images (85 mm x 110 mm chamber section) showing the flame structure at two different inlet velocity ranges of ~ 6 m/s and ~ 12 m/s for $\varphi = 0.83$ with different O₂ mole fractions 26 %, 29 %, 34 %.

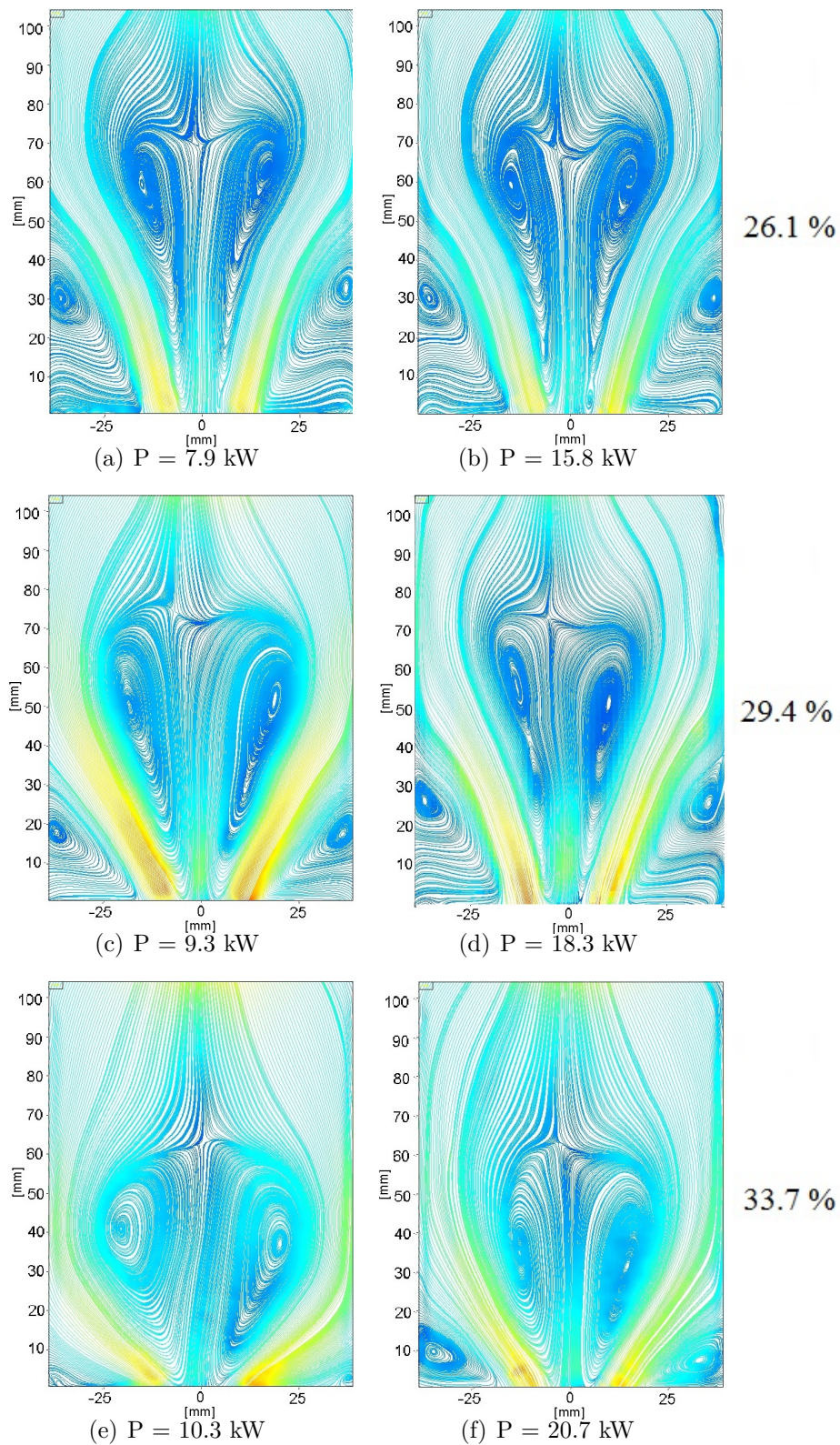


Figure 5.15: Streamlines colored by stream-function showing the average (200 PIV images) flow field at two different inlet velocity ranges of ~ 6 m/s and ~ 12 m/s for $\varphi = 0.83$ with different O₂ mole fractions 26 %, 29 %, 34 %.

maintained their structure. An unstable transitioning flame configuration was observed for the 29.4 % O₂ flame. The flame was seen to move between the flat flame and conical flame configurations.

The increase in flow velocity to 12 m/s results in the flames occupying locations further downstream of the burner face for all oxidizers. The 29.4 % O₂ excites thermo-acoustic oscillations unlike that at 6 m/s. The following section looks into these oscillations in detail.

5.1.3 Thermo-acoustic oscillation mechanism

A consequence of the change in flame location with an increase in the O₂ concentration is the onset of thermo-acoustic instabilities in the flames. This was seen at operating conditions of comparable thermal power and comparable inlet velocities (section 5.1.1 and 5.1.2). The mechanism of thermo-acoustic oscillations has been described previously. The time-scales associated with the mixing and combustion processes are a characteristic of a burner configuration and given operating condition (see section 2.1.3). The modes of acoustic oscillations are also system dependent. When the time scales of combustion processes and acoustics modes become similar a resonant oscillation occurs. The mode of thermo-acoustic oscillations that have been observed in the burner used correspond to that of a Helmholtz resonance. The frequency of the mode based on simulations is 295 Hz [126]. The cyclic process during a single oscillation as observed in previous work on this burner can be broken into 4 parts (see figure 2.6). The parts correspond to the filling of combustion chamber with fresh charge, the combustion of the fresh gas and increase in flame area, a reduction of inlet velocity and lastly the reduction of flame zone area to a minimum before the cycle repeats itself. The time-scale associated with the fresh gas reaching the combustion zone and therefore the maximum heat release is approximately 0.5 times the period of the oscillation for this burner[28]. This corresponds to a convective time-scale of 1.69 ms for the Helmholtz resonance frequency of 295 Hz. An increase in the O₂ concentration causes the flame to move closer to the burner face. The convective time-scale of the fresh charge to the heat release zone must approach this value in order to excite thermo-acoustic oscillations.

An estimate of this can be obtained from the average flow field by calculating the time taken for the gas flow entering the combustion chamber to reach the main combustion zone. An Abel inversion based on cylindrical flame symmetry along the burner axis has been performed to obtain planar heat release information. The figure 5.16 shows the Abel inverted images overlapped with the streamlines of the incoming flow for the three oxidizer oxyfuel flames. The Abel-inverted OH*-chemiluminescence images have been binarized using a threshold of 20 % of the maximum chemiluminescence intensity for all images. The

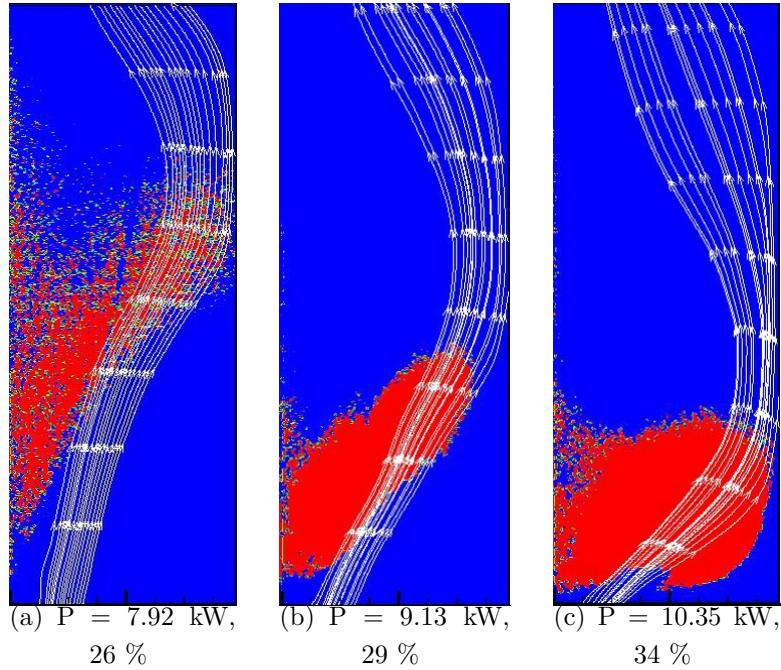


Figure 5.16: Streamlines of average flow emerging from the chamber inlet overlapped (39 mm x 105 mm) with binary Abel inverted OH^* -chemiluminescence image at an inlet velocity of ~ 6 m/s for $\varphi = 0.83$ with different O_2 mole fractions.

convective time delay for the flow from the burner inlet to reach the outer boundary of the binarized heat release zone is calculated for imaginary particles along each streamline. An average of the time-scale for all the stream-lines is then estimated. The table 5.4 shows the time delays calculated for flames with average inlet velocities of 6 m/s and 12 m/s at $\varphi = 0.83$. Also shown is the frequency of thermo-acoustic oscillation as recorded by microphones placed in the combustion chamber. As the oxidizer O_2 concentration increases the time-scale associated with the fresh charge reaching the combustion zone is reduced. The values approach those required for exciting the Helmholtz resonance modes which have been calculated for the burner and combustion chamber geometry [126]. The location of the heat release is dependent on the interaction of flow and chemical kinetics. The parameter that significantly changes in the above configuration is the flame speed due to change in oxidizer. The change in flame speed is primarily responsible for the change in the flame shape and its location which in turn leads to a change in the convective time-scales associated with fresh charge reaching the combustion zone. The time-scale reduces to values that are similar to the time-scales of a Helmholtz oscillation in the burner-combustion chamber system, thereby exciting thermo-acoustic instabilities. It must be noted that this flame is partially premixed, therefore this time-scale also contains effects related to the mixing of the fresh charge and hot exhaust products to form combustible reactants.

Composition	Average inlet velocity (m/s)	Measured Frequency (Hz)	Acoustic time-scale (s)	Convective time-scale (s)
26 % O ₂	6 m/s	-	-	0.0084
	12 m/s	-	-	0.0063
29 % O ₂	6 m/s	-	-	0.0055
	12 m/s	227	0.0022	0.0021
34 % O ₂	6 m/s	243	0.002	0.0014
	12 m/s	293	0.0017	0.0011

Table 5.4: Convective delay times of fresh charge to the heat release zone for 26 %, 29 % and 34 % O₂ flames for $\varphi = 0.83$.

The 29.4 % flame which does not excite thermo-acoustic oscillations at 6 m/s starts exciting thermo-acoustic oscillations at 12 m/s. The flame stabilization under these conditions cause a similar reduction in the convective time-scales to values that correspond to the Helmholtz resonance mode in the system. The frequency of the oscillations increases with an increase in flow rate from 6 m/s to 12 m/s, which is typical for a Helmholtz resonance type of oscillation. The reduced time-scales with an increase in O₂ concentration corresponds well to an increase in the thermo-acoustic frequency. It must be noted that the calculated time-scales are consistently smaller than those estimated from the measured frequency. This is to be expected since the actual fuel nozzle is located below the burner surface by an offset of 4.5 mm. So in reality, the delay of the combustible mixture to the combustion zone is larger than that observed through PIV data that tracks information a few millimeters above the burner surface. Of the different flame compositions the 29.4 % O₂ flame was found to be the least conducive to thermo-acoustic oscillations with this burner. The flame shape was also similar to a typical conical swirl flame. Therefore this flame was the subject of detailed investigations using Raman spectroscopy for specific conditions and high pressure experiments.

5.1.4 Thermo-chemical states of swirl stabilized oxyfuel flames

Detailed information regarding the thermo-chemical state of 30 % O₂ oxyfuel flames in regions such as the inlet flow, IRZ, ORZ, and shear layers was obtained using laser Raman spectroscopy. This has been used to draw comparisons to similar air flames. The operating conditions corresponding to the measurements are shown in table 5.5. The conditions represent the stable conical swirl flame configurations. As seen in section 5.1.1.2 and 5.1.2.3 the effect of the change in equivalence ratio on the flame shape was negligible. Hence, the results can be extended to flames at stoichiometric conditions

5. RESULTS

	Composition	φ	V_{in-avg} (m/s)	Re_{inlet}	Power (kW)	T_{adia} (K)
Flame 1	30 %	0.8	15.5	23770	21.3	1981
Flame 2	30 %	0.76	10.3	15820	14.3	1926

Table 5.5: Conditions of oxyfuel flames with Raman measurements where V_{in-avg} is the average inlet velocity based on diameter of 25 mm, Re_{inlet} is inlet Reynolds number for same diameter, and T_{adia} is adiabatic flame temperature for inlet temperature of 293 K.

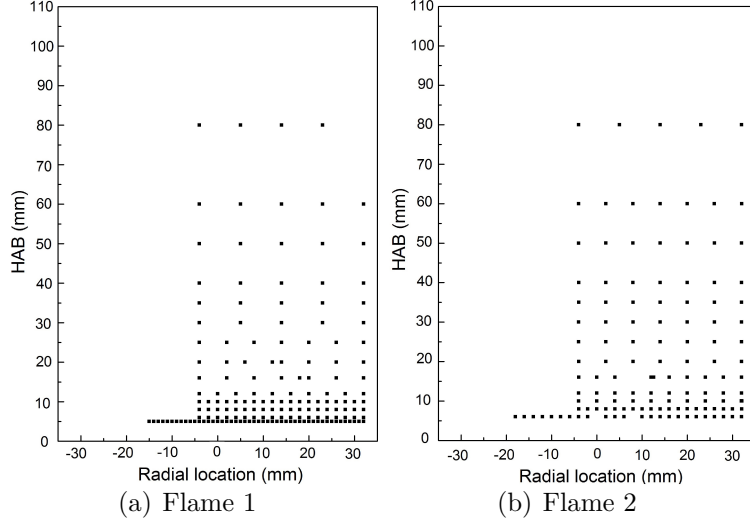


Figure 5.17: Locations in the combustion chamber where Raman measurements have been performed for the oxyfuel flames.

with appropriate consideration to changes in flame behavior documented in the above sections. The experimental setup for these measurements is described in section 3.4.3. The figure 5.17 shows the locations on the combustion chamber symmetry plane where the Raman measurements have been performed. In the following section each of the flames is described in detail.

The temperature, heat release (Abel inverted OH^* -chemiluminescence) and species concentration distributions for half the burner width on the symmetry plane of the combustion chamber are shown in figure 5.18. The averages are from 300 single shot laser measurements. The values correspond to the midpoint of the 1-D Raman probe volume and are Favre averages. The contours are obtained by means of interpolating the point-wise Raman data in OriginLab software. The region of high chemiluminescence (Fig. 5.18(a)) intensity lies in the ISL. The temperatures reach a maximum value in both flames downstream of this zone. There is no fuel in the ORZ and the gas temperatures in it are lower than the maximum combustion temperatures observed in the IRZ. Due to the higher charge flow rate in Flame 1, the fresh low temperature gas is seen to penetrate further into the combustion chamber than Flame 2. As a result maximum flame

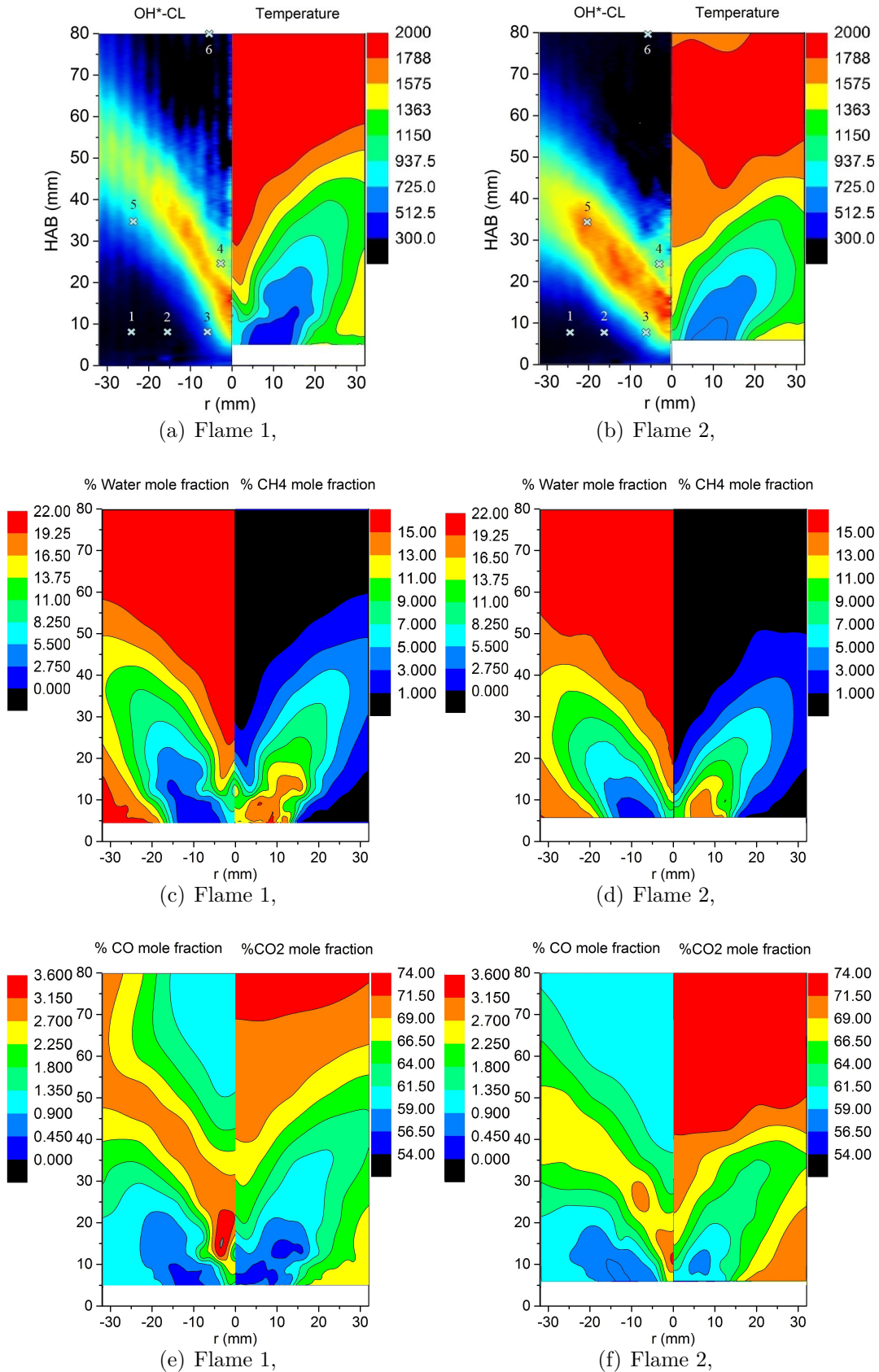


Figure 5.18: Average temperature and species distribution contours for Flame 1 and Flame 2 from Raman measurements (Note: Crosses and numbers in figures 5.18(a) and 5.18(b) represent points for detailed chemical state discussion)

temperatures are reached further downstream for Flame 1 in comparison to Flame 2. The increase in temperature correlates well with the increase in water concentration and reduction in methane concentration in figures 5.18(c) and (d). Oxyfuel flames have significantly higher CO concentrations compared to air flames due to the high CO₂ content and associated thermal dissociation reactions. The equilibrium CO concentrations of air and 30 % O₂ flames at an equivalence ratio of 0.76 are 220 ppm and 1761 ppm respectively. High concentrations of CO are seen in the ISL where the fuel conversion to CO₂ occurs. These values reduce to equilibrium concentrations further downstream. Concurrently the CO₂ concentrations reach their maximum indicating completed combustion. The concentrations of CO are higher for Flame 1 than Flame 2. This is possibly due to the slightly higher equivalence ratio in Flame 1. A more detailed look into the thermochemical state of the gas at different locations in the flame is obtained by relating the mixture fraction to the temperature and composition. The mixture fraction is typically used in non-premixed and partially premixed combustion to discern the mass fraction in a given region originating from the fuel stream. It is an indicator of the mixing of fuel and oxidizer and can be used together with Raman species and temperature information to determine the chemical state of a mixture at a particular location. For hydrocarbon air flames, the C-atoms and H-atoms present in the fuel are used as a reference, and the mixture fraction is obtained by tracking mass conservation of these atoms. However, for oxyfuel flames the C-atom is also present in the form of diluent in the oxidizer. Therefore it is not an accurate reference for the mixture fraction. Instead the H-atom present in methane has been used to determine the mixture fraction. The fraction of hydrogen atoms present at any location in the flame is defined as:

$$Z_{H,flame} = \mu_{H,CH_4} \times X_{CH_4} + \mu_{H,H_2O} \times X_{H_2O} + \mu_{H,H_2} \times X_{H_2} \quad (5.1)$$

where $Z_{H,flame}$ is the mass fraction of hydrogen atoms in the flame, $\mu_{H,Y}$ denotes the molecular weight of hydrogen atoms in a given species Y , whose mole fraction is X_Y . The mixture fraction f is then defined as

$$f = \frac{Z_{H,flame}}{Z_{H,fuel}} \quad (5.2)$$

where $Z_{H,fuel}$ is the mass fraction of H-atoms in the fuel.

The figures 5.19 to 5.21 show the temperature, methane mole fraction and water mole fraction scatter plots of Flame 1 at different locations. The six locations in the flame at which this information has been depicted is shown in figure 5.18(a). The individual points in the scatter plot represent single laser shot results from a gas volume of 0.75 mm length and 0.5 mm diameter from which the Raman signal information has been obtained. Additionally, equilibrium flame compositions for adiabatic conditions have been calculated

for different global mixture fractions to compare the thermo-chemical states. The global mixture fraction is representative of the global flame equivalence ratio and is denoted by the vertical line in the figures. The calculation of equilibrium conditions was performed using the GRI Mech 3.0 mechanism in Cantera software.

The point 1 ($r=24$ mm, $h=8$ mm) is located in the ORZ. The temperature (fig. 5.19(a)) of the gas is 641 K lower than the adiabatic flame temperature. The low temperature in the ORZ is indicative of high heat transfer losses to the burner plate. The gas in this region of the combustion chamber has low flow velocities as seen in the PIV measurements. The consequently higher residence times result in high conductive, convective and radiative heat transfer losses. The radiation heat transfer losses are expected to be high due to CO_2 that is present in large concentrations in the oxyfuel flames. The mixture fraction of the gas in the region corresponds to a slightly leaner composition than the global mixture fraction. This is thought to be caused due the lower proportion of fuel which is entrained into the OSL in comparison to the ISL, which is then recirculated into the ORZ. The gas is predominantly reacted with indications of small quantities of methane present (Fig.5.20(a)). The concentration of the water (Fig.5.21(a)) is close to the equilibrium values, however laterally shifted on the temperature axis due to the low gas temperatures. The lower part of the dotted line showing the mole fraction of water from equilibrium calculations represents the lean branch of flames where temperature and concentration increases with an increase in the equivalence ratio. The temperature reaches a maximum close to stoichiometric conditions, which is followed by lowering of the temperatures for richer conditions where there is an initial increase in water concentration. Point 2 ($r=16$ mm, $h=8$ mm) represents gas in the OSL formed between the ORZ and incoming gas. The gas mixture is significantly leaner than the global mixture fraction indicating large quantities of oxidizer in this region (Fig.5.19(b), depicted by vertical line). The temperature of the gas is in the range of 350 K to 1500 K and is lower than the adiabatic flame temperatures for corresponding mixture fractions. The difference in temperature to adiabatic flame temperature increases as the global mixture fraction is approached, indicative of an interaction with low temperature burnt gases from the ORZ. The richer samples of gas are predominantly at a lower temperature pointing to non-reacted methane from fresh gas in the region. The methane concentrations (Fig.5.20(b)) are quite low in this region and the mixture composition corresponds well with the average methane concentration shown in figure 5.18(c). The proportion of water represents (Fig.5.21(b)) a range of gas states where almost pure oxidizer with no water is present together with burnt gas having almost equilibrium concentrations of it. The range of concentrations replicate the states of the gas as seen in the temperature plot and is suggestive of an intense mixing of burnt gas possibly from the ORZ and unburnt fresh charge. The point 3 ($r=6$ mm, $h=8$ mm) is located in the ISL. The temperature of

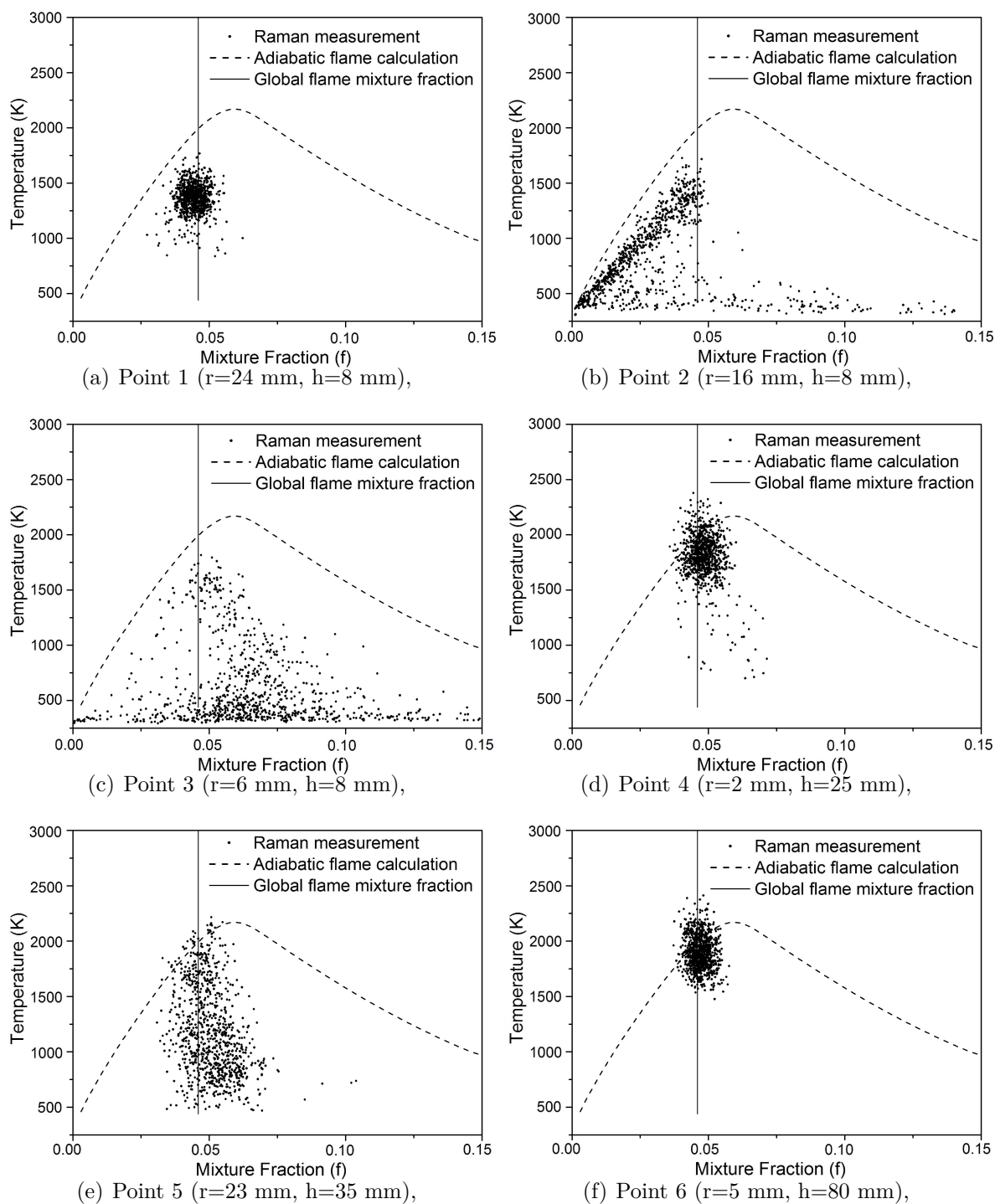


Figure 5.19: Scatter plots showing Temperature of gas mixture in Flame 1 at different locations.

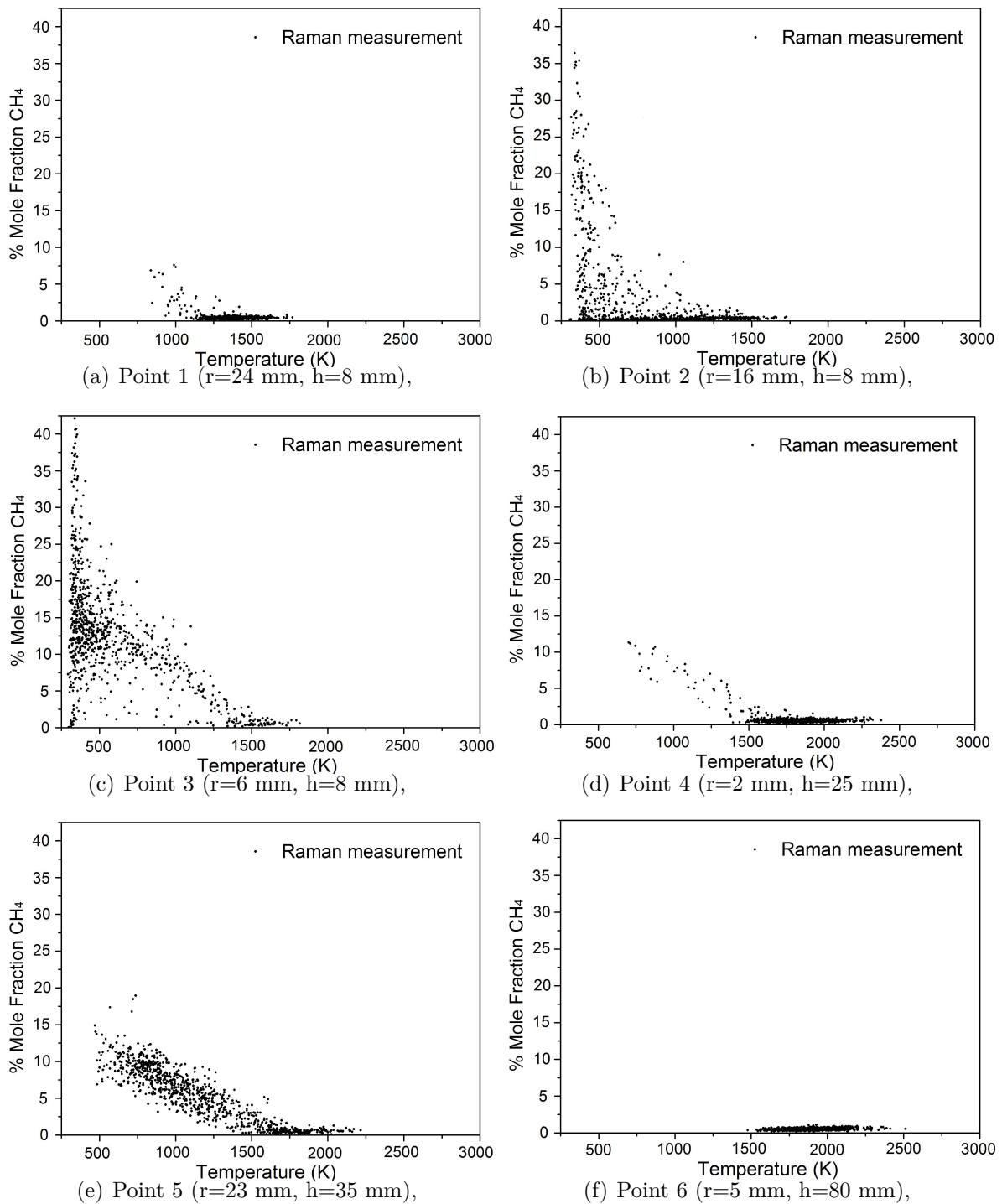


Figure 5.20: Scatter plots showing distribution of methane concentration in gas for Flame 1 at different locations.

5. RESULTS

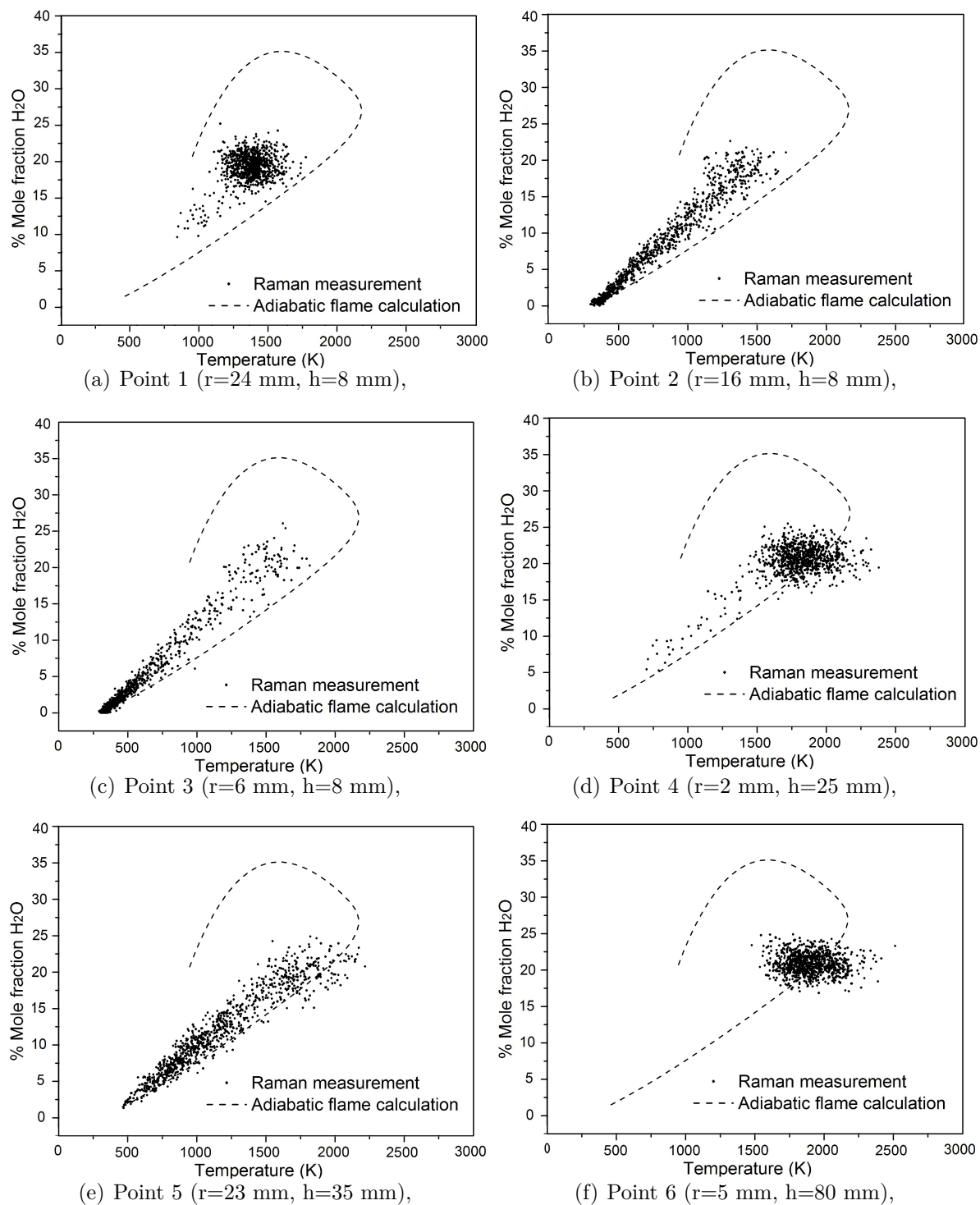


Figure 5.21: Scatter plots showing distribution of water concentration in gas for Flame 1 at different locations.

the gas in this region is largely under 1000 K (Fig.5.19(c)) and its composition shows a low temperature fuel rich mixture (Fig.5.20(c)). The gas is considerably richer than that in the OSL described at point 2 indicating that a large portion of the incoming fuel is entrained into this region. The existence of instances of temperature in the range of 1500 to 1700 K suggests the presence of burnt gas, which is also seen in the small quantities of water shown in figure 5.21(c). The large scatter in the composition and temperature is indicative of an active mixing of fuel and oxidizer in the region.

Point 4 ($r=2$ mm, $h=25$ mm) represents a point in the IRZ. The average temperatures (Fig.5.19(d)) here are lower than the adiabatic flame temperature by 250 K. The mixture fraction is slightly richer than the global mixture fraction. The quantity of fuel in the region is almost negligible indicating that mostly reacted gas is present. The water concentration in the region corresponds well to that from the adiabatic concentrations. However, the temperature of the gas is slightly below the adiabatic values. This is thought to be caused due to the high concentrations of CO which were observed in this region as shown in figure 5.18(e). The maximum flame temperatures were measured in locations further downstream where the CO is completely combusted. Point 5 ($r=23$ mm, $h=35$ mm) is located near the region of high OH*-chemiluminescence intensity. The temperature distribution in figure 5.19(e) points to the presence of a well mixed charge at intermediate states of combustion progress with a composition close to the global mixture fraction. The transition from mixed reactants at low temperature to combusted products is also evident in the methane concentrations shown in figure 5.20(e). The methane concentration lies between 0 to 15 % unlike points 2 and 3 where the concentrations range from 0 to 40 %. The concentration reduces almost linearly with temperature denoting the reaction progress. The water concentration (Fig.5.21(e)) is also seen to increase with the temperature. This region represents the core zones where the turbulent mixing and reaction of the gases occur to form combusted products. Point 6 ($r=5$ mm, $h=80$ mm) is located further downstream where no further heat release is detectable. The temperature, methane and water concentrations correspond very well to the expected equilibrium values. The scatter in the mixture fraction and temperature stems from the uncertainty associated with the statistical nature of the Raman scattering process which has been discussed previously.

For Flame 2 the figure 5.22 displays the temperature scatter plots for the same locations as in Flame 1. The average flow velocity for this flame is 66 % lesser and the equivalence ratio is slightly leaner than Flame 1. In the ORZ (Point 1, $r=24$ mm, $h=8$ mm) there is mostly high temperature gas similar to that in Flame 1. The methane and water concentrations (not shown) indicated the presence of burnt gas as in Flame 1. The temperature in the ORZ is 505 K lower than the adiabatic flame temperature. At the same location in Flame 1 the gas temperature was 621 K lower than the adiabatic flame

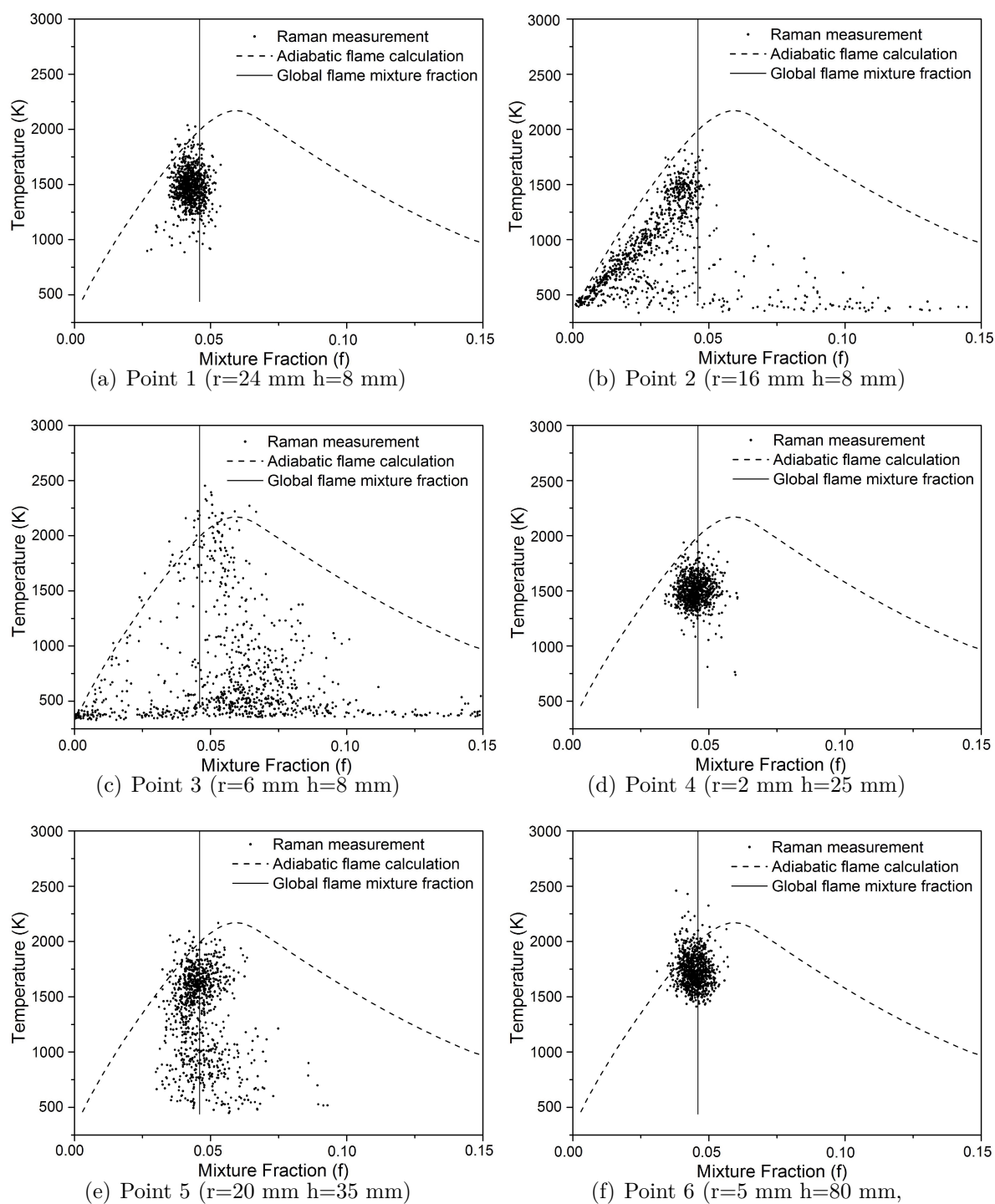


Figure 5.22: Scatter plots showing the temperature of gas mixture in Flame 2 at different locations.

temperature. The reduced temperature difference to adiabatic conditions in this flame is possibly caused due to the higher proximity of the flame to the burner face in comparison to Flame 1. The consequent heat transfer to the burner plate might assist in shifting the state of thermal equilibrium to higher temperatures in comparison to Flame 1. A comparison to air flames performed in the next section further highlights this difference. At point 2 ($r=16$ mm, 8 mm) in the OSL, the composition of the gas (Fig.5.22(b)) is very similar to that at a similar location in Flame 1. The gas consists of a lean mixture of predominantly burnt gas with traces of fresh gas. The gas in the ISL (Point 3, $r=6$ mm, $h=8$ mm) as shown in figure 5.22(c) has mostly an unreacted fuel rich mixture again bearing a strong similarity to that in Flame 1. At point 4 in the IRZ gas temperature is around 445 K lower than that at equilibrium conditions. The water composition was seen to be close to equilibrium concentrations and there was almost no fuel detected here. In this region of the flame a significant amount of CO was observed (see Fig.5.18(f)), which is completely combusted further downstream. The temperatures in this region of the IRZ and further downstream are lower in comparison to Flame 1 (see Fig. 5.18(b)). An alteration in the heat transfer characteristic of this flame in comparison to Flame 1 is thought to cause this behavior. This is discussed further below in the comparison with air flames. The Point 5 is located in a region of high OH^{*}-chemiluminescence intensity indicating high heat release and temperature in the flame. In comparison, the OH^{*}-chemiluminescence intensity was lower in Flame 1 at the same location. The scatter plot in figure 5.22(e) reflects the chemical state of the gas in this region. A majority of the samples detected contained high temperature gas suggestive of burnt products correlating with the high OH^{*}-chemiluminescence intensity detected. However there is also a significant quantity of gas that is not completely reacted. This point is indicative of a region of transition of fresh gas to burnt products with a greater proportion of reacted gas present than at a similar location in Flame 1. The lower flow velocities in this flame in comparison to Flame 1 shift the heat release zone closer to the burner face resulting in a larger proportion of the gas having combustion products. At Point 6 the gas contains mainly burnt products. The temperature of the gas is lower than the equilibrium temperature by around 150 K unlike that in Flame 1. The flow velocity and thermal power of this flame is lower than that of Flame 1. Heat losses can be expected to be accentuated in oxyfuel flames due to the presence of CO₂. The lower flow velocities in Flame 2 increases the residence time of the flow in the combustion chamber and is thought to increase heat loss from the burnt gas to the combustion chamber leading to lower gas temperatures in the products further downstream. The lower combustion gas temperatures further downstream result in lower temperature gas being recirculated to the flame zone through the IRZ. This combined with the partial oxidation of the fuel to CO explains the larger temperature difference to equilibrium conditions seen at point 4.

The Raman spectroscopy results show that the chemical state of the gas in the OS� and ISL remains quite similar for both flames. The gas in the IRZ is also seen to be in a state of transition from fresh gas to burnt products in both flames and contains significant amount of CO. A reduction in the flow velocity and thermal power influenced the temperatures in the IRZ and ORZ. In both flames the temperatures in the ORZ were significantly lower than the equilibrium values pointing to large heat transfer losses caused possibly due to the presence of CO₂. The temperature reduction in the ORZ was reduced for Flame 2 which burned at closer proximity to the burner. However, the higher temperatures in the ORZ concurred with the presence of lower temperatures in the IRZ indicative of higher heat loss in the burnt products caused possibly due to increased residence time at lower flow velocities. The change in heat transfer characteristics of oxyfuel flames due to change in flow velocities and the presence of CO₂ needs further investigation. In the following section a detailed comparison of air and oxyfuel flames is performed.

5.2 Comparison of air and oxyfuel flames at atmospheric pressure

The study so far has shown that the type of oxidizer used in oxyfuel burners determines the flame stabilization obtained, and this can vary considerably. In this section comparisons are drawn between oxyfuel flames and air flames studied with the same burner in order to find similarities and differences in the flame behavior. The comparison is non-trivial as it must take into consideration the difference in physical and chemical properties of air and the different oxyfuel mixtures. To begin, the change in flame shape when operating the burner with air and oxyfuel mixtures at similar conditions is looked into. The thermo-chemical states of the air flames and reference oxyfuel flames are compared.

The figure 5.23 illustrates the change in flame shape of air flames and oxyfuel flames at similar flow conditions. The images of air flame correspond to visible flame luminescence, while that of oxyfuel flames are from line of sight OH*-chemiluminescence. A 85 mm x 110 mm section of the combustion chamber is shown. The change in flame shape at different equivalence ratios for the air flames resembles the behavior due to change in oxidizer dilution of oxyfuel flames. This similarity is based on the change in three parameters which are the change in reactivity, mixing and total volume flow rate of oxidizer (air and O₂/CO₂). For oxyfuel flames the reduced CO₂ dilution enhances reactivity, as does the increase in equivalence ratio for air flames. For the air flames the volume flow of the air is reduced, while for oxyfuel flames the CO₂ dilution reduces. Lower flow velocities and higher reactivity assists flame stabilization closer to the burner face. As in the case

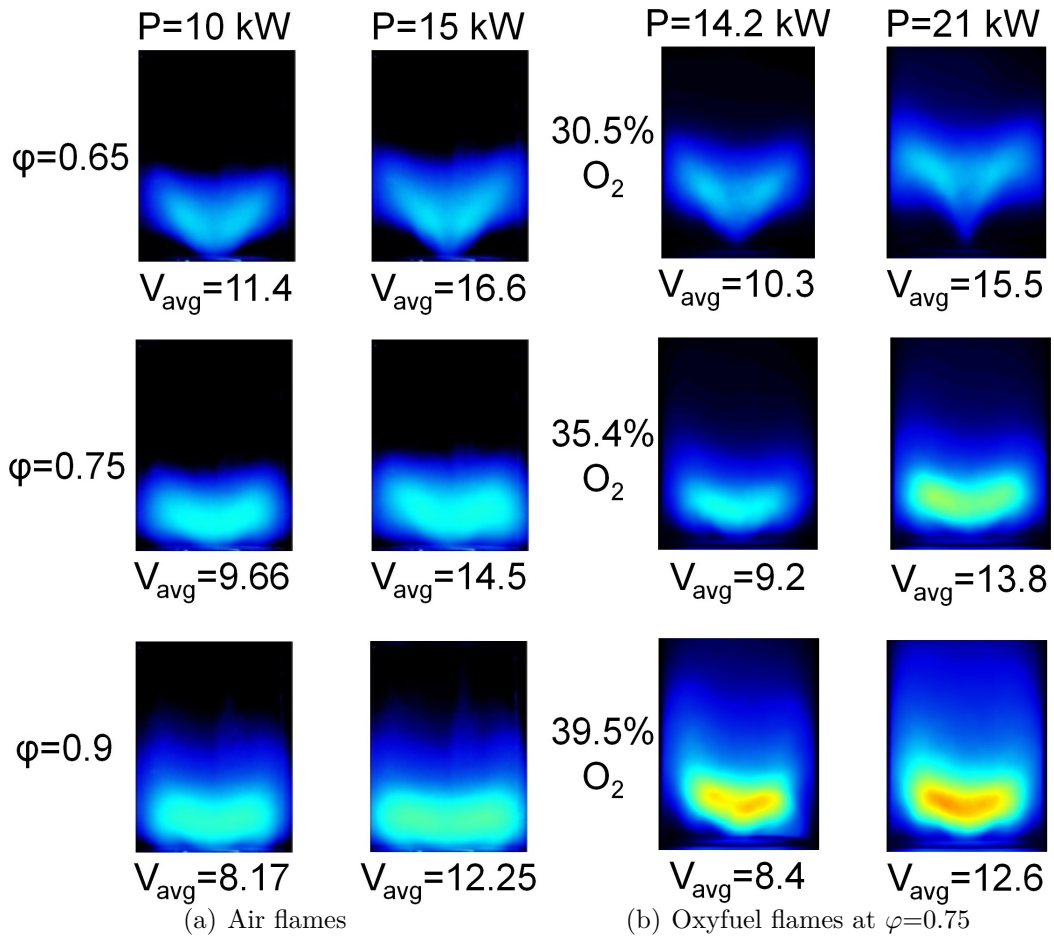


Figure 5.23: Comparison of air (visible flame luminosity) and oxyfuel (OH^* -chemiluminescence) flame behavior.

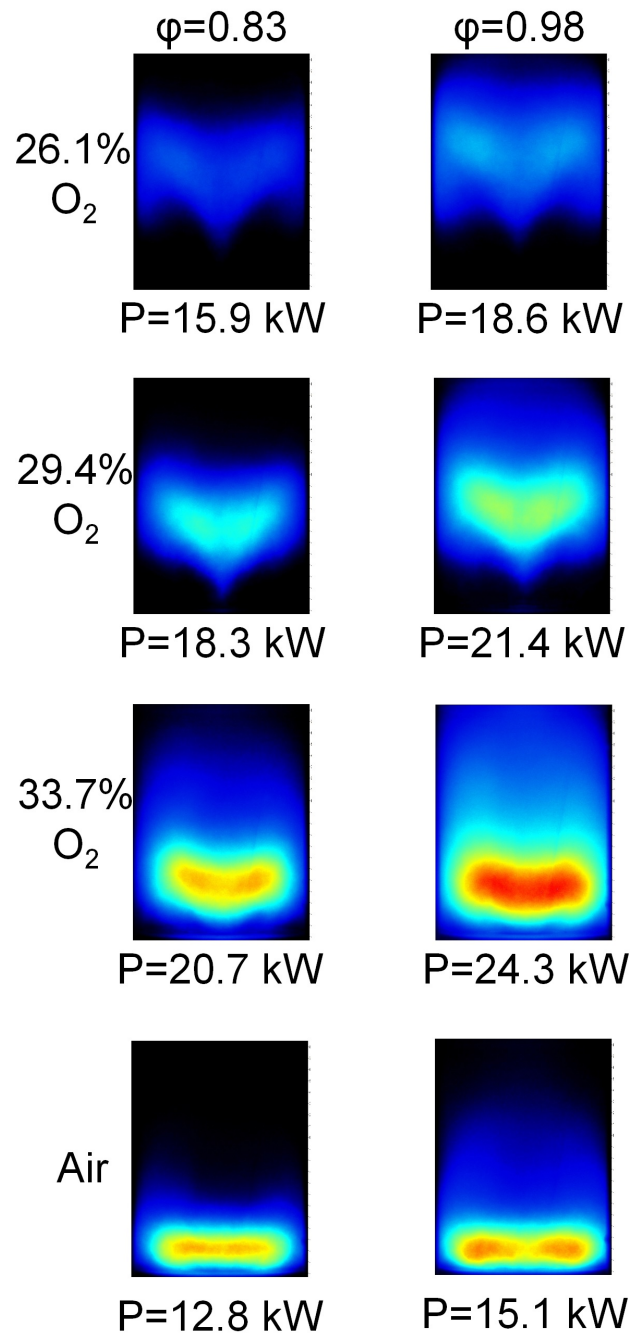


Figure 5.24: Comparison of oxyfuel and air flame behavior at average inlet flow velocity of 12 m/s using averaged OH*-chemiluminescence images.

of oxyfuel flames, the movement of the flame close to the burner face results in thermoacoustic oscillations for air too. The frequency of these oscillations are shown in figures 4.2. The figure 5.24 shows another comparison of average OH*-chemiluminescence images (200 short exposures) of oxyfuel and air flames for the same equivalence ratios at an inlet flow velocity of 12 m/s. The proximity of the flame to the burner face increases with O₂ concentration and is the highest for air flames. Air flames are similar to oxyfuel flames having higher than 34 % O₂ concentration. The air flame also excited thermo-acoustic oscillations whose frequency was higher than that of the oxyfuel flames. The reactivity of oxyfuel flame mixtures approaches that of air flames as the quantity of CO₂ dilution is reduced. The figure 5.25 illustrates this by comparing premixed laminar flame speeds of different methane-oxyfuel flames compositions to methane air flames. The laminar flame speeds are at 1 atm and 298 K reactant temperature. The experimental measurements depicted as points are from Dong [127] and Vagolopoulos [128]. The methane-air simulation values from Dong using a GRI-Mech 3.0 are shown. Laminar flame speed calculations for oxyfuel oxidizers containing different proportions of O₂ are also shown. A methane mechanism (RD-v06-NGQ) developed and validated at DLR Stuttgart has been used [3, 74] for the calculations. For the oxyfuel mixtures containing 26 % O₂ the laminar flame speed is less than that of lean air flames ($\varphi \leq 0.6$). The laminar flame speed of stoichiometric 30 % O₂ flames approaches that of air flames at $\varphi=0.65$. Similarly, the stoichiometric flame speeds of 34 % O₂ and 38 % O₂ oxyfuel flames are similar to that of air at $\varphi=0.8$ and $\varphi=0.9$. The change in flame shape correlates well to the change in chemical behavior. However, it must be kept in mind that due to the different densities of the oxyfuel oxidizers, the mass flow rates and corresponding thermal powers of the air and oxyfuel flames are different. This means that the quantity of fuel being supplied to the burner and hence mixing is different. The higher O₂ concentration in the oxyfuel mixtures in comparison to air results in a scaling up of the thermal power for the same equivalence ratio and average inlet flow velocity. This consequently influences the relative momentum of the oxidizer and fuel, as well as their velocity ratios, which alter the mixing processes at the inlet of the flow into the combustion chamber. For the above conditions, the momentum and velocity ratio between the air and fuel streams was calculated and is shown in figure 5.26. The average flow velocity used for the estimation was based on the neck diameter of the outer swirl nozzle for the oxidizer, while the fuel flow velocities were calculated based on the area of fuel injection. The momentum ratio of the air flames is the highest and it reduces as the O₂ concentration in the oxyfuel oxidizers is increased. The higher density of oxyfuel oxidizers due to the presence of CO₂ increases the oxidizer momentum, however since the concentration of O₂ is higher in such oxidizers compared to air the quantity of fuel increases accordingly for a given equivalence ratio. The resultant momentum and velocity ratios are lower than that of air flames and reduce as the

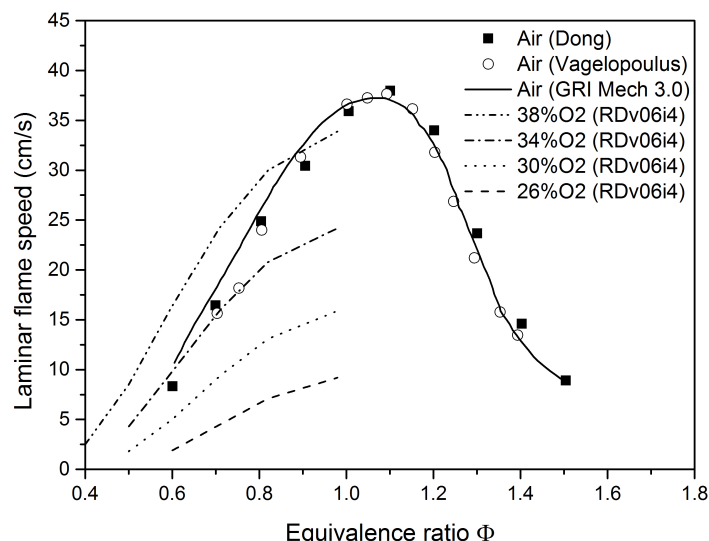


Figure 5.25: Premixed laminar flame speeds of methane mixtures with air and oxyfuel at 1 atm at 298 K.

O_2 concentration is increased. The 26 % O_2 flames have momentum and velocity ratios comparable to that of the air flame. The reduced reactivity of such flames in comparison to air however points to difficult conditions for stabilization closer to the burner face as seen by the flame stabilization further downstream for such flames. Extinction events related to flame stretch might play an important role in flame stabilization for oxyfuel flames with low O_2 concentrations due to the reduced reactivity. As the O_2 concentration increases for the oxyfuel flames the momentum and velocity ratios decrease and the flames move closer to the burner face. The mixing of fuel and oxidizer is therefore not as critical as the chemistry. The Raman measurements illustrate this in further detail.

The figure 5.27 compares the temperature fields for the oxyfuel Flames 1 and 2 discussed in section 5.1.4 to the air Flames A and C from section 4.2. The images have been normalized to the maxima of the respective quantities for the comparison. The flame conditions are not similar, however the flame shapes exhibited are typical to swirl stabilized flames. The relative behavior of the air and oxyfuel flames can therefore be compared. The premixed laminar flame speeds of air flames at $\varphi=0.65$ are comparable to that of $\varphi=0.75$ and 30 % O_2 flames. The average flow velocity for Flame A is nearly 4 times that of Flame C. The region of high OH^* -chemiluminescence (red colour) and hence heat release is concentrated in a small region (in Abel inverted OH^* -chemiluminescence half-images) with a radial extent for Flame C of nearly 20 mm and extending to a height of around 30 mm. This corresponds well with the temperature and water distributions in the IRZ which contains mostly burnt gas. The maximum temperatures are reached at a height of 58 mm for Flame A and around 44 mm for Flame C. The high temperature burnt gas is present in the flame root and is expected to assist flame stabilization.

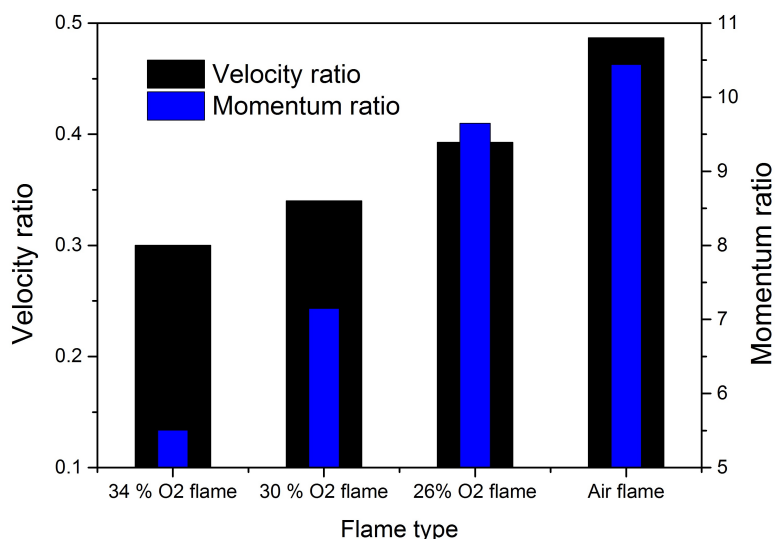


Figure 5.26: Oxidizer to fuel momentum and velocity ratios at flow entry into the combustion chamber for different flames in figure 5.24

The fuel has been largely consumed along the burner axis for both flames. Both flames maintain this character despite the different flow conditions and thermal loading.

The oxyfuel flames are operated at richer conditions in comparison to the air flames. The volume flow rate of both oxyfuel flames is lower than that of Flame A. The flow rates of Flame 2 and Flame C are however comparable. The Abel inverted OH*-chemiluminescence of the oxyfuel flames is quite different to that of the air flames. In contrast to the concentrated high intensity region seen near the flame base in the air flames, the OH*-chemiluminescence intensity here is distributed over a larger region for both flames. The IRZ of Flame 1 has high temperatures which do not extend to the flame base as in the case of the air flames. The fuel concentrations in both oxyfuel flames extend much further downstream than those of the air flames indicating that the consumption is slower. This is suggestive of poorer flame stabilization as a result of slower chemistry. The effects of heat transfer in the case of CO₂ for oxyfuel flames are detectable in the ORZ. For Flame A it is seen that the normalized temperatures in the ORZ are higher than those in Flame C. These differences in temperatures are thought to be caused due to changes in heat transfer accompanied by change in flow conditions. As the flow velocities reduce from Flame A to Flame C the residence times increase which facilitate cooling of the gases in the ORZ due to increased heat loss. The relative heat loss for Flame C is also lesser compared to Flame A due to the reduced thermal power. In the case of oxyfuel flames the reduction of velocities from Flame 1 to Flame 2 has an opposite effect on the temperatures in the ORZ with an increase in temperature with increased residence times. The heat conductivity of the oxyfuel mixtures is lower as the heat conductivity of CO₂ is lower than that of N₂ in air. The contrasting behavior of the air and oxyfuel flames is

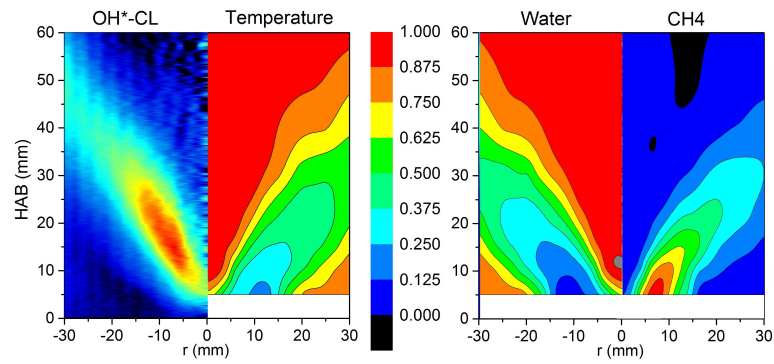
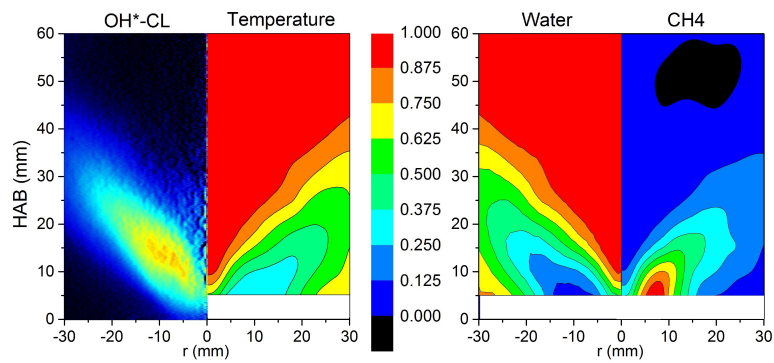
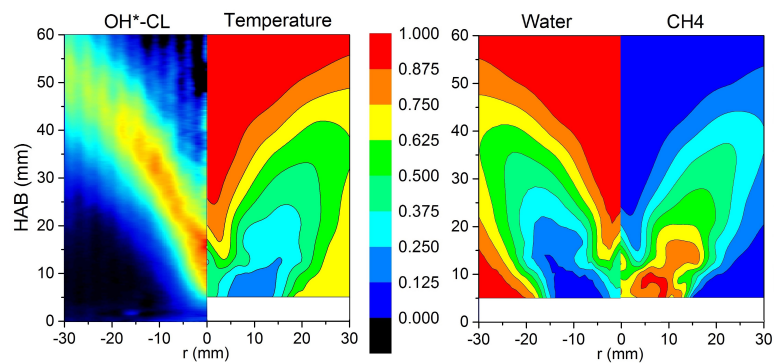
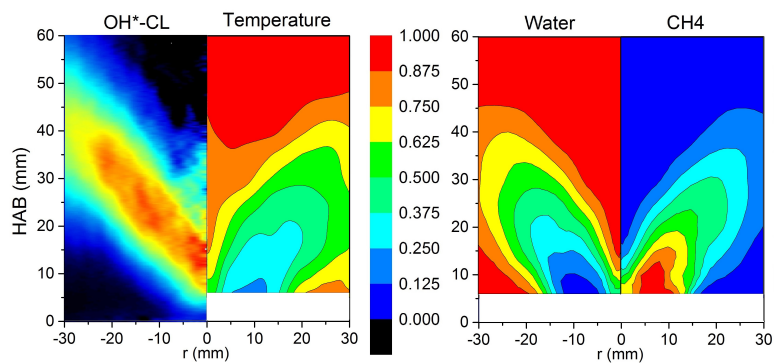
(a) Flame A (Air, $\varphi=0.65$)(b) Flame C (Air, $\varphi=0.55$)(c) Flame 1 (Oxyfuel, 30 % O₂, $\varphi=0.8$)(d) Flame 2 (Oxyfuel, 30 % O₂, $\varphi=0.76$)

Figure 5.27: Comparison of oxyfuel and air flames using Raman spectroscopy information from different flames on symmetry plane of swirl burner.

suggestive of a change in the balance between conduction, convection and radiative heat transfer that occurs close to the burner due to the presence of CO₂. Increased radiation heat transfer to the burner face plate due to proximity of flame zone combined with the reduced flow velocities in the ORZ and the presence of CO₂ is thought to shift the equilibrium temperature to higher values. A more detailed study is however required to better understand the nature of this behavior.

Although both the air and oxyfuel flames here show a typical conical flame shape, the flame stabilization of the 30 % oxyfuel flames is poorer. The premixed laminar flame speeds of the lean air flames ($\varphi=0.6$ to 0.7) and 30 % O₂ ($\varphi=0.75$ to 0.8) oxyfuel flames are comparable. The better stabilization of air flames despite this chemical similarity can be explained through the differences in charge characteristics in the flame base. The partially premixed nature of these flames means that the charge present in the flame base can be richer or leaner than the overall equivalence ratio. The premixed laminar flame speeds of air operation increase by 3.5 times from lean condition of $\varphi=0.6$ to $\varphi=1.0$. In comparison any sort of inhomogeneities in charge preparation contribute to only a factor of 1.7 increase in laminar flame speeds for the oxyfuel flame. The 30 % oxyfuel flames are hence unable to exploit the advantage traditionally associated with partially premixed and diffusion flame stabilization as used for air. The increased O₂ concentration in oxyfuel flames results in a scale up of burner thermal power and flame movement closer to the burner face. The consequently larger fuel quantity and lesser flame speeds make combustion conditions difficult at the flame base. Depending on the eventual O₂ concentration used in a real application these effects suggest the use of burner scaling and alternate mixture preparation for suitable flame stabilization. A more detailed discussion of this together with recommendations from the elevated pressure measurements is presented in the conclusions. The following sections look into this comparison of oxyfuel and air flames under conditions of preheating and elevated pressures.

5.3 Difference between atmospheric pressure and elevated pressure burner

Before the results pertaining to the high pressure experiments on the burner are discussed, in this section the differences in the operating characteristics between the atmospheric and high pressure burner are highlighted. The burners have been described in detail in section 3.1. It must be noted that in case of the high pressure burner approximately 16 % of the oxidizer flow is directed to the back of the burner face plate through impingement holes. The flow cools the face plate at the high thermal loading and elevated pressure.

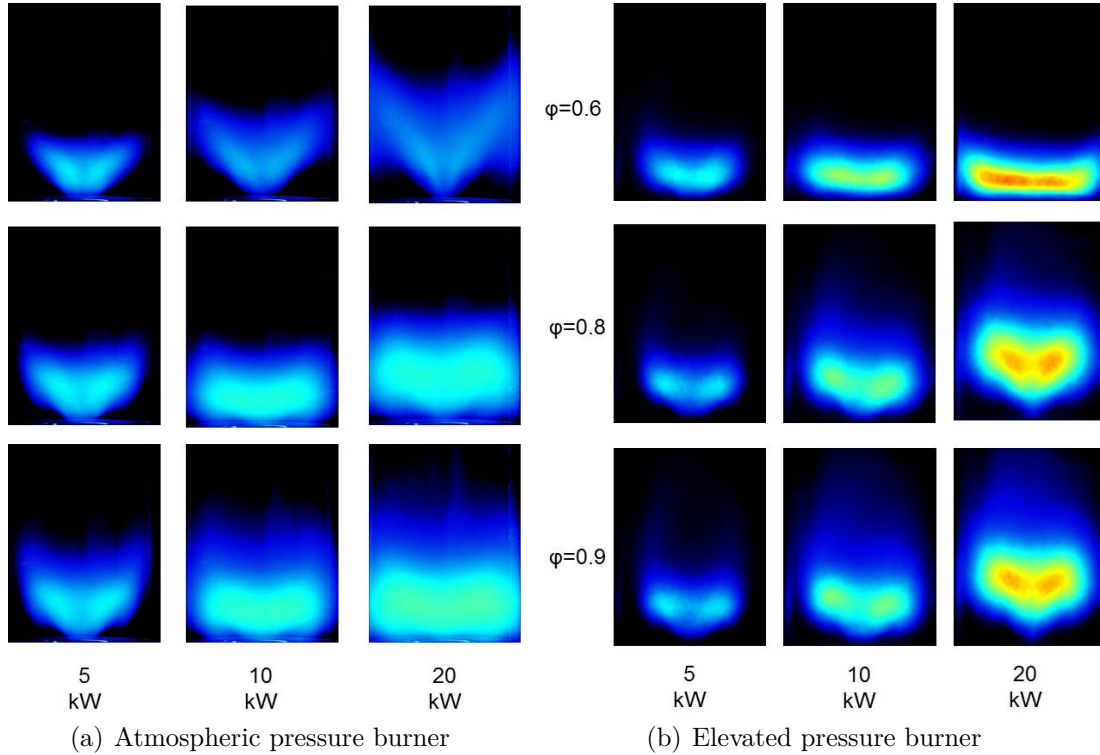


Figure 5.28: Methane-air flame stabilization at similar operating conditions using the two burners at atmospheric pressure conditions and 300 K gas inlet temperature.

This cooling flow is then re-introduced into the combustion chamber axially through a 1 mm slit along the perimeter of the chamber. In order to obtain the difference in flame stabilization images were obtained for comparable flow conditions in both burners using CH_4/air flames. The figure 5.28 shows the change in flame shape for different operating conditions. The equivalence ratio is representative of the overall flame conditions. The images for the atmospheric burner are photographs of visible flame luminosity and that for the elevated pressure burner are from OH^* -chemiluminescence.

The most significant difference in the burners is for flames which are operated at the lean overall equivalence ratio of 0.6. The flames in the atmospheric burner are conically shaped, while those in the high pressure burner are flat. For the thermal power of 5 kW the flame is conically shaped in both burners and remains similar for all equivalence ratios. At 10 kW however contrasting effects are seen in the atmospheric and elevated pressure burners. The flames in the atmospheric burner change from conically shaped to a flat flame shape at higher equivalence ratios, while the opposite effect is seen in the elevated pressure burner. This behavior remains similar for the 20 kW flames. Through the use of a portion of the flow for impingement cooling, the primary combustion zone in the elevated pressure burner is richer. The flames at $\varphi = 0.6$ in the elevated pressure burner have a similar equivalence ratio in the primary combustion zone to that in the atmospheric pressure burner at $\varphi = 0.8$. The flames in the elevated pressure burner are therefore

similar in character to that in the atmospheric pressure burner for correspondingly leaner equivalence ratios. For flames with $\varphi = 0.8$ and $\varphi = 0.9$ the richer primary combustion zone in the elevated pressure burner means that a new region of flame stabilization for the burner is achieved where the flames are conically shaped. In the following section the results from the investigations on the high pressure burner for investigation with oxyfuel and air flames at elevated pressures are presented.

5.4 Oxyfuel and air flames at elevated pressures

The oxyfuel flames investigated at atmospheric conditions showed a conical flame shape and thermo-acoustic free stabilization for 29-30 % O₂ in comparison to other compositions. The laser Raman spectroscopy results showed lower temperatures in the IRZ and flame base pointing to lower reactivity of such mixtures in comparison to air despite a similar flame shape. Before one considers using such oxidizers in a real gas turbine the influence of operating such a burner closer to actual gas turbine conditions needs to be investigated. In this section the results of oxyfuel and air flame investigations at elevated pressures of 5 bar are presented. The burner has been modified for high pressure operation and the differences to the original burner have been discussed previously. Under gas turbine like conditions the oxidizer entering the burner is at a higher temperature and pressure due to the compression process. To simulate this, the HIPOT test rig described in section 3.1.2 has been used. It must be noted that the experiments were no longer performed with pure methane, but commercial natural gas.

In this section, firstly the effect of oxidizer preheating and pressure rise are described to associate with the results at atmospheric conditions. A comparison of air and oxyfuel flame behavior at elevated pressure is then presented. The flames exhibited a rather unconventional flame structure and thermo-acoustic oscillations over a large operating range. Hence, the focus is subsequently directed to understanding the flow phenomena observed and draw relevant comparisons between air and oxyfuel flames under similar operating conditions. High repetition rate laser diagnostics were used to understand the complex flame dynamics. The 30 % O₂ oxyfuel flame and air flames have been employed for the detailed investigation.

5.4.1 Effect of preheating and elevated pressure

The oxidizer was heated up to 653 K and the operating pressure was 5 bar. The figure 5.29 shows the influence of an increase in the inlet temperature and pressure on the flame shape for a flame with a power density of 30 kW/bar. The images are of OH*-chemiluminescence intensity averaged over 200 short exposures for 30 % O₂ oxidizer

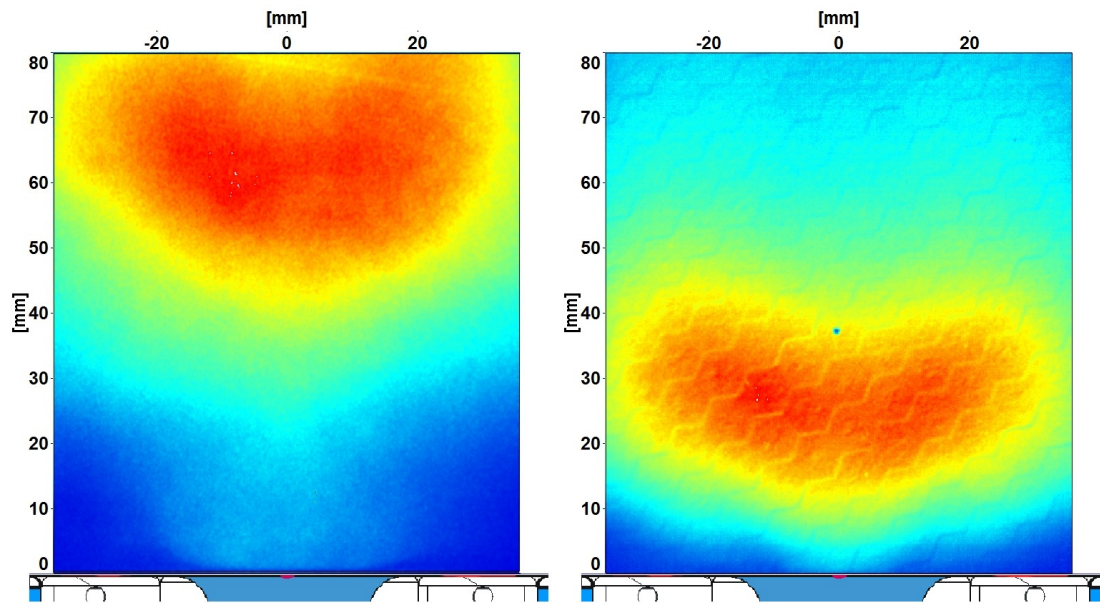
oxyfuel flames at an overall $\varphi = 0.95$. The natural gas composition for these flames is shown in table 5.6. The natural gas flame in figure 5.29(a) corresponds to composition 1, while the flames 5.29 (b) and (c) correspond to composition 2. The influence of the natural gas composition on the flame shape was found to be negligible. As the oxidizer preheat temperature is increased the flame moves closer to the burner face, despite an increase in the average inlet velocity. An increase in temperature from conditions in figure 5.29(a) to figure 5.29(b) involves a change in an inlet velocity of 2.03, while calculations using the mechanism described in section 5.2 showed a laminar flame speed increase by a factor of 3.5. For experiments under atmospheric conditions it has been observed that an increase in flow velocities caused the flames to be shifted downstream. Here the increase in velocity is accompanied by increased reactivity due to high preheat temperatures. This assists flame stabilization for similar velocities closer to the burner face in a similar manner to the increase in oxidizer O_2 concentration seen before. The shape of the flame is therefore similar to the lifted flat flames observed under atmospheric conditions. These flames were also seen to excite thermo-acoustic instabilities.

When the pressure is increased from 1.5 bar to 5 bar for similar average inlet velocity, the main region of heat release shifts even closer to the burner surface. Unlike the preheated flame at 1.5 bar the main region of heat release is no longer typical. The conical region of heat release in the ISL is replaced by a more open flat flame region. Although at first these flames appear to be of a similar nature to the flat flames observed in the burner at atmospheric pressure, closer examination revealed another flame character. The flames' heat release occurred at close proximity to the burner window in this case, unlike the flat flames observed before. The IRZ also appeared wider than that in the atmospheric pressure flat flames. All three flames discussed here excited thermo-acoustic oscillations at 101, 270 and 282 Hz respectively.

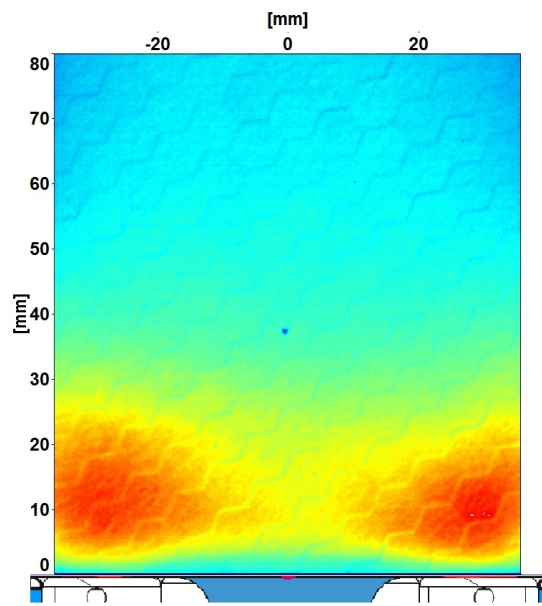
The flame shape at elevated pressures undergoes a significant change compared to that observed at atmospheric conditions. At atmospheric conditions the flat flames burned close to the burner face exciting thermo-acoustic oscillations. An attachment to the burner face and combustion chamber windows was not observed. The flames here in contrast displayed this behavior forming what is known as a wall jet type of flame [23]. This change in flame character was examined with air flames to form a comparison of burner characteristics for the two types of oxidizer and is the subject of the next section.

5.4.2 Effect of change in thermal power and equivalence ratio for air and 30 % O_2 oxyfuel flames

The unconventional flame shapes obtained under high pressure conditions were further investigated and compared to air flames for similar average inlet flow velocities and equiv-



(a) Preheat=321 K, $p=1.5$ bar, $V_{avg}=15.46$ m/s, Power=44.8 kW
 (b) Preheat=653 K, $p=1.5$ bar, $V_{avg}=31.6$ m/s, Power=44.8 kW



(c) Preheat=653 K, $p=5$ bar, $V_{avg}=31.6$ m/s, Power=150 kW

Figure 5.29: 30 % O_2 oxyfuel flames at $\varphi = 0.95$ showing the effect of change in preheating ((a) and (b)) as well as the effect of increase in pressure ((b) and (c)) of operation.

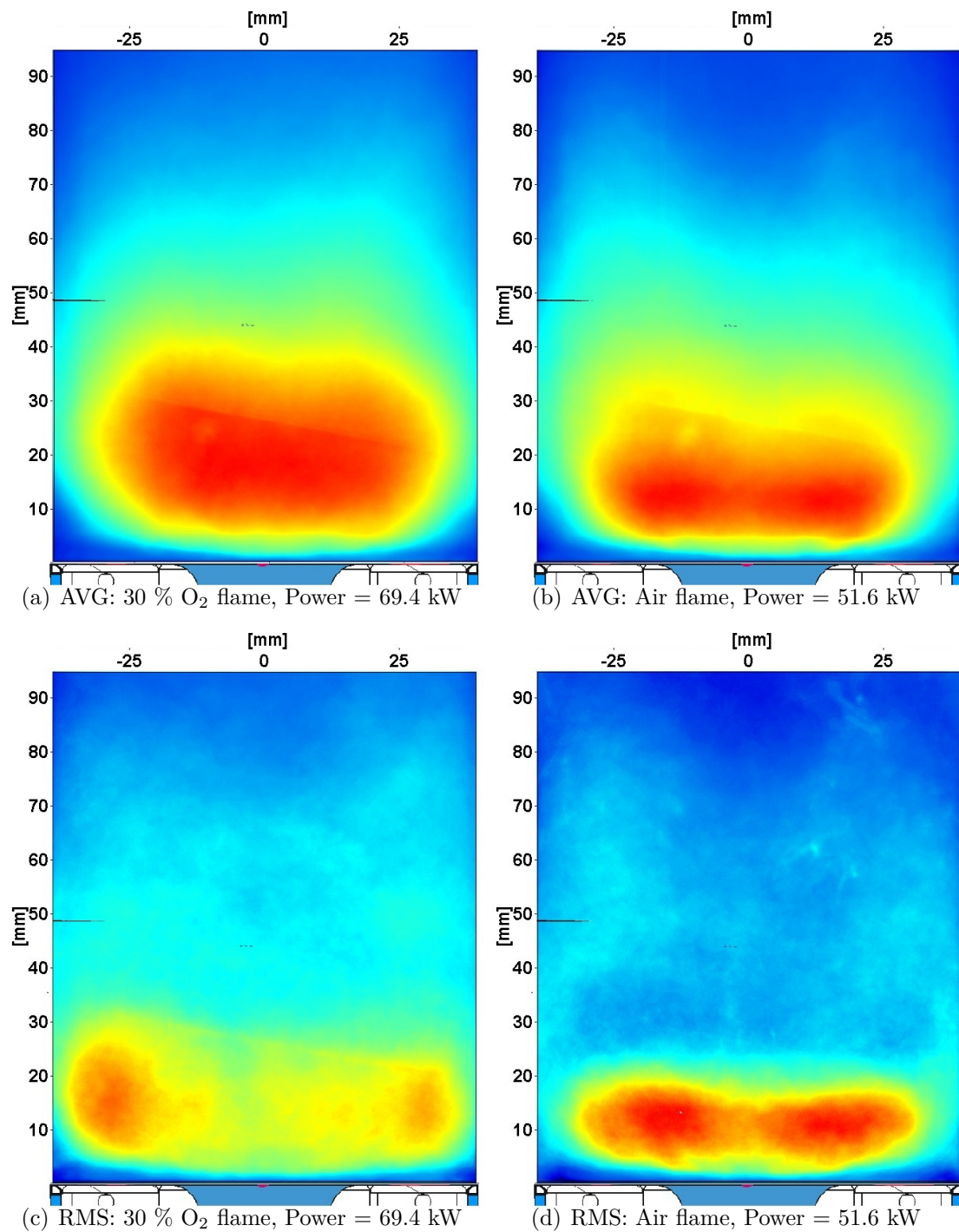


Figure 5.30: Average and RMS images of 200 short exposure OH*-chemiluminescence for oxyfuel and air flames under similar conditions at elevated pressure (5 bar) for $\varphi=0.87$ and $V_{avg} \approx 16$ m/s.

	CH ₄	C ₂ H ₆	C ₃ H ₈	N ₂	CO ₂
Composition 1	90.80 %	4.27 %	1.05 %	2.44 %	1.41 %
Composition 2	92.63 %	3.06 %	0.75 %	1.21 %	0.97 %
Composition 3	95.28 %	2.90 %	0.61 %	0.99 %	0.82 %

Table 5.6: Composition of natural gas for high pressure experiments.

alence ratios. In this section OH*-chemiluminescence intensity recordings from 200 short exposure images are discussed. The flames were investigated at overall equivalence ratios of 0.87 and 0.99 for inlet velocities of approximately 16 m/s and 31 m/s. The composition of the natural gas during this experiments was composition 3 as in table 5.6.

The figure 5.30 compares 30 % O₂ oxyfuel and air flame at an equivalence ratio of 0.87 and average inlet velocity of 16 m/s at 5 bar pressure. The images show average and RMS distribution of OH*-chemiluminescence normalized to maximum intensity in respective recordings. Both, oxyfuel and air flames at 16 m/s have in comparison to the atmospheric flames an unconventional flame stabilization with close proximity to the burner surface. The area of heat release of the oxyfuel flames is larger compared to the air flames. The quantity of fuel being supplied to the oxyfuel flames at the same equivalence ratio is also higher by around 33 % as a result of the higher O₂ concentration in the oxidizer. The RMS distribution images show differences in the region of fluctuations, where larger fluctuations in the oxyfuel flames are mainly observed close to the chamber windows. In contrast the heat release fluctuations for the air flames are not in proximity to the window. The difference in the RMS distribution is attributed to differences in the stabilization of the two flames. The oxyfuel flames under this condition displayed a transitional behavior, where the flame would periodically lift off and flashback to the burner surface. The figure 5.31 below shows a sequence of non-correlated images from the oxyfuel and air flames to describe this behavior. The first image in the sequence (Fig.5.31(a)) shows an instance where the heat release is occurring further downstream of the burner face in a lifted configuration. The second instance is that of the flame flashing back and causing heat release across the entire chamber width at close proximity to the burner face. The subsequent images show a reduction of the heat release in this anchored flame position. For the air flames (Fig.5.31(b)), the sequences show a flame which is stabilized close to the burner face. The air flames show a nearly constant flame width although the intensity varies due to the presence of thermo-acoustic oscillations at a frequency of 240 Hz. Both air and oxyfuel flames display oscillations albeit of a different nature. The transitioning flame behavior of the oxyfuel flame is suggestive of a slightly weaker flame stabilization than the air flame under similar conditions.

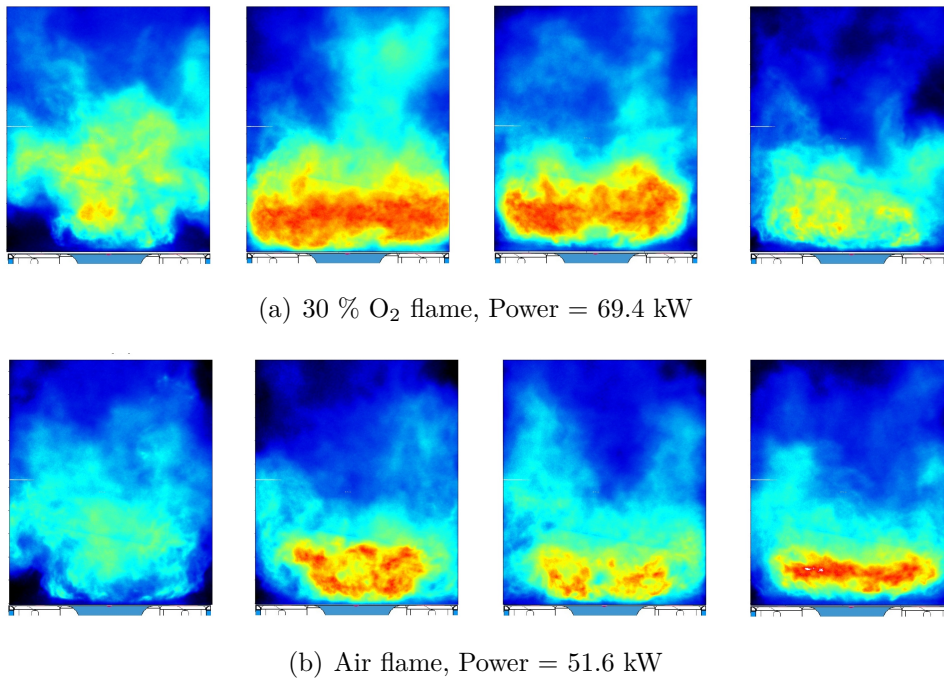


Figure 5.31: An uncorrelated sequence of short exposure OH*-chemiluminescence images for oxyfuel and air flames under similar conditions at 5 bar for $\varphi=0.87$ and $V_{avg} \approx 16$ m/s.

As the inlet velocity is increased, both air and oxyfuel flames maintain the flatter flame shape (Fig.5.32). The region of heat release extends even further across the combustion chamber width. The oxyfuel flames burn over a wider region in comparison to the air flames, and visual inspection showed that the flames were closer to the windows of the combustion chamber. The RMS images of the flames reveal this aspect where the oxyfuel flames have significantly higher fluctuations of chemiluminescence intensity near the windows in comparison to the air flames where fluctuations are similar to the low velocity configuration of 16 m/s. Both these flames excited consistent thermo-acoustic oscillations at 212 Hz for oxyfuel and 279 Hz for air flames, unlike at the lower velocity of 16 m/s where transitioning flames were observed. The higher frequency of the air flames is consistent with the observations under atmospheric conditions seen in section 5.2. The reactivity of the 30 % O₂ oxyfuel mixture was shown to be lesser than that of the air flames under atmospheric conditions. The higher thermal power of the oxyfuel flame relative to the air flame also means that a larger quantity of fuel needs to be combusted, however at a lower reactivity than that with air. This combination is thought to cause the flame to move closer to the chamber window and increase the fluctuations as observed in the RMS distribution.

The equivalence ratio of the flames was increased for similar conditions from 0.87 to 0.99. The figure 5.33 shows average OH*-chemiluminescence images of oxyfuel and air flames at average inlet velocity of approximately 16 m/s and 31 m/s. The increase in

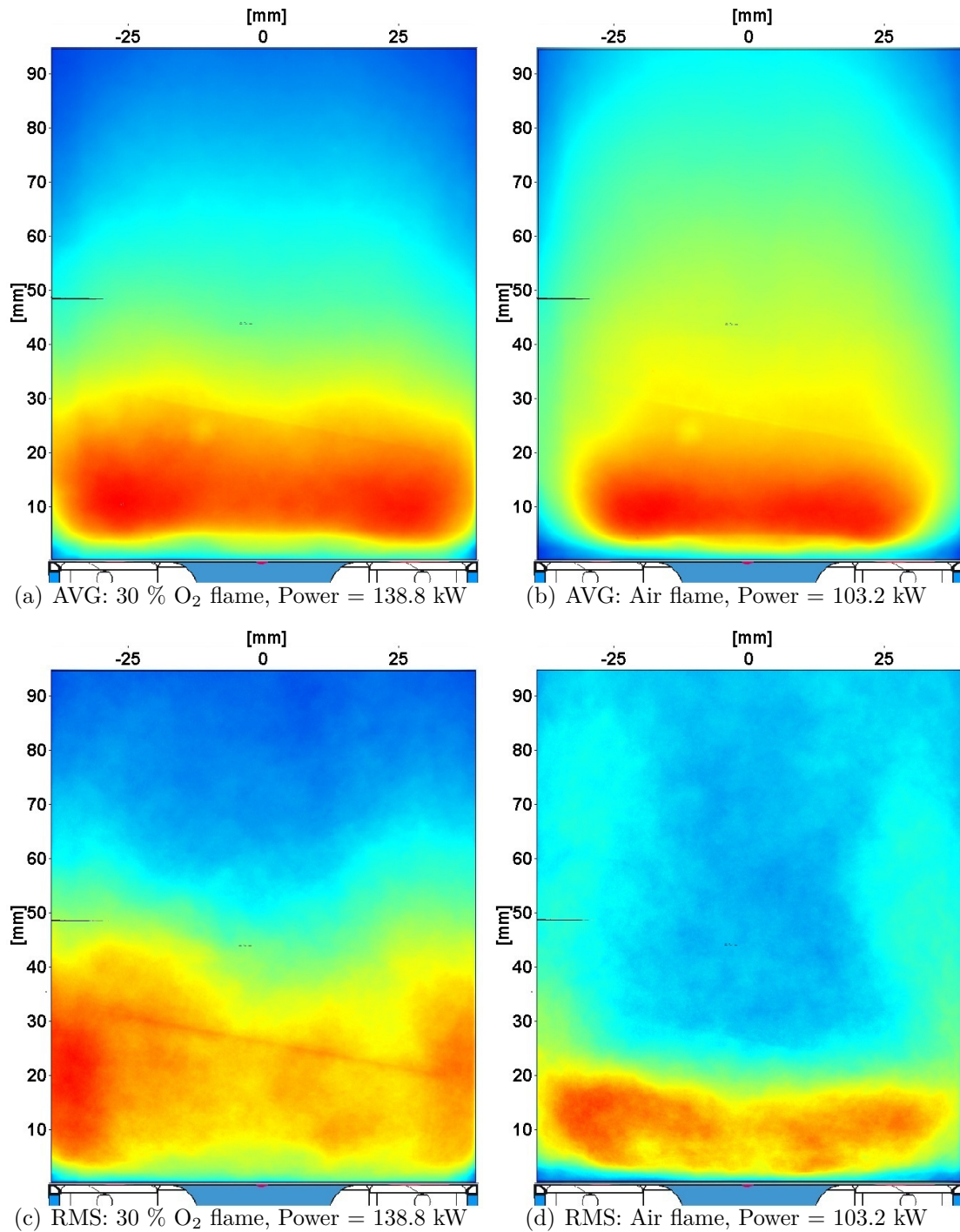


Figure 5.32: Average and RMS images of 200 short exposure OH*-chemiluminescence for oxyfuel and air flames under similar conditions at 5 bar for $\varphi=0.87$ and $V_{avg} \approx 31$ m/s.

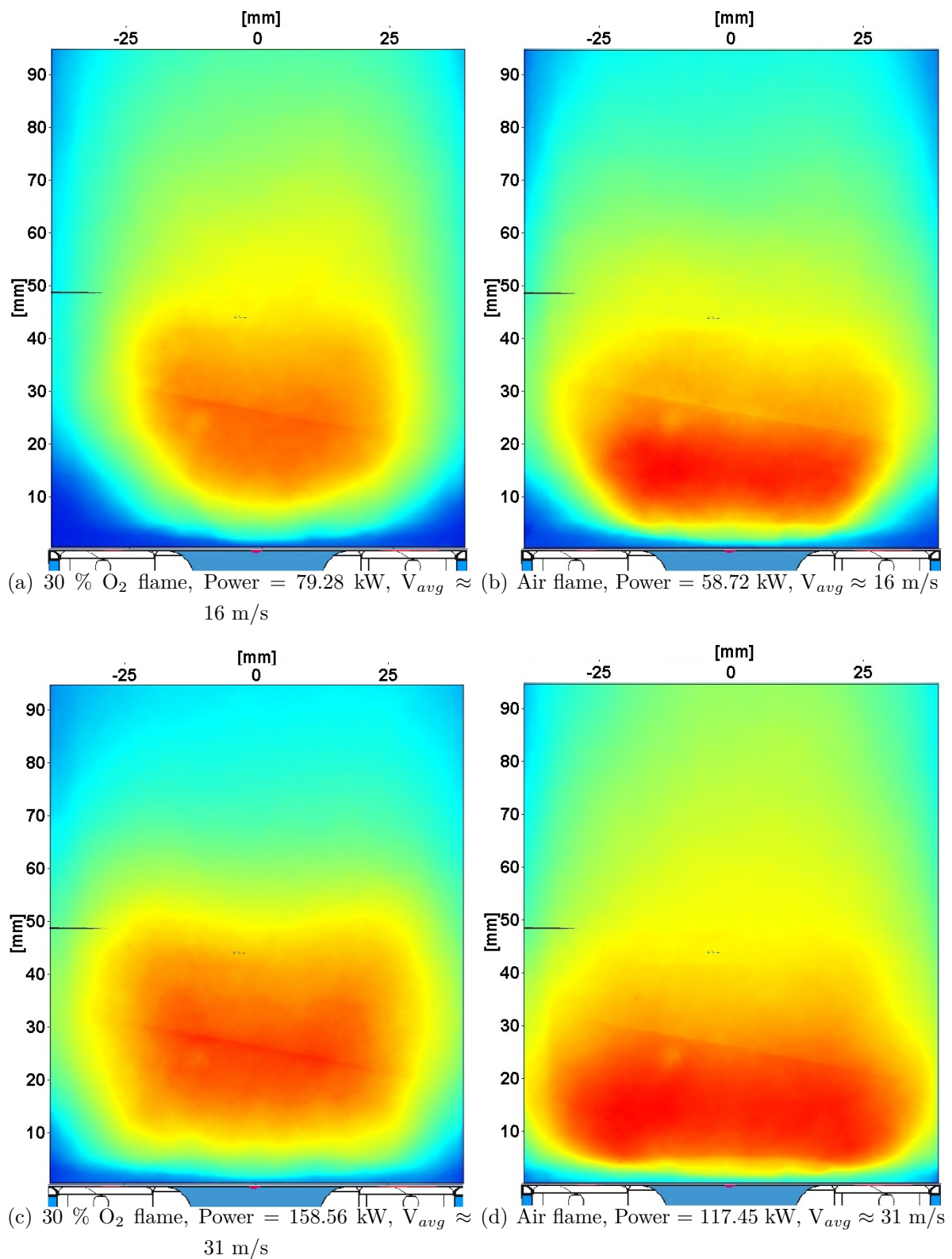


Figure 5.33: Average images (200 exposures) of OH*-chemiluminescence for oxyfuel and air flames at different inlet velocities and $\phi=0.99$ at pressure of 5 bar.

equivalence ratio changes the shape of the flames. The oxyfuel flame remains close to the burner near the flow inlet and moves away from the chamber windows. The flame in figure 5.33(a) exhibited instabilities of a similar nature to that of the lean flame at 16 m/s discussed above with the flame periodically moving to the burner face. At the higher inlet flow velocity of 31 m/s the region of heat release for the oxyfuel flames becomes almost polygonal in shape. The flame operation also resulted in the formation of soot, which was observed throughout the combustion chamber both for air and oxyfuel flames. In comparison to the leaner oxyfuel flames discussed above, the flames at $\varphi = 0.99$ occupy a location further downstream. The air flame in figure 5.33(b) shows an increase in the region of heat release at higher equivalence ratio. The proximity of heat release to the burner face is higher than that of the comparable oxyfuel flame and no flame transitioning was observed. With an increase in the inlet velocity (Fig. 5.33(d)) the flame heat release for the air flame occurs across the entire burner width. As seen at the leaner conditions the flame anchoring was better for the air flames in comparison to the oxyfuel flames. Both oxyfuel and air flames exhibited consistent thermo-acoustic oscillations at 31 m/s with a thermo-acoustic frequency of 204 Hz and 279 Hz respectively.

The investigations showed that under similar conditions both air and oxyfuel flames undergo a significant change in flame shape at elevated pressure conditions. The 30 % O₂ flames at atmospheric conditions were predominantly stable over a range of operating conditions. However, with preheating of the oxidizer and increased pressure both air and oxyfuel flames display an uncharacteristic flame shape and thermo-acoustic oscillations over a wide range of operation. The stabilization of the oxyfuel flames is poorer than that of air flames with flames located closer to the windows and having larger fluctuations. The poorer stabilization was manifested by instabilities which cause periodic flame transition to the burner face at lower flow velocities. The frequency of the thermo-acoustic instabilities was higher for air flames in comparison to the oxyfuel flames. The flame shape and instabilities associated with both flames are a characteristic of the burner. The laminar flame speed of premixed hydrocarbon mixtures is known to reduce with increase in pressure [37]. A change in burner aerodynamics at elevated pressure and lower reactivity might be causing flame stabilization closer to the windows. The characteristic flame shape observed with the burner has been explored in further detail in the following section. The tendency of both oxyfuel and air flames to excite thermo-acoustic oscillations near stoichiometric conditions is also explored.

5.4.3 Burner aerodynamics at elevated pressures

The unconventional flame shape at elevated pressure is thought to be influenced by the converging-diverging nozzle section of the burner which directs flow into the combus-

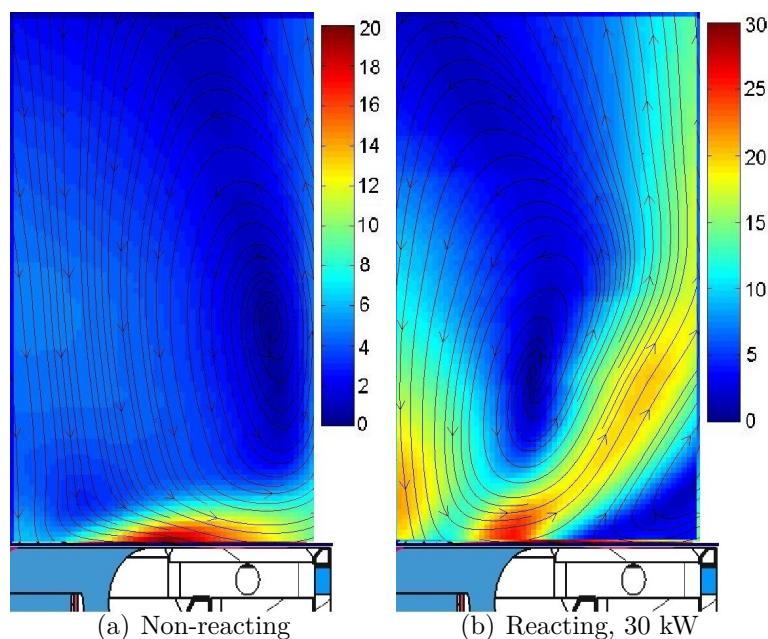


Figure 5.34: Average flow field streamlines overlaid with absolute velocity contours in background representing a 40 mm x 65 mm section of the combustion chamber. Non-reacting flow and reacting flow for natural gas air flames at 1.5 bar and average inlet velocity of 31 m/s and $\varphi=0.83$ shown.

tion chamber. In order to confirm this simultaneous two component PIV and OH^* -chemiluminescence measurements were performed at a frame rate of 3 kHz using the experimental setup described in section 3.5.1. The high speed laser diagnostics enable the detection of unsteady flow phenomena that affect the flame dynamics. Both reacting and non-reacting flows were studied for air flames to determine the influence of the flame on the flow field. The data was also time resolved so as to associate each recording to the phase of the pressure oscillation in the combustion chamber. The conditions of the experiments are described in the table 3.7. The experiments were restricted to measurements with air for the reacting flow since the oxyfuel flames burned very close to the combustion chamber windows. The consequent rapid window deterioration in the presence of PIV particles resulted in poor PIV signal quality. Non-reacting flow measurements with oxyfuel were therefore conducted to ascertain differences in the oxyfuel and air flows.

The figure 5.34 shows the average velocity field of a non-reacting and a reacting case at 1.5 bar. The streamlines in the images show that for the non-reacting flow the fresh charge coming into the combustion chamber is directed towards the burner face instead of penetrating the combustion chamber. The flow impinges on the windows and turns axially forming a large recirculation zone which extends into the burner inlet. This type of swirl flow is referred to as a wall jet and has been shown by Gupta to occur at high swirl numbers [23]. The high speed flow data was analyzed using a POD analysis to

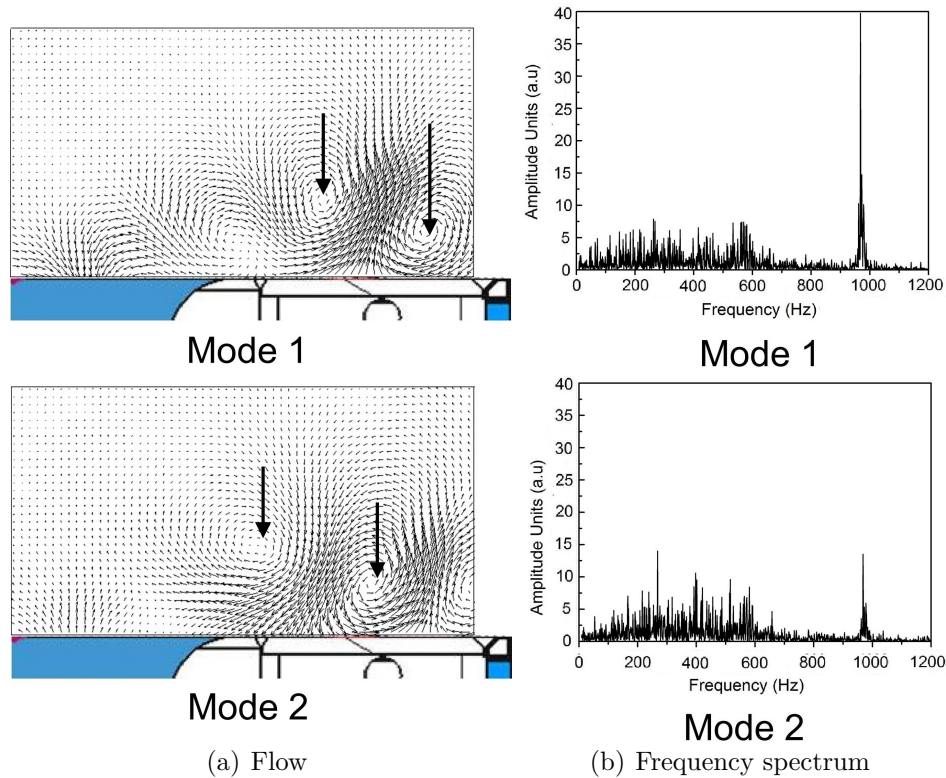


Figure 5.35: Flow characteristic (37 mm x 20 mm section) and Fourier analysis frequency spectrum of 1st and 2nd mode of the non-reacting air flow at 1.5 bar for an average inlet velocity of 31 m/s.

detect coherent flow structures in the flow fluctuations. The figure 5.35 shows the first two modes for the non-reacting flow together and its frequency spectrum. A Fourier analysis was performed on the temporal coefficients to obtain the frequency spectrum of the fluctuations. Although in the mean sense the flow is seen to be attached to the burner surface, the POD modes show the formation of vortices indicated by the arrows in figure 5.35. The frequency analysis of these modes revealed a frequency of 968 Hz. Optical access to events below the burner surface is not possible, hence only the resultant effects of any flow separation phenomena can be detected. The POD analysis of the data suggests the formation of periodic flow structures that are convected laterally over the burner surface before they turn axially to be convected downstream. This is indicative of periodic flow separation at the burner lip.

With the presence of combustion the flow separates from the burner surface forming an ORZ. Under reacting conditions this flame excited thermo-acoustic oscillations at 362 Hz. The figure 5.36(a) shows the POD modes of reacting flow PIV data. The 1st mode indicates the presence of a single vortical structures while the 2nd mode shows two such structures. The frequency spectra of both these modes revealed a peak at 362 Hz. This corresponded to the frequency of the thermo-acoustic oscillations that were

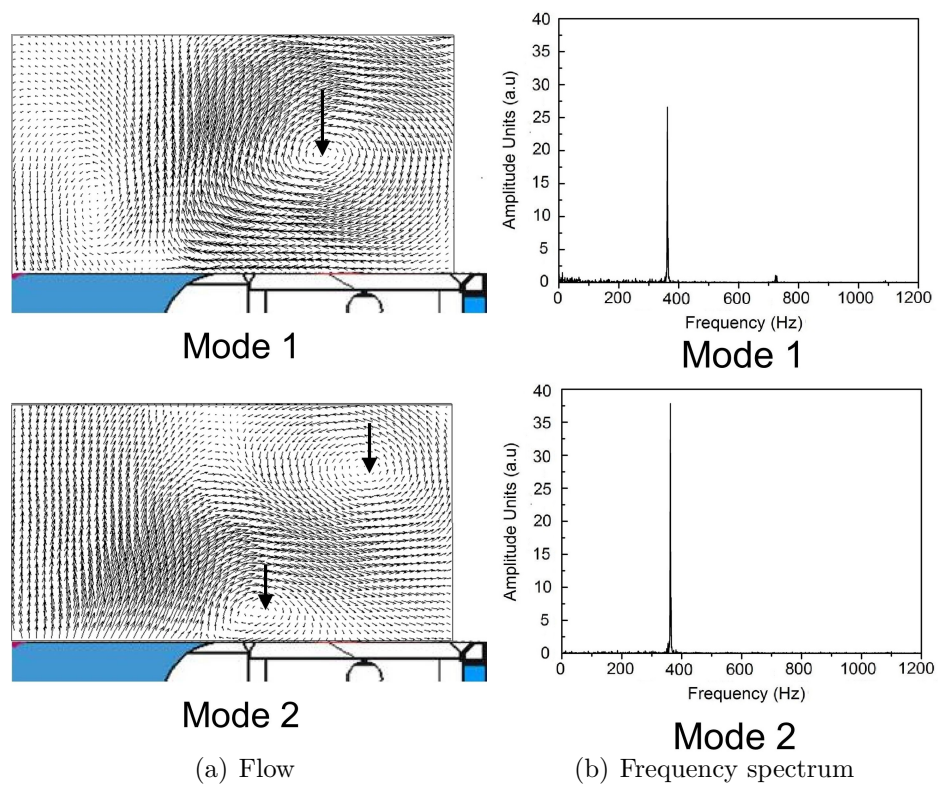


Figure 5.36: Flow characteristic (37 mm x 20 mm section) and Fourier analysis frequency spectrum of 1st and 2nd mode of the reacting air flow at 1.5 bar for an average inlet velocity of 31 m/s and $\varphi=0.85$.

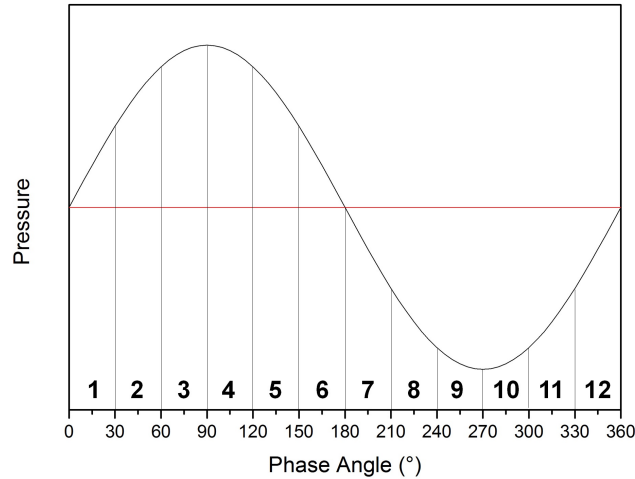


Figure 5.37: Method used for numbering phases of pressure oscillations for phase resolved analysis.

measured using pressure probes placed in the combustor. In order to obtain information regarding the flame dynamics and related thermo-acoustic oscillations, phase resolved average information of the heat release and flow was calculated. A single period of the oscillation was divided into 12 phases based on the amplitude of the pressure fluctuation in the combustion chamber as shown in figure 5.37. It must be noted that the actual location of the pressure probe was not in the combustion chamber, but at a distance of approximately 35 cm away from the pressure tap in the chamber. Therefore the peak pressure in the combustion chamber has a phase offset to that used for this analysis. At each measurement location approximately 5.4 s of data was recorded at 3 kHz. This results in an average of 1012.5 images per phase, which is statistically significant for the averaging process.

The figure 5.38 shows the phase averaged images of the oscillation depicting the line of sight OH*-chemiluminescence on the left and the flow field streamlines with background colored by resultant velocity on the right. From phase 1 to phase 4 the intensity of the chemiluminescence decreases indicating a reduction in the heat release rate to almost complete blow out. The velocities at the inlet of the combustion chamber are increasing and the incoming flow is seen to creep along the burner surface similar to the non-reacting case before being directed axially close to the combustion chamber windows. There is no discernible ORZ from phase 1 to phase 4. From phase 5 onwards the heat release increases to a maximum at phase 8. During this period, the incoming fresh gas and the flow in the IRZ show a significant velocity increase. This increase in velocity corresponds to the gas expansion in all directions due to the onset of combustion. During this period the width of the IRZ reduces and coincides with the formation of an ORZ. A detachment of the flow from the burner surface is evident. The high IRZ velocities during this phase reduce

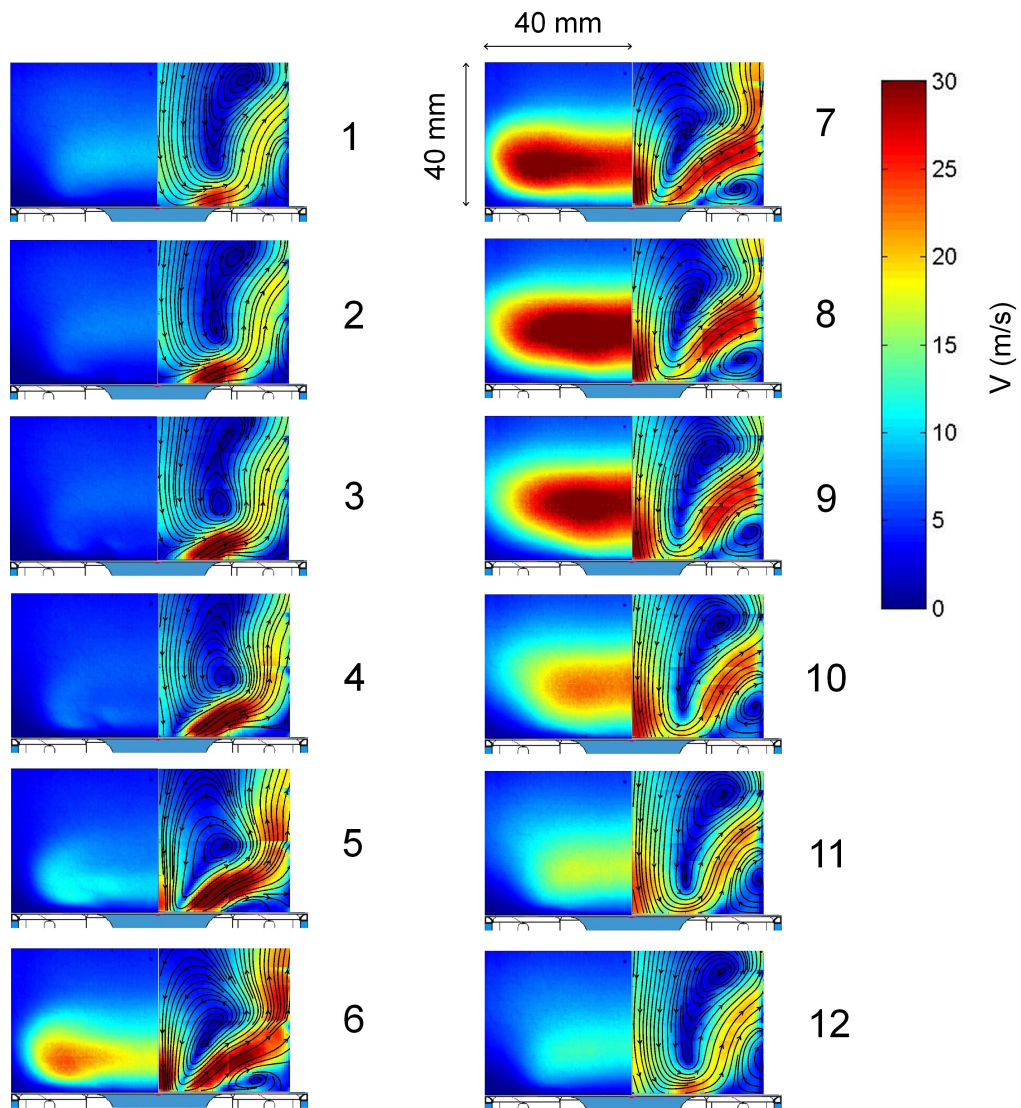


Figure 5.38: Combined OH*-chemiluminescence (left) and PIV (right) phase averaged images corresponding to different phases of pressure oscillations in the combustion chamber for the air flame at 1.5 bar in table.3.7

the flow of fresh gas into the combustion chamber. The phases 8 to 12 represents the consequent reduction in the heat release. Here the extent of the ORZ is gradually reduced as the incoming flow is directed again along the burner surface, before the cycle repeats. The first two modes of the POD shown above for this case represent these alternative events that involves the formation and destruction of the ORZ. This is thought to be related to flow separation and vortex formation events that are initiated at the burner lip and propagate into the combustion chamber as seen in the non-reacting flow.

With an increase in pressure the non-reacting flow maintained a similar character to the lower pressure case. However the reacting flow as seen in the previous section moved closer to the combustion chamber windows. The figure 5.39 shows the average velocity fields for the 5 bar measurements. The impact of the combustion process on the flow is evident with the flow directed more axially, although a distinct detachment of the flow from the burner surface is not observed. The periodical flow structures detected at the thermo-acoustic oscillation frequency as seen at 1.5 bar were also observed under these conditions. The frequency of these structures corresponded to the thermo-acoustic oscillation frequency of 383 Hz.

The above treatment looked at the burner aerodynamics at elevated pressure with air flames. There is a marked difference to the flow field in comparison to atmospheric conditions. The flow dynamics for the oxyfuel conditions was also studied and compared to that of air. For the non-reacting oxyfuel flow conditions at 1.5 bar the time averaged flow remained similar to that of the non-reacting air flow. The figure 5.40 shows the first two POD modes of the flow along with the frequency spectrum of the temporal coefficients for the two modes. The modes are similar to that of the air flames. The spectrum of the temporal coefficient reveals a similar frequency as for the air cases at 957 Hz corresponding to the flow separation at the burner lip. For the non-reacting air flow the frequency band from 200 to 600 Hz showed a broadband noise related to the turbulent fluctuations. In the case of oxyfuel conditions two distinct frequencies at 400 Hz and 557 Hz are detected. Phase resolved analysis of the 400 Hz frequency revealed a Helmholtz resonance like oscillation of the incoming flow. The 557 Hz frequency is a result of the interaction of the Helmholtz oscillation with the periodical flow separation at the burner lip. For the air case these oscillations are thought to be also present, but are not as distinct as for the oxyfuel case. The dynamics of the cold flow hence are similar for oxyfuel and air conditions.

The Abel inverted OH*-chemiluminescence half images of air and oxyfuel flames at 1.5 bar and 5 bar for similar equivalence ratios and inlet velocity are shown in figure 5.41. The air flames at 1.5 bar and 5 bar have a heat release zone that is closer to the burner face compared to the oxyfuel flames. The increase of pressure to 5 bar influences the oxyfuel flame significantly with a drastic shift in the heat release zone towards the

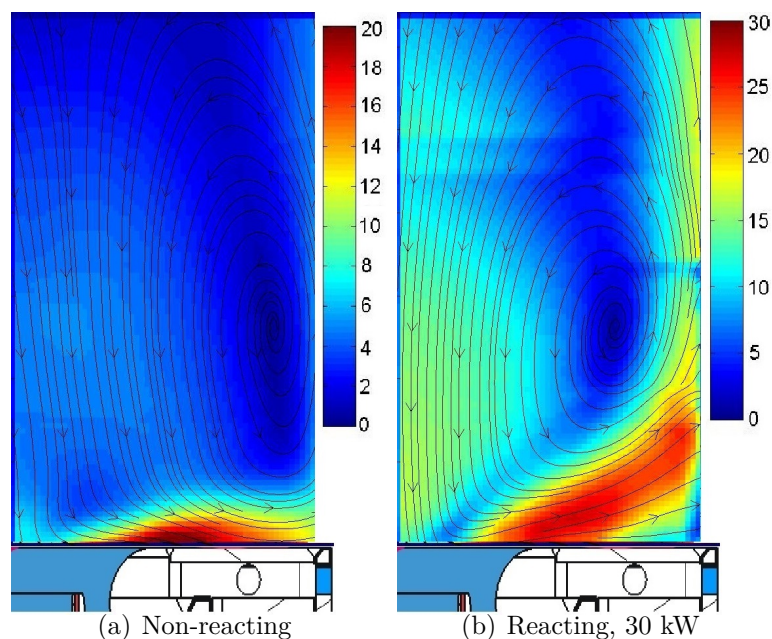


Figure 5.39: Average flow field streamlines overlaid with absolute velocity contours in background representing 37 mm x 65 mm section of combustion chamber. Non-reacting flow and reacting flow for natural gas air flames at 5 bar and average inlet velocity of 31 m/s and $\varphi=0.83$ shown.

window. The increase of pressure is known to reduce laminar flame speeds [37]. As the inlet flow velocities remain similar to that at 1.5 bar, the movement of the flame closer to the window is thought to be caused by the reduction in the mixture reactivity at elevated pressures. Regions of flow stagnation and reduced velocities near the window are conducive to flame stabilization. The oxyfuel and air flames at 1.5 bar and 5 bar exhibited thermo-acoustic oscillations. The frequency of oscillations for air flames was higher than that for oxyfuel. The frequency for oxyfuel flames was 280 Hz at 1.5 bar and varied between 220 Hz to 270 Hz at 5 bar. In sections 5.1.3 and 5.2 the frequency of the thermo-acoustic oscillations increased as the reactivity of the oxyfuel mixtures increased from 30 %O₂ to 34 %O₂ and when air was used. This was traced back to the increase in the laminar flame speed with change in oxidizer composition and to higher laminar flame speeds for air flames. The higher reactivity was correlated with a shorter path and time-scales for the convection of fresh gas into the reaction zone. The frequency of oscillations were correspondingly higher. At elevated pressures this effect is seen again with higher frequency of thermo-acoustic oscillation of air flames in comparison to oxyfuel flames.

Based on the experimental investigations it is evident that the burner aerodynamics play a crucial role in the flame stabilization of both oxyfuel and air flames at elevated pressures. The non-reacting flow is directed along the burner surface and the flame causes the flow to detach from the burn surface at 1.5 bar. The flow does not detach from the

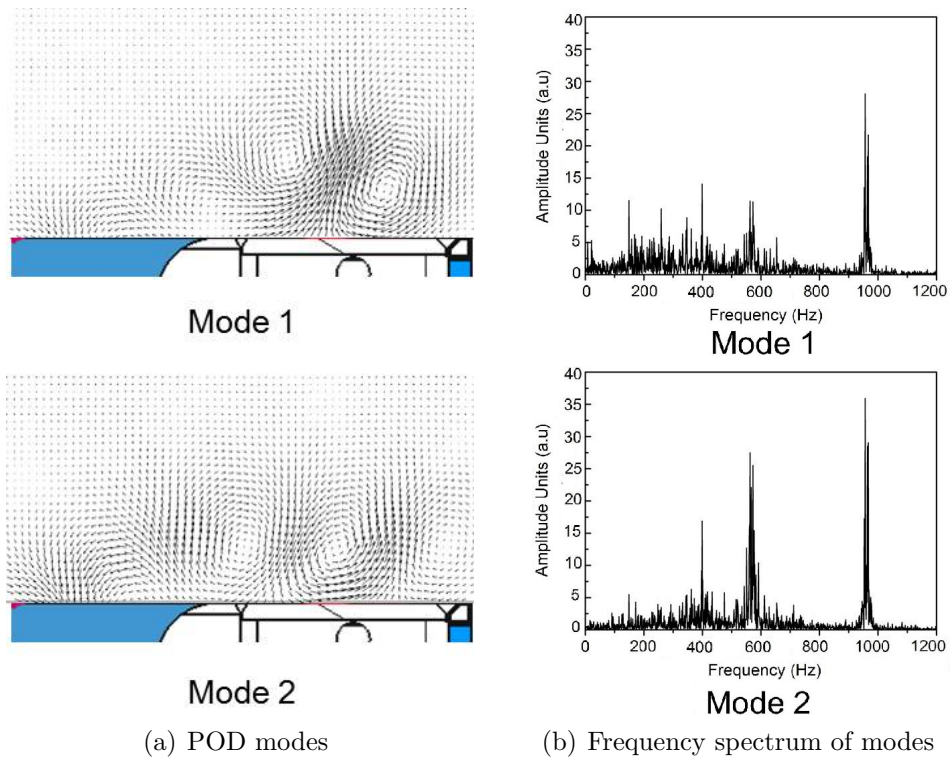


Figure 5.40: Fourier analysis spectrum of temporal component of 1st and 2nd modes from POD analysis of flow information representing a 40 mm x 20 mm section of the combustion chamber close to the burner surface for non-reacting oxyfuel conditions at 1.5 bar.

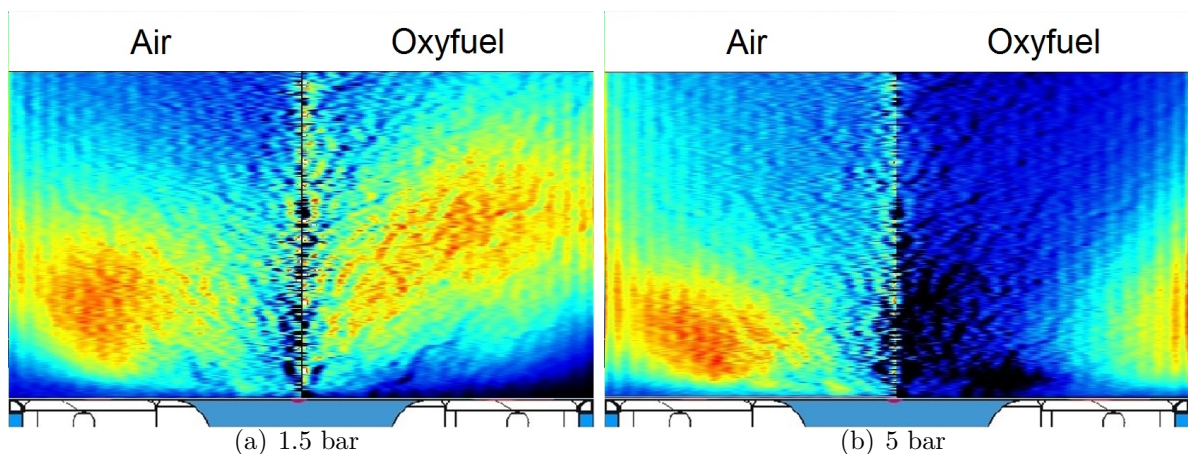


Figure 5.41: Abel inverted OH^* -chemiluminescence half images of preheated air and oxyfuel flames with $V_{avg}=31$ m/s and $\varphi=0.83$ at 1.5 bar and 5 bar.

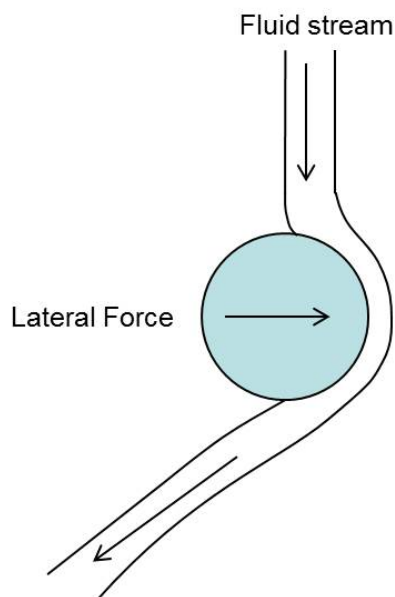


Figure 5.42: Sketch of Coanda effect for fluid flow near curved surface.

burner surface at elevated pressures. It is thought that the flow remains attached to the burner face due to the Coanda effect [129] occurring at the contoured nozzle section of the burner. The figure 5.42 describes the Coanda effect. This is a well known fluid dynamic effect which occurs when a flow along a curved surface is directed towards the curved surface as a result of pressure gradients due to acceleration or separation of fluid along the curved surface which cause the flow to follow the surface. The exact reason behinds the change in burner characteristics at elevated pressures is unknown. The behavior is thought to be linked to the change in exhaust nozzle diameter and the redirection of a small amount of oxidizer for burner cooling along the chamber windows. The exhaust nozzle at atmospheric conditions had a diameter of 40 mm while that at elevated pressure had a diameter of 18 mm to isolate the combustion chamber acoustically from the rest of the test rig. The entrainment of the main burner flow into the cooling flow also increases the tendency of obtaining fluid flow along the burner surface. However, both oxyfuel and air flames excite thermo-acoustic instabilities for similar operation. The frequency of the oscillations for air flames was found to be higher than that of oxyfuel flames. This was consistent with observations at atmospheric pressure where the lower reactivity of oxyfuel flames resulted in higher convective time-scales. The flames obtained at elevated pressure are not optimal for a gas turbine burner operation due to the proximity of the flames to the burner surface and thermo-acoustic oscillations. The behavior of both air and oxyfuel flames could however be correlated. With modifications to the burner geometry so as to reduce the impact of the Coanda effect the 30 % O_2 flame can be expected to yield relatively stable flames using burners operating with air.

6

Conclusions

For oxyfuel gas turbines that operate with CO₂ as the main diluent, new burners need to be designed that account for the difference in properties to that of air. The differences in properties are due to the higher heat capacity, lower conductivity and viscosity, active radiation heat transfer and a more active involvement of CO₂ in chemical reactions. The proportion of CO₂ influences the physical properties and the reactivity of these mixtures. The laminar flame speeds of oxyfuel mixtures changes significantly with the extent of CO₂ dilution. Therefore the extent of CO₂ dilution determines the flame stabilization as well as the flame temperatures.

Oxyfuel flames have been investigated using optical diagnostics under atmospheric and elevated pressure conditions using a previously well researched partially premixed swirl burner. Unlike air flames where the thermal power and equivalence ratio influence flame behavior when the reactant temperatures are kept constant, oxyfuel flames are influenced by the ratio of O₂/CO₂ present in the oxidizer. Different oxyfuel oxidizer compositions with varying ratios of O₂ to CO₂ were investigated. The study was performed at comparable thermal powers and comparable inlet velocities. In both instances, the increased flame speed and higher flame temperatures of higher O₂ concentration oxidizers favored flame stabilization closer to the burner face. Oxidizers having between 26 to 30 % O₂ displayed conical flame form. The flame stabilization of oxidizers with 26 % and lower O₂ concentrations was poor as the flames burned further downstream from the burner face and excited low frequency instabilities. The 30 % O₂ flames were stable over a large range of operation and appeared visually similar to typical air flames observed previously in the burner. For 34 % and higher O₂ oxidizers, flat flames at close proximity to the burner face were observed. The flames consistently excited thermo-acoustic oscillations over a wide range of operating conditions. An analysis of the flow data showed that an increase in the O₂ concentration results in a decrease of the convective time-scales of the fresh charge to reach the zone of heat release. The flame stabilization closer to the burner face reduces the time-scales to values that cause resonance with Helmholtz oscillation modes in the

system. This correlated with the increased frequency of thermo-acoustic oscillations with higher O₂ concentrations. The coherent flow structures in the flame changed with the amount of CO₂ dilution. The precessing vortex core which plays an important role in the mixing of unburnt and burnt gas and hence flame stabilization became wider and less distinct at low CO₂ dilution. For a O₂ concentrations of 34 %, it was replaced by a toroidal vortex structure, which has previously not been detected for this burner. Due to the change in coherent flow structures for different O₂ concentrations the flames reacted differently to changes in equivalence ratio. The proximity of the flat flames to the burner face increased for stoichiometric operation while that of conically shaped flames reduced. The changes were however small in comparison to those caused due to O₂ concentration. With an increase in the average flow velocity and thermal power the flames occupied positions further downstream of the burner face. While 26 % to 30 % O₂ flames maintained a conical flame shape, the flat flames moved away from the burner forming lifted flat flames. In order to obtain conically shaped flames at high O₂ concentrations higher inlet flow velocities are required, which can be achieved by reducing the burner nozzle diameter. Conversely flame stabilization with low O₂ concentration oxidizers would be favored by the use of a larger inlet nozzle to reduce flow velocities. The thermal power rating of the flames increased with O₂ concentration for similar flow conditions. In order to adapt existing air burners for oxyfuel operation a burner scale up or scale down would be required based on the quantity of CO₂ diluent flowing through the burner.

Raman spectroscopy measurements performed on two 30 % O₂ flames based on visual similarity to air flames showed that the flames had large quantities of CO in the inner shear layer (ISL). The maximum combustion temperatures were reached further downstream of the ISL where the CO was completely oxidized. The heat transfer characteristics of the flames changed with a reduction in the flow velocity. The temperature drop in the outer recirculation zone relative to adiabatic flame conditions increased with increase in flow velocity, while the temperature drop in the IRZ and further downstream regions of the combustion chamber reduced at higher flow velocity. The differences in temperature drop are thought to be related to heat transfer effects that change due to the presence of CO₂ and change in the residence time of the flow at different flow velocities. This aspect needs further investigation, however the results indicate a sensitivity of oxyfuel flames to heat transfer to the burner and combustion chamber. The burner and chamber geometry are therefore expected to play a crucial role in enhancing or reducing flame stabilization.

A comparison of the oxyfuel flames and air flames was performed under atmospheric conditions. The change in flame shape with increased CO₂ dilution of the oxidizer was similar to the effect of decrease in equivalence ratio in the air flames. Laminar flame speed calculations showed that values of lean air flames ($\varphi=0.65$) were similar to values

of stoichiometric 30 % O₂ concentration oxyfuel flames. For stoichiometric operation comparable laminar flame speeds for air and oxyfuel flames are obtained for a composition of nearly 40 % O₂. At similar inlet flow velocities the effect of this was confirmed as the flames changed from conically shaped flames to flat flames with increased O₂ concentration and air operation. The conical flame shape in this burner was obtained for 30 % O₂ oxyfuel flames and lean air flames. A comparison of the Raman data for the oxyfuel and air flames showed that the 30 % O₂ oxyfuel flames had lower temperatures in the flame anchoring zone and a more distributed region of heat release. The fuel penetrated further into the combustion chamber for the oxyfuel flame indicating weaker stabilization. The advantage of partially premixed combustion for the 30 % O₂ oxyfuel flames was lesser due to the lower change in flame speed with equivalence ratio in comparison to air flames. The comparison also revealed differences in the heat transfer characteristics of the air and oxyfuel flames.

Subsequently 30 % O₂ oxyfuel flames were investigated with the modifications to the same burner under elevated pressure (5 bar) and gas turbine like conditions. The introduction of preheating to simulate gas turbine burner inlet conditions (653 K) and elevated pressures changed the flame shape relative to atmospheric burner operation. A fourth flame shape also known as wall jet flame was observed. The difference to flat flames observed at atmospheric conditions was the increased proximity to not only the burner face but also the chamber windows. Both oxyfuel and air flames exhibited this behavior. The flame stabilization of the 30 % O₂ oxyfuel flames was poorer than that of air flames. The oxyfuel flames exhibited periodic flame transitioning to the burner face. Both air and oxyfuel flames exhibited persistent thermo-acoustic oscillations under stoichiometric operating conditions. The flame behavior was strongly influenced by the changed burner aerodynamics at elevated pressure. In non-reacting and reacting flows high repetition rate PIV measurements were performed for selected oxyfuel flames and similar air flames. The measurements were performed at 1.5 bar and 5 bar conditions. The non-reacting flow followed the curved lip structure of the burner nozzle into the combustion chamber for both air and oxyfuel operation. The reacting cases however showed difference in behavior at 1.5 bar and 5 bar. At 1.5 bar the flow detaches from the burner surface due to combustion and forms an outer recirculation zone (ORZ). This behavior was absent for the 5 bar case with the flow remaining attached to the burner surface. The thermo-acoustic oscillations were characterized by the presence of periodic vortex shedding from the burner lip at the thermo-acoustic frequency. The thermo-acoustic frequency reduced with the use of oxyfuel flames at similar average inlet velocity in comparison to air flames. The decrease in thermo-acoustic frequency for oxyfuel operation was similar to that observed under atmospheric conditions and is attributed to the faster reactivity of air flames in comparison to oxyfuel flames which changes the delay associated with fresh

charge reaching fully combusted state. The high pressure investigations reveal that the current burner configuration is not suitable for real gas turbine operation due to the burner lip. The differences however between oxyfuel and air flames are consistent to those observed at atmospheric conditions.

In order to minimize the cost of obtaining oxygen by air separation stoichiometric operation is crucial to oxyfuel combustion. However this type of operation increases the combustion temperature and limits the region of stable burner operation. Based on the above results a multitude of approaches are evident for gas turbine burner operation with oxyfuel mixtures. The approaches can be distinguished based on the extent of CO₂ dilution implemented in such gas turbines as the following:

- Alternate burner concepts for lower than 30 % O₂ oxidizers
- Operating current air burners with 30 % O₂ oxidizer
- Burner scale down and burner staging for higher than 30 % O₂ burners

Low O₂ concentrations flame were difficult to stabilize with the current burner configuration. The low laminar flame speeds and their reduced dependence on equivalence ratio indicated that the benefit of partially premixed combustion is lesser. In order to operate such oxyfuel flames alternate burner concepts which employ premixed combustion and promote easy mixing of exhaust gas with fresh charge would be suitable. The FLOX[®] burner concept could be beneficial for such oxidizers. The second approach provides a viable option for operating current gas turbines with oxyfuel mixtures. Although the flame stabilization of the 30 % O₂ flame was poorer than that of air, the wide range of stable operation indicates that with small modification to current air burners these flames are applicable to existing gas turbines. However, the high combustion temperatures at the turbine inlet due to stoichiometric combustion need to be reduced with further post combustion CO₂ dilution. The third approach offers the possibility of using high O₂ concentration flames in a staged flame configuration. The benefit of good flame stabilization at high O₂ concentration can be utilized to obtain primary flame anchoring as in a pilot burner system, while temperature reduction can be achieved by operating a higher CO₂ dilution configuration to reduce combustion temperatures. The occurrence of high thermo-acoustic oscillations for such O₂ concentrations could prove to be a challenge. Since this behavior is system dependent, careful consideration of different acoustic modes in the system would be required in the design of such a gas turbine. Which of these approaches find application needs further investigation together with other components of an oxyfuel gas turbine. The individual components and their interaction needs to be studied in order to identify an optimized solution.

Bibliography

- [1] J. M. Amann, M. Kanniche, and C. Bouallou. Natural gas combined cycle power plant modified into an O₂/CO₂ cycle for CO₂ capture. *Energy Conversion and Management*, pages 510–521, 2009. xvii, 3, 18, 19
- [2] H. Jericha, E. Goettlich, W. Sanz, and F. Heitmeir. Design optimisation of the Graz cycle prototype plant. In *Proceedings of ASME Turbo Expo 2003: Power for Land, Sea, and Air*, number GT2003-38120, 2003. xvii, 3, 19, 20
- [3] T. Kick, J. Herbst, and C. Naumann. Oxyfuel laminar flame speed measurements. Technical report, Institute of Combustion Technology, DLR, Stuttgart, 2008. xvii, 22, 23, 84, 114
- [4] European Commission. *EU energy in figures - Pocketbook 2014*. Publication office of the European Union, 2014. 1
- [5] DOE-NETL. DOE/NETL carbon dioxide capture and storage RD&D Roadmap. Technical report, DOE, 2010. 1, 3
- [6] H. M. Kvamsdal, K. Jordal, and O. Bolland. A quantitative comparison of gas turbine cycles with CO₂ capture. *Energy*, pages 10–24, 2007. 1, 18, 19, 20
- [7] R. Gabbrielli and R. Singh. Thermodynamic performance analysis of new gas turbine combined cycles with no emissions of carbon dioxide. In *Proceedings of ASME Turbo Expo 2002: Power for Land, Sea and Air*, GT-2002-30117, 2002. 1, 18
- [8] C. Hendriks. *Carbon dioxide removal from coal-fired power plants*. PhD thesis, Utrecht University, Netherlands, 1994. 2
- [9] J. Koornneef, T. Keulen, A. Faaij, and W. Turkenburg. Life cycle assessment of a pulverized coal power plant with post-combustion capture, transport and storage of CO₂. *International Journal of Greenhouse Gas Control*, 2:448–467, 2008. 2

-
- [10] IPCC. Carbon Capture and Storage. Technical report, Intergovernmental Panel on Climate Change, 2005. 2, 18
- [11] M. Ishida and H. Jin. A new advanced power generation system using chemical-looping combustion. *Energy*, 19 (4):415–422, 1994. 2
- [12] <http://www.vattenfall.com/en/ccs/schwarze-pumpe.htm>. 3
- [13] Global CCS institute. The Global status of CCS. Technical report, Global CCS Institute, 2014. 3
- [14] B. J. P. Buhre, L. K. Elliott, C. D. Sheng, R. P. Gupta, and T. F. Wall. Oxy-fuel combustion technology for coal-fired power generation. *Progress in Energy and Combustion Science*, 31:283–307, 2005. 3
- [15] R. Kehlhofer, F. Hannemann, F. Stirnimann, and B. Rukes. *Combined-Cycle Gas & Steam Turbine Power Plants*. PennWell Corporation, 2009. 3, 9
- [16] P. Mathieu and R. Nihart. Zero-Emission MATIANT Cycle. *Journal of Engineering for Gas Turbines and Power*, 121:116–120, 1999. 3, 18
- [17] E. I. Yantovski, K. N. Zvagolsky, and E. A. Gavrilenko. The COOPERATE - Demo power cycle. *Energy Conversion and Management*, 36:861–864, 1996. 3, 18
- [18] O. Bolland and P. Mathieu. Comparison of two CO₂ removal options in combined cycle power plants. *Energy Conversion and Management*, 39:1653–1663, 1998. 3, 18
- [19] A. Amato, R. Hudak, D. R. Noble, D. Scarborough, A. D. Peter, J. M. Seitzman, and T. C. Lieuwen. Methane oxy-combustion for low CO₂ cycles: Blowoff measurements and modeling. In *Proceedings of the ASME Turbo Expo 2010: Power for Land, Sea and Air*, 2010. 3, 22, 24
- [20] Y. Ju, G. Masuya, and P. D. Ronney. Effects of radiative emission and absorption on the propagation and extinction of premixed gas flames. In *Twenty-Seventh Symposium (International) on Combustion / The Combustion Institute*, pages 2619–2626, 1998. 3, 23
- [21] D. L. Zhu, F. N. Egolfopoulos, and C. K. Law. Experimental and numerical determination of laminar flame speeds of methane/(Ar, N₂, CO₂)-air mixtures as function of stoichiometry, pressure, and flame temperature. In *Twenty-Second Symposium (International) on Combustion / The Combustion Institute*, pages 1537–1545, 1988. 3, 22

- [22] F. Liu, H. Guo, and G. J. Smallwood. The chemical effect of CO₂ replacement of N₂ in air on the burning velocity of CH₄ and H₂ premixed flames. *Combustion and Flame*, 133:495–497, 2003. Brief Communication. 3, 22
- [23] A. K. Gupta. *Swirl flows*. Abacus Press, 1984. 3, 12, 14, 15, 121, 129
- [24] A. H. Lefebvre and D. R. Ballal. *Gas turbine combustion: Alternative Fuels and Emissions*. CRC Press, 2010. 3, 9, 11
- [25] P. Weigand, W. Meier, X. R. Duan, W. Stricker, and M. Aigner. Investigations of swirl flames in a gas turbine model combustor I. Flow field, structures, temperature, and species distributions. *Combustion and Flame*, 144:205–224, 2006. 3, 68, 69
- [26] W. Meier, X. R. Duan, and P. Weigand. Investigations of swirl flames in a gas turbine model combustor II. Turbulence-chemistry interactions. *Combustion and Flame*, 144:225–236, 2006. 3, 68, 69, 72
- [27] R. Giezendanner, O. Keck, P. Weigand, W. Meier, U. Meier, W. Stricker, and M. Aigner. Periodic combustion instabilities in a swirl burner studied by phase-locked planar laser-induced fluorescence. *Combustion Science and Technology*, 175:721–741, 2003. 3, 33, 71
- [28] W. Meier, I. Boxx, M. Stoehr, and C. D. Carter. Laser-based investigations in gas turbine model combustors. *Experiments in Fluids*, 49:865–882, 2010. 3, 12, 98
- [29] W. Meier, P. Weigand, X. R. Duan, and R. Giezendanner-Thoben. Detailed characterization of the dynamics of thermoacoustic pulsations in a lean premixed swirl flame. *Combustion and Flame*, 150:2–26, 2007. 3
- [30] A. M. Steinberg, I. Boxx, M. Stoehr, C. D. Carter, and W. Meier. Flow-flame interactions causing acoustically coupled heat release fluctuations in a thermo-acoustically unstable gas turbine model combustor. *Combustion and Flame*, 157:2250–2266, 2010. 3, 15, 72
- [31] R. Sadanandan, M. Stoehr, and W. Meier. Simultaneous OH-PLIF and PIV measurements in a gas turbine model combustor. *Applied Physics B: Lasers and Optics*, 90:609–618, 2008. 3, 72
- [32] M. Stoehr, I. Boxx, C. Carter, and W. Meier. Dynamics of lean blowout of a swirl-stabilized flame in a gas turbine model combustor. In *Proceedings of the Combustion Institute*, volume 33, 2011. 3, 72, 81, 94

-
- [33] R. J. Hunt. The history of the industrial gas turbine (Part 1 The First Fifty Years 1940-1990). Institution of Diesel and Gas Turbine Engineers, 2011. 7
- [34] R. E. Sonntag, C. Borgnakke, and G. J. van Wylen. *Fundamentals of thermodynamics*. John Wiley and Sons, 2003. 7
- [35] H. I. H. Saravanamuttoo, G. F. C. Rogers, H. Cohen, and P. Straznicky. *Gas turbine theory*. Pearson Education Canada, 2008. 8
- [36] D. G. Wilson and W. Korakianitis. *The Design of High-Efficiency Turbomachinery and Gas Turbines*. Prentice Hall, 1998. 8
- [37] S. R. Turns. *An introduction to combustion: Concepts and applications*. McGraw Hill, 2000. 11, 22, 73, 128, 135
- [38] J. G. Wuenning and J. A. Wuenning. Flame oxidation to reduce thermal NO-formation. *Progress in Energy and Combustion Science*, 23:81–94, 1997. 12
- [39] J. Zhang. *Micro injection fuel/air premixer/combustion*. PhD thesis, 2007. 12
- [40] A. Cavaliere and M. de Joannon. Mild Combustion. *Progress in Energy and Combustion Science*, 30:329–366, 2004. 12
- [41] N. Syred. A review of oscillation mechanisms and the role of the precessing vortex core (PVC) in swirl combustion systems. *Progress in Energy and Combustion Science*, 32:93–161, 2006. 12, 15
- [42] J. M. Beer and N. A. Chigier. *Combustion aerodynamics*. Elsevier Science Ltd, 1972. 15
- [43] N. Peters. *Turbulent combustion*. Cambridge Monograph on Mechanics, 2000. 15
- [44] S. Roux, G. Lartigue, T. Poinso, U. Meier, and C. Berat. Studies of mean and unsteady flow in a swirled combustor using experiments, acoustic analysis, and large eddy simulations. *Combustion and Flame*, 141:40–54, 2005. 15, 16
- [45] K. Oberleithner, S. Terhaar, L. Rukes, and C. O. Paschereit. Why nonuniform density suppresses the Precessing Vortex Core. *Journal of Engineering for Gas Turbine and Power*, 135, 2013. 15
- [46] M. Stoehr, I. Boxx, C.D. Carter, and W. Meier. Experimental study of vortex-flame interaction in a gas turbine model combustor. *Combustion and Flame*, 159:2636–2649, 2012. 15, 69

- [47] A. M. Steinberg, C. M. Arndt, and W. Meier. Parametric study of vortex structures and their dynamics in swirl-stabilized combustion. In *Proceedings of the Combustion Institute*, volume 34, pages 3117–3125, 2013. 16
- [48] L. Rayleigh. The explanation of certain acoustical phenomena. *Nature*, 18:319–321, 1878. 16
- [49] T. Lieuwen and V. Yang. *Combustion instabilities in gas turbine engines: Operational experience, fundamental mechanisms and modeling*. American Institute of Aeronautics and Astronautics, 2005. 16, 18
- [50] T. Kuramochi, A. Ramirez, W. Turkenburg, and A. Faaij. Comparative assessment of CO₂ capture technologies for carbon-intensive industrial processes. *Progress in Energy and Combustion Science*, 38:87–112, 2012. 18
- [51] E. I. Yantovski. Stack downward zero emission fuel-fired power plants concept. *Energy Conversion and Management*, 37:867–877, 1996. 18
- [52] M. D. Staicovici. Further research zero CO₂ emission power production: the COOLENERG process. *Energy*, 27:831–844, 2002. 18
- [53] N. Zhang and N. Lior. Two novel oxy-fuel power cycles integrated with natural gas reforming and CO₂ capture. *Energy*, 33:340–351, 2008. 18
- [54] R. E. Anderson, L. C. Hoffman, and F. Viteri. Integration of "Clean Energy Systems" technology with air separation units, gas turbines, and steam turbines into zero-emission power plants. In *Natural Gas Technologies Conference II, Phoenix, Arizona.*, 2004. 18
- [55] O. Marin, Y. Bourhis, N. Perrin, P. Di Zanno, F. Viteri, and R. Anderson. High efficiency, zero emission power generation based on a high temperature steam cycle. In *28th international technical conference on coal utilization and fuel systems, NETL, Clearwater, Florida, USA.*, 2003. 18
- [56] W. Sanz, H. Jericha, M. Moser, and F. Heitmeir. Thermodynamic and economic investigation of an improved Graz cycle power plant for CO₂ capture. *Journal of Engineering for Gas Turbines and Power*, 127:765, 2005. 18, 20
- [57] T. Hammer, J. Keyser, and O. Bolland. Natural gas Oxy-Fuel cycles - Part 2: Heat transfer analysis of a gas turbine. *Energy Procedia 1*, pages 557–564, 2009. 18
- [58] R. Naqvi, O. Bolland, O. Brandvoll, and K. Helle. Chemical looping combustion analysis of natural gas fired power cycle with inherent CO₂-capture. In *Proceedings of the ASME turbo EXPO 2004, Vienna, Austria.*, 2004. 18

-
- [59] T. Griffin, S. G. Sundkvist, K. I. Asen, and T. Bruun. Advanced zero emission gas turbine power plant. In *Proceedings of ASME turbo expo 2003, Atlanta, USA.*, 2003. 19
- [60] S. Rezvani, O. Bolland, F. Franco, and Y. Huang. Natural gas Oxy-Fuel cycles - Part 3: Economic evaluation. *Energy Procedia 1*, pages 565–572, 2009. 19
- [61] H. Jericha, W. Sanz, and E. Goettlich. Design concept for large output Graz cycle gas turbines. In *Proceedings of the ASME Turbo Expo 2006: Power for Land, Sea and Air*, number GT2006-90032, 2006. 19
- [62] S. G. Sundkvist, A. Dahlquist, and J. Janczewski. Concept for a combustion system in oxyfuel gas turbine combined cycles. *Journal of Engineering for Gas Turbines and Power*, 2014. 19
- [63] G. Woollatt and F. Franco. Natural gas oxy-fuel cycles - Part 1: Conceptual aerodynamic design of turbo-machinery components. *Energy Procedia 1*, pages 573–580, 2009. 19
- [64] R. E. Ulfnes, O. Bolland, and K. Jordal. Modelling and simulation of transient performance of the semi-closed O₂/CO₂ gas turbine cycle for CO₂-capture. In *Proceedings of the ASME Turbo Expo 2003: Power for Land, Sea and Air*, 2003. 19
- [65] http://en.wikipedia.org/wiki/Oxy-fuel_welding_and_cutting. 21
- [66] <http://webbook.nist.gov/chemistry/>. 22
- [67] http://combustion.berkeley.edu/Combustion_Laboratory/gri-mech/version30/text30.html. 22, 78
- [68] <http://www.cantera.org>. 22, 78
- [69] A. Amato, R. Hudak, D. R. Noble, D. Scarborough, A. D. Peter, J. M. Seitzman, and T. C. Lieuwen. Methane oxy-combustion for low CO₂ cycles: measurements and modeling of CO and O₂ emissions. In *Proceedings of ASME Turbo Expo 2010: Power for Land, Sea and Air*, 2010. 22
- [70] D. Yossefi, S. J. Ashcroft, J. Hacohen, M. I. Belmont, and I. Thorpe. Combustion of methane and ethane with CO₂ replacing N₂ as a diluent. *Fuel*, 74, 1995. 22
- [71] D. Yossefi, M. R. Belmont, Maskell S. J., and G. Ben-Dor. Stimulation and implementation of laminar flow reactors for the study of combustion systems of ethane, methane and deborane. *Fuel*, pages 173–181, 1998. 22

- [72] C. Zhang, A. Atheya, and K. Lee. Sooting structure of methane counterflow diffusion flames with preheated reactants and dilution by products of combustion. In *Twenty-Fourth Symposium (International) on Combustion / The Combustion Institute*, pages 1049–1057, 1992. 22
- [73] F. Liu, H. Guo, O. L. Gulder, and Smallwood G. J. The chemical effects of carbon dioxide as an additive in an ethylene diffusion flame: Implications for soot and NO_x formation. *Combustion and Flame*, 125:778–787, 2001. 22
- [74] J. Herzler and C. Naumann. Shock-tube study of the ignition of methane/ethane/hydrogen mixtures with hydrogen contents from 0 % to 100 % at different pressures. In *Proceedings of the Combustion Institute*, volume 32-1, pages 213–220, 2009. 22, 84, 114
- [75] E. L. Petersen, D. F. Davidson, and R. K. Hanson. Kinetics modeling of Shock-Induced Ignition in Low-Dilution CH₄/O₂ Mixtures at High Pressures and Intermediate Temperatures. *Combustion and Flame*, 117:272–290, 1999. 22
- [76] J. Ruan, H. Kobayashi, T. Niioka, and Y. Ju. Combined effects of nongray radiation and pressure on premixed CH₄/CO₂/O₂ flames. *Combustion and Flame*, 124:225–230, 2001. 23
- [77] K. Maruta, K. Abe, S. Hasegawa, S. Maruyama, and J. Sato. Extinction characteristics of CH₄/CO₂ versus O₂/CO₂ counterflow non-premixed flames at elevated pressures up to 0.7 MPa. In *Proceedings of the Combustion Institute*, volume 31, pages 1223–1230, 2007. 23
- [78] N. Lallemand, J. Dugue, and R. Weber. Measurement techniques for studying Oxy-Natural gas Flames. *Journal of the Institute of Energy*, March, 1999. 23
- [79] J. C. Sautet, L. Salentey, M. Ditaranto, and J. M. Samaniego. Length of natural gas-oxygen non-premixed flames. *Combustion Science and Technology*, 166:131–150, 2001. 23
- [80] M. Ditaranto and J. Hals. Combustion instabilities in sudden expansion oxy-fuel flames. *Combustion and Flame*, 146:493–512, 2006. 23
- [81] T. C. Williams, C. R. Shaddix, and R. W. Schefer. Effect of syngas composition and CO₂-diluted oxygen on performance of a premixed swirl-stabilized combustor. *Combustion Science and Technology*, 180:64–88, 2008. 24

- [82] R. S. Barlow. Laser diagnostics and their interplay with computations to understand turbulent combustion. In *Proceedings of the Combustion Institute*, volume 31, pages 49–75, 2007. 31
- [83] K. Kohse-Hoeinghaus and J. B. Jeffries. *Applied combustion diagnostics*. Taylor and Francis, 2002. 31
- [84] C. J. Lawn. Distributions of instantaneous heat release by the cross-correlation of chemiluminescent emissions. *Combustion and Flame*, 123:227–240, 2000. 31
- [85] H. N. Najm, P. H. Paul, C. J. Mueller, and Wyckoff. P. S. On the Adequacy of Certain Experimental Observables as Measurements of Flame Burning Rate. *Combustion and Flame*, 113:312–332, 1998. 31
- [86] H. Buechner, C. Hirsch, and W. Leuckel. Experimental investigations on the dynamics of pulsed premixed axial jet flames. *Combustion Science and Technology*, 94:219–228, 1993. 32
- [87] J. O Keller and K. Saito. Measurements of the combusting flow in a pulse combustor. *Combustion Science and Technology*, 53:137–163, 1987. 32
- [88] C. O. Paschereit, E. Gutmark, and W. Weisenstein. Control of thermoacoustic instabilities and emissions in an industrial-type gas-turbine combustor. In *Twenty-Seventh Symposium (International) on Combustion*, 1998. 32
- [89] C. J. Dasch. One-dimensional tomography: a comparison of Abel, onion-peeling, and filtered backprojection methods. *Applied Optics*, 31, 8, 1992. 32
- [90] N. Anikin, R. Suntz, and H. Bockhorn. Tomographic reconstruction of the OH*-chemiluminescence distribution in premixed and diffusion flames. *Applied Physics B: Lasers and Optics*, 100:675–694, 2010. 32
- [91] N. A. Worth and J. R. Dawson. Tomographic reconstruction of OH*-chemiluminescence in two interacting turbulent flames. *Measurement Science and Technology*, 24:1–11, 2013. 32
- [92] O. H. Nestor and H. N. Olsen. Numerical methods for reducing line and surface probe data. *SIAM review*, 2-3, 1960. 32
- [93] H. Chehouani and M. El Fagrich. Adaptation of the Fourier-Hankel method for deflection tomographic reconstruction of axisymmetric field. *Applied Optics*, 52-3:439–448, 2013. 32

- [94] E. Durst, A. Melling, and J. H. Whitelaw. *Principles and practice of Laser-Doppler anemometry*. Academic Press Inc (London), 1976. 33
- [95] M. Raffel, C. E. Willert, S. T. Wereley, and J. Kompenhans. *Particle image velocimetry: A practical guide*. Springer, 2007. 33, 35
- [96] R. J. Adrian and J. Westerveel. *Particle image velocimetry*. Cambridge University Press, 2011. 33, 61
- [97] G. Berkooz, P. Holmes, and J. L. Lumley. The proper orthogonal decomposition in the analysis of turbulent flows. *Annual Review of Fluid Mechanics*, 25:539–575, 1993. 36
- [98] M. Stoehr, R. Sadanandan, and W. Meier. Phase-resolved characterization of vortex-flame interaction in a turbulent swirl flame. *Experiments in Fluids*, 51:1153–1167, 2011. 36, 81
- [99] L. Sirovich. Turbulence and the dynamics of coherent structures part I: coherent structures. *Quarterly of Applied Mathematics*, XLV:561–571, 1987. 36
- [100] LaVision GmbH. *DaVis 8.0 software manual*. 36
- [101] C. V. Raman and K. S. Krishnan. A new type of secondary radiation. *Nature*, 121:501–502, 1928. 37
- [102] A. C. Eckbreth. *Laser diagnostics for combustion temperature and species*. Gordon and Breach Science Publishers, 1996. 37, 39
- [103] Siemens. *Sitrans FC Massflo Handbook[®]*. 44
- [104] Brooks instrument. *Brooks[®] Smart-Series digital mass flow meters and controllers: Installation and Operation Manual*. 45
- [105] <http://www.sulzer.com/en/Products-and-Services/Agitators-Mixers-and-Dispensers/Static-Mixers>. 45
- [106] H. Ax, P. Kutne, W. Meier, K. Koenig, U. Maas, A. Class, and M. Aigner. Low pressure premixed CH₄/air flames with forced periodic mixture fraction oscillations: Experimental approach. *Applied Physics B: Lasers and Optics*, 94:705–714, 2009. 49
- [107] S. Prucker, W. Meier, and W. Stricker. A flat flame burner as calibration source for combustion research: Temperatures and species concentrations of premixed H₂/air flames. *Review of Scientific Instruments*, 65:2908–2911, 1994. 51, 52

-
- [108] P. Weigand, R. Lueckerath, and W. Meier. Documentation of flat premixed CH₄/air standard flames: Temperatures and species concentrations. Technical report, Institute of Combustion Technology, DLR, Stuttgart, -. 52
- [109] C. Morley. Gaseq v 0.79. <http://www.gaseq.co.uk/>, 2005. 52, 58
- [110] E. Colombo. Kalibrierung einer 1D Raman Messanlage und Validierung durch Einzelschussmessung einer Standard-Jetflamme. Technical report, Institute of Combustion Technology, DLR, Stuttgart, 2005. 52
- [111] U. Stopper. *Weiterentwicklung und Anwendung der Laser-Raman-Streuung zur Untersuchung industrieller Vormischflammen in einer Hochdruckbrennkammer*. PhD thesis, University of Stuttgart / DLR, Institute of Combustion Technology, 2014. 52
- [112] Bronkhorst HIGH-TECH. *General instructions digital mass Flow / Pressure instruments laboratory style / IN-FLOW*. 53
- [113] Bronkhorst CORI-TECH. *General instructions digital mass flow instrument CORI-FLOW*. 53
- [114] T. G. Beckwith, N. L. Buck, and R. D. Maragoni. *Mechanical measurements*. Addison-Wesley Publishing Company, Inc, 1995. 55
- [115] H. Ax. *Experimentelle Untersuchung magerer laminarer Niederdruckflammen mit periodisch variierender Gemischzusammensetzung*. PhD thesis, University of Stuttgart / DLR, Institute of Combustion Technology, 2013. 59
- [116] N. J. Lawson and J. Wu. Three-dimensional particle image velocimetry: experimental error analysis of a digital angular stereoscopic PIV system. *Measurement Science and Technology*, 8:1455–1464, 1997. 63
- [117] M. Stoehr and P. Weigand. Photographs and OH*-chemiluminescence image of swirl stabilized flames. Internal communication. 65
- [118] W. Meier, X.R. Duan, and P. Weigand. Reaction zone structures and mixing characteristics of partially premixed swirling CH₄/air flames in a gas turbine model combustor. In *Proceedings of the Combustion Institute* [118], pages 835–842. 68, 152
- [119] M. Stoehr. PIV velocity field of methane/air swirl stabilized flame. Internal communication. 69

- [120] X. R. Duan, W. Meier, P. Weigand, and B. Lehmann. Phase-resolved laser Raman scattering and laser Doppler velocimetry applied to periodic instabilities in a gas turbine model combustor. *Applied Physics B: Lasers and Optics*, 80:389–396, 2005. 71
- [121] R. Giezendanner-Thoben, U. Meier, W. Meier, and M. Aigner. Phase-locked temperature measurements by two-line OH PLIF thermometry of a self-excited combustion instability in a gas turbine model combustor. *Flow, Turbulence and Combustion*, 75:317–333, 2005. 71
- [122] R. Giezendanner-Thoben. *Untersuchung von Verbrennungsinstabilitäten mit phasenkorrelierten Lasermesstechniken*. PhD thesis, University of Stuttgart / DLR, Institute of Combustion Technology, 2006. 71
- [123] M. Stoehr and W. Meier. Coherent structures in partially premixed swirling flames. In *12th International Symposium On Flow Visualization*, 2006. 72
- [124] M. Stoehr, R. Sadanandan, and W. Meier. Experimental study of unsteady flame structures of an oscillating swirl flame in a gas turbine model combustor. In *Proceedings of the Combustion Institute*, 2009. 72
- [125] I. Boxx, M. Stoehr, C. Carter, and W. Meier. Temporally resolved planar measurements of transient phenomena in a partially pre-mixed swirl flame in a gas turbine model combustor. *Combustion and Flame*, 157:1510–1525, 2010. 72
- [126] M. Stoehr and W. Meier. Experimental and Numerical Study of Limit-cycle Thermoacoustic Oscillations in a Gas Turbine Model Combustor. In *European Combustion Meeting, Lund, Sweden*, 2013. 98, 99
- [127] Y. Dong, C. M. Vagelopoulos, G. R. Spedding, and F. N. Egolfopoulos. Measurement of laminar flame speeds through digital particle image velocimetry: Mixtures of methane and ethane with hydrogen, oxygen, nitrogen, and helium. In *Proceedings of the Combustion Institute*, volume 29, pages 1419–1426, 2002. 114
- [128] C. M. Vagelopoulos and F. N. Egolfopoulos. Direct experimental determination of laminar flame speeds. In *Twenty-Seventh Symposium (International) on Combustion / The Combustion Institute*, pages 513–519, 1998. 114
- [129] R. Wille and H. Fernholz. Report on the first European mechanics colloquium, on the Coanda effect. *Journal of Fluid Mechanics*, 23-4:801–819, 1965. 137

Resume

Personal details

Name	Bhavin K Kapadia
Date of Birth	19. September 1980
Place of Birth	Valsad, India
Citizenship	Indian

Education

04/1989-06/1998	Clarence High School - Bangalore, India
09/1998-09/2002	P.E.S Institute of Technology - Bangalore, India Bachelor of Mechanical Engineering
08/2003-02/2006	Indian Institute of Science - Bangalore, India Master of Science (Mechanical Engineering) Development of a single cylinder SI engine for Biogas operation

Work experience

03/2006-08/2008	Senior Engineer Honeywell Technology Solutions - Bangalore, India Evaluation and application of combustion models in aircraft engine CFD simulation software
10/2008-03/2015	Scientific Assistant and PhD Student Institute of Combustion Technology, German Aerospace Center - Stuttgart, Germany Application of optical and laser based measurement techniques such as OH*-chemiluminescence, PIV and Raman Spectroscopy in the development of gas turbine burners and fuel cells
04/2015 - 11/2015	Engineering Consultant Alten Engineering - Ruesselsheim, Germany Development of high pressure fueling systems for multicylinder gasoline engines
12/2015 -	Design Responsible Engineer Adam Opel AG - Ruesselsheim, Germany Design, development and release of high pressure fueling systems for multicylinder gasoline SI engines